Exact diagonalization studies of quantum simulators

A dissertation submitted for the degree of *Philosophiæ Doctor*

David Raventós i Ribera

Institute of Photonic Sciencies, ICFO

Abstract

Understand and tame complex quantum mechanical systems to build quantum technologies is one of the most important scientific endeavour nowadays. In this effort, Atomic, molecular and Optical systems have clearly played a major role in producing proofs of concept of several important applications. Notable examples are Quantum Simulators for difficult problems in other branches of physics i.e. spin systems, disordered systems, etc., and small sized Quantum Computers. In particular, ultracold atomic gases and trapped ion experiments are nowadays at the forefront in the field.

This fantastic experimental effort needs to be accompanied by a matching theoretical and numerical one. The main two reasons are: 1) theoretical work is needed to identify suitable regimes where the AMO systems can be used as efficient quantum simulators of important problems in physics and mathematics, 2) thorough numerical work is needed to benchmark the results of the experiments in parameter regions where a solution to the problem can be found with classical devices.

In this dissertation, we present several important examples of systems, which can be numerically solved. The technique used, which is common to all the work presented in the dissertation, is exact diagonalization. This technique works solely for systems of a small number of particles and/or a small number of available quantum states. Despite this limitation, one can study a large variety of quantum systems in relevant parameter regimes. A notable advantage is that it allows one to compute not only the ground state of the system but also most of the spectrum and, in some cases, to study dynamics.

The dissertation is organized in the following way. First, we provide an introduction, outlining the importance of this technique for quantum simulation and quantum validation and certification. In Chapter 2, we detail the exact diagonalization technique and present an example of use for the phases of the 1D Bose-Hubbard chain. Then in Chapters 3 to 6, we present a number of important uses of exact diagonalization. In Chapter 3, we study the quantum Hall phases, which are found in two-component bosons subjected to artificial gauge fields. In Chapter 4, we turn into dynamical

gauge fields, presenting the topological phases which appear in a bosonic system trapped in a small lattice. In Chapter 5, a very different problem is tackled, that of using an ultracold atomic gases to simulate a spin model. Quantum simulation is again the goal of Chapter 6, where we propose a way in which the number-partitioning problem can be solved by means of a quantum simulator made with trapped ions. Finally, in Chapter 7, we collect the main conclusions of the dissertation and provide a brief outlook.

Extracte

Entendre i controlar sistemes complexos regits per la mecànica quàntica per a construir tecnologies quàntiques és un dels reptes més rellevants de la ciència en l'actualitat. Els sistemes atòmics, moleculars i òptics han jugat clarament un rol capital en aquest esforç, produint proves de concepte per a diverses aplicacions de consideració. Exemples notables en són els simuladors quàntics dissenyats per a resoldre problemes complicats d'altres branques de la física, com ara sistemes d'espins, sistemes desordenats, etc.... i ordinadors quàntics de dimensions reduïdes. En particular, els experiments amb gasos d'àtoms ultrafreds i amb trampes iòniques són la punta de llança del camp en l'actualitat.

El fantàstic afany experimental ha d'anar associat amb d'altres teòric i numèric que el corresponguin. Les raons principals són: 1) els estudis teòrics són necessaris per tal d'identificar règims adients en què els sistemes AMO puguin ésser emprats com a simuladors quàntics eficients de problemes rellevants de la Física i les Matemàtiques, 2) els treballs numèrics exhaustius són necessaris per a contrastar els resultats dels experiments en regions de paràmetres en què els dispositius clàssics són capaços de trobar solucions.

En aquesta tesi, presentem diversos exemples de sistemes rellevants que poden ésser resolts numèricament. La tècnica emprada –que és comuna per a tot el treball– és la diagonalització exacta. L'ús d'aquesta tècnica és limitat a sistemes amb nombres baixos partícules i/o pocs estats quàntics accessibles. Malgrat aquesta limitació, es poden estudiar una gran varietat de sistemes quàntics en els règims rellevants dels paràmetres de control. Un avantatge notable és el fet que permet calcular no només l'estat de mínima energia del sistema, sinó que també la majoria de l'espectre i, en alguns casos, àdhuc estudiar-ne la dinàmica.

La tesi s'organitza tal i com prossegueix. En primer lloc, proveïm una introducció, subratllant la importància d'aquesta tècnica per a la simulació quàntica i la validació quàntica i certificació. En el capítol 2, detallem la tècnica de la diagonalització exacta i presentem un exemple del seu ús per a les fases per a una cadena de Bose-Hubbard unidimensional. En els capítols del 3 al 6, presentem alguns usos rellevants de la diagonalització

exacta. En el capítol 3, estudiem les fases degudes a l'efecte Hall quàntic en un sistema de dues components de bosons sotmesos a camps de gauge artificials. En el capítol 4, canviem a camps de gauge dinàmics, presentant les fases topològiques que apareixen en un sistema de bosons atrapats en una petita xarxa reticular. En el capítol 5, s'hi tracta un problema ben diferent, el d'emprar gasos d'àtoms ultrafreds per a per a simular un model d'espín. La simulació quàntica és de nou l'objectiu del capítol 6, en què proposem una forma en què el problema de la partició de nombres pot ésser resolt per mitjà d'un simulador quàntic construït amb trampes iòniques. Finalment, en el capítol 7, recollim les conclusions principals del treball i donem una breu opinió del futur d'aquesta investigació.

Extracto

Entender y controlar sistemas complejos regidos por la mecánica cuántica para construir tecnologías cuánticas es una de los retos científicos más relevantes en la actualidad. Los sistemas atómicos, moleculares y ópticos han jugado claramente un rol capital en este esfuerzo, produciendo pruebas de concepto para diversas aplicaciones de consideración. Notables ejemplos son los simuladores cuánticos diseñados para resolver problemas complicados de otras ramas de la física, como lo son los sistemas de espines, sistemas desordenados, etc.... i los ordenadores cuánticos de dimensiones reducidas. En particular, los experimentos con gases de átomos ultrafríos y con trampas iónicas son la punta de lanza del campo en la actualidad.

El fantástico empeño experimental tiene que ir asociado a otros teórico y numérico que le correspondan. Las principales razones son: 1) los estudios teóricos son necesarios para identificar regímenes adecuados en que los sistemas AMO puedan ser usados cómo simuladores cuánticos eficientes para problemas relevantes de la Física y las Matemáticas, 2) los trabajos numéricos exhaustivos son necesarios para contrastar los resultados de los experimentos en regiones de parámetros en que los dispositivos clásicos sean capaces de encontrar soluciones.

En esta tesis, presentamos diferentes ejemplos de sistemas relevantes que pueden ser resueltos numéricamente. La técnica usada –que es común en todo el trabajo– es la diagonalización exacta. El uso de ésta técnica está restringido a sistemas con números bajos de partículas i/o estados cuánticos accesibles. A pesar de esta limitación, se puede estudiar gran variedad de sistemas cuánticos en los regímenes relevantes de los parámetros de control. Una ventaja notable es que permite calcular no sólo el estado de mínima energía del sistema, sino que también la mayoría del espectro e, en algunos casos, incluso estudiar la dinámica.

La tesis se organiza como sigue. En primer lugar, ofrecemos una introducción, subrayando la importancia de esta técnica para la simulación cuántica y la validación cuántica y certificación. En el capítulo 2, detallamos la técnica de la diagonalización exacta y presentamos un ejemplo de su uso para una cadena de Bose-Hubbard unidimensional. En los capítulos del 3 al

6, presentamos algunos usos relevantes de la diagonalización exacta. En el capítulo 3, estudiamos las fases debidas al efecto Hall cuántico en un sistema de dos componentes de bosones sometidos a campos de gauge artificiales. En el capítulo 4, cambiamos hacia campos gauge dinámicos, presentando las fases topológicas que aparecen en un sistema de bosones atrapados en una pequeña malla reticular. En el capítulo 5, se trata un problema bien diferente, el de usar gases de átomos ultrafríos para simular un modelo de espín. La simulación cuántica es de nuevo el objetivo del capítulo 6, en que proponemos una forma en que el problema de la partición de números puede ser resuelta mediante un simulador cuántico construido con trampas iónicas. Finalmente, en el capítulo 7, recogemos las conclusiones principales de los trabajos y damos una breve opinión del futuro de ésta investigación.

This dissertation could not have been possible without the guidance and collaboration of my colleagues at ICFO, specially the members of the Quantum Optics Theory group. I would like to thank Dr. Alessio Celi and Prof. Luis Santos for allowing me to contribute to their research. I am also very grateful for the opportunity given to me by Dr. Tao Shi and Prof. Ignacio Cirac and the research team at Max Planck Institut für Quantenoptik.

Exceptional greetings should be given to Dr. Tobias Graß, and my supervisors Prof. Bruno Juliá Díaz and Prof. Maciej Lewenstein, not only for their unavoidable guidance and apparently infinite wisdom, but also for their priceless support. If I would have to start a PhD thesis again, the only thing I knew would be who I wanted to be the advisors without thinking twice about it.

I would like to also greet my parents and my brother for their support during the course of the different degrees I have been through. Special greetings should be given as well to my partner, Iris Llop, for her undying support under any circumstance.

Contents

1 Introduction 15

2 Cold bosons in optical lattices: a tutorial for Exact Diagonalization 21

- 2.1 Introduction 21
- 2.2 The Bose-Hubbard model and its characterization 24
  - 2.2.1 Useful quantities 25
  - 2.2.2 Phases of the BH model 28
- 2.3 Exact diagonalization 31
  - 2.3.1 Basis states and their ordering 33
  - 2.3.2 Use of sparse matrices to store the Hamiltonian matrix 34
  - 2.3.3 Geometry of the lattice 36
  - 2.3.4 Diagonalizing the Hamiltonian 37
- 2.4 Boundary between Mott insulator and superfluid 39
  - 2.4.1 Overlap. 40
  - 2.4.2 Insulating gap. 43
  - 2.4.3 Finite-size effects of the gap. 48
  - 2.4.4 Summary 52
- 2.5 Beyond the standard BHM 52
  - 2.5.1 Phase transitions in a deeply biased lattice 53
  - 2.5.2 Attractive interactions: Localization 56
  - 2.5.3 Exact Diagonalization for other problems: quantum Hall physics 59

3 Quantum Hall phases of two-component bosons 61

- 3.1 Introduction 61
- 3.2 System and trial wave functions. 65
- 3.3 Yrast line. 67
- 3.4 Edge physics of the IQH phase. 67
- 3.5 Backward moving edge states. 69
- 3.6 Forward moving edge states. 71

3.7 Experimental realization. 73
3.8 Conclusions. 73

4 Topological phases of lattice bosons with a dynamical gauge field 75
4.1 Introduction 75
4.2 Theoretical model 77
4.3 Energy gaps 79
  4.3.1 Case of one excess particle 81
  4.3.2 Mott insulator 84
  4.3.3 Case of one hole 86
4.4 Topological phases 86
  4.4.1 Single particle and non-interacting cases 86
  4.4.2 Interacting many-body case 88
  4.4.3 Static field case 88
4.5 Mean field Phase diagram 89

5 Modified spin-wave theory of cold bosons on an inhomogeneous triangular lattice 95
5.1 Introduction 95
5.2 Basics of SQL physics 97
5.3 Description of the atomic model and map to the spin model 101
5.4 Modified spin-wave theory 105
5.5 Result from the modified spin wave analysis 115
  5.5.1 Optimization and stability 115
  5.5.2 Phase diagram predicted by spin wave at half-filling 117
  5.5.3 Phase diagram predicted by spin wave at generic filling 118
5.6 Exact diagonalization study 120
  5.6.1 Homogeneous system ($V_i = 0$) 122
  5.6.2 Inhomogeneous system ($V_i \neq 0$) 134
5.7 Conclusions and Outlook 139

6 Quantum annealing for the number partitioning problem using a tunable spin glass of ions 143
6.1 Introduction 143
6.2 Quantum annealing in spin glass systems of trapped ions . 144
6.3 Results 149
    6.3.1 Tunable spin-spin interactions 149
    6.3.2 Classical Mattis model 151
    6.3.3 Increasing complexity 153
    6.3.4 Quantum phases 155
    6.3.5 Simulated quantum annealing 159
    6.3.6 Scalability 161
    6.3.7 Spin pattern in the quantum Mattis model 165
6.4 Details of the semiclassical approximation 168
    6.4.1 Hamiltonian 169
    6.4.2 Equations of motion 170
    6.4.3 Annealing protocol 170
    6.4.4 Fidelity of the annealing protocol 172
    6.4.5 Semiclassical approximation 173
    6.4.6 Comparison to full quantum evolution 174
6.5 Finite temperature effects on the annealing protocol 180
    6.5.1 Classical thermal phonons 180
    6.5.2 Effects of temperature on the protocol 181
    6.5.3 Thermal tolerance of the Lamb-Dicke regime 183

7 Conclusions 185

A Appendix 193
A.1 Subroutines for the labelling procedure 193
A.2 Composite Fermion construction 196
A.3 Evaluation of the Chern number 200
A.4 Robustness of the semiclassical calculation 203
A.5 Optimal bias for the exponential annealing function 203

Bibliography 204

CHAPTER 1

INTRODUCTION

The central theme of this doctoral thesis are exact diagonalizations. The exact diagonalization is a method that can be used to analyse not too large closed quantum many body systems, described by an Hamiltonian. Using exact diagonalization one can analyse the static properties of the system in question, i.e. its ground state or low energy excited states. Alternatively, one can use these states to study the Hamiltonian dynamics of the system.

Even though, due to numerical complexity, one can apply exact diagonalization only to the systems of small, or better to say not too large size, the method is very successful for the following reasons:

- The method has a direct experimental relevance, since many experiments are performed with small or moderate size systems;
- Recent papers indicate that attaching moderate size systems to "entanglement bath" on the boundary might mimic perfectly statics, and even thermodynamics of infinite systems [1];
- Last, but not least, the results obtained with exact diagonalization

may be used for finite size scaling, and thus may allow to infer about the thermodynamical limit.

There are two areas of the contemporary quantum many body physics with which exact diagonalizations are intimately connected: quantum simulations, one of the four pillars of the quantum technologies, and quantum certification and validation, an absolutely essential part of all of the quantum technologies, unfortunately sometimes forgotten and neglected. We comment on them below.

Quantum simulators (QS) Quantum simulators constitute one of the most mature pillars of quantum technologies. As pointed out in [2], the first book devoted entirely to quantum simulators, the ideology of QS may be described as follows: There exist many interesting quantum phenomena/classical hard-to-compute problems (example: superconductivity, travelling salesman) These phenomena may have important applications but are often difficult to be described/understood with standard computers. Maybe we can use another, simpler and better controllable quantum system to simulate, understand and control these phenomena? Such a system would thus work as quantum computer of special purpose, i.e. quantum simulators [3] QS of strongly correlated quantum systems were first proposed in the context of ultracold atoms in optical lattices for the Bose Hubbard model in [4], and confirmed in experiment in [5]. Although it is perhaps still too early to confirm their genuine quantum advantage, for the last decade they start to provide results that can hardly be achieved by the classical supercomputers (for reviews see [2, 6–11]). So far, QS concern mostly the models and problems of condensed matter physics, but they start to address hard-to-simulate-classically questions of high energy physics, computer science and mathematics. Quantum annealers, such as D-Wave machines address general (even NP-complete) classical optimization problems. QS may be realized in many platforms, such as for instance ultracold trapped atoms (cf. [12, 13]), ultracold atoms in optical lattices (cf. [14, 15]), atoms in arrays of optical tweezers [16], ultracold trapped ions [17], quantum dots arrays [18], NV-centers in diamond [19], circuit

QED [11], Josephson/supeconducting qubit arrays [20], polariton systems [21, 22], photonic platforms [10, 23]. Just to quote very recent spectacular achievements of QS, let us mention recent works on Fermi Hubbard model [24], quantum many body localization [25], or quantum droplets [26]. So far, most of the experimental realization of QS concern problems that belong to physics: AMO, condensed matter. The experimens on QS of high energy physics problems have only begun, and mostly concern toy models [27, 28]. D-Wave machines and similar machines based on superfluid qubits offer solutions of NP-hard optimization problems, using quantum annealing, or better to say adiabatic quantum computing. D-Wave claim also to be able to solve some optimization/sampling problems relevant to machine learning applications. The challenges of QS design concern thus alternatives to existing quantum annealing that could offer alternative approaches to NP-hard problems. Extending the areas of science covered by QS might serve to meet these challenges.

Quantum validation and certification (QVC) This is the area of quantum information science that deals with validating and certifying that what we generate in experiments is actually what we want to generate. For QS of hard to compute systems, one usually seeks regime of parameters, where the classical simulations are efficient and validate the results there [2]. Quantum certifications are aimed at demonstration that quantum states obtained in simulation/preparation protocols do have the desired quantum properties with respect to correlations, entanglement, non-locality, etc. This inevitably related to the studies of entanglement [2, 29, 30], area laws [31–38] and non-locality [39] in many body systems. Obviously, the primary applications of QVC methods are at the QS-QVC link. Validation and certification requires precise experimental detection methods such for instance atomic microscope with single site resolution [14, 15, 40], combined with novel theoretical tools, such as state-of-art quantum Monte Carlo (QMC) methods [41]. For estimation of ground states energy/cost function of the system/optimization problem in question, one can frequently use variational methods to obtain upper bounds. There exist also semi-definite programming methods to obtain lower bounds [42–44]. Robustness of QS can be tested by employing controlled disorder or noise [45]. Entanglement certification can be achieved by measuring Rényi entanglement entropies. Originally, the idea was to consider two or more copies of the system in question [46], but the experimental realization of it was very demanding [47]. In Refs. [48, 49] a splendid trick was proposed to extract Rényi entropies from applying random unitary operations to the single system – similar trick was used to characterize entanglement on many body localization in Ref. [50]. Certification should in principle be based on device independent quantum information processing (DIQIP) [51], and, indeed, recently there were several proposals for DI entanglement certification [52], nonlocality [53, 54], nonlocality depth [55], and entanglement depth [56].

Validation is possible by going to the regime of parameters where the QS is accessible to efficient classical simulation. This may happen for large systems in some situations (lack of frustration, etc., ...), but it practically always happen for not too large systems. This is exactly the domain of exact diagonalizations.

Below we describe in short the contents of the subsequent chapters of this thesis. Each of these chapters is based on original results and a paper in the internationally acclaimed journal.

Plan of the thesis

Chapter 2 is based on original tutorial article about exact diagonalizations, published in Journal of Physics B [57]. Exact diagonalization techniques are a powerful method for studying many-body problems. Here, we apply this method to systems of few bosons in an optical lattice, and use it to demonstrate the emergence of interesting quantum phenomena like fragmentation and coherence. Starting with a standard Bose-Hubbard Hamiltonian, we first revise the characterization of the superfluid to Mott insulator transitions. We then consider an inhomogeneous lattice, where one potential minimum is made much deeper than the others. The Mott insulator phase due to repulsive on-site interactions then competes with the trapping of all atoms in the deep potential. Finally, we turn our attention to attractively interacting systems, and discuss the appearance of strongly correlated phases and the onset of localization for a slightly biased lattice. The chapter is intended to serve as a tutorial for exact diagonalization of Bose-Hubbard models.

Chapter 3 is based on the original article, published in Phys. Rev. B [58]. The recent production of synthetic magnetic fields acting on electroneutral particles, like atoms or photons, has boosted the interest in the quantum Hall physics of bosons. Adding pseudospin-1/2 to the bosons greatly enriches the scenario, as it allows them to form an interacting integer quantum Hall (IQH) phase with no fermionic counterpart. Here we show that, for a small two-component Bose gas on a disk, the complete strongly correlated regime, extending from the integer phase at filling factor $\nu = 2$ to the Halperin phase at filling factor $\nu = 2/3$, is well described by composite fermionization of the bosons. Moreover we study the edge excitations of the IQH state, which, in agreement with expectations from topological field theory, are found to consist of forward-moving charge excitations and backward-moving spin excitations. Finally, we demonstrate how pair-correlation functions allow one to experimentally distinguish the IQH state from competing states, like non-Abelian spin singlet (NASS) states.

Chapter 4 is based on the original article, published in Phys. Rev. A [59]. Optical lattices with a complex-valued tunnelling term have become a standard way of studying gauge-field physics with cold atoms. If the complex phase of the tunnelling is made density-dependent, such system features even a self-interacting or dynamical magnetic field. In this chapter we study the scenario of a few bosons in either a static or a dynamical gauge field by means of exact diagonalization. The topological structures are identified computing their Chern number. Upon decreasing the atom-atom contact interaction, the effect of the dynamical gauge field is enhanced, giving rise to a phase transition between two topologically non-trivial.

Chapter 5 is based on an original article, published in Phys. Rev. B [60]. Ultracold bosons in a triangular lattice are a promising candidate for observing quantum spin liquid behaviour. Here we investigate, for such system, the role of a harmonic trap giving rise to an inhomogeneous density. We construct a modified spin-wave theory for arbitrary filling, and predict the breakdown of order for certain values of the lattice anisotropy. These regimes, identified with the spin liquid phases, are found to be quite robust upon changes in the filling factor. This result is backed by an exact diagonalization study on a small lattice.

Chapter 6 is based on several original publications [61, 62], Exploiting quantum properties to outperform classical ways of information-processing is an outstanding goal of modern physics. A promising route is quantum simulation, which aims at implementing relevant and computationally hard problems in controllable quantum systems. Here we demonstrate that in a trapped ion setup, with present day technology, it is possible to realize a spin model of the Mattis type that exhibits spin glass phases. Remarkably, our method produces the glassy behaviour without the need for any disorder potential, just by controlling the detuning of the spin-phonon coupling. Applying a transverse field, the system can be used to benchmark quantum annealing strategies which aim at reaching the ground state of the spin glass starting from the paramagnetic phase. In the vicinity of a phonon resonance, the problem maps onto number partitioning, and instances which are difficult to address classically can be implemented.

Recently it has been demonstrated that an ensemble of trapped ions may serve as a quantum annealer for the number-partitioning problem . This hard computational problem may be addressed employing a tunable spin glass architecture. Following the proposal of the trapped ions annealer, we study here its robustness against thermal effects, that is, we investigate the role played by thermal phonons. For the efficient description of the system, we use a semiclassical approach, and benchmark it against the exact quantum evolution. The aim is to understand better and characterize how the quantum device approaches a solution of, an otherwise, difficult to solve NP-hard problem.

Chapter 7, finally, contains our conclusions and outlook.

CHAPTER 2

COLD BOSONS IN OPTICAL LATTICES: A TUTORIAL FOR EXACT DIAGONALIZATION

2.1 Introduction

The Bose-Hubbard model (BHM), originally introduced in order to describe different phenomena in condensed matter physics [63], has gained new impact in the field of quantum gases [2], following the experimental realization of the model in a setup with cold atoms in optical lattices [5]. In particular, the prediction of a phase transition from a superfluid (SF) to a Mott insulator (MI) has been confirmed. The origin of this transition is genuinely quantum, that is, it is driven by quantum fluctuations, which are controlled by the Hamiltonian parameters, interaction and hopping strength, and which are present also at zero temperature.

The advantages offered by cold atoms for studying quantum phase transitions are clear. First, in these systems, high isolation from the surrounding environment is achievable. There have been recent advances in producing different sort of lattice configurations, determining the Hamiltonian parameters. Second, atom-atom interactions are tunable via Feshbach resonances. These properties allow one to use ultracold atomic systems as quantum simulators of theoretical models that are not tractable with classical computers. Although different techniques are able to capture ground state properties of the Bose-Hubbard Hamiltonian, the solution of the full model, that is complete spectrum and eigenstates, appears to be intractable with classical techniques. Exact diagonalization techniques, which in principle allow one to solve the full problem with high accuracy, suffer from the clear shortcoming of being restricted to fairly small many-body quantum systems [64].

Several approaches have been used to study the BHM: Bogoliubov techniques at small interactions [65], perturbative ones at large interactions [66, 67], Gutzwiller mean-field approaches [4, 68], field-theoretic studies [69–71], etc. Ground state properties can be studied by means of DMRG methods [72, 73] and Quantum Monte-Carlo techniques [74].

While the phase boundary between the Mott insulating phase and the superfluid phase is well-defined in the thermodynamic limit, where symmetry-breaking gives rise to a non-zero order parameter, the situation is less unique for finite systems. In particular, as reviewed in Ref. [75] and also pointed out in [73], there is still uncertainty on the precise value of the transition from Mott to superfluid in 1D systems. In particular quantum Monte-Carlo studies have produced slightly disagreeing results on the critical value of the parameters [76–78]. In view of this, further study of the Mott transition is needed, using different techniques and applying different definitions. Here, exact methods allow to extract quantities not reachable by means of other methods, such as eigenstates, eigenenergies and the entanglement spectrum.

In this work we consider small lattices which we study using exact diagonalization (ED). We apply and compare different signatures of the MI-SF transition: Given the full ground state of the system, a simple figure of merit is the overlap between the numerical solution and analytical trial states for the Mott and the SF phase. To capture the phase boundary more accurately, we extract the single-particle insulating gap from the energy spectra at different numbers of atoms. Performing a finite size scaling, we determine the parameters for which the gap would close in the thermodynamic limit, indicating the transition to the superfluid phase.

Interesting new phenomena are brought into the problem by a simple modification of the model, assuming a lattice with one highly biased site attracting the atoms. This gives rise to a series of quantum phase transitions upon changing the lattice depth: For certain values, number fluctuations in the system become strong while the average number of particles on the biased site is decreased by one.

Finally, we consider the case of attractive interactions. Similarly to the two-site case discussed in Refs. [79, 80], strong fragmentation is found in the ground state of the system for a small attractive interaction. Direct diagonalization allows us to quantitatively discuss the appearance of many-body correlations in the ground state. Considering a slightly biased lattice, we study the onset of localization in the system as the attraction is increased.

The present chapter is also intended to provide a detailed, tutorial like, description of the methods employed to perform the exact diagonalization of the model. Our work complements other tutorial like ones, like reference [81], as we also incorporate a state-of-the-art discussion of the definition of the transition between the MI and superfluid phases.

This work is organized as follows: The BHM is introduced in Sec. 2.2. In Sec. 2.2.1, we introduce different quantities used to characterize the system behaviour, such as eigenvalues of the one body density matrix, and the populations of the Fock states. They allow us to discern if the system is condensed and to measure its spatial correlations. We also define different entropies in order to capture important properties about the system with a single scalar value. In Sec. 2.2.2, we present the phases exhibited by the Bose-Hubbard model. In Sec. 2.3 we explain the exact diagonalization techniques used together with a detailed description of how to perform them. In Sec. 2.4 we present the U/t value at which the MI-SF phase transition takes place for the BHM at filling 1, applying several finite size studies to our exact diagonalization results. In Sec. 2.5, we go beyond the standard BHM: In Sec. 2.5.1, we study an inhomogeneous lattice, and observe several transitions as the hopping and/or interaction strengths are varied, and in

Sec. 2.5.2, we turn to attractive interactions, focusing on the appearance of correlated states. In Sec. 2.5.3, the reader is briefly introduced to the treatment of quantum Hall effects with Exact Diagonalization.

2.2 The Bose-Hubbard model and its characterization

We start considering the standard Bose-Hubbard model which contains two terms: the hopping term, which allows the exchange of particles between the sites, related to the kinetic energy, and the on-site interaction term, which can be repulsive or attractive. The Hamiltonian of the model reads,

$$\hat{\mathcal{H}} = -\sum_{j\neq k}^{M} t_{k,j}\hat{a}_j^\dagger \hat{a}_k + \frac{U}{2}\sum_{i=1}^{M}\hat{n}_i(\hat{n}_i - 1) \equiv \sum_{j\neq k}^{M}\hat{\mathcal{T}}_{k,j} + \sum_{i=1}^{M}\hat{\mathcal{U}}_i \tag{2.1}$$

where $\hat{a}_j^\dagger$ ($\hat{a}_j$) creates (annihilates) one particle in the jth site and $\hat{n}_i = \hat{a}_i^\dagger \hat{a}_i$ is the number of particles operator in the ith site, being M the number of sites. A convenient finite basis, with a fixed number of particles N, is given by the states of the Fock space restricted to N particles,

$$|\beta\rangle \equiv \left|n_1^\beta, n_2^\beta, \cdots, n_M^\beta\right\rangle \equiv \frac{1}{\sqrt{n_1! n_2! \dots n_M!}}\left(\hat{a}_1^\dagger\right)^{n_1}\left(\hat{a}_2^\dagger\right)^{n_2} ... \left(\hat{a}_M^\dagger\right)^{n_M}|\text{vac}\rangle \tag{2.2}$$

where n_i^β is the number of bosons at the ith site in the state $|\beta\rangle$, and β is the labelling of the Fock states. Since the number of bosons N in the system is fixed, n_i^β satisfies $\sum_i^M n_i^\beta = N$ for any state $|\beta\rangle$. Arbitrary states can be written in this orthogonal basis,

$$|\Phi\rangle = \sum_{\beta}^{\mathcal{N}_N^M} c_\beta |\beta\rangle , \tag{2.3}$$

with $c_\beta \in \mathbb{C}$. For total number of bosons N and sites M there are $\mathcal{N}_N^M$ Fock states in the basis. This number is the number of ways of placing N

particles in M sites, see Table 2.1,

$$\mathcal{N}_N^M = \binom{N+M-1}{N} = \frac{(N+M-1)!}{N!\,(M-1)!} \,. \tag{2.4}$$

If the particles were fermions instead of bosons, the number of basis states is,

$$\mathcal{N}_N^{M,\text{fermions}} = \binom{M}{N} \,. \tag{2.5}$$

2.2.1 Useful quantities

Let us introduce some quantities that we will use in this work to discuss the characterization of the BHM.

Fragmentation in the ultracold gas.

The generalization of the concept of Bose-Einstein condensation to interacting systems was introduced by Penrose and Onsager [82, 83]. They established a condensation criterion in terms of the one-body density matrix (OBDM),

$$\rho^{(1)}\left(\mathbf{r},\mathbf{r}'\right) = \left\langle \psi^\dagger\left(\mathbf{r}'\right)\psi\left(\mathbf{r}\right)\right\rangle , \tag{2.6}$$

where the field operator $\psi^\dagger$ creates a boson at position $\mathbf{r}$ and $\langle\cdots\rangle$ is the thermal average at temperature T. Since $\rho^{(1)}$ is a Hermitian matrix, it can be diagonalized. The eigenvectors are termed natural orbitals, and the eigenvalues are their corresponding populations.

The way to find out if a given state is condensed involves the computation of the OBDM and its diagonalization in order to study the size of the populations of its eigenstates. In second quantization, the definition of the OBDM $\rho_{k,l}$ of a state $|\Phi\rangle$ is,

$$\rho_{k,l} = \langle\Phi|\,\hat{a}_l^\dagger\hat{a}_k\,|\Phi\rangle \,. \tag{2.7}$$

N,M	1	2	3	4	5	6	7	8	9	10	11	12	13
1	1	2	3	4	5	6	7	8	9	10	11	12	13
2	1	3	6	10	15	21	28	36	45	55	66	78	91
3	1	4	10	20	35	56	84	120	165	220	286	364	455
4	1	5	15	35	70	126	210	330	495	715	1001	1365	1820
5	1	6	21	56	126	252	462	792	1287	2002	3003	4368	6188
6	1	7	28	84	210	462	924	1716	3003	5005	8008	12376	18564
7	1	8	36	120	330	792	1716	3432	6435	11440	19448	31824	50388
8	1	9	45	165	495	1287	3003	6435	12870	24310	43758	75582	125970
9	1	10	55	220	715	2002	5005	11440	24310	48620	92378	167960	293930
10	1	11	66	286	1001	3003	8008	19448	43758	92378	184756	352716	646646
11	1	12	78	364	1365	4368	12376	31824	75582	167960	352716	705432	1352078
12	1	13	91	455	1820	6188	18564	50388	125970	293930	646646	1352078	2704156
13	1	14	105	560	2380	8568	27132	77520	203490	497420	1144066	2496144	5200300

Table 2.1: Size of the Hilbert space for N bosons in M sites, $\mathcal{N}_N^M$ for $N, M = 1, \ldots, 13$.

But writing the state $|\Phi\rangle$ as in Eq. (2.3), we explicitly get,

$$\rho_{k,l} = \sum_{\alpha,\beta}^{\mathcal{N}_N^M} c_\alpha^* c_\beta \langle\alpha| \hat{a}_l^\dagger \hat{a}_k |\beta\rangle \,. \tag{2.8}$$

From the diagonalization of the OBDM in an arbitrary basis, one obtains,

$$\rho_{i,j} = n_i^{\mathrm{OBDM}} \delta_{i,j} \,, \tag{2.9}$$

where n_i^{OBDM} is the ith largest eigenvalue of the OBDM.

In order to simplify the information given by the eigenvalues of the OBDM of a given state, we introduce an entropy based on the von Neumann one, S_1, which will be used in the following. It is defined as,

$$S_1 = -\sum_{i}^{M} p_i \ln p_i \,, \tag{2.10}$$

with $p_i = n_i^{\mathrm{OBDM}}/N$ the normalized eigenvalues of the OBDM. So, $\sum_i p_i = 1$. The minimum of S_1 is 0 and corresponds to $p_i = \delta_{i,1}$. The entropy S_1 has a maximum which equals $\ln M$ when $p_i = 1/M$, $\forall i$. So, its maximum value corresponds to a uniform probability distribution (fragmented condensate [84]), whereas the minimum corresponds to a Kronecker-δ distribution, full condensation. In all computations, the entropy has been divided by its maximum value, $\ln M$, in order get a non-extensive quantity, bounded by 0 and 1.

The entropy S_1 measures condensation, as defined by the Penrose-Onsager criterion. When the value is 0, the system is condensed. When it is $\ln M$, it is completely fragmented. When the value is the logarithm of a certain integer r, the state is fragmented in r states.

Spatial correlations from Fock-space coefficients.

In order to quantify the correlations between the particles on different sites, we take advantage from the fact that our Fock basis builds on spatially localized single particle states. We define a second entropy S_D, which measures the clustering of particles in the Fock space,

$$S_D = -\sum_{\beta}^{\mathcal{N}_N^M} |c_\beta|^2 \ln |c_\beta|^2 \,, \tag{2.11}$$

where c_β are the coefficients of the decomposition of a given state into the Fock basis $|\beta\rangle$, Eq. (2.3). In the same way as the entropy S_1 allowed us to distinguish between condensed and fragmented states, the entropy S_D distinguishes between many-body states which are represented by a single Fock state ($S_D = 0$), and superpositions of many Fock states ($S_D > 0$). Apparently, if only few Fock states contribute to a many-body state, there is a high amount of spatial correlations in the system, which thus can be captured by the value of S_D. The entropy S_D is the von Neumann entropy of the diagonal ensemble after tracing off one site. This means that it provides the von Neumann entropy after a long-term time evolution in a local Hamiltonian $\hat{\mathcal{H}} = \sum_i \epsilon_i \hat{n}_i$, with ϵ_i local energies. Note that in the case of solely two-sites, the entropy S_D coincides with the left-right bipartite entropy [80].

2.2.2 Phases of the BH model

The homogeneous case of the Hamiltonian (2.1), with $t_{k,j} = t$, becomes exactly solvable in two limiting cases: $t/U = 0$ and $t/U \to \infty$. We take ground states in these two cases as analytical trial states for the two quantum phases exhibited by the model: the non-interacting limit provides a trial state for the SF phase, while the system without hopping yields a trial state for the MI phase.

Mott Insulator regime.

When $t/U \to 0$ with $U > 0$, the system is dominated by the repulsive interactions, and it minimizes energy by reducing the number of pairs in each site. So, the GS of the system is a state with $q \equiv N/M$ particles on each site, where q is a positive integer, i. e., a Mott insulator state. This corresponds to one many-body state of the Fock basis and it reads,

$$|\Phi_{\mathrm{MI}}(q)\rangle = \prod_{i=1}^{M} \frac{(\hat{a}_i^\dagger)^q}{\sqrt{q!}} |0\rangle = |q \cdots q\rangle \; . \tag{2.12}$$

The first excited state looks like a MI state where a particle has been annihilated in one site and created in a different site, i. e., it is a quasiparticle-quasihole excitation of the MI state. When the particle is created in the ith site and the hole is localized in the jth one, the first excited state reads,

$$|\Phi_{\mathrm{MI}}(q)\rangle^{(1)} = \frac{1}{q} \hat{a}_i^\dagger \hat{a}_j \, |\Phi_{\mathrm{MI}}(q)\rangle \, . \tag{2.13}$$

The Mott insulator is an insulator in the sense that the "transport" of one particle from one site to another costs a finite amount of energy (the energy gap ΔE). In the MI state, when q particles are in one site, the value of the interaction term in that site is $(U/2)q(q-1)$. When in the MI state, a particle hops from one site to another, the value on the interaction term is $(U/2)(q-1)(q-2)$ in the site where the particle comes from and $(U/2)(q+1)q$ in the site where the particle goes. This situation coincides with the first excitation of the MI state. So, the energy difference of the MI state and its excitation is,

$$\Delta E = \frac{U}{2} \left[(q-1)(q-2) + (q+1)q - 2q(q-1) \right] = U. \tag{2.14}$$

Thus, the MI phase has a characteristic energy gap $\Delta E = U$ in the energy spectrum which separates the ground state from the excitations.

We consider systems at filling one, that is, $q = N/M = 1$. In the MI phase, there is one particle in each site and $S_1 = \log M$. Due to the fact that in this phase the GS coincides with a single Fock state, S_D is zero. Since the number of particles q in each site is a well-defined integer, there are no fluctuations on the on-site number of particles in the Mott phase. The MI phase also has a finite correlation length ξ, defined in $\langle a_i a_j \rangle - \langle a_i \rangle \langle a_j \rangle \propto \mathrm{e}^{-|\mathbf{r}_i - \mathbf{r}_j|/\xi}$ as a measure of the spatial range of pair correlations.

Superfluid regime.

When $U/t \to 0$, the hopping rules the system and each particle becomes completely delocalized over all sites of the lattice. So, we can write the single particle state as,

$$|\phi_{\mathrm{sp}}\rangle = \frac{1}{\sqrt{M}} \sum_{i=1}^{M} \hat{a}_i^\dagger \, |0\rangle \ . \tag{2.15}$$

Since there are no interactions, the state of the whole system is a properly symmetrized product of the single particle state up to the number of particles. So,

$$|\Phi_{\mathrm{SF}}\rangle = \frac{1}{\sqrt{N!}} \left[\frac{1}{\sqrt{M}} \sum_{i=1}^{M} \hat{a}_i^\dagger \right]^N |0\rangle \ . \tag{2.16}$$

Then, the squared coefficients of the decomposition of the SF state into the Fock basis follow a poissonian distribution in the sense that its variance $\mathrm{Var}\left(|c_\beta|^2\right)$ coincides with its mean $\left\langle |c_\beta|^2 \right\rangle$ [5].

The SF state is characterized by a vanishing gap (since there is no interaction, the only contribution to the gap comes from the hopping term), large fluctuations in the on-site number of particles and a divergent correlation function. In the SF phase, all particles are delocalized, that is, each one of them has the same probability of presence in all sites of the lattice, without interacting with each other. Since all the particles in the system have the same single particle wavefunction, the system is condensed and so, $S_1 = 0$. The SF state involves many Fock states with a non-uniform distribution. The entropy S_D, defined in Eq. (2.11), is larger than in the Mott phase, but it will never equal 1 because the distribution is not uniform. Increasing the number of particles in the system, the value of the entropy S_D in the SF phase decreases. In contrast to S_1, the entropy S_D does not exhibit an extremal value. In Sec. 2.5, we will encounter cases where the distribution of coefficients is closer to a uniform distribution, giving rise to even larger values of S_D.

2.3 Exact diagonalization

Let us depiece how we have performed the exact diagonalization of the Hamiltonian, Eq. (2.1). The same procedure may be applied to many models involving particles with bosonic and/or fermionic statistics.

Exact diagonalization is the straightforward way to obtain the eigenvalues and eigenvectors of a Hamiltonian. Naively, we first need the Hamiltonian written in matrix form in a particular basis of states, solving a system of linear equations. The apparent drawback is the fast growth of the dimension of this matrix, defined by the size of the basis, see Table 2.1. In general, obtaining the full spectrum of the Hamiltonian, eigenvectors and eigenvalues, requires a number of operations which scales as $\left(\mathcal{N}_N^M\right)^3$. This makes the problem already intractable for fairly small quantum systems, and strictly impossible for larger ones.

Once the Hamiltonian matrix (or its action on arbitrary state vectors) is known, there are two classes of algorithms, direct and iterative methods, which can be used to completely or partially diagonalize a matrix, that is to find (at least) some of its eigenvalues and eigenvectors:

- **Direct methods** perform similarity transformations to the hermitian (non-hermitian) matrix of interest until it is written in a reduced form. Hermitian matrices (general non-Hermitian) are reduced to symmetric tridiagonal (upper Hessenberg) matrices. Once the matrix of interest is in the reduced form, it can be eigendecomposed in an efficient way with LU (QR) decomposition for Hermitian (non-Hermitian) matrices. LU and QR decompositions are procedures to efficiently factor a matrix into the product of a lower (L) and upper (U) triangular matrices and an orthogonal (Q) and upper triangular (R) matrices, respectively.

- In the **iterative projection methods**, the matrix operator spectrum is shifted in order to make the eigenvectors of interest the ones with maximal eigenvalues. Then, the transformed matrix is applied to a trial vector or a set of them. They are only guaranteed to converge for most matrices using Krylov subspace methods. In those, the subspace closed by the succession of acting from 0 to $m-1$ times the matrix onto the trial vector(s) is a $m \times m$ subspace $\mathcal{K}_m$ called Krylov subspace. When orthonormalizing the vectors of $\mathcal{K}_m$, the corresponding matrix of the transformation is a $m \times m$ Hessenberg matrix. Inverting it with direct methods, we can recover the m-iteration approximate eigenvectors and hence, the corresponding eigenvalues. The iteration increasing m is continued until convergence under tolerance values is reached. Notice that they are able to approximate a number of eigenvalues and eigenvectors without any need to solve the entire system. Despite some of them are able to solve the entire system, it is not practical in most applications, due to a much larger number of operations than required by direct methods.

The direct methods are the only ones that are able to truly diagonalize a matrix, up to rounding machine errors, while the second ones obtain approximate partial solutions of increasing precision in an iterative way. On the other hand, direct methods require enough memory to store the full Hamiltonian and the similarity matrix, while iterative methods only need storage for a few state vectors. Matrix elements needed to compute the action of the Hamiltonian onto a state vector can either be determined on the fly, or stored in a less costly sparse-matrix format.

In our case, we have used an iteration projection method for sparse, Hermitian problems: the Lanczos algorithm with Gram-Schmidt ortonormalization. In order to implement it, a number of libraries are publicly available. Most of them only require a function which computes the action of the Hamiltonian on any given input vector, as explained below. The Lanczos method does not deal with degeneracy as well as other methods as the Jacobi-Davidson or the Band Lanczos methods. We have used an Implicitly Restarted Lanczos with a large enough Krylov subspace to overthrow the degeneracy limitations. It is important to know that there exist some preconditioners that transform the Hamiltonian, making it cheaper to evaluate in terms of operations or increasing the convergence for certain diagonalization methods, such as the Jacobi-Davidson. An extensive and very pedagogical review about not only hermitian problems, but numerical solving of algebraic eigenvalue problems can be found in Ref. [85].

2.3.1 Basis states and their ordering

In order to identify all the states of the basis, every state needs to have an associated label. The basis states should have a known and unique ordering, since it must be able to run loops over the vectors of the basis, so that it is able to evaluate actions on arbitrary states. Computing the action of the Hamiltonian on the vectors of the basis has to be as efficient as possible because of the repeated iterations. In this work we have used the *Ponomarev* ordering [86]. It provides an efficient way to have all vectors of the basis labelled with a single integer ranging from 1 to the exact dimension of the Hilbert space, $\mathcal{N}_N^M$. In the procedure devised by Ponomarev, the mapping between a Fock state and its integer label can be carried out in both directions using a few, simple computational steps. It builds on a recursive relation for the dimensions of Hilbert spaces of different number of particles,

$$\mathcal{N}_N^M = \sum_{n=0}^{O} \mathcal{N}_{N-n}^{M-1} \quad \text{with } N, M, O > 0\,, \tag{2.17}$$

where O is the maximum occupancy per site, which sometimes is taken smaller than N to speed up the computations. Eq. (2.17) allows one to devise a counting algorithm covering all numbers from 1 to $\mathcal{N}_N^M$. To perform the mapping, one first needs to evaluate all $\mathcal{N}_n^m$ occurring in Eq. (2.17).

Once this information has been obtained, the algorithm first re-writes the Fock state, determining the occupations of the M orbitals, into an N-component array $(m_1, m_2, \ldots, m_N)$, where m_i denotes the orbital in which the ith atom is. This becomes a simple one-to-one map by demanding $m_i \geq m_j$ for $i < j$. The integer label of the Fock state, n_β, is then obtained as

$$n_\beta = 1 + \sum_{j=1}^{N} \mathcal{N}_j^{M-m_j}\,. \tag{2.18}$$

With this, we can straightforwardly map a Fock state onto an integer label running from 1 to $\mathcal{N}_N^M$. The opposite map is slightly more complicated, as it involves an iterative procedure: Given n_β, we find m_N by determining the largest $\mathcal{N}_N^m < n_\beta$. We then identify $m_N = m$, and continue to determine m_{N-1} by finding the largest $\mathcal{N}_{N-1}^m < n_\beta - \mathcal{N}_N^{m_N}$, and so on.

Let us see some examples. Consider for instance $N = M = O = 6$, with the $\mathcal{N}_n^m$ given in Table 2.2, and the Fock vector $|\beta\rangle = |103020\rangle$. This tells us that the first site is occupied by one atom, the third site is occupied by three atoms, and the fifth site is occupied by two atoms. Accordingly, we re-write this information in agreement to the rule $m_i \geq m_j$ for $i < j$ as $(m_1, m_2, m_3, m_4, m_5, m_6) = (5, 5, 3, 3, 3, 1)$. Plugging this into Eq. (2.18), the integer label is then found as:

$$n_\beta = 1 + \mathcal{N}_1^1 + \mathcal{N}_2^1 + \mathcal{N}_3^3 + \mathcal{N}_4^3 + \mathcal{N}_5^3 + \mathcal{N}_6^5 = 258. \tag{2.19}$$

In Table 2.2 we illustrate this mapping graphically for a second example, and explain how to operate in the inverse direction, that is from the integer label to the Fock state.

The inverse procedure, to go from the index to the actual Fock state is also fairly simple, subroutines coded in Fortran are provided in A.1.

In our bosonic case, we have used the Fock states of populations of the lattice sites, see Eq. (2.2), allowing up to N particles per site and restricting the total number of particles in the system to N. For fermions the main difference is that the maximum population per site is 1, due to the Pauli exclusion principle, the labelling scheme works well simply considering $O = 1$ in Eq. (2.17)

2.3.2 Use of sparse matrices to store the Hamiltonian matrix

Since Hamiltonians are hermitian, roughly half of the entries in the matrix are easily derived from the other half. This fact can be used to reduce storage memory, and to prevent us from redundant computations. Moreover, Hamiltonians of physical models are typically not very dense. In the case of the Bose-Hubbard model, different states in the Fock basis are connected through hopping processes, but clearly this leads to non-zero matrix elements only between Fock states differing in two entries.

									n_{6-M}
	6	1	6	21	56	126	252	462	
	5	1	5	15	35	70	$\underline{\mathbf{126}}$	$\underline{\mathbf{210}}$	**2**
	4	1	4	10	20	$\underline{\mathbf{35}}$	56	84	**1**
M	3	1	3	6	$\underline{\mathbf{10}}$	15	21	28	**1**
	2	1	2	3	4	5	6	7	**0**
	1	1	$\underline{\mathbf{1}}$	$\underline{\mathbf{1}}$	1	1	1	1	**2**
	0	1	0	0	0	0	0	0	**0**
	0	0	1	2	3	4	5	6	
					N				

Table 2.2: Number of Fock states for a given N and M. The diagram shows the procedure to obtain the index for the Fock vector $|\beta\rangle = |211020\rangle$ for $N = 6$ and $M = 6$. The corresponding index is $n_\beta = 1 + 210 + 126 + 35 + 10 + 1 + 1 = 383$ out of the 462 states in the Hilbert space. The inverse procedure can also be read out, starting with $n_\beta = 383$, we look for the largest number in the $N = 6$ column which is already smaller than n_β, in this case, 210, we put one particle in the first mode, then we compare the remained with the values in the $N = 5$ column, turns out larger than 126, and so on. In A.1 we provide explicit Fortran codes for the procedures.

The most benefits of this sparseness can be made, if the matrix is stored in a sparse matrix format. We then only care about the non-zero elements which are stored in three 1D arrays of length L, with L being the number of non-zero elements. Typically, $\mathcal{N} < L \ll \mathcal{N}^2$, with $\mathcal{N}$ the Hilbert space dimension. Two of these arrays carry the integer labels of the pairs of states which are connected by the Hamiltonian (i.e. column and row of every non-zero matrix element). The third array stores the complex amplitude of such process, i.e. the value of the corresponding matrix element. In the case of the BHM, the length L is bounded from above by $(1 + Mz)\mathcal{N}_N^M$, where z is the coordination number. Each Fock state can (at most) be connected to Mz other states through hopping processes, and to itself through the interaction.

2.3.3 Geometry of the lattice

In our computations we have considered a chain of atoms, but the topology and coordination number of the lattice could easily be changed. All information about the lattice is stored in an $M \times z$ array of adjacencies A. Its elements a_δ^i contain, for each site i, the labels δ of all neighbouring sites.

This can be extended to any kind of neighbourhood (nearest neighbours, next nearest neighbours, superlattices, anisotropic models, fully connected models, ...). We then simply define a generalized array A of dimension $M \times z \times w$. Here, w counts the different types of neighbourhoods, and z is the largest coordination number in any neighbourhood. For instance, assume a 2D lattice with nearest- and next-nearest-neighbour hopping. Each site is then connected to 4 nearest neighbours, as well as 4 next-nearest neighbours, thus $z = 4$. We have two different types of connections, thus $w = 2$. Or consider a triangular lattice. In the isotropic case, each site is equally connected to six neighbours, e.g. $z = 6$ and $w = 1$. If the model becomes anisotropic, we have three types of connections, $w = 3$, to two different sites, $z = 2$.

The important advantage of implementing the lattice geometry as described here is its flexibility, specially in the implementation on inhomogeneous and anisotropic models. The counterpart, it should be said, is that it does not make use of lattice symmetries, like translational symmetry in the case of periodic boundaries, or parity symmetry for finite lattices. Since the Hamiltonian commutes with the corresponding symmetry operator, the Hamiltonian matrix is block-diagonal in the eigenbasis of a symmetry operator. The diagonalization can then be performed within each block separately. A comprehensive instruction for implementing translational symmetry in the exact diagonalization code can be found in Ref. [81]. The largest block in the translationally invariant eigenbasis has a dimension which is approximately by a factor $1/M$ smaller than the full Hilbert space of N bosons on M sites.

2.3.4 Diagonalizing the Hamiltonian

As mentioned earlier, diagonalization algorithms differ greatly, but all of them need to calculate the action of the Hamiltonian onto the basis vectors. In exact methods the outcome of this calculation is stored in a matrix, and the unitary transformation diagonalizing this matrix is determined numerically. The advantage of the direct method is the fact that they provide the full spectrum of the Hamiltonian. However, direct methods are only feasible for matrix sizes on the order to $10^4 \times 10^4$, e.g. 7 particles in 10 sites, see Table 2.1.

Beyond that, only iterative methods can be employed. Even where direct methods are still possible, iterative methods are much faster in providing only a few eigenvalues and eigenvectors. Iterative methods repeatedly apply the Hamiltonian with a shifted spectrum (eventually inverted) on a set of state vectors, thereby filtering out an effective subspace of interest. This procedure can be designed such that the invariant subspace corresponds to the low-energy subspace. Since it is typically much smaller than the total Hilbert space, direct methods can finally be used to diagonalize the Hamiltonian within the low-energy subspace.

While the iterative methods do not require that the action of the Hamiltonian on a basis vector is stored in memory, nevertheless this information is frequently needed in order to perform the iterative multiplications. Thus, in particular if memory restrictions forbid to store this information, it is crucial for these algorithms to quickly evaluate the action of the Hamiltonian on a base vector “on the fly”. For this goal, the labelling scheme presented above is an important ingredient.

Let us analyse the different steps the diagonalization algorithm has to go through. Consider an arbitrary state represented as a state vector in the Fock basis, $|\Phi\rangle = \sum_{\beta}^{\mathcal{N}_N^M} c_\beta \, |\beta\rangle$. The Hamiltonian is applied in two nested iterative operations:

- One loop runs through all elements in the Fock basis, $i_\beta = 1, \ldots, \mathcal{N}_N^M$. In this loop, we perform a map from the state label i_β onto the occupation numbers.

- A second loop runs through all non-zero terms in the Hamiltonian, $\hat{H} = \sum_j \hat{H}_j$, where $\hat{H}_j$ is a monomial of creation and annihilation operators, e.g. $H_j = \hat{a}_3^\dagger \hat{a}_5^\dagger \hat{a}_2 \hat{a}_{14}$. Clearly, each step in this loop maps the state $|\beta\rangle$ onto a new basis state $|\beta'\rangle$, with an amplitude w_j^β:

  $$\hat{H}_j \, |\beta\rangle = w_j^\beta \, |\beta'\rangle \, . \qquad (2.20)$$

  It is straightforward to determine both the new state $|\beta'\rangle$ in the occupation number basis, and the amplitude w_j^β. Using the mapping from occupation numbers onto state labels, we also find $i_{\beta'}$.

Accumulating the amplitudes w_j^β in the $i_{\beta'}$th component of the new state vector, both loops together produce $|\Phi'\rangle = \hat{H} \, |\Phi\rangle$. In summary, the main computational task is the mapping between labels and states back and forth, and application of monomials to the states. Since any operation relies on the previous, all operations on the nested loops may run in parallel in a computer. Let us exemplify this for two of the monomials in Eq. (2.1). As an initial state we take the Fock state 383 from Table 2.2, e.g. $|\Phi\rangle = \sum_i \Phi(i) \, |i\rangle = |383\rangle$, or $\Phi(i) = \delta_{i,383}$. First, we translate the Fock state into the occupation-number basis: $|\beta\rangle = |211020\rangle$. Then, we apply all monomials, e.g.

$$\begin{aligned} \frac{U}{2}\hat{n}_1(\hat{n}_1-1)|211020\rangle &= \frac{U}{2}2\times 1|211020\rangle \\ -t_{1,2}\hat{a}_2^\dagger \hat{a}_1|211020\rangle &= = -2t_{1,2}|121020\rangle\,, \end{aligned} \tag{2.21}$$

The first monomial corresponds to an interaction term. It is diagonal in the Fock basis and thus is easily evaluated. We accumulate on the output vector, $\Phi'(383)+U\Phi(383)\rightarrow\Phi'(383)$. The second monomial represents a tunnelling term, and is not diagonal in the Fock basis, that is, it changes the state. The new state and the amplitude can easily be found, and using the Ponomarev mapping, we finally identify the label of the new state, $n_{121020} = 210+56+35+10+1+1=313$. This means, we accumulate the amplitude on that position of the resulting vector, $\Phi'(313)-2t_{1,2}\Phi(383)\rightarrow\Phi'(313)$ in this case.

Once we have this procedure, the iterative methods will perform a number of calls to this procedure in order to obtain approximate values for the desired part of the spectrum. In this work we have used the ARPACK package [87], which requires on the order of 600 calls to this action to obtain the first 10 states of the Hamiltonian. With this, we are able to obtain the ground state and first excitations of systems of up to 5×10^6 states.

2.4 Boundary between Mott insulator and superfluid

We are now ready to apply the exact diagonalization method to the Bose-Hubbard model. Our goal is to find the value of t/U at which the MI is no longer the GS of the system and it starts to be a SF in an infinite system with $N=M$, which is known as the critical value of the order parameter of the MI-SF transition at filling $q=1$. Although we also show a few results for the 2D square lattice, our focus is on a homogeneous 1D Bose-Hubbard chain with nearest neighbour hopping. The superfluid to Mott-insulator phase transition exhibited by the BHM with a commensurate number of particles, $N/M\in\mathbb{N}$, in d dimensions belongs to the $(d+1)$D XY model universality class. For the 1D model, the exhibited phase transition is of the Berezinskii-Kosterlitz-Thouless type [63] (BKT). This phase transition is known to be infinite order —every derivative of the free energy is continuous— and very sensitive to finite size effects. As we will see in this section, this makes the determination the phase boundary extremely hard.

In order to interpret our numerical results, we will follow three different strategies: In Sec. 2.4.1, we will consider the ground state vectors and determine their overlap with the analytic trial wave functions for the Mott phase and the SF phase. In Sec. 2.4.2, we will analyse the insulating gap which in the thermodynamic limit closes at the transition point. In Sec. 2.4.3, the scaling behaviour of the system is analysed. We shall stress that all three approaches come with their own limitations, which will be discussed in each subsection. Accordingly, it is also not surprising that each method produces quantitatively different results.

In all calculations, we restrict ourselves to hopping between neighbouring sites k and j, $t = t_{k,j}$. This keeps the essential symmetries to produce the Mott insulator to superfluid phase transition, cf. Ref. [88]. We also take $U = 1$, as only the ratio between t and U determines the system behaviour (for $U > 0$).

2.4.1 Overlap.

Since we have the eigenstates of the system, which is a quantity that not every method is able to obtain, we may try to use this information to find the transition value. Then, we will compare the obtained ground states at different values of U/t with the analytical solution of the system in the cases $U/t = 0$ and $U/t = +\infty$. In particular, we compute the overlap between GS and trial states as a function of U/t,

$$OV = \left| \left\langle \Phi_{\text{Analytic}} \middle| \Phi_{\text{GS}} \right\rangle \right| . \tag{2.22}$$

This overlap is never expected to be zero for finite systems, since the two trial states become orthogonal only in the thermodynamic limit. Analyti-

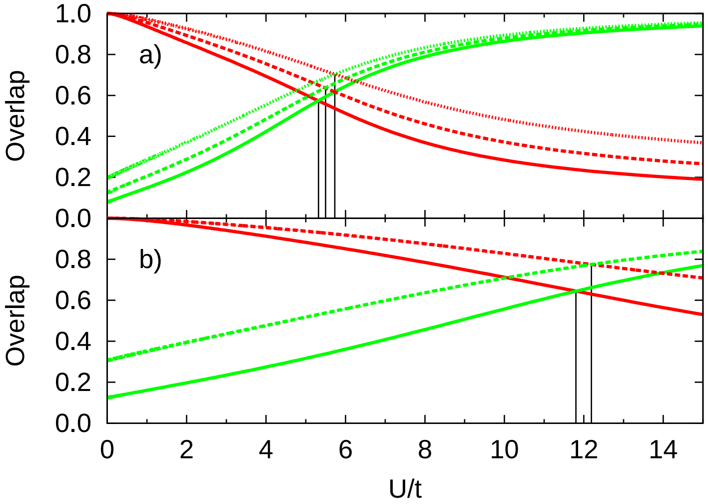

Figure 2.1: a) Overlap of the GS of the system with the analytical SF (red) and MI (green) states in 1D lattices with periodic boundary of 5 (dotted line), 6 (dashed line) and 7 (solid line) sites. b) Computations in 2D: 2x2 (dashed line) and 3x2 (solid line) lattices with periodic boundary. The abscissa where the two overlaps have the same value is marked to ease visualization. Filling factor $q = 1$ so, $N = M$ in all the cases.

cally, we find

$$\left|\left\langle \Phi_{\mathrm{MI}}\left(q\right) \middle| \Phi_{\mathrm{SF}}\right\rangle\right| = \sqrt{\frac{N!}{(M)^{N}(q!)^{M}}}. \tag{2.23}$$

Therefore, this method is ill-conditioned for the BKT transition, but we show it for illustrative purposes. Nevertheless, the overlap OV can estimate the phase boundary by looking for the value U/t where both overlaps, for the MI and the SF phase, cross each other, that is, the GS of the system populates them equally, see Fig. 2.1. We denote this value by $(U/t)_N$, as it depends on the number of particles N. Performing a finite size study [89],

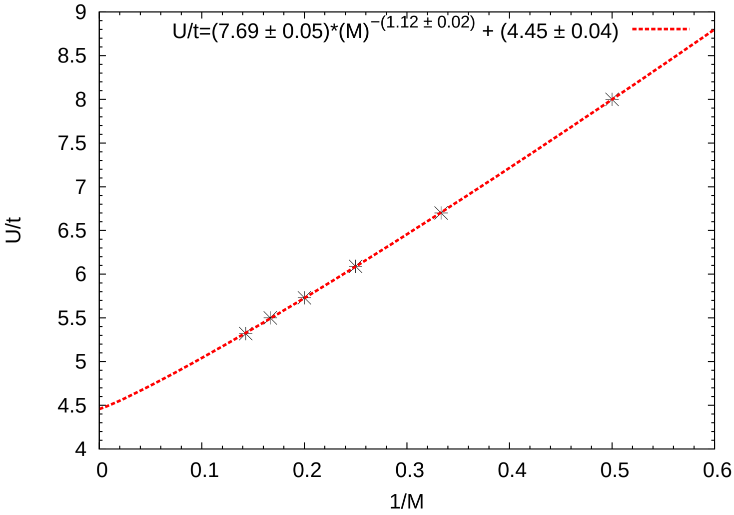

Figure 2.2: Finite-size scaling: The value of U/t at which the crossing of the overlaps happens is plotted as a function of $1/M$ for a 1D system with periodic boundary. The fitting to the analytical form, $U/t = a(M)^{-b} + c$ has been made with the non-linear least-squares Marquardt-Levenberg algorithm. This fit is used to extrapolate to the thermodynamic limit as explained in the text.

we estimate the critical value in the thermodynamic limit, $(U/t)_\infty$, by extrapolation. We assume a size-dependency given by $\left(\frac{U}{t}\right)_{\mathrm{M}} = AM^{-b} + \left(\frac{U}{t}\right)_\infty$, and perform the finite size study for the 1D systems.

This is a naive approach that is routinely used in the study finite-size effects of FQH systems. The size-dependency is chosen as a power with a variable exponent in place of a linear relation in order to capture any correction depending on non-integer powers.

The finite size study is shown in Fig. 2.2. The extrapolated value for the phase transition in the thermodynamic limit is $U/t = 4.45 \pm 0.04$, or, $t/U = 0.224 \pm 0.002$ with a reduced $\chi^2 = 6 \times 10^{-5}$. It is far indeed from most values in the literature, cf. Ref. [69] for an overview. The value found here lies between the one from third-order strong-coupling expansion [67] and the one from density-matrix renormalization-group calculations [76].

Thus, based on our knowledge of overlaps in a small system, we are able to predict the phase diagram in the thermodynamic limit, although the overlap itself is certainly not a good figure of merit for the BKT phase transition. In the following subsection, we take the opposite (and more systematic) approach, which characterizes the phase boundary via an order parameter which, in the thermodynamic limit, vanishes exponentially in one of the phases.

2.4.2 Insulating gap.

By means of exact diagonalization, we are able to find the ground state energy of the system with N particles in M sites at a given value of t/U, $E_0\left(t/U, M, N\right)$, in units of U, with machine precision.

According to Ref. [63], in the phase diagram of the BMH model, the critical value of the MI to SF phase transition is the value of t/U at which the upper and lower boundaries of each Mott lobe cross each other. We will try to exploit that idea defining an order parameter as the difference in ordinates between the two boundaries as function of t/U, following Ref. [78]. In the infinite system, that order parameter vanishes for the SF phase, as the boundaries cross each other at the transition value. Meanwhile, it remains finite as long as the GS of the system is the MI state. At first, we set a definition to find the upper and lower boundaries of the Mott lobes. According to Ref. [63], the upper (lower) boundary of a Mott lobe is given by exciton energy of one particle (hole) in the system. That is, the chemical potentials of the systems with M sites containing $M+1$ ($M-1$) particles. Then, we can find the upper (lower) boundary of the Mott lobe at filling q of the system of M sites, $\mu^{+}_{M,q}\left(t/U\right)$ ($\mu^{-}_{M,q}\left(t/U\right)$), as,

$$\mu^{+}_{M,q}\left(t/U\right) = E_0\left(t/U, M, qM+1\right) - E_0\left(t/U, M, qM\right) \tag{2.24}$$

$$\mu^{-}_{M,q}\left(t/U\right) = E_0\left(t/U, M, qM\right) - E_0\left(t/U, M, qM-1\right). \tag{2.25}$$

In Fig. 2.3, the value of $\mu^{+}_{M,q=1}\left(t/U\right)$ and $\mu^{-}_{M,q=1}\left(t/U\right)$ is plotted as a function of t/U for $M=4$ to $M=12$. This figure shows the famous Mott

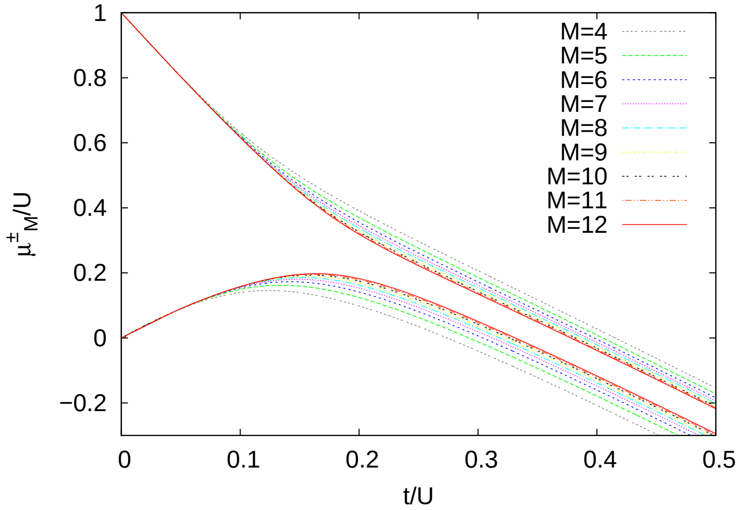

Figure 2.3: Boundaries of the Mott insulator region with $N/M = 1$ for finite size systems. The sizes are $M = 4, 5, 6, 7, 8, 9, 10, 11, 12$. The upper family of curves is μ^+_M and the lower is μ^-_M.

lobes for finite systems. Notice that for our finite sizes and fixed number of particles, the boundary never closes, that is, the upper and the lower boundary of the lobe do not merge. However, it can clearly be seen how these two boundaries approach each other upon increasing the number of particles.

The energy gap in the MI phase, for any value of t/U, corresponds to the particle-hole excitation, which is the difference between $\mu^+_{M,q}(t/U)$ and $\mu^-_{M,q}(t/U)$ for a fixed t/U. So, we define the single-particle excitation gap of the lobe with filling q in a system with M sites as,

$$\begin{aligned}\Delta_{M,q}(t/U) =& \mu^+_{M,q}(t/U) - \mu^-_{M,q}(t/U) \\ =& E_0(t/U, M, qM+1) + E_0(t/U, M, qM-1) - 2E_0(t/U, M, qM)\ .\end{aligned} \tag{2.26}$$

In the standard quantum phase transitions the single-particle excitation gap is particularly well suited as an order parameter because in an infinite system it vanishes in the superfluid phase, meanwhile it remains finite in the MI phase. Unfortunately, the single particle gap is not well suited to locate the transition in the 1D case. In the BKT transition the gap is exponentially weak near the criticality, hardly detectable in finite systems. Hence, the formula above is by construction incorrect for small gaps in the Mott insulator phase. In addition, the studied systems exhibit finite size gaps due to the small size. Those gaps may dominate the single-particle excitation gap in the transition and clearly do in the superfluid phase, and besides, they can have different extrapolation exponents than the single-particle excitation gap. Obviously, a reliable extraction of the gap is also possible from Monte-Carlo methods, and possibly they will do a better job for this transition. The analysis of the energy gap performed in the present case, leads indeed to the results which do not have a clear physics meaning; nevertheless, one can estimate quite well the position of the criticality from that.

For simplicity, we define the single-particle excitation gap in the Mott lobe of filling 1 as $\Delta_M\left(t/U\right) \equiv \Delta_{M,q=1}\left(t/U\right)$. In Fig. 2.4, the value of $\Delta_M\left(t/U\right)$ is plotted as a function of t/U for M from $M=4$ to $M=12$. Notice that the gap does not vanish due to the mentioned domination of the finite size gaps in the superfluid phase, at large values of t/U, while the vanishing gap is an intrinsic property of the superfluid in the thermodynamic limit.

In order to determine the value of t/U for which the phase transition takes place, we have used values of $\Delta_M\left(t/U\right)$ as the plotted in Fig. 2.4 for M from $M=3$ to $M=13$. We have used here the fitting method from Ref. [78]: For every value of t/U, we fit $\Delta_M\left(t/U\right)$ to a fifth-degree polynomial of the inverse of the size, $1/M$. This expression has six fitting parameters. The constant term of the polynomial is $\Delta_\infty\left(t/U\right)$, which corresponds to the single-particle excitation gap of the thermodynamic system ($M\to\infty$) as function of t/U. Then, the phase transition takes place at the value of t/U for which $\Delta_\infty\left(t/U\right)$ just vanishes. The determination of $\Delta_\infty\left(t/U\right)$ through the regression is just a hidden extrapolation to the in-

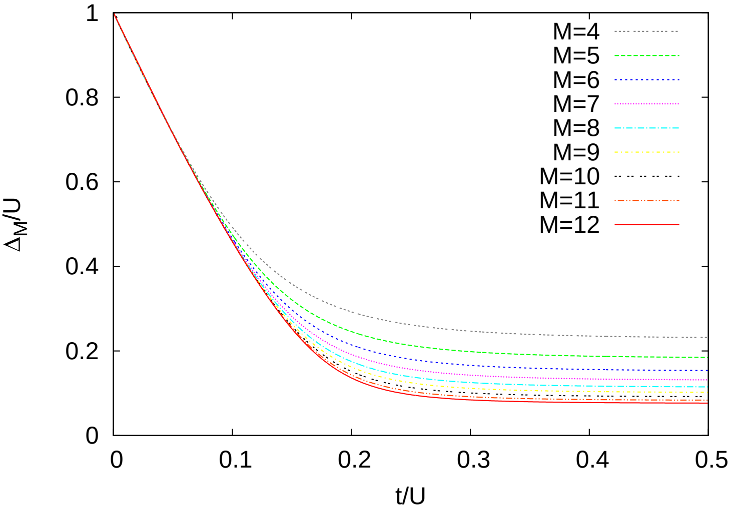

Figure 2.4: Single-particle excitation gap in the regime $q = 1$, for finite size systems. The sizes are $M = 4, 5, 6, 7, 8, 9, 10, 11, 12$.

finite system. Following Ref. [78], the behaviour of the extrapolation to $M \to \infty$ could imply a non-integer extrapolation exponent that a polynomial expression could not properly capture. In order to extrapolate the proper value of $\Delta_\infty(t/U)$ in the region where the finite size gaps could potentially play a role ($t/U \gtrsim 0.24$), we have used a fitting expression as function of $1/M^\alpha$ instead of $1/M$, where α is a positive real exponent. This adds one extra free parameter to the fitting expression.

The obtained values of $\Delta_\infty(t/U)$ as function of t/U for three sets of sizes $M \in \{3, ..., 13\}$, $M \in \{4, ..., 13\}$ and $M \in \{5, ..., 13\}$ are shown in Fig. 2.5, along with the corresponding value of the exponent α. The log scale has been used for an easier visualisation of the vanishing point. In Fig. 2.5, the behaviour of $\Delta_\infty(t/U)$ in units of U is roughly similar for every set of sizes: it starts at 1 for $t/U = 0$ and monotonically decreases to 0 at $t/U \approx 0.285$. For $t/U \gtrsim 0.285$, the different sets show different behaviours: The set with sizes $M \in \{3, ..., 13\}$ shows negative, small values of $\Delta_\infty(t/U)$, while the

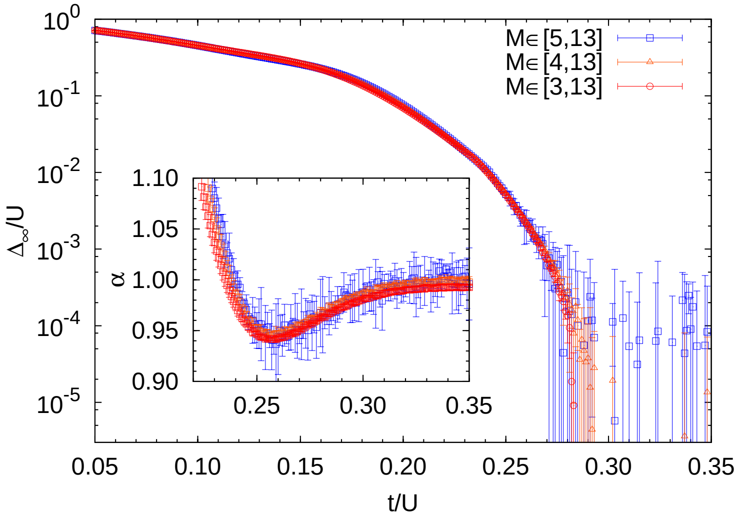

Figure 2.5: Extrapolated value Δ_∞ as a function of t/U in a log scale for three different sets of sizes. The inset shows the value of the fitting parameter α as a function of t/U for each set of data. The errorbars show the 95% confidence intervals.

set with sizes $M \in \{5, ..., 13\}$ shows even smaller, positive and negative values, whose errorbars make them mainly compatible with 0. The set with sizes $M \in \{4, ..., 13\}$ shows an intermediate behaviour. It shows positive and negative values of $\Delta_\infty(t/U)$, that are smaller in magnitude than in the former set, but they are more biased to negative values than in the latter set. Some of the values are incompatible with 0. Obviously, any value $\Delta_\infty(t/U) < 0$ is clearly non-physical. Still, the value of $\Delta_\infty(t/U)$ and its dependence on t/U suggest that are a reasonable way to identify the criticality. The value of $\Delta_\infty(t/U)$ deep in the SF phase is not zero as we know it should, but a negative small value. This is because we did an extrapolation from small, finite sizes that led to an inaccurate values of the y-intercept, $\Delta_\infty(t/U)$. As we restrict the analysis to sets of larger sizes, the value of $\Delta_\infty(t/U \to \infty)$ goes closer to zero, becoming less negative, and even erratic around zero. Consequently, we will treat any small negative value as what it is: an non-physical value that has been obtained just because it is the one that better meets the fitting relation with data from small systems. So, the estimation of the critical value $(t/U)_c$ will be the value of t/U for which Δ_∞ crosses zero for first time and its uncertainty will be the difference between the latter value and the value of t/U at which the errorbar has crossed zero for first time. Then, the obtained critical value for the sets $M \in \{3, ..., 13\}$, $M \in \{4, ..., 13\}$, and $M \in \{5, ..., 13\}$ using this method is $(t/U)_c = 0.285 \pm 0.002$,$(t/U)_c = 0.292 \pm 0.006$, and $(t/U)_c = 0.283 \pm 0.009$ respectively. Being conservative, we estimate the critical value with this method as the mean of the latter values, weighted with the relative error, giving $(t/U)_c = 0.286 \pm 0.017$. Notice that the set of bigger sizes has 8 different sizes and its data is fitted with an expression with up to 7 free parameters. The fact that this system is minimally overdetermined leads to some instability in the values of the fitting parameters and to bigger uncertainties.

The fitting parameter α has remained within the range $[0.94, 1.00]$ for all the values of t/U used in the analysis. Notice that the transition value of the Ref. [78], $(t/U)_c = 0.275 \pm 0.005$, is compatible with ours. Interestingly enough, our values of the fitting parameter α near the transition are also compatible with their value $\alpha = 0.95$. Also notice the strong discrepancy with the estimation from the previous naiver method. Despite this method is nothing more than an elaborated extrapolation to infinite size, the final result with this method is within the range of the most recent studies. It is also compatible with most of values in the literature, due to its broad uncertainty margins.

2.4.3 Finite-size effects of the gap.

We may try to focus in a more general procedure in order to try to get rid of the finite size effects. The way to proceed in most of phase transitions is the general finite-size scaling hypothesis. According to it, close to the phase transition, and with the proper finite-size power rescaling of the order and control parameters, the curves for different sizes should collapse into a single curve, independent of the size of the system, called universal scaling function. In our case, order and control parameters would be $\Delta_{M,q}$ and t/U, respectively. Regrettably, the exponential closing of the gap characteristic of the BKT transition does not allow such development. Since the gap in the superfluid phase closes as $\Delta \sim \exp\left[-\frac{g}{\sqrt{|(t/U)_c - t/U|}}\right]$ —with g being an unknown constant—, the finite-size corrections become logarithmically small, not potentially as the finite-size scaling hypothesis assumes and therefore, the finite-size power rescaling is not suitable. As a consequence of this behaviour, the BKT transition is known to converge to the thermodynamic limit very slowly when increasing the size of the system. This is, in order to get rid of finite size effects, order parameter curves corresponding to sizes from a wide range of orders of magnitude are essential.

We have followed an approach similar to the one of the authors of Refs. [73] and [90]. They propose an ansatz for the scaling relation of the single-particle excitation gap, $\Delta'_{M,q}(t/U) = M\Delta_{M,q}(t/U)\left[1 + \frac{1}{2\ln(M)+C}\right]$ where $\Delta^{'}_{M,q}(t/U)$ is the rescaled gap, and C is an unknown constant. Those authors found that $C \to \infty$ for the standard BHM so, the logarithmic correction becomes negligible. We defined the rescaled reduced control parameter as $\tilde{t} \equiv \frac{t/U-(t/U)_c}{(t/U)_c} M^a$, where a is an scaling exponent. The former takes the value $\tilde{t}_c = 0$ at criticality. We also propose the rescaling $\Delta'_M \equiv \Delta_M M^b$ for the order parameter, where b is an scaling exponent. Both, a and b are related to the critical exponents of the universality class of the phase transition. From it we already knew that they should be $a = 1/2$ and $b = 1$, respectively. Notice that this implies a potential relation that will deviate from the one given by [73] for large enough systems. Although ED does not allow to compute large enough systems to obtain finite-size effect free results, we proceed with the analysis of the obtained results for illustrative purposes.

We use the fact that, at criticality, the order parameter collapses in a single size-independent universal curve to find the proper exponents and the critical value of the phase transition through a minimization of the squared differences between curves of different sizes. Far from the phase transition, the subleading terms overcome the scaling relation and then, the rescaled order parameter depends on the size of the system. The problem is to determine how far from the phase transition the system starts to exhibit resolvable finite size effects, and so, which interval of data points has to be taken in consideration for the minimization. We call $\tilde{t}^-$ ($\tilde{t}^+$) the lower (upper) limit of that interval. That is, the curves of the rescaled order parameter follow the same curve in the interval $\left[\tilde{t}^-, \tilde{t}^+\right]$ around the criticality. Then, we define the figure of merit of the minimization as,

$$S\left((t/U)_c, a, b\right) = \sum_{M>M'} \int_{\tilde{t}^-}^{\tilde{t}^+} \Delta'_M\left(\tilde{t}\right) - \Delta'_{M'}\left(\tilde{t}\right) d\tilde{t}\,. \tag{2.27}$$

where the integral is calculated numerically over interpolation of the data points with cubic splines.

Since we don't know how far from the critical point the system starts to exhibit resolvable finite size effects, we try to collapse the curves for several system sizes M as function of $\tilde{t}^-$ and $\tilde{t}^+$ with the following procedure:

- For a given value of $\tilde{t}^-$, we fix $\tilde{t}^+ = -\tilde{t}^-/e$, since we have visually realized that the lowest values of S are achieved when $\tilde{t}^+ \sim -\tilde{t}^-/2$ holds.
- We minimize S changing the set of parameters $\left((t/U)_c, a, b\right)$.

Then, we find an optimum set of parameters $\left((t/U)_c, a, b\right)$ as a function of $\tilde{t}^-$. We may expect that when $\tilde{t}^-$ is very small, the number of data points is not enough to properly describe the universal scaling function, due to the lack of resolution. On the other side, when $\tilde{t}^-$ is large enough, the finite size effects play a role and the curves are no longer collapsed in the universal scaling function. This leads to obtaining parameters that are size-dependant and not related to the universal scaling function.

For a range of $\tilde{t}^-$ in between, we may expect to have a constant, size-independent values of the parameters, showing a plateau. This is due to the fact that the curves are collapsed in a universal scaling function, which has the same parameters for any choice of $\tilde{t}^-$ and sizes M. In order to

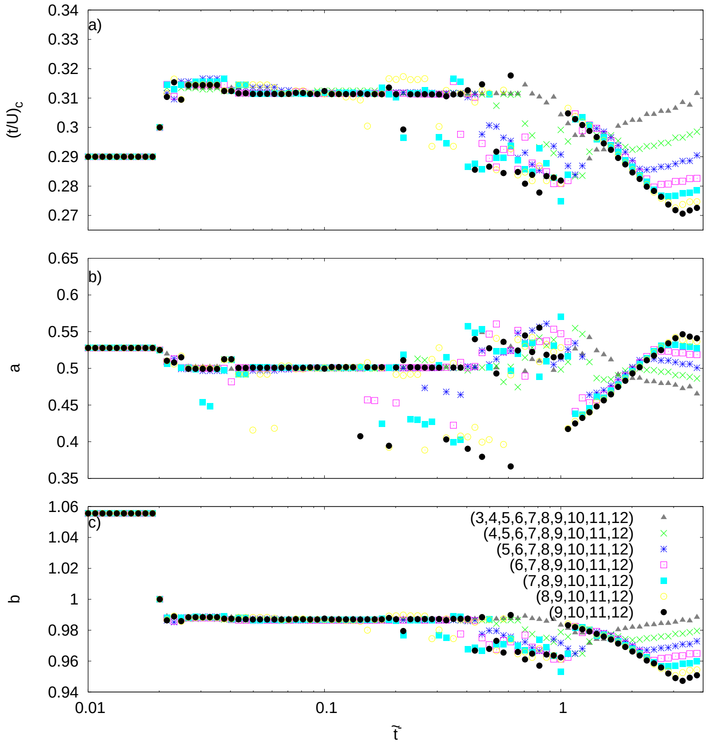

Figure 2.6: Optimal values of $(t/U)_c$, a and b as a function of $\tilde{t}^-$ to collapse several sets of system sizes M.

control those possible size dependency of the parameters $((t/U)_c, a, b)$, we have computed those parameters taking in account different sets of curves: pairs of consecutive sizes ($M = 11$ and 12, 9 and 10, 7 and 8, ...), subsets of the larger systems (from $M = 9$ to 12, from 8 to 12, ...) and for all of them.

The parameters $(t/U)_c$, a, and b for a several size sets are shown in Fig. 2.6. According to those results, the estimated values are: $(t/U)_c = 0.3115 \pm 0.0010$, $a = 0.5010 \pm 0.0010$, and $b = 0.9870 \pm 0.0010$. The fact that the parameters that we have found do not have a resolvable size dependency seems quite noticeable. It is because our set of sizes are too clustered to resolve the differences due to the size. Notice that we have let both exponents, a and b, to vary, despite we know their value. This allows to explore a broader area of the space of parameters to improve the final value of $(t/U)_c$, and let the minimization find the proper scaling exponents by itself. Additionally, it gives us a proof of the goodness of the scaling. As a matter of fact, the value of the exponent b is several error bars below the expected value $b = 1$. It is due to the fact that the small sizes we studied didn't allowed to get rid of the finite-size effects. Then, the analysis has led to a non-universal coefficient. Reminding that the size corrections in the BKT transition are logarithmic becomes clearer that the set of sizes shall include sizes with larger orders of magnitude. It has to be stated that potential scaling relations are wrong for analysing the BKT transition, but with this treatment a good value is fortuitously obtained because of the small sizes studied —given that the value obtained for the exponent b does not correspond to the expected, 1. Finally, the collapse of various system sizes with those parameters is shown in Fig. 2.7.

2.4.4 Summary

Given that the most recent numerical results localize the BKT transition at values t/U between 0.26 and 0.31, we must clearly state that our first approach considering the overlaps fails, as it yields $(t/U)_{\mathrm{crit}} = 0.224 \pm 0.002$. Despite the nature of the BKT and the weakness of the gap even in the insulating phase, the second method produces a result which agrees with the literature, $(t/U)_{\mathrm{crit}} = 0.286 \pm 0.017$. Also our third approach, the scaling analysis, produces a result which is still compatible with the literature, 0.3115 ± 0.0010, although the underlying scaling hypothesis does not hold for the BKT transition.

2.5 Beyond the standard BHM

A number of modifications to the standard Bose-Hubbard model have been studied. Those modifications include different topologies and coordination

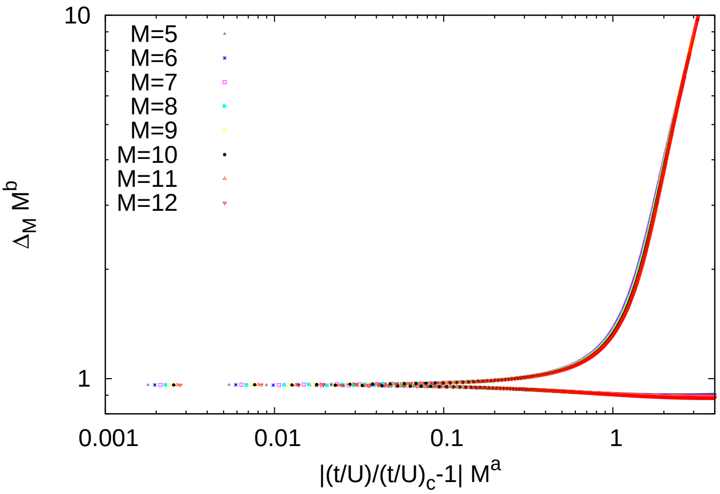

Figure 2.7: Collapse of the curves for $M = 5,6,7,8,9,10,11,$ and 12 sites for the estimated parameters $(t/U)_c = 0.3115$, $a = 0.501$, and $b = 0.987$ in a log-log scale.

numbers of the lattice, inhomogeneous potentials, negative interactions, additional neighbouring interactions, long range interactions, among others. Exact diagonalization very suitable for most of those modifications, due to the lack of assumptions on the parameters. We have played with a couple of modifications: inhomogeneous lattices, and attractive on-site interactions.

2.5.1 Phase transitions in a deeply biased lattice

An interesting modification of the SF to MI transition is obtained by considering a lattice with a large attractive bias. In this case the tendency to form a superfluid is suppressed, as in the limit of weak interactions the particles prefer to localize on the biased site. Increasing repulsive interactions, the system reaches the Mott phase, undergoing several transitions in which the number of particles on the biased site is reduced by one. The large inhomogeneity is produced by making the potential energy in the kth site much lower than the others. Theoretically, we take it into account by adding the term $-\epsilon \sum_i^M \hat{n}_i \delta_{i,k}$ to the Bose-Hubbard Hamiltonian.

To evaluate the effect of the bias potential in the system, we introduce the fluctuation of the number operator in the ith place,

$$(\Delta \hat{n}_i)^2 = \left\langle (\hat{a}_i^\dagger \hat{a}_i)^2 \right\rangle - \left\langle \hat{a}_i^\dagger \hat{a}_i \right\rangle^2 . \tag{2.28}$$

It can be written explicitly with the number operators in the Fock basis. Moreover, due to the fact that the Fock states are eigenstates of $\hat{n}_i$, the only non-zero contribution occurs when $|\beta'\rangle = |\beta\rangle$. So,

$$(\Delta \hat{n}_i)^2 = \sum_\beta |c_\beta|^2 \langle \hat{n}_i \rangle_\beta^2 - \left[\sum_\beta |c_\beta|^2 \langle \hat{n}_i \rangle_\beta \right]^2 , \tag{2.29}$$

where $\langle \hat{n}_i \rangle_\beta$ means $\langle \beta | \hat{n}_i | \beta \rangle$. The fluctuation of the on-site number of particles may serve as a precursor of a phase transition which involves redistribution of the particles in the ground states. In the presence of a strong bias potential, $\epsilon \gg t$, several peaks of the number fluctuations occur upon tuning U/t.

In Fig. 2.8, we chose $\epsilon = 100t$, and study a square lattice consisting of a single plaquette, that is, four sites. Accordingly, we observe $N - 1 = 3$ peaks of the number fluctuations upon tuning from $U/t = 0$ to large values of U/t. In order to infer which mechanisms produces the fluctuations, we have calculated the population of each site in the lattice, simply by taking the diagonal values of the OBDM, plotted in Fig. 2.8. When the fluctuation reaches a maximum, the population in the biased site decreases by one. Between two consecutive fluctuation peaks, the populations remain mainly constant, showing plateaus with a step structure. The last peak of the fluctuations, occurring at the largest value of U/t, indicates a transition into the MI phase: We find that for larger values of U/t, the population of all the sites takes the same integer value q, and the fluctuation decrease monotonically to zero.

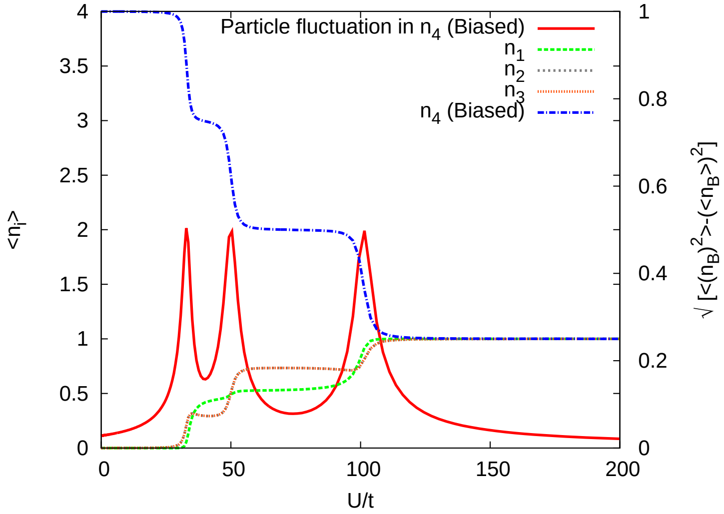

Figure 2.8: Transition from the fully localized state to the MI phase in a deep biased 2x2 lattice with open boundary condition. The bias is taken to be $\epsilon = 100t$ in the 4th site. The values of the average population of all sites is depicted together with the fluctuation of the number of particles in the biased site (red solid curve). The direct hopping between the 4th site and the 1st is not allowed and hopping between the 4th and the 2nd and 3rd are equivalent. Note the clear peaks in the number fluctuation for fixed values of U/t corresponding to the transitions described in the text.

The values of U/t for which fluctuation maxima appear can be parametrized by $U/t = 100/i$, for $i = 1, \cdots, N-1$. These values are easily explainable for the MI with $q = 1$, keeping in mind the Hamiltonian in Eq. (2.1): the migration happens when the energy of keeping the particles in the same site becomes greater than extracting one particle from the biased site to place it in other site without particles,

$$\frac{U}{2} n_B(n_B - 1) - \epsilon n_B = \frac{U}{2}(n_B - 1)(n_B - 2) - \epsilon(n_B - 1)\,, \tag{2.30}$$

where we have neglected the hopping term t, which is small compared to ϵ and U. The subindex B denotes the biased site. From this equation, we obtain the condition,

$$U = \frac{\epsilon}{n_B - 1}, \tag{2.31}$$

where n_B is a positive integer which $1 < n_B \leq N$.

As can be seen in Fig. 2.8, in general the unbiased sites are not equally populated. When the interaction is large enough to expel the first particle from the biased site, the second most populated site is the one which is not directly connected to the biased site. This might appear counter-intuitive in the first place, but one has to bear in mind that a particle on this site benefits from having two empty neighbours, allowing to reduce energy by tunnelling processes to these sites. On the other hand, once a second particle is pushed out from the biased site, the situation changes, and two nearest neighbours of the biased site become more populated. But now, two particles occupying these two sites still can share the empty neighbouring site for virtual tunnelling.

2.5.2 Attractive interactions: Localization

As studied for the two-site case in Refs. [79, 80], systems with attractive interactions feature large quantum superpositions due to the several competing single-particle ground states [84].

For $U/t = -\infty$, all the particles in the system will aggregate in a single site, so the GS is the Fock state with N particles in the ith site and 0 in the other sites. But this state is M-degenerate. Due to this degeneracy, the ground state can be a superposition of these M states. Each one of them aggregates the system in one different site of the lattice. In this state, when a particle is fixed in one site, all the rest cluster there. So, this state is highly correlated. For the two site case, the ground state build a so-called NOON state [79].

In any practical implementation there will be small imperfections that will trigger small biases between the sites. It is thus expected, that for sufficiently large attractive interactions in realistic systems, the GS will be

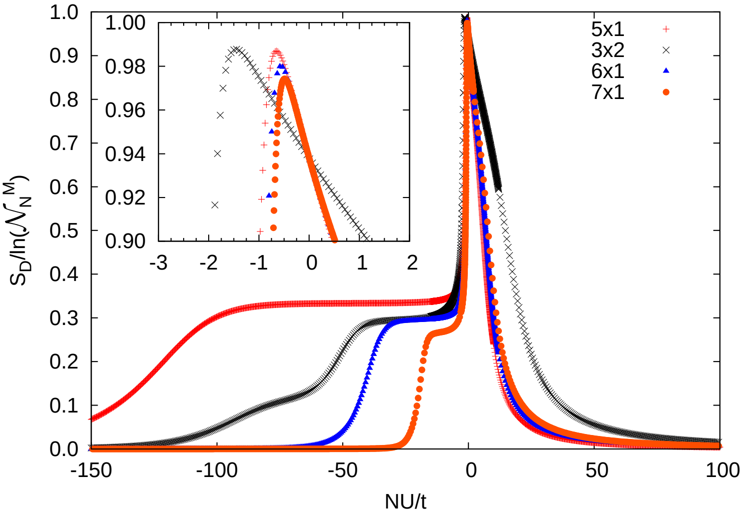

Figure 2.9: Entropy S_D of the GS in a system with attractive interactions, for 5 to 7 particles in different geometries with periodic boundaries. The plot is zoomed in order to appreciate the weakly attractive regime. In particular, it is worth emphasizing the fact that the maximum of the entropy, maximal delocalization in Fock space, is not achieved for zero interaction but for slightly attractive one. The bias is $\epsilon = 10^{-10}t$.

unique with all particles clustered in one site. To account for such effects, we consider a slightly biased case which favours one site, the kth.

The localized condensate (LC) state in the kth site of the lattice, reads,

$$|\Psi_{\mathrm{LC}}(k)\rangle = \frac{1}{\sqrt{N!}}(\hat{a}_k^\dagger)^N |0\rangle\,. \tag{2.32}$$

In this state, as in the MI, the number of particles in each site is well defined and the correlation length vanishes. Different from the MI, also the energy gap vanishes, and its value is given by the value of the bias. Since this state is a single state of the Fock basis with all the particles localized in the same site, the values of S_1 and S_D are both 0.

It is noticed that if several sites on the lattice were biased significantly more than the rest, it could be possible to obtain a fragmented condensate. It is also possible to engineer the number of fragmented fractions by setting a number of biased sites in the lattice.

To understand the system behaviour for intermediate values of the attractive interactions, we apply exact diagonalization and calculate the entropy S_D as function of NU/t. The results are depicted in Fig. 2.9. The entropy has its maximum in the attractive regime, not at $U/t = 0$ where the entropy S_1 exhibits a minimum. This observation implies that the GS of a weakly attractive system is more uniformly distributed over the Fock basis than the GS of the SF phase. Increasing the attractive interaction, but keeping the bias smaller than the gap, the system is in a cat-like state, with $S_D = \ln(M)$. By cat-like state we mean a superposition state of events that mutually exclude each other from happening simultaneously, in this case, the superposition of clustering all the particles in every site of lattice. Finally, for even stronger attraction, the gap becomes smaller than the bias. Then the bias term dominates and the system localizes on a single site, with a single Fock state being the ground state.

The phenomenon is similar to the one studied in Ref. [80]. There, the system is found to go from a binomial distribution in Fock space, to a very homogeneous one at slightly attractive interactions. Further increasing the interactions, the distribution does not become more homogeneous, but instead starts to develop peaks around each of the two-sites, which corresponds to the two superposed states of the cat-like structure. In presence of a small bias, further increasing the attractive interaction, the system localizes.

Effects in the weakly attractive regime in higher dimensions than 1D are finite-size effects, since in the thermodynamic limit, a soft-core system of bosons collapses at any finite value of attractive interactions [91]. In 1D, due to the interplay between the kinetic energy and the attractive interaction energy, bright soliton solutions arise from the Gross–Pitaevskii equation [92].

Notice that in the weakly attractive regime, the number of populated Fock states increases when interactions are strengthened, but the distribution becomes less uniform. This behaviour is more pronounced in the cases with open rather than periodic boundary conditions, as open boundary provide a natural bias with less connected sites at the edge of the system.

2.5.3 Exact Diagonalization for other problems: quantum Hall physics

When it comes to studying Bose-Hubbard models with Exact Diagonalization, the reader has to notice that, despite its insurmountable size limitations, one strength of the method is its applicability to a wide range of problems. As example, just adding complex values to the tunnelling, models with gauge potentials can be studied.

In this section, we will briefly outline how the method can also be applied to continuum systems. As an example, we choose the fractional quantum Hall effect, which can be exhibited by fermionic particles (electrons), but also by bosons, e.g. a cold gas of bosonic atoms rotating around the z axis in 2D [93]. In this bosonic scenario, we shall find some analogies to the treatment of the Bose-Hubbard model.

The first step for treating the problem by exact diagonalization again is to construct a basis for the Hilbert space. In the quantum Hall effect, the single-particle energy levels are the Landau Levels (LLs), and it is usually enough to consider only one LL, for bosons the lowest LL (LLL). All states in the LLL are degenerate, and can be labelled by a quantum number $l \geq 0$, the angular momentum along the rotation axis. These angular momentum eigenstates play a role analogous to the sites in the Bose-Hubbard model, and it allows to map between the basis for the Bose-Hubbard model onto the basis of bosons in the LLL. Since, in principle, there are infinitely many single-particle states, though, we have to truncate the basis at a sufficiently large $l = l_{\mathrm{max}}$. Due to rotational symmetry, the total angular momentum L along z is conserved. This provides a natural value $l_{\mathrm{max}} = L$ for truncating the Hilbert space, but in practice the available angular momentum will be distributed more equally between all particles, so l_{max} can be chosen much smaller, at the order $l_{\mathrm{max}} \sim L/N$ for N bosons.

In contrast to the Bose-Hubbard model, due to the degeneracy of single particle levels in the fractional quantum Hall problem, there is no single-particle term in the Hamiltonian. Taking into account a trapping potential only introduces a L-dependent energy shift. The interactions, though, are much more difficult to treat than in the Bose-Hubbard model, as two particles at l and l' may scatter to arbitrary orbitals $(l+l')/2+x$ and $(l+l')/2-x$. The interactions may lift the huge single-particle degeneracy, and may give rise to a unique state describing a fractional quantum Hall phase. In order to interpret the numerical results, one tries to identify the fractional quantum Hall phases by scanning through different values of L, searching for pronounced gaps. Similar to our strategy presented in Sec.2.4.1, one can then compare the numerical ground state with trial wave functions by evaluating their overlaps.

In practical applications, the number of particles is clearly restricted to a small numbers, $N \lesssim 20$. The studies of mixtures of multicomponent systems restricts the computations to even smaller numbers. For those systems, a subspace containing every Fock-Darwin state of every species [58] is constructed. The total Hilbert space is direct sum of the subspaces, and hence, the total dimension of the space is the product of dimensions of those subspaces.

CHAPTER 3

QUANTUM HALL PHASES OF TWO-COMPONENT BOSONS

3.1 Introduction

The classical Hall effect is studied at the undergrad level. In the usual setting one has a two-dimensional rectangular metal plate. A voltage is applied to two of the opposing sides of the rectangle, thus inducing a current between the two sides. The Hall effect appears when one adds to this configuration a perpendicular magnetic field. In this case, a net transversal current appears. This current is found to increase if the applied field is increased. The explanation of course is that the electrons of the first current get deflected due to the action of the magnetic field, thus producing a net transversal current. Interestingly, this simple picture broke down when the applied magnetic fields where extremely intense. In 1980, von Klitzing reported a quantization of the Hall conductance [94], that is, as he increased the magnetic field, the conductance of the sample only changed in discrete steps. This phenomenon was the so called integer Quantum Hall effect. The explanation came from quantum mechanics and was directly linked to the Landau Level structure of the single particle spectrum of a 2D electron in the presence of a external magnetic field. Later on, fractional Hall phases were also reported [95], which could not be explained in a non-interacting picture. The most notable one, was the so-called Laughlin state [96], which explained a simple non-integer fraction. The Laughlin phase is a quantum liquid where the electrons are strongly correlated and whose low energy excitations are anyonic. These phases were described by topological properties, and thus, the Hall quantization was understood as arising from the topological properties of the ground state manifold of the system [97].

As commented in the previous chapters, ultracold atomic experiments provide a very clean and controllable setup in which several intricate condensed matter problems can be efficiently simulated. An appealing one is clearly the quantum Hall effect. At first, it seems difficult to simulate the physics of charged particles subjected to magnetic fields with neutral atoms, which basically do not get deflected by magnetic fields. The way out is to generate so called synthetic magnetic fields, that is, configuration which mimic the same physics. The first attempt in this direction was to consider ultracold atomic gases trapped in quasi 2D traps, subjected to fast rotation [93]. In this case, the mathematical resemblance between the Coriolis forces and the magnetic forces does the job [98]. This approach has actually been experimentally explored with ultracold bosons, producing phases with a large number of quantized vortex states [99]. In recent years, a different approach has been proposed, namely to produce synthetic gauge fields for ultracold atoms by profiting from the accumulation of Berry phase in certain configurations of lasers [see review, [100]].

Recent progress in producing strong synthetic gauge fields in neutral systems like atomic quantum gases [100, 101] or photonic fluids [102] has catalysed the research in bosonic quantum Hall states. While in the fractional quantum Hall (FQH) regime the bosonic states are often simply the counterparts of fermionic states, a significant difference occurs for non-interacting particles: Instead of forming an IQH liquid as fermions do, the bosons' fate is to condense. However, as has been strikingly predicted by effective field theory [103, 104], this does not exclude the possibility of an IQH phase of bosons. This phase can be obtained in a two-component system at filling factor $\nu = 2$. As has been confirmed by numerical studies [105–107], repulsive two-body contact interaction favours this phase against competing FQH phases. In contrast to the fermionic case, interactions are a crucial ingredient for the integer quantum Hall physics of bosons.

Different from FQH states, integer quantum Hall states have no anyonic excitations, nor do they exhibit topological degeneracies in non-trivial geometries (e.g. tori). Nevertheless, they possess topologically protected edge states which due to Wen's edge-bulk correspondence [108] make them distinct to conventional bulk insulators. A particularly appealing property of the edge in spin-singlet systems is the fact that it can be excited in twofold ways: by spinless charge excitations ("holons") or by charge-neutral spin excitations ("spinons") [109]. For the edge of the bosonic IQH phase, a K-matrix description predicts opposite velocities for these two types of excitations [104], as a consequence of one positive and one negative eigenvalue of the K-matrix. This interesting property has been discussed before for a FQH state of spin-1/2 fermions at $\nu = 2/3$ in a singlet [110, 111].

In the context of FQH physics, two-component Bose gases have been considered in a torus geometry [112, 113], where ground state degeneracies suggest them as a candidate for realizing NASS phases [114]. Quantum many-body states with non-Abelian excitations are particularly relevant, as their use for topological quantum computations has been proposed [115]. A recent study of two-component bosons in a spherical geometry [106], however, gave rise to some controversy: Competitors of the NASS states are the composite fermion states which have Abelian topological order.

In this chapter we shed further light on the quantum Hall physics of two-component bosons by performing a systematic numerical study in a disk geometry. After briefly introducing different trial wave functions, we study for $N = 6$ particles all incompressible states on the Yrast line, starting with the IQH state at $L_z = 9$ (in units of $\hbar$) and ending with the Halperin state at $L_z = 21$, where the system is able to fully avoid contact interaction. We find all the incompressible states to be well described by the composite fermion (CF) approach [116]. We then study (for $N = 8$) the edge excitations of

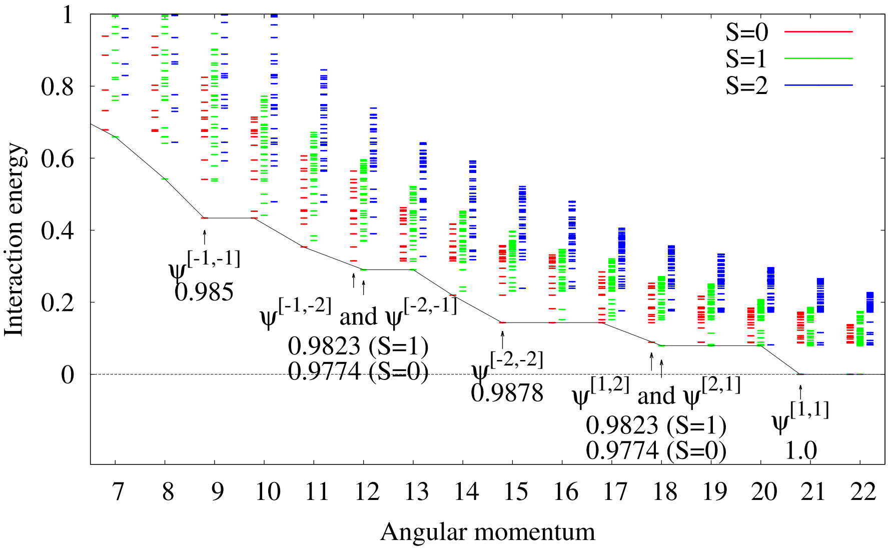

Figure 3.1: (Color online) Yrast line for $N = 6$: For the incompressible states (marked by arrows) we give the overlap with corresponding CF wavefunctions.

the IQH phase. Apart from some exceptions in the forward-moving branch, we find number and spin of the edge excitations to precisely agree with the predictions from effective theory. A model of the edge states based on CF theory is found to accurately describe the wave functions of the backmoving states. It is shown that the forward moving states can be modelled by multiplying the ground state wave function with symmetric polynomials. Finally, we demonstrate how pair-correlation functions distinguish the IQH state from competing states in an experiment.

3.2 System and trial wave functions.

We study a system of N two-component bosons described by the Hamiltonian

$$H = \sum_{i}^{N} \frac{[p_i - A(z_i)]^2}{2m} + \frac{m}{2}\omega^2 |z_i|^2 + V_0 \sum_{i<j} \delta(z_i - z_j)\,, \tag{3.1}$$

where $z_i = x_i + iy_i$ represents the position of the boson, $A(z) = \frac{B}{2}(x, -y)$ is a gauge potential, m, V_0, and ω are positive parameters specifying the mass, the two-body interaction strength, and the frequency of a harmonic confinement. The single-particle part of H has a Landau level (LL) structure, and is solved by Fock-Darwin (FD) states $\varphi_{n,\ell}$, which in the lowest Landau level (LLL) read $\varphi_{0,\ell}(z) \propto z^\ell \exp(-|z|^2/4)$, in units of length given by $\lambda = \sqrt{\hbar/(M\omega_0)}$, and $\omega_0 \equiv \sqrt{\omega^2 + \frac{B^2}{4m^2}}$.

One way to account for interactions is the CF theory developed by Jain [116]. It provides a compelling picture to understand both IQH and FQH phases on an equal footing: By attaching magnetic fluxes to each particle, one obtains CFs, which are assumed to behave like non-interacting particles, that is, they fill one or several LLs. Originally, this theory has been formulated for fermions, but it has been extended to bosonic quantum Hall phases triggered by the experimental progress in producing synthetic gauge fields acting on ultracold atoms [117]. Recently, CF states for two-component Bose systems have been introduced and studied in a spherical geometry [106].

Here we consider a system on a disk, for which a similar CF construction is detailed in the Appendix. Omitting the omnipresent Gaussian factor, the wave functions at angular momentum L_z read

$$\Psi_{L_z}^{[n_a,n_b]} = \mathcal{P}_{\text{LLL}} \left[\Phi_{n_a}(\{z_a\})\ \Phi_{n_b}(\{z_b\}) J_1(\{z\})\right] . \tag{3.2}$$

The last term is a Jastrow factor $J_1(\{z\}) = \prod_{i<j}(z_i - z_j)$, which attaches one magnetic flux to each particle, turning the bosons into CFs. The wave function of the composite particles is given by the Slater determinants Φ_{n_a} and Φ_{n_b}, for particles of type a and b, respectively. The indices $n_{a(b)}$ yield

the number of LLs occupied by the CFs. If $n_a = n_b$, the total spin is zero, $S = 0$. Importantly, negative n_a and n_b shall refer to flux-reversed LLs: $\Phi_{-n} \equiv \Phi_n^*$. Finally, $\mathcal{P}_{\mathrm{LLL}}$ projects back into the LLL of the bosonic system. We perform this projection in the standard way by replacing conjugate variables z^* by derivatives ∂_z.

The only difference between Eq. (3.2) and the corresponding definition on a sphere is the fact that in closed geometries the number of states in each LL is finite. This gives rise to the notion of "completely filled" LLs, and the state $\Psi^{[n_a,n_b]}$ is uniquely defined. Depending on the sign of $n = n_a + n_b$, its filling factor is $\nu_\pm = n/(n \pm 1)$. Contrarily, on a disk, there is more than one way to distribute N_a (N_b) particles in n_a (n_b) LLs. Typically each choice leads to a different total angular momentum L_z, such that wave functions at different angular momentum L_z correspond to the same filling factor ν in the thermodynamic limit. Note that, for $|n_a| = |n_b| = 1$, however, the wave functions are unique also on a disk. In particular, $\Psi^{[-1,-1]}$ has $L_z = N^2/4$ and corresponds to an integer filling factor, $\nu = 2$. In contrast to all other CF wave functions with fractional filling, this wave function might describe an IQH liquid.

Another important trial wave function, obtained within the CF theory by putting all composite particles to the LLL ($\Psi^{[1,1]}$), is the Halperin state [118], explicitly given by:

$$\Psi_{\mathrm{H}} \sim \prod_{i<j} (z_{ia} - z_{ja})^2 \prod_{i<j} (z_{ib-} z_{jb})^2 \prod_{i,j} (z_{ia} - z_{jb}) \ . \tag{3.3}$$

It is a spin singlet wave function at filling $\nu = 2/3$, with zero energy in a two-body contact potential, and describes an Abelian FQH phase. A series of non-Abelian quantum Hall states can be constructed from it by forming k clusters, putting each cluster into a Halperin state, and symmetrizing over all possible clusterizations [114]. In this way, one obtains the NASS states at filling factor $\nu = 2k/3$ as the zero-energy eigenstates of $(k + 1)$-body contact interaction.

3.3 Yrast line.

We have studied $N = 6$ two-component bosons in the LLL on a disk by exactly diagonalizing the SU(2)-symmetric two-body contact interaction. The presence of an additional harmonic trapping in H which is invariant under spatial rotations along the z-axis and under spin rotations will not modify the eigenstates of the system, but simply increase the energy eigenvalues by a value proportional to L_z. Properly choosing the trapping frequency, one can tune the ground state of the system to different L_z.

The system's Yrast line (i.e. the spectrum of the interaction energy at fixed L_z), is shown in Fig. 3.1. Different $L_z = 9, 12, 15, 18, 21$ correspond to incompressible states, that is, here an increase of angular momentum will not (directly) lead to a decrease in energy. Notably, for all these L_z it is possible to construct CF states. Moreover, exact ground states and CF states agree in spin, and have very good overlap (> 0.97). At $L_z = 21$, the overlap equals 1, as the Halperin state of Eq. (3.3) becomes the exact ground state. At $L_z = 18$, two CF states with $S_z \equiv (N_a - N_b)/2 = 0$ can be constructed: $\Psi^{[1,2]}$ and $\Psi^{[2,1]}$. Accordingly, the ground state is a triplet, but notably, also the antisymmetric combination of the two states gives rise to a quasi-degenerate singlet state. For $L_z = 15$, the CF construction yields a unique singlet phase, $\Psi^{[-2,-2]}$, with overlap 0.9878 and large gap. For $L_z = 12$, the situation is similar to $L_z = 18$, with a triplet ground state and a quasi-degenerate singlet state obtained from two possible CF states, $\Psi^{[-1,-2]}$ and $\Psi^{[-2,-1]}$. The incompressible phase with smallest L_z is found for $L_z = 9$: the clearly gapped ground state is a singlet and has large overlap (0.985) with $\Psi^{[-1,-1]}$.

3.4 Edge physics of the IQH phase.

We now focus on this lowest-L_z state on the Yrast line, for which we can extend our numerical study to $N = 8$ particles and, accordingly, $L_z = 16$. Compared to $N = 6$, we find an only slightly smaller overlap, $|\left\langle \mathrm{GS} \middle| \Psi^{[-1,-1]} \right\rangle| = 0.9709$. As $\Psi^{[-1,-1]}$ describes a spin singlet with integer filling $\nu = 2$, and

ΔL_z	-4	-3	-2	-1	+1	+2	+3	+4
number of singlets	2	1	1	0	1	2	3	5
number of triplets	2	2	1	1	0	0	0	0
number of quintets	1	0	0	0	0	0	0	0

Table 3.1: Number of modes of H_{edge} with $v_s < 0$ and $v_c > 0$.

the phase turns out to be strongly gapped and incompressible, all prerequisites for an IQH phase are fulfilled. Previous studies provided evidence of the integer topological character of this phase by analysing spectral properties [105–107], and wave functions on on a sphere [106]. In the present chapter, we consider the equivalent system in a plane, and focus on the physics at the edge to characterize its topology [108].

An effective theory of the edge physics in fermionic singlet states [110] is applicable also to the bosonic IQH state. It allows for a straightforward counting of the edge excitations. This theory is based on the observation that edge excitations of a spin singlet state might either be excitations which change angular momentum of the spin-up (down) particles, or be excitations which flip the spin of some particles. Thus, the effective edge Hamiltonian has the form [110]

$$H_{\text{edge}} \propto v_s(S_z^2 + \sum_l l b_l^\dagger b_l) + v_c \sum_l l c_l^\dagger c_l \,. \tag{3.4}$$

Here, the first term denotes the spinon excitations with velocity v_s, and the second term the holon excitations with velocity v_c. The operators b_l and c_l annihilate bosonic modes at angular momentum l.

For a counting of the modes, we only consider pure charge excitations ($\langle b_l^\dagger b_l \rangle = 0$) or pure spin excitations ($\langle c_l^\dagger c_l \rangle = 0$), as mixed charge/spin excitations are expected at higher energies. Moreover, we assume that $v_c > 0$ and $v_s < 0$, such that the charge (spin) excitations are located at positive (negative) ΔL_z. As a result, we find the multiplicities listed in Table I: The spinless c modes are simply counted by the number of positive-integer sums which add up to ΔL_z. Since $S_z^2 = 0$ for all c-modes, they must be singlets. In the spinon branch, instead, we have to count the number of

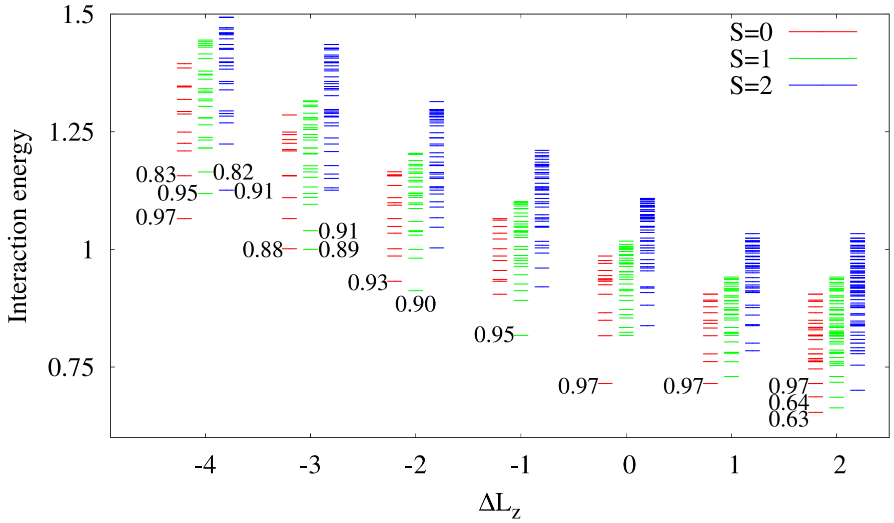

Figure 3.2: (Color online) Low-energy part of the spectrum of H, obtained by exact diagonalization of a system with $N = 8$ around $L_z = 16$. The numbers beside some states denote their overlap with the trial wave functions described in the text.

positive-integer sums which add up to $|\Delta L_z| - S_z^2$, where S_z now might take also non-zero integer values. For example, for $\Delta L_z = -1$, we might have $S_z = \pm 1$ and $\langle b_l^\dagger b_l \rangle = \delta_{l1}$, or $S_z = 0$ and $\langle b_l^\dagger b_l \rangle = 0$. These three states yield a triplet. Following this reasoning, the first occurrence of a quintet $(S = 2)$ is expected for $\Delta L_z = -4$.

3.5 Backward moving edge states.

In the spectrum shown in Fig. 3.2, we find one gapped triplet ground state at $\Delta L_z = -1$, and two quasi-degenerate gapped ground states, one singlet and one triplet, at $\Delta L_z = -2$. This perfectly matches with the counting expected from effective theory. Also at $\Delta L_z = -3$ and $\Delta L_z = -4$, the spin of the lowest states agrees with the spin predicted by effective theory, but the degeneracy lifting within the ground state manifold becomes larger than the gap to the excited states. A particularly striking confirmation of the effective theory is the fact that at $\Delta L_z = -4$ a $S = 2$ multiplet becomes member of the ground state manifold.

A simple intuitive explanation for the presence of backmoving state, which directly leads to a scheme for constructing trial wave functions, can be given in terms of the CF approach: Since the ground state, $\Psi^{[-1,-1]}$, describes an IQH phase of CFs which are subjected to a flux-reversed magnetic field, a forward-directed edge excitations of the CFs constitutes a backward-directed edge excitations of the bosons. More formally, as a consequence of the complex conjugation of the Slater determinants in $\Psi^{[-1,-1]}$, the edge excitation of the CFs (that is the shift of one or several CFs to higher angular momentum) will correspond to a reduced angular momentum of the bosons.

Following this reasoning, we have constructed trial wave functions for edge states with $-4 \leq \Delta L_z \leq -1$. For example, consider the state with $S_z = 0$ at $\Delta L_z = -1$: The ground state $\Psi^{[-1,-1]}$ consists of four spin-up and four spin-down CFs, each filling the FD states with $\ell = 0, \ldots, 3$ in the flux-reversed LLL. An edge state can then be obtained in two ways: for either the spin-up or the spin-down CFs, we replace the FD state with $\ell = 3$ by a FD state with $\ell = 4$, which after complex conjugation leads to $\Delta L_z = -1$. Strikingly, after projecting these wave functions into the LLL, both choices lead to exactly the same wave function, and we recover a single state at $S_z = 0$, as demanded by both the effective theory and the numerical results. This becomes more remarkable for $\Delta L_z < -1$: At $\Delta L_z = -2$, we find five ways to construct $S_z = 0$ edge states, but they reduce to two linearly independent states. At $\Delta L_z = -3$, ten different constructions lead to three states, and at $\Delta L_z = -4$, twenty constructions yield precisely five different states. Thus, the CF construction is in perfect agreement with the counting of modes. Apart from the counting, also the overlaps of the trial states with the exact states are remarkably high. They are explicitly given within Fig. 3.2, and for any of the eleven edge states in the interval

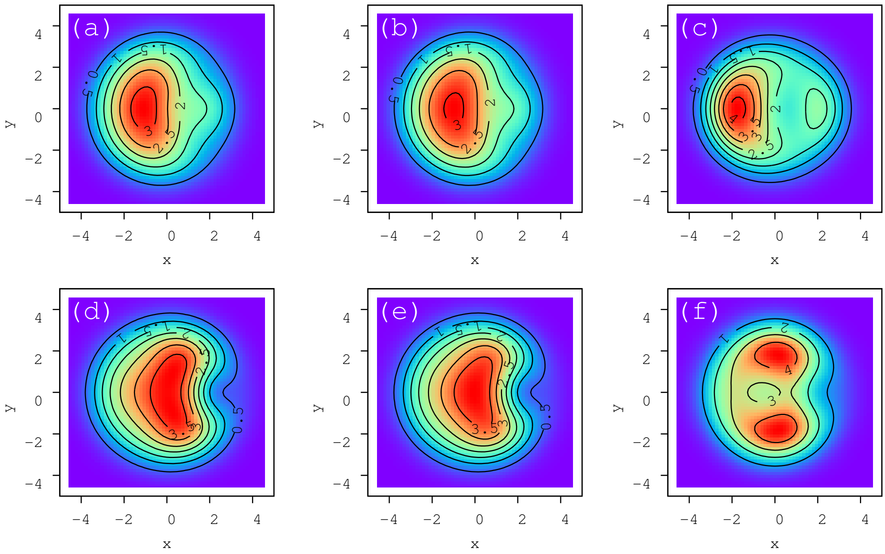

Figure 3.3: (Color online) Spin-dependent pair-correlation function for $N = 8$ particles, showing the probability density of finding one particle with given spin after fixing another particle of the same spin (a–c) or of opposite spin (d–f) to $(x, y) = (2.5, 0)$. In plots (a) and (d), the system is in the exact ground state at $L_z = 16$. in (b) and (e), the system is in the corresponding CF state, and in (c) and (f), it is in the $\nu = 4/3$ NASS phase.

$-4 \leq \Delta L_z \leq -1$ they are larger than 0.82, demonstrating the power of the CF description.

3.6 Forward moving edge states.

For $\Delta L_z > 0$, the effective theory predicts spin singlet ground states, with degeneracy $1, 2, 3, 5, \ldots$ for $\Delta L_z = 1, 2, 3, 4, \ldots$. Indeed we find a single singlet ground state at $\Delta L_z = 1$, though it is not separated by a large gap from a second, low-lying triplet state, see Fig. 3.2. Also at $\Delta L_z = 2$, there is a singlet ground state, but a nearby second state in the spectrum is a triplet state, instead of a second spin singlet. At $\Delta L_z = 3$, even the ground state is a triplet. It has been argued that forwardmoving edge states have a large velocity and thus merge with bulk excitations, spoiling the spectral structure expected from effective theory [106, 110]. Moreover, we note that the state $\Psi^{[-1,-1]}$ is the first incompressible state on the Yrast line. Therefore, while backmoving modes of this state do not interfere with forward moving edge modes of other incompressible states, the forwardmoving excitations of $\Psi^{[-1,-1]}$ are expected to mix with backmoving modes of an incompressible triplet phase at $L_z = 20$ (for $N = 8$).

Nevertheless, it is possible to identify some states in the spectrum of Fig. 3.2 as forward moving edge states of $\Psi^{[-1,-1]}$. We construct them by multiplying the ground state by homogeneous polynomials which are symmetric in all variables. Such excitation might either act on the bosons, that is on the wave function $\Psi^{[-1,-1]}$, or on the composite fermions, that is on the CF wave function *before* LLL projection. Remarkably, the latter approach yields slightly better results.

For $\Delta L_z = 1$, the construction yields one singlet, having overlap 0.9709 with the exact state. Note that this is precisely the overlap of the exact ground state at $\Delta L_z = 0$ with $\Psi^{[-1,-1]}$, suggesting that the construction of the edge itself is exact, and the slight deviation of the overlap from unity is caused by a discrepancy between the ground state at $L_z = 16$ and the CF state. Also, the ground states at both $\Delta L_z = 0$ and $\Delta L_z = 1$ have exactly the same energy.

At $\Delta L_z = 2$, the energy of only the sixth state in the spectrum, a singlet, matches with the ground state energy at $\Delta L_z = 0$. This state is well reproduced (again overlap 0.9709) by our construction of edge states which now yields two singlet states. At lower energies, we find two singlet states, two triplet states, and one $S = 2$ multiplet. Each of the two singlet states has an overlap around 0.63 with our edge state construction, suggesting that a linear combination of the two states would reasonably well agree. In that way, we can, out of the three low-energy singlet states, recognize two as the edge states predicted by effective theory.

3.7 Experimental realization.

We propose to use a system of two-component Bose atoms subject to two independent strong synthetic fields, employing the method of Ref. [119]. To this aim one can use two microwave couplings of opposite circular polarization to couple, for instance, $F = 1$, $M = \pm 1$ and $F = 2$, $M = \pm 2$ states of ^{87}Rb (employing methods proposed in Ref. [120] and pioneered for spin-dependent lattices in Refs. [121, 122]), or $F = 3$, $M = \pm 3$ and $F = 4$, $M = \pm 4$ states of ^{133}Cs, as realized recently in Ref. [123]. The proposed scheme could be tuned from the microscopic regime to the macroscopic regime, where it could resolve a competition between NASS and the CF state at $\nu = 4/3$ in the thermodynamic limit [106], or for $N \geq 16$, non-accessible by exact diagonalization. The favoured phase could be detected by a measurement of correlations, which has been demonstrated with single atom resolution in Refs. [14, 15]. Here, the same method can be used by switching on rapidly a deep lattice to localize the atoms.

To illustrate how correlations may identify the phase, we refer to a different competition which takes place for $N = 8$ at $L_z = 16$: Here the CF picture with the $\nu = 2$ state describes well the ground state (overlap 0.97), but an alternative trial wave function is the $\nu = 4/3$ NASS state (overlap 0.52). Note that the CF state and the NASS state themselves have overlap 0.41, despite their different topological order. The overlaps certainly give a clear picture in favour of the CF state, but they are not accessible to experiment. Instead, measuring the pair-correlation functions allows to distinguish clearly between CF and NASS state, as shown in Fig. 3.3.

3.8 Conclusions.

We have studied quantum Hall phases of two-component bosons on a disk. All incompressible phases are understood in the CF picture. The edge states identify the IQH phase of bosons. This phase could be realized in experiments with cold atoms, and detected by measuring pair-correlation functions.

CHAPTER 4

TOPOLOGICAL PHASES OF LATTICE BOSONS WITH A DYNAMICAL GAUGE FIELD

4.1 Introduction

In the previous chapter we considered a setup in which ultracold bosons where subjected to static artificial gauge fields. In that case, we could mimic or simulate the physics of the fractional quantum Hall effect. An important current goal in the race for building quantum simulators of complex problems in physics and other fields is to go one step further and simulate dynamical gauge fields. The long-term goal is the simulation of quantum electromagnetism or chromodynamics, that is, of models where matter interacts with dynamical fields, as described in Refs. [124–128]. In the case of quantum chromodynamics (QCD), the need for accurate methods to study its non-perturbative domain is clearly desirable. Currently, the most accurate methods to study statics aspects of QCD is lattice QCD, a formulation of the of the theory on lattices which is solved with the help of large supercomputing facilities, see for instance the some of the recent achievements on the mass of the proton and neutron from lattice QCD calculations [129]. Quantum simulators of such systems, could, in principle, allow one also to study dynamical and scattering processes.

The current situation is still far from allows for a quantum simulation of QCD. Current quantum simulation with artificial gauge potentials are exploring the variety of interesting physics related to background gauge fields: spin liquid phases [130], topological phases evidenced by non-zero Chern numbers [131], or quantum Hall phases with edge currents [132, 133]. Indeed, an intermediate step might be the realization of simpler but nevertheless dynamical gauge fields, engineering an occupation number-dependent tunnelling term [134–141].

In this chapter, we consider a specific dynamical gauge field and apply exact diagonalization techniques to shed light on the involved interplay between the atoms' external degree of freedom and the system's $U(1)$ gauge potential. The atoms are confined to a two-dimensional optical lattice, where a gauge field is present due to a density-dependent complex phase of the tunnelling parameter t. Deep in the Mott phase, where density fluctuations are strongly suppressed, the gauge potential is static. We follow the system's evolution upon decreasing the ratio U/t, where U parametrizes the strength of the repulsive on-site interactions. For sufficiently weak interactions, topological transitions, not present in the system with a static gauge field, are found in the system with a dynamical gauge potential.

In our study the system is assumed to be close to filling one, where for large enough atom-atom interaction the Mott insulating state provides a vacuum-like configuration. In the strongly interacting regime, an extra-particle on top of the Mott insulator can be viewed as a single particle in a static gauge potential with a fixed magnetic flux per plaquette. This configuration therefore reproduces Hofstadter physics [142]. Due to computational limitations, our study addresses a 3×3 lattice with $4\pi/3$ flux per plaquette. Twisted periodic boundary conditions allow for reducing finite-size effects. The low-energy subspace is clearly divided into three gapped bands. Chern number calculations demonstrate the non-trivial topological nature of the bands. Since a hole in the Mott insulator does not feel any gauge potential, the extra-particle configuration also captures the behaviour in a larger Mott insulator with a particle-hole excitation. Upon decreasing the interaction, we find deviations from this single-particle picture. For a dynamical gauge potential we find that the ground state undergoes a topological phase transition before it becomes topologically trivial in the limit $U \to 0$.

The chapter is organized as follows. First, in Sec: 4.2, we describe our theoretical tools, including the density dependent Hamiltonian we are considering. Then in Sec. 4.3 we present results for the different band gaps found, comparing the case of a dynamical field and the one of an static external field. The characterization of the topological properties by means of Chern numbers is presented in Sec. 4.4. In Sec. 4.5 a phase diagram through a Mean Field approach is presented in order to give an intuitive idea of the behaviour of the system in the infinite size case. In addition, the Appendix A.3 includes the procedure used to compute Chern numbers for the many-body bands to characterize the topological phases.

4.2 Theoretical model

Cold atoms in optical lattices are well described by a Hubbard model combining nearest-neighbour hopping processes and on-site interactions [2]. The effect of a (synthetic) magnetic field is taken into account by a Peierls phase in the hopping parameter. For instance, if $\hat{b}_{k,l}$ ($\hat{b}^\dagger_{k,l}$) denotes the annihilation (creation) of a particle at site (k,l), the hopping term in a constant magnetic field with magnetic flux φ per plaquette is written in the Landau gauge as

$$\hat{\mathcal{H}}_{\text{Landau}} = -t \sum_{k,l} \left(\mathrm{e}^{\mathrm{i}\varphi l} \hat{b}^\dagger_{k,l} \hat{b}_{k+1,l} + \hat{b}^\dagger_{k,l} \hat{b}_{k,l+1} + \text{h.c.} \right) . \tag{4.1}$$

Here, t is a real-valued parameter associated with the kinetic energy of the particles. We consider a two-dimensional system of scalar bosons. Im-

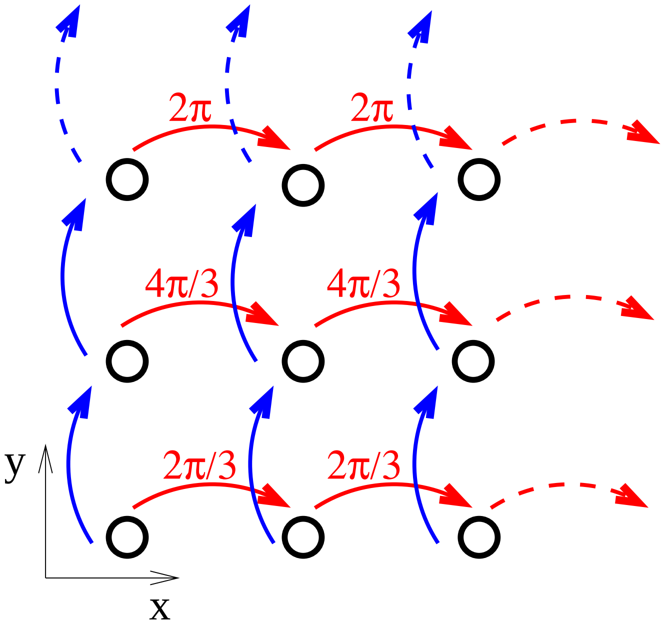

Figure 4.1: Brief rendition of the considered density dependent Hamiltonian. As an example we provide the phase acquired for the single particle case, $\hat{\mathcal{H}}_{\text{Landau}}$, with $\varphi = 2\pi/3$. The solid lines represent the tunnelling terms, the dashed ones correspond to the periodic boundary conditions considered.

portant quantities like the energy spectrum of the Hamiltonian are gauge-independent, that is, alternative hopping Hamiltonians with complex phases along the x-direction or along both the x- and y-direction would lead to the same results as long as the flux per plaquette remains the same. A schematic representation of the hopping structure is given in Fig. 4.1.

A possible implementation of Hamiltonians like $\hat{\mathcal{H}}_{\text{Landau}}$ goes back to Ref. [143]. In this chapter, we are interested in a situation where the gauge field becomes dynamical, that is, the complex phase factor should in some form depend on the positions of the atoms. A simple dynamical gauge field is obtained by letting the phase depend on the occupation numbers,

$$\hat{\mathcal{H}}_{\mathrm{dyn}} = -\,t\sum_{k,l}\Big(\hat{b}^{\dagger}_{k,l}\mathrm{e}^{\mathrm{i}\varphi l\left(\hat{n}_{k,l}+\hat{n}_{k+1,l}\right)}\hat{b}_{k+1,l} + \hat{b}^{\dagger}_{k,l}\hat{b}_{k,l+1} + \mathrm{h.c.}\Big)\,. \tag{4.2}$$

The experimental implementation of density-dependent gauge fields as those of Hamiltonian (2) can be done using similar techniques as those recently discussed in Refs. [138, 139]. Particular details of how to implement it fall beyond the scope of the present study.

This choice of the density dependent field is particularly attractive as it has one specific limit in which the topological properties of the system can be easily understood. Deep in the Mott insulating phase, where the number operators $\hat{n}_{k,l}$ can be replaced by an integer number n, this Hamiltonian reduces to the form of a $\hat{\mathcal{H}}_{\mathrm{Landau}}$. The amount of particle number fluctuations and thereby the dynamical features of the gauge potential are controlled by the interaction term, $\hat{\mathcal{H}}_{\mathrm{int}} = \frac{U}{2}\sum_{k,l}\hat{n}_{k,l}(\hat{n}_{k,l}-1)$. With this, the full Hamiltonian reads

$$\hat{\mathcal{H}} = \hat{\mathcal{H}}_{\mathrm{dyn}} + \hat{\mathcal{H}}_{\mathrm{int}}\,. \tag{4.3}$$

We will take an additional constraint on the Hilbert space, stemming from the implementation scheme described in Ref. [138], namely, the maximum occupancy per site will be set to two bosons.

To clarify our discussion we will compare our results to those obtained with an static field, that is,

$$\hat{\mathcal{H}}_{\mathrm{st}} = \hat{\mathcal{H}}_{\mathrm{Landau}} + \hat{\mathcal{H}}_{\mathrm{int}}\,. \tag{4.4}$$

4.3 Energy gaps

We have concentrated on the filling case around one by means of exact diagonalization. We have focused on a 3×3 lattice at $\varphi = 4\pi/3$, and take the interaction strength U (in units of t) as the main tuning parameter.

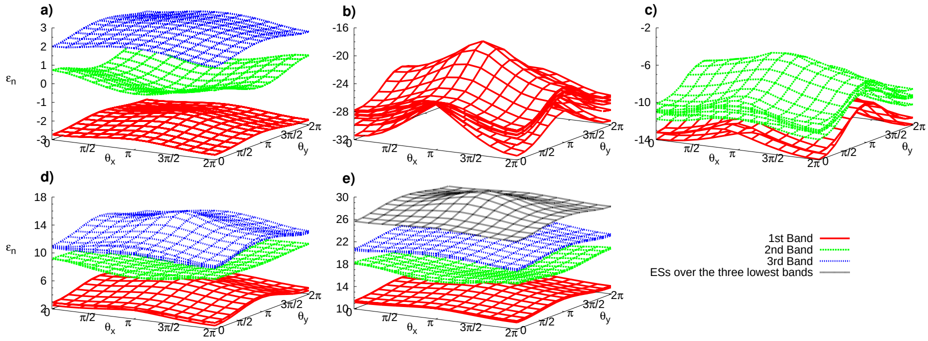

Figure 4.2: Energy spectrum as a function of the twisted boundary conditions for several systems under $\hat{\mathcal{H}}_{\text{st}}$ with a flux per plaquette $\varphi = 2\pi/3$ in a 3×3 lattice. Degenerated states forming bands have the same color. a) Single particle case. b)–e) Energies of the ten lowest eigenstates of the system with 10 particles for the interaction values: b) $U = 0t$, c) $U = 4t$, d) $U = 13t$ and e) $U = 20t$. ESs means Excited States.

As argued above, this also controls the influence of the dynamical gauge field. To gain meaningful results despite the small system size, we apply twisted boundary conditions with twist angles θ_x and θ_y. With this, the energy spectrum ϵ_i of the Hamiltonian becomes a function of the twist angles, $\epsilon_i(\theta_x, \theta_y)$. Degeneracies of different levels which would be lifted due to the finite system size manifest themselves in crossings of bands $\epsilon_i(\theta_x, \theta_y)$. Accordingly, we define the gap above a level ϵ_i as

$$\Delta\epsilon_i = \min\left[\epsilon_{i+1}\left(\theta_x, \theta_y\right) - \epsilon_i\left(\theta_x, \theta_y\right)\right] . \tag{4.5}$$

If $\Delta\epsilon_i$ is zero, that is, if band i and band $i + 1$ have (at least) one crossing, we consider these levels a degenerate manifold. To check whether the manifold is separated from higher levels by a gap, we then have to consider $\Delta\epsilon_{i+1}$. In general, the gap above a k-fold manifold including the

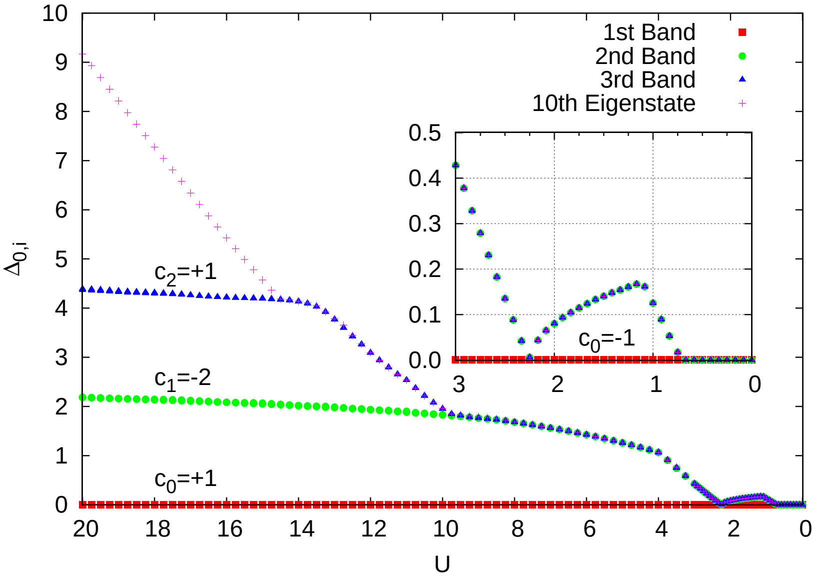

Figure 4.3: Gap above each band, [as defined in Eq. (4.6)], between consecutive eigenstates of $\hat{\mathcal{H}}$ as function of the on-site interaction parameter U. The system is a 3×3 lattice with 10 particles with the parameter $\varphi = 2\pi/3$ and $t = 1$. We take into account the Hilbert constraint to a maximum of two bosons per site. The three lowest bands have degeneracy 3. and the labels correspond to the Chern number of each band.

levels $i, \ldots, i+k$ is defined as

$$\Delta_{i,i+k} = \sum_{j=i}^{i+k-1} \Delta\epsilon_j \, . \tag{4.6}$$

4.3.1 Case of one excess particle

We start our analysis with the tunnelling of a system with one particle more than the number of sites. That is, in our 3×3 lattice we consider $N = 10$

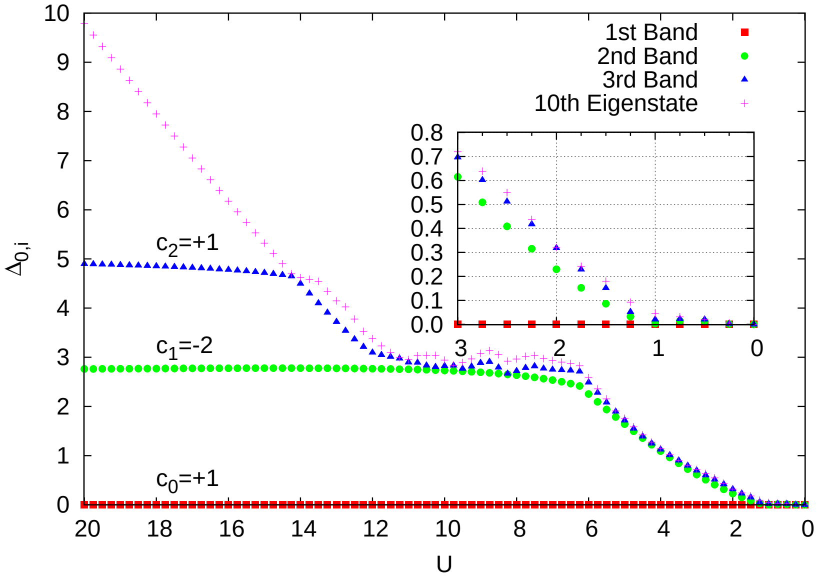

Figure 4.4: Same description as in Fig. 4.3, but with the dynamical gauge field replaced by an external magnetic field with a flux per plaquette $\varphi = 4\pi/3$. That is, $\hat{\mathcal{H}}\,(\phi) \to \hat{\mathcal{H}}_{\mathrm{st}}\,(2\phi)$.

bosons. On the strongly interacting side, this is equivalent to having a single particle on top of a fluctuating vacuum. For large U, fluctuations are strongly suppressed, and the kinetic Hamiltonian (4.2) reduces to the one of a particle in a static magnetic field, Eq. (4.1), with flux 2φ. Accordingly, the physics of a single particle in a magnetic field should describe the low-energy behaviour of our system. Indeed, no difference is seen between the shape of the single-particle spectrum of the Hamiltonian (4.1), Fig. 4.2 a), and the (low-energy part) of the one of the many-body spectrum of Hamiltonian (4.3) at large U, Fig. 4.2 e). In both cases, we find the energy spectrum to be split into three gapped manifolds, each of them consisting of three states. In the many-body system, a gapless high-energy manifold lies above the third band.

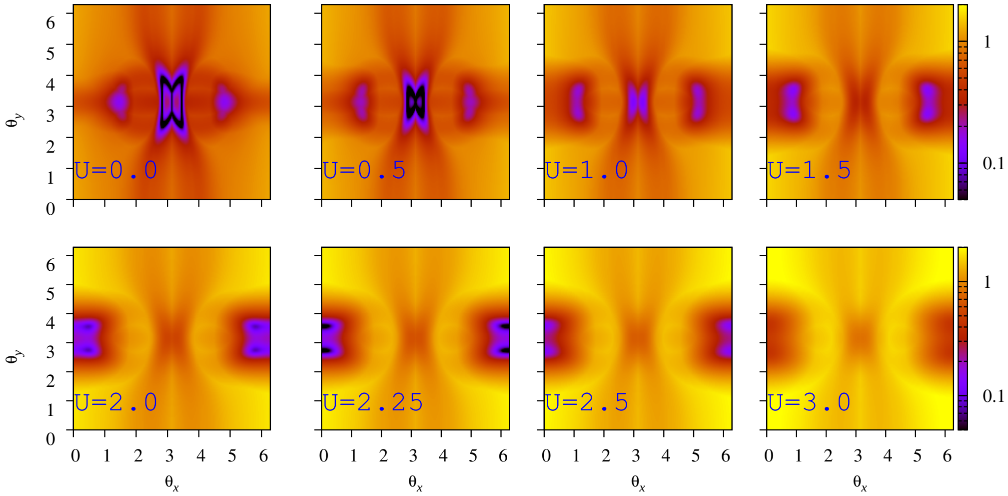

Figure 4.5: Energy difference between the third and fourth states in the spectrum of a system under $\hat{\mathcal{H}}$ with 10 particles in a 3×3 lattice, signalling the gap between the ground state manifold and next excited state. The different panels correspond to different values of U. In all cases, $\varphi = 2\pi/3$ and $t = 1$.

Deviations from this structure appear when U is decreased, see Fig. 4.2(b–e) and Fig. 4.3. The dynamical mechanism is the following. As U is decreased, the number of holon-doublon excitations increases, the single-particle picture described above is no-longer valid. First, for $U \approx 15$, the gap between the third band and the high-energy manifold closes, as the first doublon-holon excitations have the same energy as the third single particle state. Subsequently, at $U \approx 10$, also the gap to the second band is closed. These gap closings indicate phase transitions in excited states. At $U \simeq 2.25$, also the gap to the lowest band is closed. Thus, up to $U \simeq 2.25$ the ground state manifold has a topological structure similar to the case of a single particle subjected to an external magnetic field of 2φ. This value of U is a bit higher than the value at which we found a gapless phase for the filling one case described below. Thus, the main picture of a single particle on top of a Mott insulating background is consistent.

Remarkably, further lowering the value of the interaction another threefold-degenerate gapped manifold appears for $0.67 \lesssim U \lesssim 2.25$. Only for $U \lesssim 0.67$ the system enters in a gapless phase. We note that for $0.67 \lesssim U \lesssim 2.25$ the gap is small, of the order of 10% of the involved energy scales. It is a merit of the twisted boundary conditions that the three lowest states are clearly identified as an adiabatically connected manifold, separated from the other levels by a gap. In fact, if we look at the system for a fixed value of θ_x and θ_y, or alternatively for open boundary conditions, the gap cannot be distinguished from the energy splitting between states in the degenerate manifold. The evolution of the gap between the ground state manifold and the next excited state for the all values of θ_x and θ_y is given in Fig. 4.5. The gap above a manifold as function of U is shown in Fig. 4.3 . For $U \simeq 0.67$ the gap closes at $(\theta_x, \theta_y) \simeq (\pi, \pi)$. The next closing, for $U \simeq 2.25$ appears close to $(\theta_x, \theta_y) \simeq (0, \pi)$. This could diminish the prospects for an experimental detection of this phase in the plane geometry, but since an experiment would realize a much bigger system, there is hope that finite-size degeneracy splitting would be sufficiently small to identify the finite gap.

In Fig. 4.4, we contrast our findings to the scenario with static magnetic field. As expected, at large U the differences between Fig. 4.3 and 4.4 are minor. Also for a static magnetic field, increasing U subsequently closes the gaps above the third and the second band. However, the gap above the ground state remains finite up to $U \simeq 1$ and, for $U < 1$, it vanishes.

4.3.2 Mott insulator

At precisely filling one, for 9 particles on 9 lattice sites, see the upper panel of Fig. 4.6, we find a unique gapped ground state for $U \gtrsim 2.1$, which is connected to the Mott insulator as an exact solution for $U \to \infty$. This phase is trivial in the sense that it corresponds to a vacuum, where deviations from integer filling exist only as fluctuations. For $U \lesssim 2.1$, we find a gapless phase, that is, despite the presence of the dynamical gauge field, no topological structure protected by an energy gap emerges in this scenario.

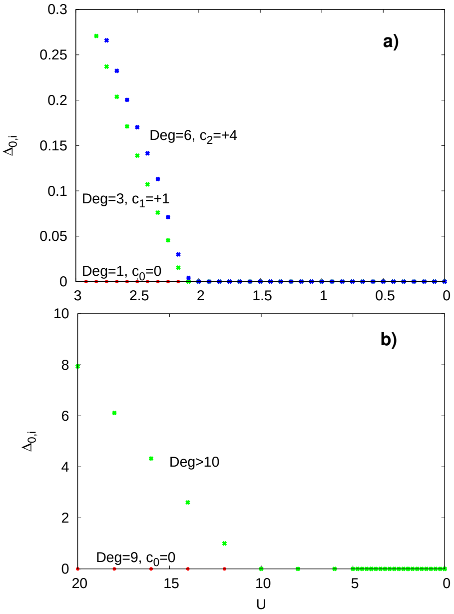

Figure 4.6: Energy gap, see Eq. (4.6), between consecutive eigenstates of $\hat{\mathcal{H}}$ as function of the on-site interaction parameter U. We take into account the Hilbert constraint to a maximum of two bosons per site. The upper and lower panels are for $N = 9$ and $N = 8$, respectively.

The first and second excited bands are three- and six-fold degenerate, respectively. They are topologically non-trivial and their Chern numbers are +1 and +4. This excited bands coincide, in degeneracy and topology, with the lowest band of the non-interacting systems with one and two particles in the same lattice, as they are explained in Section 4.4. These excited bands can be understood as one and two particle-hole excitations on the top of the Mott insulator, when the particle feels an effective static magnetic field and the hole do not.

4.3.3 Case of one hole

We also study the tunnelling of a single hole. That is, in our 3×3 lattice we consider $N = 8$ bosons. The gap structure we find is shown in Fig. 4.6 b). As expected, we find that increasing the interaction up to $U \simeq 10t$, a gap opens between the nine-fold degenerate manifold, understood as one hole moving in the Mott-insulating background, and the rest of the states. The ground state manifold is found to have a trivial topological order.

4.4 Topological phases

In the previous section we have discussed the energy gaps appearing for the case of one excess particle, the filling one, and the one hole case. The only case in which we have found non-trivial topological structures is for the case of one excess particle. In the following we present the Chern number obtained compared to the case of an external field of flux $4\pi/3$.

4.4.1 Single particle and non-interacting cases

First, we calculate the Chern numbers of the single-particle system described by $\hat{\mathcal{H}}_{\text{Landau}}$, that is, of the bands shown in Fig. 4.2 a). We obtain the values $\{1, -2, 1\}$. In this case, the calculation can either be done via Fourier transformation, taking the parameters k_1 and k_2 to be components of the wave vector [144], or with twisted boundary conditions, taking the twist angles θ_x and θ_y as parameters k_1 and k_2 [145]. In the latter case, the discretization of parameter space is arbitrary, but we observe quick convergence of the Chern numbers to fixed numbers upon refining the discretization.

The non-interacting case can be related to the single particle case although some caution should be exercised. For instance, direct computation of the Chern number of the ground state manifold for $N = 2$, 3, and 4 particles in the 3×3 lattice we consider gives $c = 4, 10$ and 20, respectively. These can be obtained by noting that due to the bosonic symmetry, we have a combinatorial factor stemming from the number of times the Fock basis

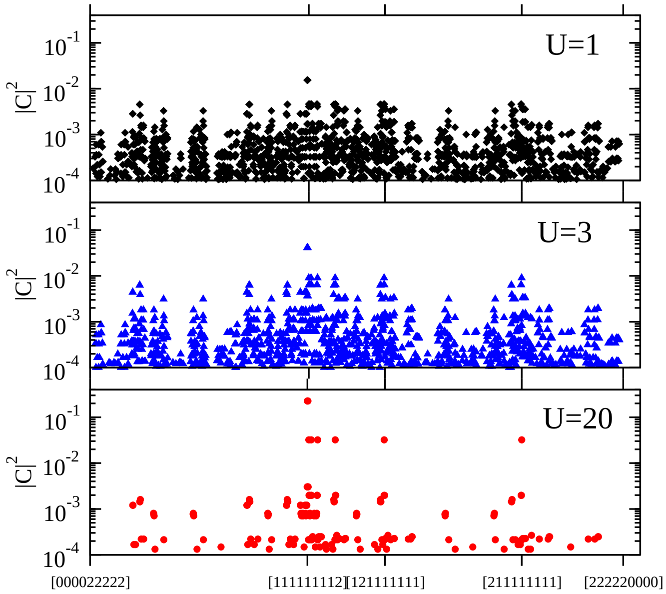

Figure 4.7: Squared coefficients of the ground state of the density dependent $\hat{\mathcal{H}}$ for $\theta_x = \theta_y = 0$ in the Fock basis in lexicographical order. A few notable states, one particle on top of a Mott insulator, are marked. The three panels corresponds to three values of the interaction, $U = 1, 3$ and 20. For these values, the Chern number of the ground state manifold is -1, $+1$ and, $+1$, respectively.

covers the threefold degenerate band. This can be evaluated giving,

$$c_0^{(N)} = \frac{N}{3}\binom{N+3-1}{N} c_0^{(1)} = c_0^{(1)}\binom{N+2}{3}, \tag{4.7}$$

where $c_0^{(1)}$ is the single particle Chern number of the GS manifold, $c_0^{(1)} = 1$.

4.4.2 Interacting many-body case

To calculate the Chern numbers of many-body states, we exclusively resort to the twisted boundary conditions. For the three gapped manifolds appearing at $U \lesssim 15$, see Fig. 4.3, we obtain the same Chern numbers as for the single particle bands: $\{1, -2, 1\}$. These numbers remain constant for each manifold until the closing of the corresponding gap. Upon closing the gap, the second and the third bands simply merge with the energy continuum, for which no Chern number can be computed. This is easily understood as for large enough interactions the many-body ground state is well described as consisting on a Mott-insulating background plus one particle. The lower band is given by the energy of the extra particle in the presence of an external field with flux $4\pi/3$. The closing of the bands in the higher part of the spectrum comes from the first particle-hole excitations which eventually degenerate with excitations of the excess particle. Note that even though this simple picture provides a compelling explanation it is quite remarkable that albeit the many-body state changes, as shown in Fig. 4.7, as U is decreased, the topology of the band does not change for a broad range of U.

In contrast with the above, the gap closing of the ground state at $U \approx 2.25$ separates two gapped regions, see in particular the inset of Fig. 4.3. Interestingly, we find that upon closing the band gap, the ground state Chern number changes its sign from 1 to -1. This demonstrates that a topological phase transition between two distinct, but topologically nontrivial phases is taking place. The second gap closing, at $U \approx 0.67$, merges the ground state manifold with the energy continuum which, in this sense, is a transition to a topologically trivial (gapless) phase.

4.4.3 Static field case

Finally, we note also that the three gapped manifolds found for a system with static magnetic field, with $\phi = 4\pi/3$, are characterized by the same Chern numbers $\{1, -2, 1\}$, without any transitions to distinct gapped phases. As seen in Fig. 4.4, the arguments exposed above also apply to this case and the picture of a single particle on top of a Mott-insulator is perfectly valid. The only relevant difference appears for low interaction energies. In this case, the Mott insulating phase seems to survive down to lower values of the interaction as compared to the density dependent case. Thus, density dependence phases favour the existence of superfluid regimes at larger interactions than in the static case. Also we find no trace of the first excitation being a topological phase with $c_1 = +1$ in the region $2.25 \gtrsim U \gtrsim 0.67$. In this case the limit $U = 0$ can be understood from the single-particle calculation: The ground states for N bosons are just arbitrary distributions on the $M = N_\mathrm{s}/q$ states belonging to the lowest energy band in a lattice with N_s sites at magnetic flux $2\pi/q$. This leads to a macroscopic ground state degeneracy (of 63 states in our case with $N = 10$, $N_\mathrm{s} = 9$, and $q = 3$), for which no meaningful Chern number can be defined. Recent "Chern number" measurements in non-interacting bosonic quantum gases [131] consider the Hall drift for unique but gapless many-body states, and define as a "Chern number" the average over different states.

4.5 Mean field Phase diagram

In order to get a picture of the phase diagram, we have adapted the Mean-field calculation of Ref. [136] to the Hamiltonians of interest. At first, we include a chemical potential term $-\mu \sum_{i,j} \hat{n}_{i,j}$. With the convenient substitutions $\hat{c}_{i,j} \equiv e^{\mathrm{i}\phi j \hat{n}_{i,j}} \hat{b}_{i,j}$ and $\hat{d}_{i,j} \equiv e^{-\mathrm{i}\phi j \hat{n}_{i,j}} \hat{b}_{i,j}$, the Hamiltonian in Eq. (4.3) looks like,

$$\begin{aligned} \hat{\mathcal{H}} = & \sum_{k,l} \Big\{ - t\Big(\hat{d}^\dagger_{k,l}\hat{c}_{k+1,l} + \hat{b}^\dagger_{k,l}\hat{b}_{k,l+1} + \text{h.c.}\Big) \\ & + \hat{n}_{k,l}\left[(\hat{n}_{k,l} - 1)\,\frac{U}{2} - \mu\right] \Big\} . \end{aligned} \tag{4.8}$$

At $t = 0$, all the sites are independent and the GS can exactly be represented with a Gutzwiller ansatz,

$$|\Psi_0\rangle = \bigotimes_{k,l}^{N_\mathrm{s}} |\psi\rangle_{k,l}, \qquad |\psi\rangle_{k,l} = \sum_{m=0}^{\infty} f_{k,l}^{(m)} |m\rangle_{k,l}, \tag{4.9}$$

where m is the number of particles in a site. Then, the energy due to each site filled with m particles is $\epsilon_m = U\left[\frac{1}{2}(m-1) - \frac{\mu}{U}\right] m$. and the energy of adding and subtracting one boson is,

$$\epsilon_{m+1} - \epsilon_m = U\left(m - \frac{\mu}{U}\right), \qquad \epsilon_{m-1} - \epsilon_m = U\left(\frac{\mu}{U} - m + 1\right), \tag{4.10}$$

respectively.

The MF is obtained by decoupling the hopping terms as $\hat{d}_{i,j}^\dagger \hat{c}_{i+1,j} \approx \alpha_{3,j}^* \hat{c}_{i+1,j} + \alpha_{2,j} \hat{d}_{i,j}^\dagger - \alpha_{3,j}^* \alpha_{2,j}$ and $\hat{b}_{i,j}^\dagger \hat{b}_{i,j+1} \approx \alpha_{1,j}^* \hat{b}_{i,j+1} + \alpha_{1,j+1} \hat{b}_{i,j}^\dagger - \alpha_{1,j}^* \alpha_{1,j+1}$, with the order parameters $\alpha_{1,j} \equiv \langle \hat{b}_{i,j} \rangle$, $\alpha_{2,j} \equiv \langle \hat{c}_{i,j} \rangle$ and, $\alpha_{3,j} \equiv \langle \hat{d}_{i,j} \rangle$. Then, the Hamiltonian in Eq. (4.8) becomes,

$$\hat{\mathcal{H}} = -N_\mathrm{x} t \sum_j \left(\alpha_{3,j}^* \alpha_{2,j} + \alpha_{1,j}^* \alpha_{1,j+1} + \mathrm{h.c.}\right) + \sum_{k,j} \hat{h}_{k,j}, \tag{4.11}$$

with the local Hamiltonian

$$\hat{h}_{k,j} \equiv \hat{n}_{k,j} \left[U\left(\hat{n}_{k,j} - 1\right)/2 - \mu\right] - t\hat{T}_{k,j}, \tag{4.12}$$

where $\hat{T}_{k,j} \equiv \alpha_{3,j}^* \hat{c}_{k,j} + \alpha_{2,j} \hat{d}_{k,j}^\dagger + \alpha_{1,j-1}^* \hat{b}_{k,j} + \alpha_{1,j+1} \hat{b}_{k,j}^\dagger + \mathrm{h.c.}$ and N_x is the size of the system in the x-direction. The Hamiltonian $\hat{h}_{k,j}$ has a trivial solution when $\alpha_{\gamma,j} = 0$, $\gamma = 1, 2, 3$ since the particle number fluctuations vanish at the Mott insulating phase.

When the kinetic term is negligible ($t \ll U$), the entire system is described with the basis of states with m particles per each site (k, j), $|m\rangle$. The GS is determined by μ: it is the local state $|m\rangle$ when $m - 1 < \mu < m$. Since we want to draw the Mott lobes, we include the single Fock state and particle-hole excitations in that region of the diagram. Then, since we search the boundaries close to the trivial solution, $|\alpha_{\gamma,j}| \ll 1$, and the kinetic term can be treated perturbatively. Up to first perturbation order, the local wavefunction $|\Psi\rangle$ can be written as $|\psi^{(0)}\rangle + |\psi^{(1)}\rangle$, being $|\psi^{(0)}\rangle = |m\rangle$ and

$$\begin{aligned}
|\psi^{(1)}\rangle =& -t\sum_{m'} \frac{\langle m'|\hat{T}_{k,j}|m\rangle}{\epsilon_{m'}-\epsilon_m}|m'\rangle \\
=& \frac{t}{U}\frac{\sqrt{m}\left[\alpha^*_{3,j}e^{\mathrm{i}\phi j(m-1)}+\alpha^*_{2,j}e^{-\mathrm{i}\phi j(m-1)}+\alpha^*_{1,j-1}+\alpha^*_{1,j+1}\right]}{\frac{\mu}{U}-(m-1)}|m-1\rangle \\
&+\frac{t}{U}\frac{\sqrt{m+1}\left[\alpha_{3,j}e^{-\mathrm{i}\phi jm}+\alpha_{2,j}e^{\mathrm{i}\phi jm}+\alpha_{1,j-1}+\alpha_{1,j+1}\right]}{m-\frac{\mu}{U}}|m+1\rangle
\end{aligned} \tag{4.13}$$

The first order perturbation about the solution $\alpha_{\gamma,j} = 0$ is convenient here, since the self-consistency equations define a linear map $\alpha_{\gamma,j} = \Lambda_{\gamma,j}^{\gamma',j'}\alpha_{\gamma',j'}$. Then, when the largest eigenvalue of Λ, λ_0, is larger than 1, the trivial solution is no longer stable. So, the boundary is found to be at $\lambda_0 = 1$. The self-consistency relations $\alpha_{1,j} = \langle\Psi|\hat{b}_{k,j}|\Psi\rangle$, $\alpha_{2,j} = \langle\Psi|\hat{c}_{k,j}|\Psi\rangle$ and, $\alpha_{3,j} = \langle\Psi|\hat{d}_{k,j}|\Psi\rangle$ give,

$$\begin{aligned}
\alpha_{1,j} &= \frac{t}{U}\left[A\left(\alpha_{1,j-1}+\alpha_{1,j+1}\right)+f_j\left(\phi\right)\alpha_{2,j}+f_j\left(-\phi\right)\alpha_{3,j}\right] \\
\alpha_{2,j} &= \frac{t}{U}\left[f_j\left(\phi\right)\left(\alpha_{1,j-1}+\alpha_{1,j+1}\right)+f_j\left(2\phi\right)\alpha_{2,j}+A\alpha_{3,j}\right] \\
\alpha_{3,j} &= \frac{t}{U}\left[f_j\left(-\phi\right)\left(\alpha_{1,j-1}+\alpha_{1,j+1}\right)+A\alpha_{2,j}+f_j\left(-2\phi\right)\alpha_{3,j}\right]
\end{aligned} \tag{4.14}$$

with

$$f_j\left(\phi\right) \equiv \left[A+B\left(e^{-\mathrm{i}\phi j}-1\right)\right]e^{-\mathrm{i}\phi jm}$$

$$A \equiv \frac{\frac{\mu}{U}+1}{\left[\frac{\mu}{U}-(m-1)\right]\left[m-\frac{\mu}{U}\right]}, \qquad B \equiv \frac{m}{\frac{\mu}{U}-(m-1)}.$$

For the case of the static magnetic field, the corresponding function $f_j^{\mathrm{st}}\left(\phi\right)$ reduces to $Ae^{-\mathrm{i}\phi j}$.

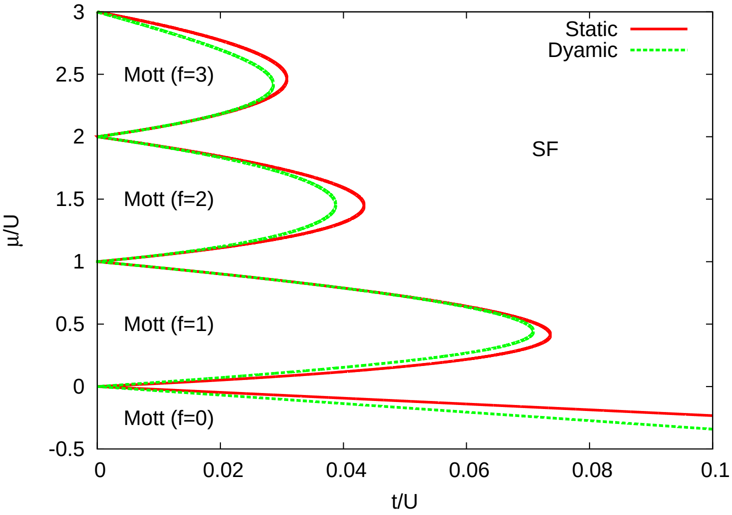

Figure 4.8: Phase boundary between the Mott insulator phase and the superfluid phase for the external and dynamical magnetic fields according to the Gutzwiller ansatz with the MF approach in the 1st perturbation order in the hopping t.

The Fock space populations of the GS of the system, Fig. 4.7, have revealed its structure: the Fock states which have a particle on top of a MI in the same row are equally populated. Then, we have tried an ansatz which is translationally invariant along the x-direction and have a 3-unit cell in the y-direction. So, in Eq. (4.14), $j = 1, 2, 3$, without periodic boundary conditions. Then, those relations define a linear system of nine coupled linear equations, being $\alpha_{\gamma,j}$ the variables. Once the matrix of the system is diagonalized as function of t, for a numeric value of U, μ (and its corresponding integer m), the expression of λ_0 is set to 1 and then the equation is solved for t. Finally, the phase boundary is obtained as a collection of points (μ, t).

We find the Mott lobes, shaped as usual in the MF approach, see Fig. 4.8. The values of the boundary do not correspond to the ones of the MF for the

2D lattice, but they are closer to the ones of the 1D case, see Ref. [69]. The structure of the GS state has revealed this to be closely related to the fact that the magnetic fields are in the Landau gauge. Our analysis also shows that the trial state is slightly more robust upon decreasing hopping t/U in the dynamic field case than in the static one. This finding qualitatively agrees with our results for the gap separation in the exact diagonalization analysis: As seen in Figs. 4.3 and 4.4, the SF regime corresponds to the gapless phase at small U, which extends to $U = 0.8$ in the dynamic case, and $U = 1.2$ in the static case. For $\mu < 0$, the boundaries of the dynamic field case and the 2D non-magnetic case coincide, as expected.

CHAPTER 5

MODIFIED SPIN-WAVE THEORY OF COLD BOSONS ON AN INHOMOGENEOUS TRIANGULAR LATTICE

5.1 Introduction

Quantum spin liquids (QSL) constitute one of the holy grails of contemporary quantum many body physics. In contrast to ferromagnetic or antiferromagnetic systems, QSL do not break the SU(2) symmetry; still similarly as spin glasses, they do exhibit some kind of long-ranged, hidden order. It is believed nowadays that gapped spin liquids exhibit exact topological order. The interests of the Quantum Optics Theory group in QSL started with the studies of antiferromagnets in kagomé lattices [146–148]. In 2009, our group realized that lattice shaking might lead to the change of tunnelling matrix elements in the optical lattices. We proposed to use this effect to realize QFL and spin liquids in the anisotropic triangular lattice [149]. Klaus Sengstock group in Hamburg started then in collaboration with us a series of works on shaken triangular lattices that has led to several publications in Science, Nature Physics, Physics Review Letters and others [130, 149–152]. So far, spin liquids in those systems has not been yet observed. Maybe, due to undesired heating effects and possible other complications. It became thus extremely important to understand what is the critical temperature and what are the phase boundaries of the spin liquid region. Philipp Hauke, in a series of papers [149, 153–155], demonstrated that boundaries of the SQL regions can be found by analysing generalized spin-wave theory. The breakdown of the spin-wave theory signalizes the appearance of exotic SQL phase in the system.

Hauke's works, although very important, did not include important elements of the experiments, namely the presence of the loose harmonic trap, keeping the atoms in the lattice together. In order to understand the effects of the trap, one has to generalize the spin-wave theory to the inhomogeneous situations. Technically, it is a very challenging task, and the present section is devoted to its analysis. The section start with extensive introduction to the QSL physics.

The chapter is structured in the following way: After introducing the system and model in Section II, we construct the modified spin wave theory in Section III. From this theory, we obtain a phase diagram in Section IV. In Section V, we consider first a small lattice using exact diagonalization. Then, we show that quasi-exact results can be obtained for much larger lattices using DMRG. The main conclusion drawn from our study, summarized in Section VI, regards the co-existence of spin liquid behaviour at different filling factors smaller than 1/2. Thus, the spin liquid phase is expected to be robust against inhomogeneities due to a trapping potential. Our finding should facilitate the experimental observation of spin liquids in optical lattice systems.

Although the present chapter focuses on a generalized mean field method and on an analytic calculation, it contains nevertheless, some comparison with exact diagonalization, obviously very restricted for straightened antiferromagnetic systems. The analytic methods used here have a lot in common with the ones that are used for preparation of exact diagonalization calculations in other systems. This chapter is an important part of the thesis, since it extends it to another type of complex quantum systems and quantum phases.

5.2 Basics of SQL physics

Quantum spin liquids (QSL)s are at the center of interest of contemporary condensed matter physics and quantum many body theory (cf. [156]) for several reasons. P. W. Anderson proposed them as a new kind of insulator: a resonating valence bond (RVB) state [157]. The interest in these state was clearly stimulated by the fact that they were soon associated with high T_c superconductivity [158]. Immediately it was realized that RVB spin liquids might exhibit topological order [159] and are related to fractional quantum Hall states [160] and chiral spin states [161].

Frustrated anti-ferromagnets (AFM) provide paradigm playground for RVB states and spin liquids (for the early reviews see [162–164]). The most prominent example is Heisenberg spin 1/2 model in a kagomé lattice. Unfortunately, they are notoriously difficult for numerical simulations, since due to the (in)famous sign problem quantum Monte Carlo methods cannot be applied. Still, a lot of information can be extracted from exact diagonalization studies (for seminal early studies see Ref. [165]). There was a lot of effort to describe QSLs with various approximate analytic approaches, such as large N expansion [166], or appropriate mean field theory [167, 168]. These studies suggested that QSLs described by RVB states represent topologically ordered states with finite energy gap, analogous to those of the famous Kitaev's Toric Code model [169].

In parallel to AFM in kagomé lattice, the so called dimer model in triangular lattice was studied intensively [170] – it was also found that it is expected to exhibit a gapped RVB phase (see also [171, 172]).

The first experimental indications of QSLs comes from studies of Mott insulator in the triangular lattices [173], and power law conductivity inside the Mott gap in certain materials [174]. More recently observations (cf. [175–177]) combine various standard and non-conventional detection methods in kagomé Heisenberg AFM, including measurements of fractionalized excitations [176]. There are also reports of QSL behavior in the, so called, *Herbertsmithites* (cf. [178]).

Recently great progress was achieved in numerical simulations of the gapped QSLs, based on the the use 1D density matrix renormalization group (DMRG) codes, "wired" on 2D tori/cylinders. This approach allowed for better insight into the properties of the ground state of the Heisenberg AFM in the kagomé lattice [179, 180]. More importantly, it allowed obtaining convincing signature of its topological Z_2 nature . This was based on numerical estimate for the, so called, topological entanglement entropy (TEE) – the quantity that unambiguously characterizes topological gapped QSLs [181, 182]. Calculations of TEE were earlier applied to the quantum dimer model in the triangular lattice [183] and to the Bose-Hubbard spin liquid in the kagomé lattice [184]. They were extended to critical QSLs [185], Toric Code [186] and lattice Laughlin states [187]. Since these calculations aim at sub-leading term in entanglement entropy, it is quite challenging to achieve good accuracy (see for instance [186, 188].

Recently, studies of AFM in kagomé lattice were extended to novel proposals for characterizing/detecting topological excitations and dynamical structure factor [189]. Several papers discuss inclusion of the chiral terms and Dzyaloshinsky-Moriya interactions, resulting in formation of chiral QSLs [190, 191]. Considerable interest was devoted also to the $J_1 - J_2$ Heisenberg model in the kagomé lattice [192] and in the square lattice [193], to the $J_1 - J_2 - J_3$ Heisenberg model in the kagomé lattice [194, 195] , and to the Kitaev-Heisenberg model [196, 197] in triangular lattices [198, 199].

Systems of ultracold atoms and ions provide a very versatile playground for quantum simulation of various models of theoretical many body physics [2, 200] – QSLs have in this context also quite long history. The first proposals for quantum simulators of the Kitaev model in the hexagonal lattice [201], and AFM in the kagomé lattice [146–148] were formulated more than ten years ago; all of them were based on smart designs and use of super-exchange interactions in optical lattices. More feasible and perhaps are experimentally less demanding proposals based on ultracold ions [202], or ultracold atoms in shaken optical lattice [149]. The latter schemes were originally designed to control the value and sign of the tunneling in Bose-Hubbard models – for original theory proposal see [203], and for the first experiments in the square lattice see [204]. They should be regarded as specific examples of generation of synthetic gauge fields in optical lattices [2, 205], or more precisely synthetic gauge fields in periodically-driven quantum systems [153].

Change of sign of tunneling in the triangular lattice is know to be equivalent of the introduction of the π-flux synthetic "magnetic" field in the Bose-Hubbard model [149, 160]. In the hardcore boson limit one obtains then an XX AFM model in the triangular lattice, which for isotropic bonds is known to have a planar Néel ground state. If, however, the bonds are anisotropic and their values t_1, $t_2 = t_3 = t\,t_1$ can be controlled, then as anisotropic parameter t goes from infinity to zero the model interpolates between an AFM in a rhombic lattice (with the conventional Néel ground state) to an AFM in the ideal triangular lattice (with the planar Néel ground state), and finally to an AFM in an array of weakly coupled 1D chains (with the conventional Néel ground state again). Exact diagonalizations and tensor network states simulations (PEPS) indicate that between these three Néel phases there exists two quite extended regions of gapped QSLs [202].

Interestingly the presence and the location of the QSL phases can be determined quite accurately using the generalized spin wave theory, which signals instability at the QSL boundaries [153, 202]. The spin wave method is impressively powerful and has been generalized and applied to frustrated bosons and Heisenberg model with completely asymmetric triangular lattice [154, 155].

We should stress that the proposal of Ref. [149] is in principle very promising, since it requires temperature of order of $(t/U)U \simeq t$ which is achievable in realistic experimental conditions, here U denotes atom-atom on site interaction energy. In fact, initial experiment demonstrated feasibility of the scheme, but were conducted far from hardcore boson limit. In these experiments a triangular array of cigar shaped Bose-Einstein condensates was realized, corresponding to a frustrated quasi-classical AFM [150], described by a classical XX spin model with the $U(1)$ symmetry, and Gaussian Bogoliubov-de Gennes quantum, or better to say quasi-classical fluctuations. In the further investigations, by exploiting control over the temporal shape of the periodic modulation, one could realize arbitrary Peierl's phases, i.e. arbitrary fluxes of the synthetic "magnetic" field through the elementary plaquette of the lattice ([151], see also [152]). This allowed for realization of a quasi-classical spin model with competing $U(1)$ and Ising Z_2 symmetries [130]. The route toward the strongly correlated regime and hardcore limit seem to be obscured, however, by uncontrolled heating mechanisms, most probably intrinsically associated with the periodic modulation scheme [205].

Even if this difficulty is overcome, another experimental aspect might prevent the observation of QSLs in such systems. Indeed the overall harmonic trapping of the atomic ensemble leads to non-constant filling factor over the optical lattice. We should expect thus formation of wedding cake structure, formed by the different quantum phases (cf. [2] and references therein). How does the phase diagram look like or change in the presence of such "experimental imperfections"? This is the question we want to answer in this chapter. To this aim we apply exact diagonalization on small lattices with open and periodic boundary conditions. On large lattices we apply modified spin-wave theory, adopted to the spatially inhomogeneous situation, which turns out to be technically much more demanding than the one pertaining to the spatially homogeneous lattice with half-integer filling. Specifically, we derive for the first time a modified spin-wave theory that works for generic homogeneous filling, which allows to study large weakly trapped systems in local density approximation. Our work provides a starting point for the future applications of tensor network state approaches like Projected Entangled Pair States (PEPS) to a moderate size lattices. These future calculations will aim at estimations of topological entropy, which so far for the considered model in the triangular lattice has not yet been accomplished even in the spatially homogeneous case with periodic boundary conditions. Studying the influence of the spatial inhomogeneities, induced by the presence of the trap or disorder, on topological entanglement entropy is a fascinating question in itself – it goes, however, beyond the scope of the present paper. While inhomogeneity due to confinement are instrinsict to ultracold atoms, our approach may be also relevant for searching QSLs in other quasi-2D condensed matter systems that present residual magnetization or inhomogeneities, for instance, due to the presence of a substrate.

The chapter is structured in the following way: After introducing the system and model in Section II, we construct the modified spin wave theory in Section III. From this theory, we obtain a phase diagram in Section IV. In Section V, we consider small systems ($N \leq 24$) using exact diagonalization. The main conclusion drawn from our study, summarized in Section VI, regards the co-existence of spin liquid behavior at different filling factors smaller than 1/2. Thus, the spin liquid phase is expected to be robust against inhomogeneities due to a trapping potential. Our finding should facilitate the experimental observation of spin liquids in optical lattice systems.

5.3 Description of the atomic model and map to the spin model

Ultracold bosons in deep optical lattices are very well described by the Bose-Hubbard model. Therefore, we will take the Bose-Hubbard Hamiltonian as a starting point for our analysis:

$$\hat{H} = \sum_{\langle ij \rangle} t_{ij} (\hat{b}_i^\dagger \hat{b}_j + \text{H.c.}) + \frac{U}{2} \sum_i \hat{n}_i (\hat{n}_i - 1) + \sum_i V_i \hat{n}_i. \tag{5.1}$$

Here, the $\hat{b}_i^\dagger$, $\hat{b}_i$ are the creation and annihilation operator at the site i of the triangular lattice, and $\hat{n}_i = \hat{b}_i^\dagger \hat{b}_i$ is the number operator of the Fock space. The first term is a possibly anisotropic nearest-neighbor hopping, with tunneling amplitudes t_{ij}. In the standard case, one would have a minus sign in front of the tunneling term. However, it is possible to control the sign (or even phase) of the tunneling, which is a crucial ingredient to generate frustration in the triangular lattice. As here we will exclusively be interested in such scenario of reversed hopping amplitude, we absorbed the sign in the definition of t_{ij}, such that standard hopping would correspond to $t_{ij} < 0$, while we will consider $t_{ij} > 0$. The second term in H

describes repulsive on-site interactions of strength $U > 0$. The last term is the trapping potential $V_i = Vr_i^2 - \mu_0, V = \frac{1}{2}m\omega^2$. Although it is present in any realistic experiment, it is often neglected in theoretical studies. The positions of a boson on site i is denoted by r_i.

If interactions U are strongly repulsive, fluctuations in particle number is suppressed. It is then justified to restrict the local Hilbert space to a subspace formed by the states with occupation number two. These states may change throughout the trap, but within a local density approximation, we may keep them fixed within a circular area in the center of the trap, and ring-shaped areas further outside, as illustrated in Figure 5.1. Each region is denoted by an integer I, according to the possible occupation within the region, $n_I = \{I-1, I\}$.

This approach allows to map the Bose-Hubbard Hamiltonian onto a spin model, using a Holstein-Primakoff transformation [206]. Within each region I, the transformation is defined as

$$\begin{aligned} \hat{S}_i^z &= (-1)^I \Big(I - \frac{1}{2} - \hat{n}_i \Big), \\ \hat{S}_i^+ &= \frac{(\hat{b}^\dagger)^I}{\sqrt{I}} \quad , \quad \hat{S}_i^- = \frac{(\hat{b})^I}{\sqrt{I}} \quad , \quad (\hat{b}^\dagger)^2 = (\hat{b})^2 = 0. \end{aligned} \tag{5.2}$$

The vanishing of squared creation or annihilation operators is due to the restriction of the local Hilbert space to two states. Using the definition of spin operators the tunneling part of the original tight-binding Hamiltonian gets transformed to $I \sum_{\langle i,j \rangle} t_{ij} \hat{S}_i^+ \hat{S}_j^-$ +H.c.. The interaction part transforms to $U(\hat{S}^z)^2 + 2U(-1)^{I+1}\hat{S}_z(I-1) + U(I^2 - 2I + 3/4)$. The trap potential gives rise to a term $V_i \hat{S}_i^z$. With $(\hat{S}^z)^2 = 1/4$, and neglecting the terms which are constant within a given region I, the dynamical part of the transformed Hamiltonian is an XX model in an inhomogeneous transverse field:

$$\hat{H}_I = I \sum_{\langle ij \rangle} t_{ij} \hat{S}_i^+ \hat{S}_j^- + \text{H.c.} + \sum_i V_i \hat{S}_i^z. \tag{5.3}$$

Before studying this Hamiltonian in the next sections using modified spin wave theory and exact diagonalization, let us briefly discuss the parameter regimes which are of interest experimentally. As mentioned before,

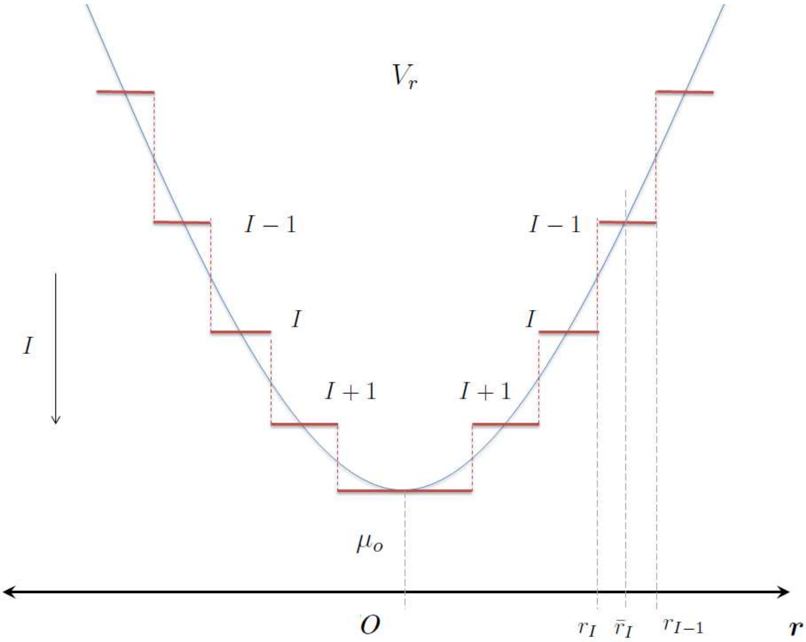

Figure 5.1: Local density approximation. The harmonic potential, which for simplicity we assume to have cylindrical symmetry, is decomposed in two contributions: a step-like profile and a smoothly varying term. Each plateau extends between the radii r_I and r_{I-1}, defined as the distances where the average occupation takes two consecutive integer values, $\langle \hat{n}_{r_I} \rangle = I$, $\langle \hat{n}_{r_{I-1}} \rangle = I - 1$. The height of the plateau is taken to be the one corresponding to half filling. The smooth terms can be then treated as a perturbation, on the same footing as the hopping term. The effective model in each plateau is thus equivalent to an anisotropic XX-spin model with an smoothly varying magnetic term.

being interested in frustration and spin liquids, the spin-spin interactions in Eq. (5.3) should be antiferromagnetic, that is, $t_{ij} > 0$. To simplify the scenario, t_{ij} should only depend on the direction of the hopping, with amplitudes along horizontal links denoted t_1, while the two links with non-

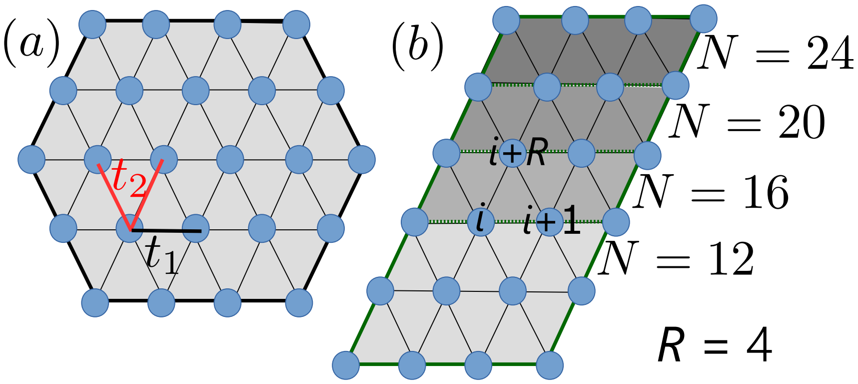

Figure 5.2: (a) A triangular lattice of $N = 24$ sites with a hexagonal shape. Horizontal hopping amplitudes are given by t_1, while hopping in the other directions have an amplitude $t_2 = t\,t_1$, where t parametrizes the anisotropy of the lattice. (b) A triangular lattice of up to $N = 24$ sites with a rhombic shape. For studying the behavior upon scaling the system size (cf. Sect. 5.6.1), we use this structure. In order to conveniently define the form factor (5.39), the spins are identified by unique position index $i = 1, \ldots, N$, starting from the bottom left. As displayed, i increases by one while moving on the right, and by the length of the row, R, while moving up right.

zero vertical component shall have an amplitude $t_2 = t\,t_1$, see Figure 5.2. The anisotropy of the lattice is then characterized by a single parameter t, which we will tune from 0, corresponding to an effective 1D system, to values greater than 2, where the lattice geometry is dominated by a rhombic structure. The energy difference between neighboring spins is of the order $\Delta V_i = V a^2 \equiv \eta\, t_1$, where a is the lattice constant, and η is a dimensionless parameter. We Assume the lattice is loaded with ^{87}Rb atoms, which has lattice constant $a = 553$ nm and a trap frequency $\omega = 2\pi \times 40$Hz; we have $\Delta V_i/\hbar = 15$Hz. This is about an order of magnitude weaker than typical interactions strengths, $t_1/\hbar \approx 150$Hz. In the modified spin wave approach, we will therefore take $V_i = 0$, while the effect of non-zero values will be addressed within the exact diagonalization study.

5.4 Modified spin-wave theory

Let us start by analyzing the spin system for constant *non-zero* magnetization, which corresponds to fillings different from $\frac{1}{2}$. Classically, we expect the spin oriented along a cone around the z-axis,

$$\mathbf{S}_i = (\sin\rho\, \cos(\mathbf{Q}\cdot\mathbf{r}_i), \sin\rho\, \sin(\mathbf{Q}\cdot\mathbf{r}_i), \cos\rho). \tag{5.4}$$

Here, $\boldsymbol{Q} = (Q_x, Q_y)$ is a vector in the xy-plane while ρ is the azimuthal angle related to the magnetization along the z-axis, i.e. to the filling of the original bosons $\nu = \langle\hat{n}\rangle - [\langle\hat{n}\rangle]$, where $[x]$ = integer part of x. For $\rho = \frac{\pi}{2}$, (5.4) reduces to the ansatz considered by [153, 207] at half filling. If we follow the standard spin-wave approach, we should choose the local basis in such a way that the new local z-axis is parallel to the vector (5.4). In this way, by applying the bosonization of the local spin we would model fluctuations *along the classical ordering* represented by (5.4). Now, such fluctuations would have component also along the z-axis. In other words, they would renormalize the filling factor. Such behavior is not acceptable from the physical point of view. Indeed, in the original bosonic Hubbard model the filling factor is a well defined quantity: the hopping term conserves the particle number, and, thus, the expectation value of the particle density which is the filling. The same argument holds for the same physical model as described as a spin system. In practice, the acceptable fluctuations are restricted to the xy-plane, and, precisely, are along the projection of the ordering vector on the xy-plane. That is to say that corrected choice for the quantization axis is the same as at half filling.

What is then the difference with respect to the half-filling case? The difference resides in the magnitude of the spin projection. If we do the reasonable assumption that the fluctuations are proportional to such length we can relate n, the local density of bosonic excitations, to the filling. As originally proposed by Takahashi [208], such density at half filling should be taken equal to the total spin, $n = S$, that to say also the bosonic excitations are at half-filling. Here, we propose a generalized Takahashi condition,

$$n = S|\sin\rho|, \tag{5.5}$$

where the angle ρ is related to the filling by the relation $\langle S^z \rangle = \nu - S = S\cos\rho$ which implies $|\sin\rho| = \frac{1}{S}\sqrt{\nu(2S-\nu)}$. This choice has further physical justification. First, it is symmetric around half filling as it should be: reversing the quantization axis $\hat{z}$ in the Dyson-Maleev transformation [209, 210] is equivalent to the replacement $\nu \to 2S - \nu$. Second, fluctuations are maximal at half-filling and are suppressed in the paramagnetic (Mott) phases, which correspond to filling $\nu = 0$ and $2S$.

As derived in previous sections, the filling factor ν is smoothly changing in the trap and relates to the harmonic potential as $\nu = [\frac{\mu}{U} + \frac{1}{2}]$, where $[x] =$ fractional part of x (the hopping term has zero mean). Thus, our analysis can be applied in local density approximation to trapped systems.

We define the local spin operators $\hat{\mathbf{S}}' \equiv (\hat{S}^{x'}, \hat{S}^{y'}, \hat{S}^{z'})$ that are related to the global ones $\hat{\mathbf{S}} = (\hat{S}^x, \hat{S}^y, \hat{S}^z)$ through the rotation

$$\hat{\mathbf{S}} = R(\theta_i)\hat{\mathbf{S}}' \equiv R(\mathbf{Q}\cdot\mathbf{r}_i)\hat{\mathbf{S}}', \tag{5.6}$$

where

$$R(\theta_i) = R_z(\theta_i)R_y(-\pi/2)R_z(\theta_i) = \begin{pmatrix} 0 & -\sin(\theta_i) & -\cos(\theta_i) \\ 0 & \cos(\theta_i) & -\sin(\theta_i) \\ 1 & 0 & 0 \end{pmatrix},$$

is the rotation that sends the vector $(0, 0, -1)$ to $(\cos\theta_i, \sin\theta_i, 0)$, i.e. along the projection of ordering vector on the xy-plane.

By composing with the Dyson-Maleev transformations

$$\begin{aligned} \hat{S}_i^{z'} &\to -S + a_i^\dagger a_i, \\ \hat{S}_i^{+'} &\to \sqrt{2S}a_i, \\ \hat{S}_i^{-'} &\to \sqrt{2S}(1 - \frac{a_i^\dagger a_i}{2S})a_i, \end{aligned} \tag{5.7}$$

we find that in the original spin basis, the bosonization is

$$S_i^{\pm} = e^{\pm i\theta_i}\left(\pm\sqrt{\frac{S}{2}}(a_i^\dagger - (1 - \frac{\hat{n}_i}{2S})a_i) + S(1 - \frac{\hat{n}_i}{S})\right), \tag{5.8}$$

where $\hat{n}_i = a_i^\dagger a_i$, $\theta_{ij} = \boldsymbol{Q} \cdot \boldsymbol{r}_{ij}$, and $\boldsymbol{r}_{ij} = \boldsymbol{r}_j - \boldsymbol{r}_i$. The effective Hamiltonian reads (up to fourth order in a or $a^\dagger$)

$$
\begin{aligned}
H &= \frac{1}{2} \sum_{<ij>} t_{ij} \left(S_i^+ S_j^- + S_i^- S_j^+ \right) \\
&= \sum_{<ij>} t_{ij} \cos\theta_{ij} \Bigg(S^2 - S(\hat{n}_i + \hat{n}_j) - \frac{S}{2}(a_i^\dagger a_j^\dagger + a_i a_j) + \frac{S}{2}(a_i^\dagger a_j + a_i a_j^\dagger) \\
&+ \hat{n}_i \hat{n}_j - \frac{1}{4}(a_i^\dagger \hat{n}_j a_j + a_j^\dagger \hat{n}_i a_i) + \frac{1}{4}(\hat{n}_j a_j a_i + \hat{n}_i a_i a_j) \Bigg) \\
&- i \sum_{<ij>} t_{ij} \sin\theta_{ij} \Bigg(S\frac{\sqrt{2S}}{2}(a_i^\dagger - a_j^\dagger - a_i + a_j) + \frac{\sqrt{2S}}{4}(\hat{n}_i a_i - \hat{n}_j a_j) \\
&- \frac{\sqrt{2S}}{2}(\hat{n}_j a_i^\dagger - \hat{n}_i a_j^\dagger - \hat{n}_j a_i + \hat{n}_i a_j) \Bigg) . \qquad (5.9)
\end{aligned}
$$

Note that this expression does not coincide with [153][Eq. 5]: indeed, the odd terms in $\sin\theta_{ij}$ are absent there as they have zero expectation value on a thermal gas of excitations. It is worth noticing that the terms in $\cos\theta_{ij}$ and $\sin\theta_{ij}$ are manifestly symmetric and antisymmetric under the exchange of indices, $i \leftrightarrow j$, respectively. Indeed, by construction the whole expression is invariant under such exchange of summed indices. Furthermore, the Hamiltonian (5.9) can be rewritten in an explicit translational invariant fashion by noticing that the sum over the links can be performed as a sum over there links coming out of a site, and then summing over all the sites. As these three lattice vectors on a triangular lattice we choose $\boldsymbol{\tau}_1 = (1,0), \boldsymbol{\tau}_2 = \frac{1}{2}(1,\sqrt{3}), \boldsymbol{\tau}_3 = \frac{1}{2}(-1,\sqrt{3})$. As H in Eq. (5.9) is non-Hermitian, following Takahashi [208], we use it in order to construct a free Energy for a gas of bosonic excitations in a generic Bogoliubov basis at temperature T, i.e.

$$
\mathcal{F} = E - T\mathcal{S} + \mu(n - S|\sin\rho|), \qquad (5.10)
$$

where E is the expectation value of H,

$$E = \frac{1}{N}\sum_{\boldsymbol{k}} \langle \nu_{\boldsymbol{k}}| \, H \, |\nu_{\boldsymbol{k}}\rangle \,, \quad \nu_{\boldsymbol{k}} \equiv \langle \alpha^{\dagger}_{\boldsymbol{k}} \alpha_{\boldsymbol{k}} \rangle = \frac{1}{\exp[w_{\boldsymbol{k}}/T] - 1}, \tag{5.11}$$

with $\alpha_{\boldsymbol{k}}$ denoting the Bogoliubov modes, see Eq. (5.16). The entropy $\mathcal{S}$ of the bosonic gas is defined as

$$\mathcal{S} = \frac{1}{N}\sum_{\boldsymbol{k}} [(\nu_{\boldsymbol{k}} + 1)\ln(\nu_{\boldsymbol{k}} + 1) - \nu_{\boldsymbol{k}} \ln \nu_{\boldsymbol{k}}]. \tag{5.12}$$

The last term in Eq. (5.10) is the modified Takahashi constraint over the density of fluctuations $n = \langle \hat{n}_i \rangle$, with μ the corresponding Lagrange multiplier or chemical potential. Here, $w_{\boldsymbol{k}}$ is energy of each mode. From the functional form of the entropy it follows that $w_{\boldsymbol{k}}$ is also the rate at which the entropy changes with changing occupation, i.e. $w_{\boldsymbol{k}} = T\frac{\partial \mathcal{S}}{\partial \nu_{\boldsymbol{k}}}$.

It seems natural to adopt this strategy since the expectation value E is in general bounded from below and depends only on the average value of the bilinears $a^{\dagger}_i a_j$, $a^{\dagger}_i a^{\dagger}_j$, and their complex conjugates. This happens because the Bogoliubov transformation is by definition linear and only the quadratic bilinears above can have non-zero matrix elements while preserving the excitation number. This physical consideration is equivalent to state that E can be calculated using Wick theorem and that linear and cubic terms give zero contribution. For convenience, we define

$$\begin{aligned} \langle a^{\dagger}_i a_j \rangle &\equiv F(r_{ij}) - \frac{1}{2}\delta_{ij}, \\ \langle a_i a_j \rangle &\equiv G(r_{ij}). \end{aligned} \tag{5.13}$$

In this notation, the generalized Takahashi constraint reads

$$F(0) = \langle a^{\dagger} a \rangle + \frac{1}{2} = S|\sin\rho| + \frac{1}{2}, \tag{5.14}$$

where $|\sin\rho|$ relates to the filling ν of the original spin system, $0 \leq \nu \leq 2S$, as $|\sin\rho| = \frac{1}{S}\sqrt{\nu(2S-\nu)}$. From (5.9) we find

$$\begin{aligned}\frac{E}{N} &= S^2\, C - 2S\, C\left[F(0)-\frac{1}{2}\right] - \frac{S}{2}\sum_J \left[c_J\cdot(G_J+G_J^*-F_J-F_J^*)\right]\\ &+ C\left[F(0)-\frac{1}{2}\right]^2 + \sum_J c_J(|F_J|^2+|G_J|^2)\\ &+ \frac{1}{4}c_J\\ &\left\{(G(0)(F_J+F_J^*-2G_J^*) - 2\left[F(0)-\frac{1}{2}\right](F_J+F_J^*-2G_J)\right\}. \end{aligned} \tag{5.15}$$

Here, we adopt the notation $F_J \equiv F(\tau_J)$, $G_J \equiv G(\tau_J)$, and we define $(c_1, c_2, c_3) \equiv (\cos(\boldsymbol{Q}\cdot\tau_1), t\cos(\boldsymbol{Q}\cdot\tau_2), t\cos(\boldsymbol{Q}\cdot\tau_3))$, $C \equiv c_1+c_2+c_3$. For convenience, we fix the energy scale such to have t_1.

If we assume that the Bogoliubov transformation is real as in [153]

$$\begin{aligned} a_{\boldsymbol{k}} &= \left(\cosh\theta_{\boldsymbol{k}}\ \alpha_{\boldsymbol{k}} + \sinh\theta_{\boldsymbol{k}}\ \alpha^\dagger_{-\boldsymbol{k}}\right),\\ a_{-\boldsymbol{k}} &= \left(\cosh\theta_{\boldsymbol{k}}\ \alpha_{-\boldsymbol{k}} + \sinh\theta_{\boldsymbol{k}}\ \alpha^\dagger_{\boldsymbol{k}}\right), \end{aligned} \tag{5.16}$$

we have that $F_J = F_J^*$, $G_J = G_J^*$, the expectation value of energy density reduces to

$$\begin{aligned}\frac{E}{N} &= \frac{1}{2}\sum_J c_J\left[\left(S+\frac{1}{2}-F(0)+F_J\right)^2 + \left(S+\frac{1}{2}-F(0)-G_J\right)^2\right.\\ &\left. + G(0)(F_J-G_J) + F_J^2 + G_J^2\right], \end{aligned} \tag{5.17}$$

which differs from the expression [153, Eq.6] not only due to the mismatch between our (5.9) and [153, Eq.5]: in fact the term $G(0)(F_J - G_J)$ is omitted as considered negligible. This approximation is justified at half filling for large S as $F_J \sim G_J \sim S$.

It is worth noticing that the structure of the minimal solution is not affected by the explicit form of E, while the consistency equations obviously are. Indeed, due to (5.16) the expectation values have the form

$$\begin{aligned} F(\boldsymbol{r}) &= \frac{1}{N}\sum_{\boldsymbol{k}} \cosh(2\theta_{\boldsymbol{k}}) e^{-i\boldsymbol{k}\boldsymbol{r}} \left(\nu_{\boldsymbol{k}} + \frac{1}{2}\right) \\ &= \frac{1}{N}\sum_{\boldsymbol{k}'} \cosh(2\theta_{\boldsymbol{k}'}) \cos(\boldsymbol{k}'\boldsymbol{r})(2\nu_{\boldsymbol{k}'} + 1), \\ G(\boldsymbol{r}) &= \frac{1}{N}\sum_{\boldsymbol{k}} \sinh(2\theta_{\boldsymbol{k}}) e^{-i\boldsymbol{k}\boldsymbol{r}} \left(\nu_{\boldsymbol{k}} + \frac{1}{2}\right) \\ &= \frac{1}{N}\sum_{\boldsymbol{k}'} \sinh(2\theta_{\boldsymbol{k}'}) \cos(\boldsymbol{k}'\boldsymbol{r})(2\nu_{\boldsymbol{k}'} + 1), \end{aligned} \tag{5.18}$$

where we use explicitly the symmetry $\boldsymbol{k} \to -\boldsymbol{k}$: the prime indicates that now the sum is performed over half of the first Brillouin zone. The condition for $\mathcal{F}$ to be minimal reduces to

$$\begin{aligned} 0 &= \frac{\partial \mathcal{F}}{\partial w_{\boldsymbol{k}}} = \frac{\partial \mathcal{F}}{\partial \nu_{\boldsymbol{k}}} \\ &= \sum_{\mu=0}^{3} \left[\frac{\partial E}{\partial F_\mu} \cos(\boldsymbol{k}\boldsymbol{\tau}_\mu) \cosh(2\theta_{\boldsymbol{k}}) + \frac{\partial E}{\partial G_\mu} \cos(\boldsymbol{k}\boldsymbol{\tau}_\mu) \sinh(2\theta_{\boldsymbol{k}}) \right] \\ &\quad - w_{\boldsymbol{k}} + \mu \cosh(2\theta_{\boldsymbol{k}}), \end{aligned} \tag{5.19}$$

$$\begin{aligned} 0 &= \frac{\partial \mathcal{F}}{\partial \theta_{\boldsymbol{k}}} = \frac{\partial \mathcal{F}}{2\partial \theta_{\boldsymbol{k}}} \\ &= \sum_{\mu=0}^{3} \left[\frac{\partial E}{\partial F_\mu} \cos(\boldsymbol{k}\boldsymbol{\tau}_\mu) \sinh(2\theta_{\boldsymbol{k}}) + \frac{\partial E}{\partial G_\mu} \cos(\boldsymbol{k}\boldsymbol{\tau}_\mu) \cosh(2\theta_{\boldsymbol{k}}) \right] \\ &\quad + \mu \sinh(2\theta_{\boldsymbol{k}}). \end{aligned} \tag{5.20}$$

Here, $\boldsymbol{\tau}_0 = (0,0)$ while $\boldsymbol{\tau}_J$, $J = 1,2,3$, have been introduced above.

The condition (5.20) is always equivalent to

$$\tanh(2\theta_{\boldsymbol{k}}) = \frac{A_{\boldsymbol{k}}}{B_{\boldsymbol{k}}}, \tag{5.21}$$

and the condition (5.19) to

$$w_{\boldsymbol{k}} = \sqrt{B_{\boldsymbol{k}}^2 - A_{\boldsymbol{k}}^2}, \tag{5.22}$$

where

$$\begin{aligned}
A_{\boldsymbol{k}} &\equiv -\sum_{\mu=0}^{3} \cos(\boldsymbol{k}\boldsymbol{\tau}_\mu) \frac{\partial E}{\partial G_\mu} \\
&= \frac{1}{2} \sum_J c_J \left(G_J - F_J + \cos(\boldsymbol{k}\boldsymbol{\tau}_J) \left(1 + 2S - 2F_0 + G_0 - 4G_J \right) \right) \\
&= \frac{1}{2} \sum_J c_J \left(G_J - F_J + \cos(\boldsymbol{k}\boldsymbol{\tau}_J) \left(2S(1 - |\sin\rho|) + G_0 - 4G_J \right) \right), \\
B_{\boldsymbol{k}} &\equiv \mu + \sum_{\mu=0}^{3} \cos(\boldsymbol{k}\boldsymbol{\tau}_\mu) \frac{\partial E}{\partial F_\mu} \\
&= \mu + \sum_J c_J \Big(-2S - 1 + 2F_0 + G_J - F_J \\
&\qquad + \cos(\boldsymbol{k}\boldsymbol{\tau}_J) \left(S + \frac{1}{2} + \frac{1}{2} G_0 - F_0 + 2F_J \right) \Big) \\
&= \mu + \sum_J c_J \Big(-2S(1 - |\sin\rho|) + G_J - F_J \\
&\qquad + \cos(\boldsymbol{k}\boldsymbol{\tau}_J) \left(S(1 - |\sin\rho|) + \frac{1}{2} G_0 + 2F_J \right) \Big),
\end{aligned} \tag{5.23}$$

in the second lines of the expression for $A_{\boldsymbol{k}}$ and $B_{\boldsymbol{k}}$ we impose the generalized Takahashi constraint.

Thus, one is getting the same result as for diagonalization of quartic Hamiltonian that in momentum space is real and symmetric under $\boldsymbol{k} \leftrightarrow -\boldsymbol{k}$. This can be the case when the expectation value E is real, but not otherwise.

At the formal level, we can use (5.21) and (5.22) that imply

$$\cosh(2\theta_{\boldsymbol{k}'}) = \sqrt{\frac{B_{\boldsymbol{k}'}^2}{B_{\boldsymbol{k}'}^2 - A_{\boldsymbol{k}}^2}},$$
$$\sinh(2\theta_{\boldsymbol{k}'}) = \frac{A_{\boldsymbol{k}'}}{B_{\boldsymbol{k}'}}\sqrt{\frac{B_{\boldsymbol{k}'}^2}{B_{\boldsymbol{k}'}^2 - A_{\boldsymbol{k}'}^2}}, \tag{5.24}$$

to write an implicit equation for the correlation functions

$$F(\boldsymbol{r}) = \frac{1}{N}\sum_{\boldsymbol{k}'}\sqrt{\frac{B_{\boldsymbol{k}'}^2}{B_{\boldsymbol{k}'}^2 - A_{\boldsymbol{k}}^2}}\cos(\boldsymbol{k}'\boldsymbol{r})(2\nu_{\boldsymbol{k}'} + 1),$$
$$G(\boldsymbol{r}) = \frac{1}{N}\sum_{\boldsymbol{k}'}\frac{A_{\boldsymbol{k}'}}{B_{\boldsymbol{k}'}}\sqrt{\frac{B_{\boldsymbol{k}'}^2}{B_{\boldsymbol{k}'}^2 - A_{\boldsymbol{k}'}^2}}\cos(\boldsymbol{k}'\boldsymbol{r})(2\nu_{\boldsymbol{k}'} + 1). \tag{5.25}$$

The following physical considerations are in order. In the zero temperature limit we are interested in, the gas of Bogoliubov excitations is expected to condense. Such condensation is consistent with the spin ordering only if the zero mode condenses, as such condensation translate into infinite range correlation in the original atomic system. The requirement of zero mode to become macroscopically occupied at low temperature, $M_0 = \int_{|\boldsymbol{k}|<\epsilon} \nu_k \sim Nn$, implies that $w_{\boldsymbol{k}=0} \to 0$, which also corresponds to $|\theta_{\boldsymbol{k}=0}| \to \infty$. Thus, this condition can be realized only for $B_{\boldsymbol{k}=0} \sim A_{\boldsymbol{k}=0}$, which implies that in the phase we are interested in, the chemical potential has to be set to zero, $\mu = 0$. Note that this also means the occupation of each mode $\nu_{\boldsymbol{k}}$ is much smaller than $\frac{1}{2}$ (at least for $S = \frac{1}{2}$). Thus, by singling out the the zero mode and using $\nu_{\boldsymbol{k}} + \frac{1}{2} \sim \frac{1}{2}$ in the expression for correlation functions, they become

$$F(\boldsymbol{r}) \sim M_0 + \frac{1}{N}\sum_{\boldsymbol{k}'\neq 0}\cosh(2\theta_{\boldsymbol{k}'})\cos(\boldsymbol{k}'\boldsymbol{r}),$$
$$G(\boldsymbol{r}) \sim M_0 + \frac{1}{N}\sum_{\boldsymbol{k}'\neq 0}\sinh(2\theta_{\boldsymbol{k}'})\cos(\boldsymbol{k}'\boldsymbol{r}), \tag{5.26}$$

and the constraint (5.14) reads

$$M_0 + \frac{1}{N}\sum_{\boldsymbol{k}'\neq 0}\cosh(2\theta_{\boldsymbol{k}'}) \ = S|\sin\rho| + \frac{1}{2}. \tag{5.27}$$

After having singled out the zero mode and constrained the occupation the function $A_{\boldsymbol{k}}$ and $B_{\boldsymbol{k}}$ should be redefined in form accordingly. In fact only $B_{\boldsymbol{k}}$ gets redefined. Indeed, by recalculating the consistency condition for an extremum of the $\mathcal{F}$ for the new definition of the correlation functions –that to say taking into account the dependence of M_0 on $\nu_{\boldsymbol{k}}$ and $\theta_{\boldsymbol{k}}$, as well as $\mu = 0$– we have

$$\begin{aligned}
0 &= \frac{\partial\mathcal{F}}{\partial w_{\boldsymbol{k}}} = \frac{\partial\mathcal{F}}{\partial\nu_{\boldsymbol{k}}} \\
&= \sum_{\mu=0}^{3}\left[\frac{\partial E}{\partial F_\mu}\left(\cos(\boldsymbol{k\tau}_\mu) - 1\right)\cosh(2\theta_{\boldsymbol{k}})\right. \\
&\qquad \left. + \frac{\partial E}{\partial G_\mu}\left(\cos(\boldsymbol{k\tau}_\mu)\sinh(2\theta_{\boldsymbol{k}}) - \cosh(2\theta_{\boldsymbol{k}})\right)\right] - w_{\boldsymbol{k}}, &(5.28)\\
0 &= \frac{\partial\mathcal{F}}{\partial\theta_{\boldsymbol{k}}} = \frac{\partial\mathcal{F}}{2\partial\theta_{\boldsymbol{k}}} \\
&= \sum_{\mu=0}^{3}\left[\frac{\partial E}{\partial F_\mu}\left(\cos(\boldsymbol{k\tau}_\mu) - 1\right)\sinh(2\theta_{\boldsymbol{k}})\right. \\
&\qquad \left. + \frac{\partial E}{\partial G_\mu}\left(\cos(\boldsymbol{k\tau}_\mu)\cosh(2\theta_{\boldsymbol{k}}) - \sinh(2\theta_{\boldsymbol{k}})\right)\right]. &(5.29)
\end{aligned}$$

The above equations again imply

$$\begin{aligned}
\tanh(2\theta_{\boldsymbol{k}}) &= \frac{A_{\boldsymbol{k}}}{B_{\boldsymbol{k}}}, \\
w_{\boldsymbol{k}} &= \sqrt{B_{\boldsymbol{k}}^2 - A_{\boldsymbol{k}}^2},
\end{aligned}$$

or alternatively

$$\cosh(2\theta_{\boldsymbol{k}'}) = \sqrt{\frac{B_{\boldsymbol{k}'}^2}{B_{\boldsymbol{k}'}^2 - A_{\boldsymbol{k}}^2}},$$

$$\sinh(2\theta_{\boldsymbol{k}'}) = \frac{A_{\boldsymbol{k}'}}{B_{\boldsymbol{k}'}}\sqrt{\frac{B_{\boldsymbol{k}'}^2}{B_{\boldsymbol{k}'}^2 - A_{\boldsymbol{k}'}^2}}. \tag{5.30}$$

The expression for $A_{\boldsymbol{k}}$ remains the same as in (5.23),

$$A_{\boldsymbol{k}} = -\sum_{\mu=0}^{3} \cos(\boldsymbol{k}\boldsymbol{\tau}_\mu)\frac{\partial E}{\partial G_\mu}, \tag{5.31}$$

while $B_{\boldsymbol{k}}$ becomes

$$B_{\boldsymbol{k}} = \sum_{\mu=0}^{3} \left(\frac{\partial E}{\partial F_\mu} \left(\cos(\boldsymbol{k}\boldsymbol{\tau}_\mu) - 1\right) - \frac{\partial E}{\partial G_\mu} \right). \tag{5.32}$$

It is easy to check that the classical order is recovered in the limit of S large. At leading order, the minimum of the free energy is just determined by the minimum of C: the $\boldsymbol{Q}$-order found is the classical result, $\boldsymbol{Q}_{Cl} = (2\arccos(-t/2), 0)$, which corresponds to $(c_1, c_2, c_3) = (\frac{t^2-2}{2}, -\frac{t^2}{2}, -\frac{t^2}{2})$. At the next order in $\frac{1}{S}$, which corresponds to the linear spin wave (LSW) calculation, we recover the ordinary spin-wave result:

$$A_{\boldsymbol{k}} \to S \sum_J c_J \cos(\boldsymbol{k}\boldsymbol{\tau}_J),$$

$$B_{\boldsymbol{k}} \to S \sum_J c_J \left(\cos(\boldsymbol{k}\boldsymbol{\tau}_J) - 2\right), \tag{5.33}$$

which imply

$$w_{\boldsymbol{k}} = 2S\sqrt{C\left(C - \sum_J c_J \cos(\boldsymbol{k}\boldsymbol{\tau}_J)\right)},$$

in particular $w_{\boldsymbol{k}=0} = 0$ as expected. It is easy to check that, for the classical order $\boldsymbol{Q}_{Cl}$, $w_{\boldsymbol{k}}$ is always real and that is by construction an extreme. In fact, as it can be checked numerically that it is also the minimal energy solution also then the terms in $\frac{1}{S}$, which corresponds to the case in which quadratic fluctuations are included. Taking into account all the terms in (5.17), which include also $\frac{1}{S^2}$ corrections and is known as modified spin wave (MSW) approach, the minimum condition is no longer algebraic. As in [153], we will search for solutions recursively, starting from the ordinary spin wave solution above. The absence of a pronounced minimal value will signal the existence of possible spin-liquid phase. In order to find the optimal $\boldsymbol{Q} = (Q_x, Q_y)$, we have to impose that the gradient is zero

$$\begin{aligned} 0 &= \frac{\partial \mathcal{F}}{\partial Q_x} = \sum_J \frac{\partial E}{\partial c_J}\frac{\partial c_J}{\partial Q_x}, \\ 0 &= \frac{\partial \mathcal{F}}{\partial Q_y} = \sum_J \frac{\partial E}{\partial c_J}\frac{\partial c_J}{\partial Q_y}. \end{aligned} \tag{5.34}$$

5.5 Result from the modified spin wave analysis

In the previous section, we have derived a modified spin wave theory for the XX spin model on a triangular lattice. We will now extract concrete results from this theoretical framework. This amounts for a minimization problem of the free energy, which is complicated due to the large amount of variables. Using the procedure described in the subsection below, we manage to perform minimization even for large lattices with hundreds of sites. As the result, we then obtain the phase diagram for a realistic experimental system as a function of the hopping anisotropy t.

5.5.1 Optimization and stability

In search for a long-range order in the quartic case, we adopt an iterative procedure. We start from the ordinary spin-wave (5.33) solution with $\boldsymbol{Q} = \boldsymbol{Q}_{Cl}$ as initial configuration. The recursive procedure works as follows. First, the values of $A_{\boldsymbol{k}}$, $B_{\boldsymbol{k}}$ at the cycle m are used to get the new correlation functions F_μ, G_μ, using Eq. (5.26). Once the correlations are substituted in the free energy, which at zero temperature reduces to the expectation value of the energy (5.17), the latter becomes a function of the ordering vector $\boldsymbol{Q}$ only, $E = E(\boldsymbol{Q})$. The new value at the cycle m of $\boldsymbol{Q}$ is, thus, determined by minimizing the $E(\boldsymbol{Q})$ in the neighborhood of optimal value of $\boldsymbol{Q}$ at the cycle m. Finally, (5.31) and (5.32) are used to update $A_{\boldsymbol{k}}$ and $B_{\boldsymbol{k}}$ as a function of the correlation functions and of the order vector. Convergence of the iterative process is assumed when the difference between the old and the updated values of $A_{\boldsymbol{k}}$ and $B_{\boldsymbol{k}}$ are below a certain threshold.

We have benchmarked the performance of this iterative approach against brute force minimization of the energy as function of the free parameters $\theta_{\boldsymbol{k}}$ and $\boldsymbol{Q}$ for different shapes and sizes of lattices with periodic boundary conditions. While the success and efficiency of the iterative approach, i.e. the number of iterations needed for achieving convergence, strongly depends on the shape of the lattice, it performs generally better than a brute force minimization and the scalability with the lattice size is pretty good. Best performance is achieved for rhombic lattices, see Figure 5.3. Converge or failure occurs after few tens of iterations. The latter manifests when $|A_{\boldsymbol{k}}|$ becomes greater than $|B_{\boldsymbol{k}}|$ for some $\boldsymbol{k}$, which corresponds to $w_{\boldsymbol{k}}$ becoming imaginary. In fact, more than a real instability, the absence of convergence signals that the approximation we have used of neglecting the occupation $\nu_{\boldsymbol{k}}$ of the modes $\boldsymbol{k} \neq 0$ is not respected. That is to say, the physical assumption of the existence of an ordered phase behind the spin-wave analysis is not verified. The comparison between the iterative approach and the brute force minimization of the free energy, which we have performed without assuming $\nu_{\boldsymbol{k}} \ll 1$ on $L \times L$ rhombic lattices with L up to 10, confirmed this scenario.

Next we have extended our iterative minimization to larger lattices. We have first studied the half-filling case for $L = 24, 100$ and for the infinite L limit, obtained by replacing the sum over $\boldsymbol{k}$ with an (numeric) integral over the first Brillouin zone.

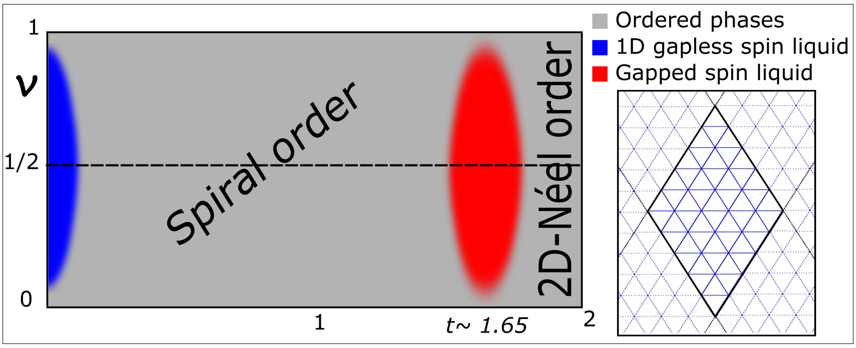

Figure 5.3: Expected phase diagram as function of the filling within the MSW approach. The two ordered phases are spiral order, $0.2 \lesssim t \lesssim 1.55$, and 2D-Néel order. Inset: a 6×6 lattice of rhombic shape with periodic boundary conditions.

5.5.2 Phase diagram predicted by spin wave at half-filling

We have first started by studying the half filling case, $\rho = \frac{\pi}{2}$. Our results are very close to the one of [153] and display the same qualitative behavior (see Figure 5.3). In particular, we observe a failure of convergence around $t \sim 0$ and for t between $1.55-1.8$. The first region is easily explained: in the limit $t \to 0$ the system reduces to disconnected $1D$-XX chains that can order separately in 1D-Néel orders with arbitrary relative phases. Thus, there is a huge degeneracy in the groundstate that should correspond to a gapless spin-liquid phase. The region around $t \sim 1.65$ appears at the interface between two classically ordered phases, the spiral order and a 2D-Néel order, which appear at lower and higher values of t, respectively. Both phases are well described by the classical order ansatz we used. It is worth noticing that the initial condition and the reflection symmetry of the Hamiltonian around the x-axis implies that our solution is respecting such symmetry i.e. the ordering vector remains parallel to the x-axis and the correlation functions respect the relations $F_2 = F(\boldsymbol{\tau}_2) = F(\boldsymbol{\tau}_3) = F_3$, $G_2 = G(\boldsymbol{\tau}_2) = G(\boldsymbol{\tau}_3) = G_3$. This implies that we can work at fixed $Q_y = 0$. For this choice, the 2D-Néel order corresponds to $Q_x = 2\pi$, while the spiral order corresponds to Q_x smoothly interpolating between 2π and π for decreasing values of the anisotropy t. While at the classical level, the 2D-Néel order is predicted to be stable for $t \geq 2$, the quantum corrections incorporated by MSW approach stabilize it also for lower values of t, as displayed in Figure 5.4. Similar results are obtained by exact diagonalization, see Figure 5.17(a). By reducing further the values of t the system enters in a non-ordered phase signaled by the absence of points from MSW. While in the neighboring regions above and below the no-convergence window the occupancy of the zero-momentum states remains large, see Figure 5.5, the values of the relative susceptibility ρ_{xx} is small in the vicinity of such window, Figure 5.6. Similarly to [153], we estimate the susceptibility by calculating the Hessian of the energy for fixed correlation functions at the minimum. In order to get an adimensional quantity we divide by the absolute value of the energy minimum, thus, $\rho_{xx} = \frac{1}{E}\frac{\partial^2 E}{\partial Q_x^2}$, and $\rho_{yy} = \frac{1}{E}\frac{\partial^2 E}{\partial Q_y^2}$. Note that $\rho_{xy} = \frac{1}{E}\frac{\partial^2 E}{\partial Q_x \partial Q_y}$ is identically zero because of the symmetry argument given above. As expected ρ_{yy} is not signaling any instability for $1.5 \leq t \leq 2$ –the optimal Q_y is identical for the spiral and 2D-Néel order– while it detects the instability at $t \sim 0$, see Figure 5.6. While for all the observables represented in Figure 5.4-5.6 the MSW results deviate considerably from the ones predicted by the LSW, they are quickly converging to a stable behavior for moderate size-lattices – for a rhombic shape lattice $L \times L$ the deviation between $L = 24$ and the continuous limit are tiny.

5.5.3 Phase diagram predicted by spin wave at generic filling

Then, we have considered lower values of ρ between 0 and $\frac{\pi}{2}$, corresponding to lower densities of Bogoliubov excitations $n = \frac{1}{2}\sin\rho = \frac{1}{2}\sqrt{\nu(1-\nu)}$, where ν is the filling. We have considered the same observables as in the half-filling case. We have found again that the results quickly saturate to a stable value for growing size of the lattices. For simplicity, we present here the results $L \times L$ rhombic-shaped lattices with periodic boundary conditions for $L = 100$. First, we notice that the values of the optimal order vector $\boldsymbol{Q}$

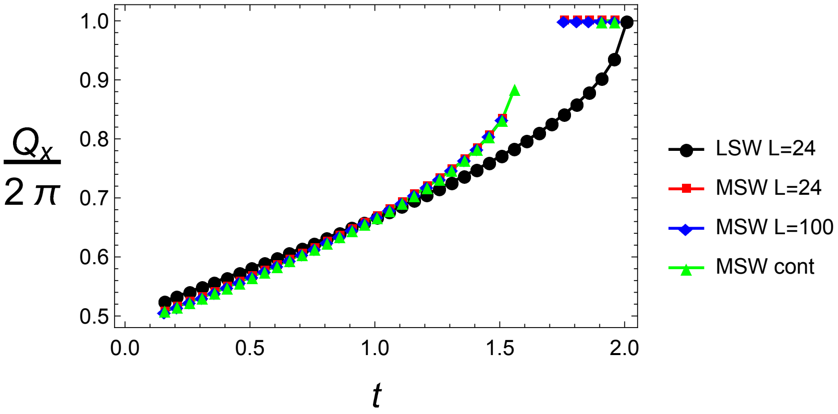

Figure 5.4: Values of the optimal Q_x: comparison of results from LSW and from MSW for different sizes of the rhombic-shape lattices with periodic boundary conditions.

remains substantially unchanged with respect to the half-filling case. While by construction $Q_y = 0$, the x-component of the order vector Q_x displays a moderate dependence on n only close to the non-convergence window, Figure 5.7. In fact, the non-convergence window changes: while it remains centered around $t \sim 1.65$, its extension shrinks smoothly while n decreases. Indications of such behavior can be detected both in the condensate fraction and in the susceptibility. Indeed, the shrinking of the non-convergence window is well evident in Figure 5.8(a) where the occupation of the zero mode M_0 is depicted. As expected M_0 is directly proportional to n, that is to say the condensate fraction $\frac{M_0}{n}$ depicted in Figure 5.8(b) is independent of n. This behavior supports the picture that the nature of the ordered phases is unchanged while their stability increase by moving away from half filling $n = \frac{1}{2}$. Further confirmation comes from the calculation of the relative susceptibilities ρ_{xx} and ρ_{yy}. While ρ_{yy} does not display a strong dependence on n, Figure 5.10, ρ_{xx} displays a sizable dependence on n only around the non-convergence window. In particular, ρ_{xx} weakly increases when n decreases, showing that the ordered phase gets smoothly more stable, Figure

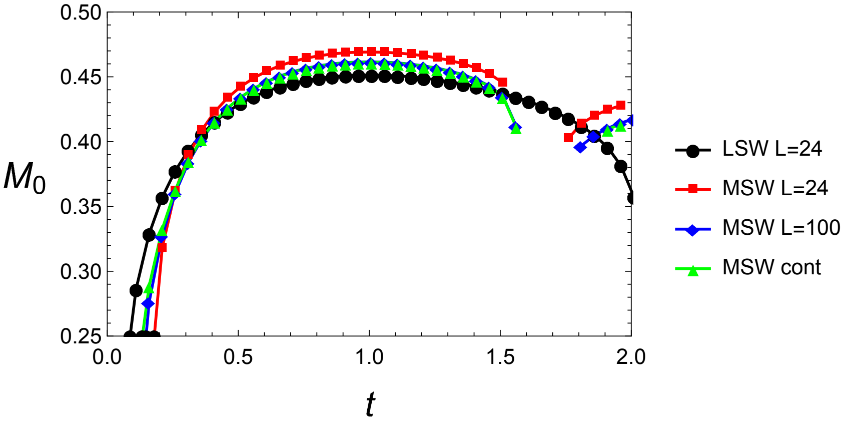

Figure 5.5: Occupation of the ground state at zero momentum corresponding to the ordered solution: comparison of results from LSW and from MSW for different sizes of the rhombic-shape lattices with periodic boundary conditions.

5.9. Thus, we conclude that by moving out of half-filling the conjectured spin-liquid phase signaled by the non-convergence window of MSW does not disappear but shrinks rather gently.

5.6 Exact diagonalization study

In this section we will study the Hamiltonian (5.3) by means of exact diagonalization. Therefore, we first note that it conserves the z-component of total spin, $S_z \equiv \frac{1}{N}\sum_i S_i^z$. This symmetry reflects conservation of particles, and allows to work in Hilbert space blocks with fixed spin polarization. Using this symmetry, we are able to exactly diagonalize systems of up to 24 sites. We mostly consider open boundary conditions (i.e. hard walls), which not only mimicks best the trapped scenario we have in mind, but also allows for arbitrary ordering vectors. We have studied different geometries, in particular the highly symmetric arrangement depicted in Figure 5.2(a),

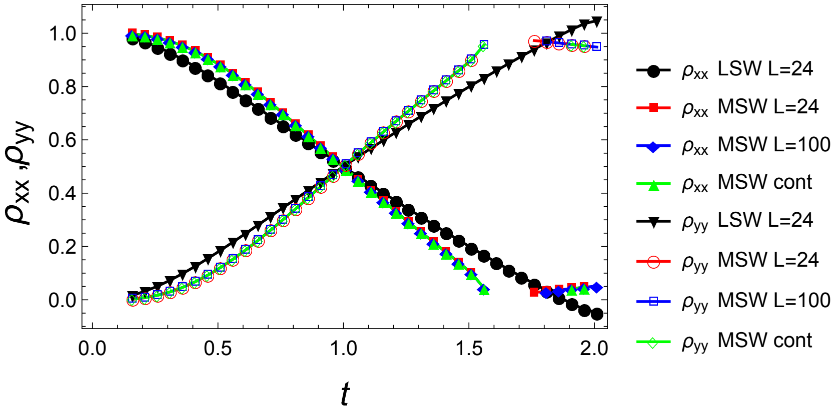

Figure 5.6: Values of the rescaled susceptibility ρ_{xx} and ρ_{yy}: comparison of results from LSW and from MSW with different lattice dimensions. Around the non-convergence window ρ_{xx} is small, signaling instability of the order. Around the non-convergence window ρ_{yy} is large as expected because the y-component of the order vector Q_y is the same for spiral and 2D-Néel order. Instead, ρ_{yy} signals the instability that leads to 1D-Néel order for $t \sim 0$.

but also rhombic arrangements shown in Figure 5.2(b), which can systematically be scaled from 12 to 24 by adding rows of four spins.

As in the spin-wave analysis, we will first consider the system within a local density approximation, assuming homogeneity within shells of different S_z. Our exact diagonalization study is exptected to capture the system behavior in the center of the trap, and we set $V_i = 0$. Afterwards, we study effects of the trapping potential on small scales, diagonalizing Eq. (5.3) at finite V_i. The exact diagonalization study presented here covers the case at half filling ($S_z = 0$) known from Refs. [153, 202], with a possible quantum spin liquid for $t \approx 0.5$ and $t \approx 1.5$. We extend this study to other polarization sectors, which become relevant if the trap leads to an increased density in the center.

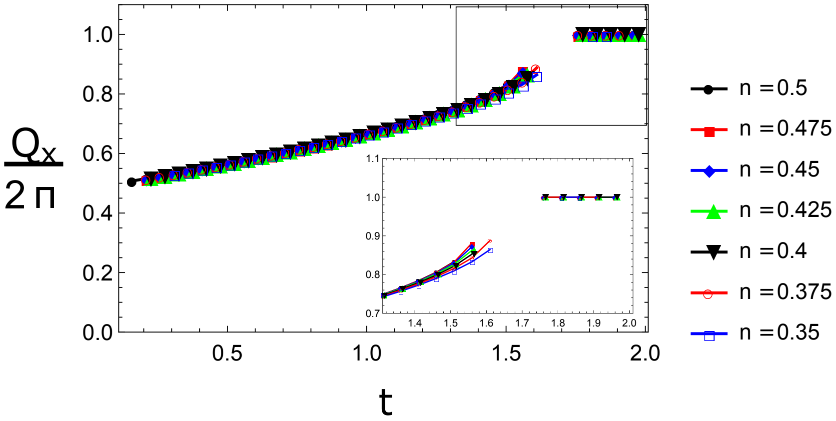

Figure 5.7: The value of the optimal Q_x depends in sizable way on the filling only close to the transition to the non-ordered region.

5.6.1 Homogeneous system ($V_i = 0$)

As an experimentally accessible quantity which allows to chararacterize the order of the system, we have calculated the magnetic structure factor $S(\mathbf{Q})$:

$$S(\mathbf{Q}) = \frac{2}{N} \sum_{i,j} \exp\left[i\mathbf{Q} \cdot (\mathbf{r}_i - \mathbf{r}_j)\right] \langle S_i^+ S_j^- + \text{h.c.} \rangle. \tag{5.35}$$

Here $\langle \cdot \rangle$ denotes the quantum average of the ground state. This quantity is the Fourier transform of the total magnetization in the S_x-S_y-plane, and therefore magnetic order is signalled by a pronounced peak. The momentum space position $\mathbf{Q}$ of the peak further characterizes the spatial ordering of the magnetization. Based on $S(\mathbf{Q})$, we define magnetization M as a relevant order parameter

$$M = \sqrt{S(\mathbf{Q})/N}. \tag{5.36}$$

At all fillings and for all anisotropies, M has a global maximum for $Q_y = 0$, with the corresponding Q_x varying between π and 2π as a function of t, see

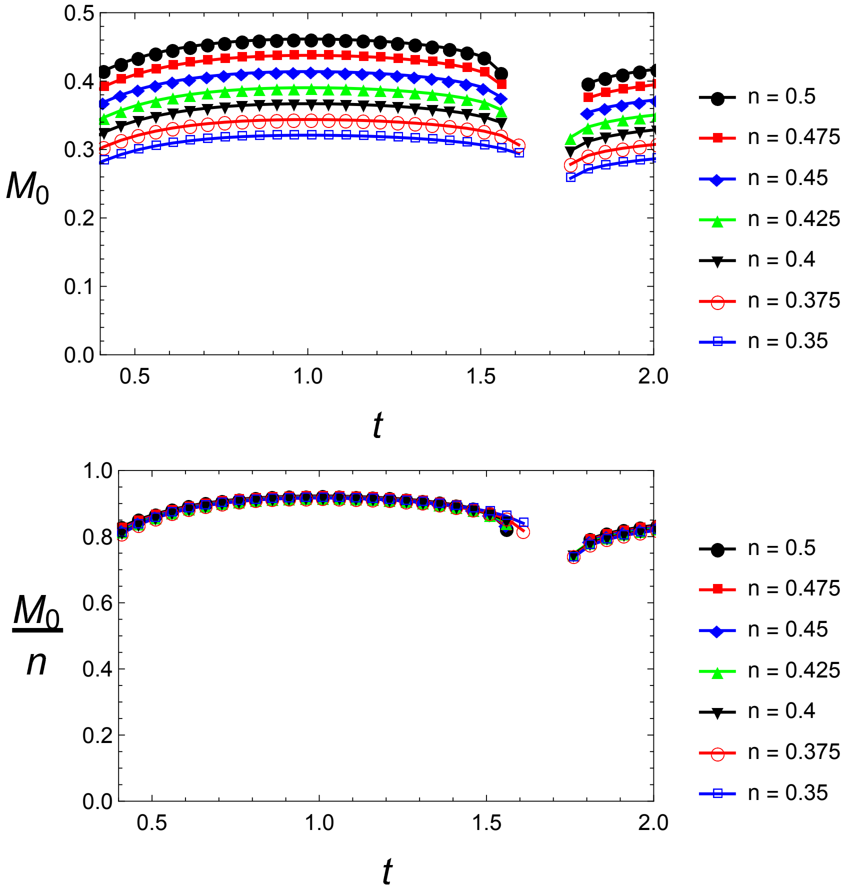

Figure 5.8: (a) Occupation of the the state at zero momentum for different filling: the non-ordered region shrinks smoothly with the filling. (b) The condensate fraction is independent of the filling in the ordered regions.

Figure 5.11(a). The two limiting values $Q_x = \pi$ and $Q_x = 2\pi$, obtained for $t = 0$ and $t \gtrsim 1.6$, correspond to an intrachain Néel order, and to a square-lattice Néel order, respectively. Remarkably, for most values of

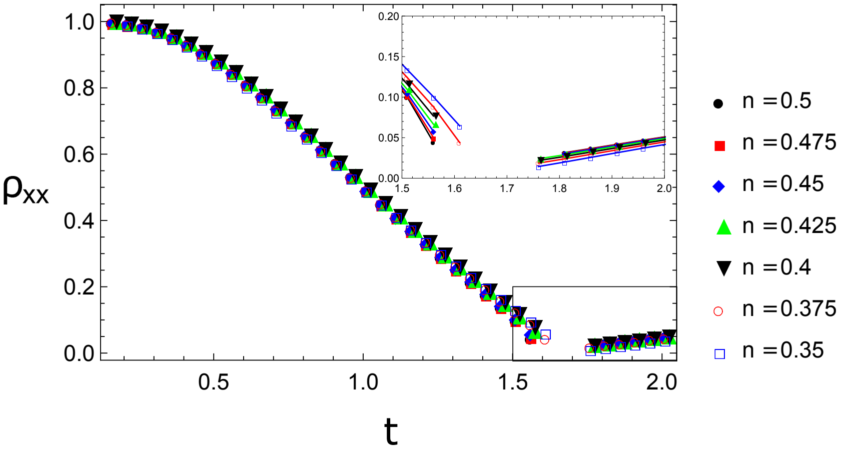

Figure 5.9: The value of the rescaled susceptibility ρ_{xx} depends sizably on the filling only close to the transition to the non-ordered region. A slighter increase of ρ_{xx} at lower n translates in an increased stability of the ordered phases.

t, the peak momentum Q_x hardly depends on the spin polarization, with the exception of a small region around $t \approx 1.5$, where $\mathrm{d}Q_x/\mathrm{d}t$ tends to infinity. This means that in a trapped system, composed of subsystems with different S_z, each subsystem would produce the same signal when the magnetic structure factor is measured. As a result, one would measure same peak as in the homogeneous system, except for a possible broadening of the peak near $t \approx 1.5$.

In Figure 5.11(b), we show the order parameter M for different polarization sectors. In comparison to Q_x, there are some quantitative dependencies on the polarization, but qualitatively, the curves still share many qualitative properties: With few exceptions, M always increases with t, but typically regions of rapid increase are followed by rather flat regimes. A strong tendency for rapid increase occurs at $t \approx 0.6$ and for $t \gtrsim\approx 1.5$. For most S_z, a small region in which M decreases with t, is found within a small region at $t \lesssim 1.5$. Note that for $S_z = 0$ this dip is absent, but instead the curve

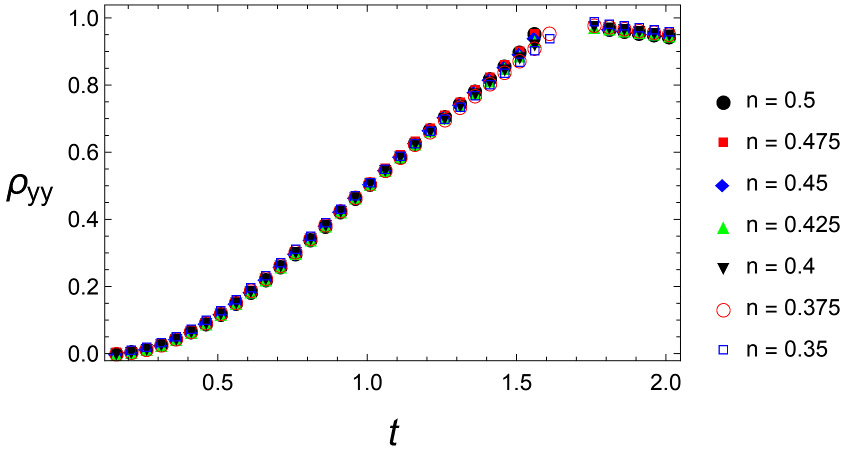

Figure 5.10: The value of the rescaled susceptibility ρ_{yy} does not depend considerably on the filling. Indeed, it is sensitive only on the transition at very low t to the the 1D behavior, which is unaffected by the filling, while is order 1 around the transition at $t \sim 1.65$.

exhibits a kink at $t \approx 1.5$, with $dM/dt = 0$. These dips/kinks might be interpreted as a signal for quantum spin liquid behavior, as they indicate the loss of the magnetic order.

We also note that, based on a PEPS study in Ref. [153] in a 20×20 lattice, another spin liquid regime is expected around $t \approx 0.5$, that is, just before the first rapid increase of M. This expectation is based on a dip in $M(t)$ near $t \approx 0.5$, which is found in larger systems. Within our study on the $N = 24$ lattice, though, the magnetic order parameter does not signal spin liquid behavior in this region.

Additional information regarding the presence or absence of magnetic order can be obtained from the dependence of the order parameter on the number of spins N. For such scaling analysis, we perform exact diagonalization at half filling on a graph as shown in Fig. 5.2(b). The results are shown in Fig. 5.12. Before analyzing the size dependecies in Fig. 5.12, we may focus on the curve for $N = 24$ and compare it with the corresponding

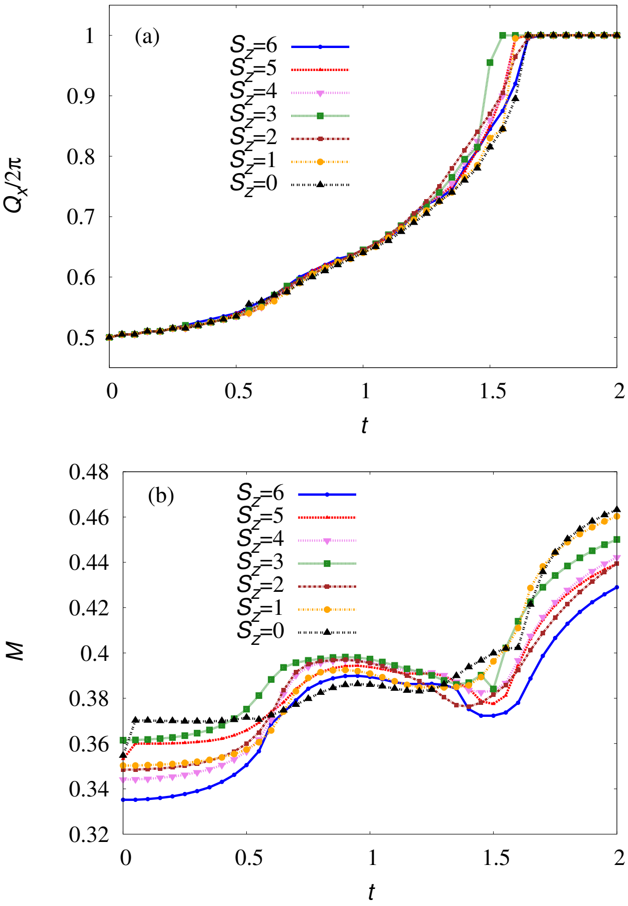

Figure 5.11: In different polarization sectors S_z, we evaluate (a) the position of peak of structure factor $S(\mathbf{Q})$ as a function of anisotropy t, and (b) the magnetic order parameter M, as defined in Eq. (5.36) from the peak value of $S(\mathbf{Q})$. We consider a homogeneous system ($B_i = 0$) with $N = 24$ spin, arranged in the hexagonal geometry shown in Figure 5.2(a).

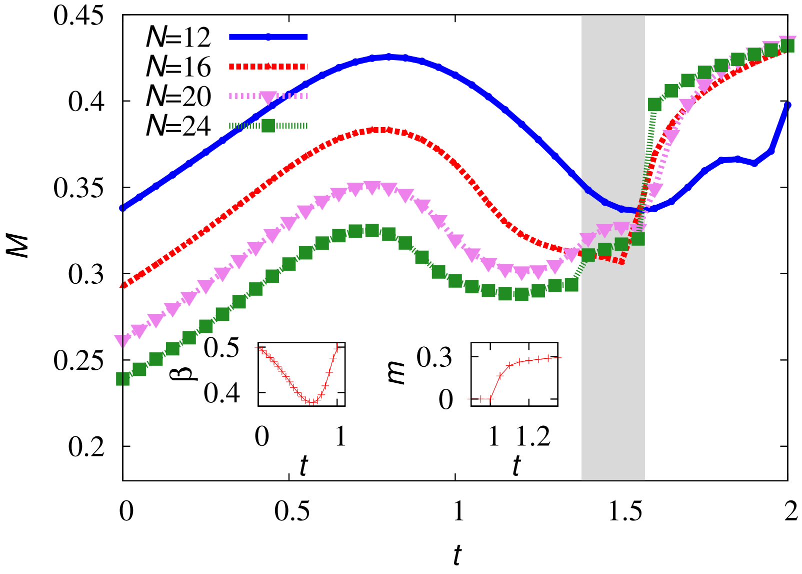

Figure 5.12: Magnetic order parameter M as a function of lattice anisotropy t, for different number of spins N in the rhombic arrangement depicted in Figure 5.2(b). The inlays show the results of extrapolating the data to $1/N \to 0$ using the fit function $f(N) = \alpha N^{-\beta} + m$, with $m > 0$. For $t \leq 1$, we get $m = 0$ and an exponent $\beta \approx 0.5$, as shown in the left inlay. For $1 < t < 1.35$, the data extrapolates to finite values of m, see right inlay. In the shaded region, $1.35 < t < 1.56$, the system is disordered in the sense that the data does not behave monotonically with N. For larger t, the data converges quickly to a size-independent value which approaches the value $M_0 = 0.437$ for a Neel-ordered square lattice [cf. Ref. [211]].

in Fig. 5.11(b). As finite-size effects should strongly depend on the geometry of the system, such comparison may help to distinguish bulk behavior from edge effects. We find that, for $t \gtrsim 1$, the magnetization M exhibits very similar behavior in both geometries, in particular regarding the kind at the $t \approx 1.5$ followed by a sharp increase. For larger values, $t \gtrsim 1.6$, the magnetization saturates. As discussed before, the kink could be the sign of a spin liquid phase, and strikingly, this feature does not depend on the geometry of the system. Also the flat regime for large t is barely affected by the geometry, and is interpreted the Neel ordered phase in a square lattice (equivalent to the rhombic lattice structure for $t \to \infty$). A striking observation which backs this interpretation is the value of M obtained at large t in the rhombic geometry: it approaches precisely the value $M = 0.437$ expected for a square lattice [211].

Next, we will analyze size dependecies which play an important role for $t \lesssim< 1.6$. The whole region can be divided into two regimes: While for $t < 1.35$ the order parameter M behaves monotically with N, this is not the case for $1.35 < t < 1.6$. We may interpret this non-monotonic behavior as a signal for the lack of magnetic order. The finite value of M can then be seen a random effect due to the limited system size. Such scenario agrees with a spin liquid phase, however, we cannot rule out complicated orderings which are, in a non-monotonic way, sensitive to the finite size of the system.

For $t < 1.35$, the monotonic behavior of $M(N)$ allows for a quantitative scaling analysis. Using the fit function $f(N) = \alpha N^{-\beta} + m$ with real fit parameters α, β, and m, we obtain the unphysical result $m < 0$ for $t < 1$. We conclude that in this regime, no magnetization survives in the thermodynamic limit, and set $m = 0$. We then find an exponent $\beta \approx 0.5$ as shown in the left inlay of Fig. 5.12. The exponent $1/2$ agrees with exponential decay of correlations, $S(\mathbf{Q})/N \sim \int_0^{\sqrt{N}} dr \ r \exp(-r/\xi) \sim 1/N$, with ξ denoting the correlation length. For $t > 1$, we obtain finite positive values of m, as shown in the right inlay of of Fig. 5.12, indicating that the system remains magnetized in the thermodynamic limit.

Another relevant quantity which can be obtained from the magnetic structure factor is the width of the peak. To account for difference in height, we normalize $S(\mathbf{Q})$ with $S(\mathbf{Q}_{\text{peak}})$. For simplicity, let us assume that the peak of the structure factor has a Gaussian shape. The width of the peak is then given by the standard deviation σ which can be obtained from the second derivative at the peak. Along the Q_x-direction we have

$$\sigma = \left(\frac{1}{S(\mathbf{Q}_{\text{peak}})} \left[\frac{\mathrm{d}^2}{\mathrm{d}Q_x^2} S(Q_x, Q_y) \right]_{\mathbf{Q}=\mathbf{Q}_{\text{peak}}} \right)^{-1/2} . \tag{5.37}$$

We have evaluated this quantity for rhombic systems as shown in Fig. 5.13. The most remarkable feature is the rapid increase of σ near $t = 1.5$, i.e. a significant broadening of the peaks for $N = 16$ and $N = 20$, indicating a loss of magnetic order. For $N = 24$, however, the data shows a slightly different behavior: Although a global maximum is still exhibited at $t = 1.5$, the extremum is less pronounced than in the other cases. Interestingly, no size dependence of σ occurs in the two limits $t \to 0$ and $t \to \infty$.

To shed more light onto the regime $1.35 < t < 1.6$, we will now consider the possibility of non-magnetized order. A clear candidate for a non-magnetized but ordered phase is the so-called valence-bond crystal (VBC). In this phase, nearest-neighbor spins are dimerized, and the dimers form a regular pattern. Since $t > 1$, dimerization should preferably occur along the two diagonal directions (i.e. those with strength t_2). We assume the simplest case, in which (spontaneously or due to the finite size) one of these two direction is chosen by all dimers. In our case, the rhombic shape in Fig. 5.2(b) enhances dimerization along the links pointing to the upper neighbor on the right. Denoting each spin with a single index i, possible dimers might be formed between spin i and spin $i + R$, where R is the number of spins in a row, see also Fig. 5.3 for an illustration of this notation. Correlations between these dimers are measured by the following structure factor:

$$\begin{aligned} S_{\mathrm{D}}(\mathbf{Q}) = & \frac{1}{N} \sum_{i \neq j} \mathrm{e}^{i\mathbf{Q}\cdot(\mathbf{r}_i - \mathbf{r}_j)} \Big[\langle (\mathbf{S}_i \cdot \mathbf{S}_{i+R})(\mathbf{S}_j \cdot \mathbf{S}_{j+R}) \rangle \\ & - \langle \mathbf{S}_i \cdot \mathbf{S}_{i+R} \rangle \langle \mathbf{S}_j \cdot \mathbf{S}_{j+R} \rangle \Big] . \end{aligned} \tag{5.38}$$

Again we define an order parameter D by considering the peak value of S_{D}:

$$D = S_{\mathrm{D}}(\mathbf{Q}_{\text{peak}})/N. \tag{5.39}$$

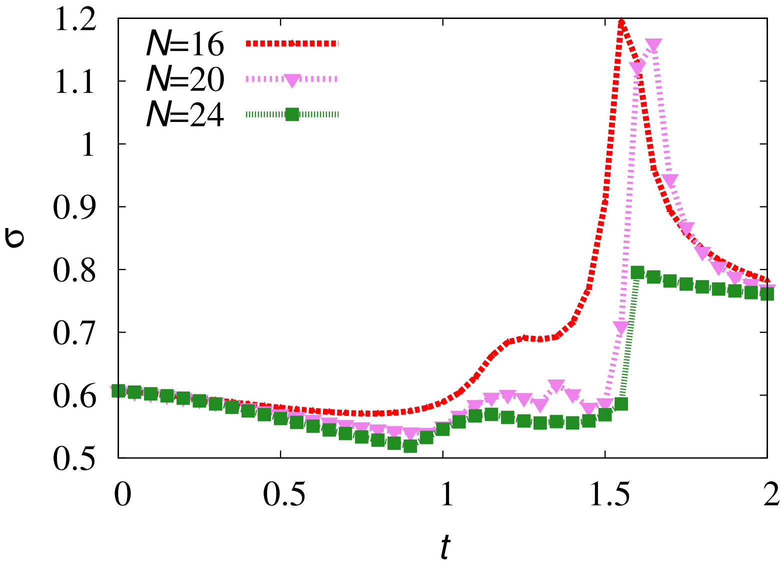

Figure 5.13: Width σ of the structure factor peak as a function of t, for a rhombic arrangement of the spins. A broadening of the peak near $t \approx 1.5$ is observed for all system sizes, but is most pronounced for smaller systems ($N = 16$ and $N = 20$).

Both the vector $\mathbf{Q}_{\mathrm{peak}}$ as well as the behavior of D as a function of t depend sensibly on the size of the system, and on the geometry, see Fig. 5.14 showing results for a rhombic system with open or periodic boundary conditions (i.e. hard walls or period). We conclude that the small finite values of D are random finite-size effects, and the flatness of most curves suggest that at no value of t VBC order is established. A single exception occurs for $N = 16$ with open boundary. However, as other sizes (in particular $N = 24$ with even number of rows) does not show any sign of a similar peak, we shall not interpret this as a sign for VBC order. Note that, due to the boundary conditions, there is only a single way of perfectly covering the whole lattice with nearest-neighbor dimers (for even number of rows). Alternative coverings leave few spins without dimer, with an energy cost which plays the biggest role in small systems. This might cause enhanced VBC order in very small systems, while does not give rise to any effects in systems with larger bulk.

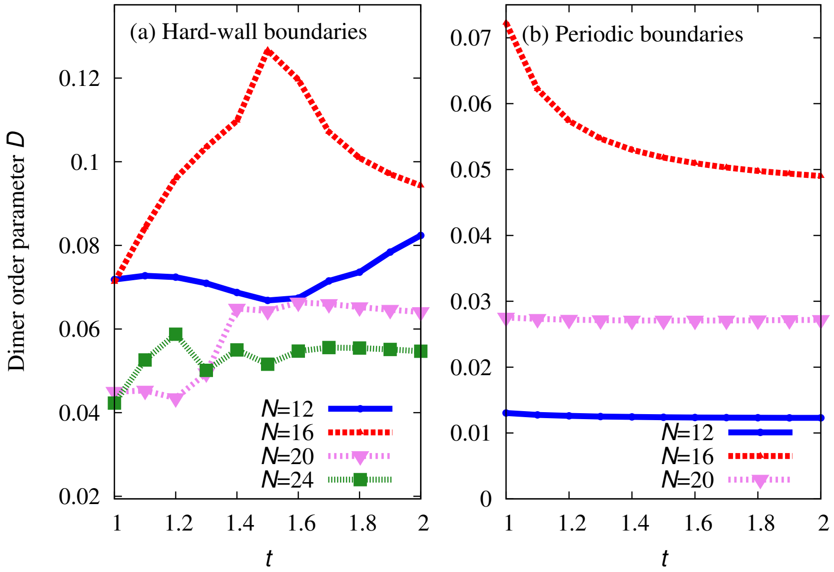

Figure 5.14: Dimer order parameter D as a function of lattice anisotropy t, for different number of spins N in the rhombic arrangement depicted in Figure 5.2(b). We consider both open boundaries (a), and periodic boundaries (b). Most curves are relatively flat at a constantly small value of D, suggesting that there is no VBC-ordered regime. The peak around $t \approx 1.5$ for $N = 16$ in an open geometry seems to be a finite-size effect, as this effect is not present for other values of N. It may be due to the limited number of perfect dimer coverings possible in small lattices.

The order parameters M and D discussed so far directly measure certain types of order, or, by excluding the corresponding order, they can give hints for spin liquid behavior. However, they cannot positively detect a spin liquid and its topological order. It is subject to current research which quantities may serve as topological order parameters, and the entanglement spectrum has been shown to be a promising candidate. In fact, Ref. [212] demonstrates that for the Haldane phase of a $S = 1$ chain, the entanglement spectrum is doubly degenerate due to a hidden symmetry. The presence of magnetic order can be detected by the entanglement spectrum through tower-of-states structures, which have been shown to be in correspondence with the low energy spectrum in a DMRG study of the $J_1 - J_2$ Heisenberg model on the triangular and the kagomé lattice [213]. Here, we restrict our discussion in the following to degeneracies of the entanglement spectrum, which does not require the determination of the quantum numbers of each entanglement eigenvector. Although degeneracies of the entanglement spectrum are not a robust criterion for topological order, it will be interesting to see whether degeneracies occur in those regimes which we have identified above as possible spin liquid phases.

The entanglement spectrum is obtained from the eigenvalues of the reduced density matrix $\rho_{\mathrm{L}} \equiv \mathrm{Tr}_{\mathrm{R}} \left|\Psi\right\rangle \left\langle\Psi\right|$. Here, Tr_{R} denotes a trace over half spins, localized on the right side of the lattice. The entanglement spectrum is then defined as $\lambda_i = -\log \rho_i$, where ρ_i denote the eigenvalues of ρ_{L}. In Figures 5.15 and 5.16, we plot the eight lowest values of the entanglement spectrum as a function of the anisotropy t in a homogeneous system of 24 spins. In Fig. 5.15, we consider a hexagonal spin arrangement and study the dependence of the entanglement spectrum on the spin polarization S_z. In Fig. 5.16, we focus on a rhombic system and consider different ways of cutting it into two subsystems. While in general the entanglement eigenvalues are not universal, certain properties of the entanglement spectrum, like degeneracies of levels, may reflect certain symmetries, and should thus be independent from the cut.

Comparing the entanglement spectra at different spin polarizations, the most interesting behavior is exhibited at $S_z = 0$. Here, the number of degeneracies strongly depends on the parameter t. In contrast, for odd polarization sectors (as illustrated in Fig. 5.15 for $S_z = 1$), each level is doubly degenerate for any t. For $S_z = 2$, the ground state level remains unique for all t, and only higher levels exhibit some t-dependent degeneracies. For $S_z = 0$, in Fig. 5.15, the most notable feature is a degenerate regime for $t \leq 0.5$ with an exact double degeneracy of each level. Doubly degenerate levels give further rise to quasi-degenerate manifolds: The ground-state level is has a four-fold quasi-degeneracy, followed by quasi-flat manifolds containing 24, 76, 176 levels. Note that the regime in which the entanglement spectrum exhibits degeneracies coincides with the regime in which a spin liquid phase was suspected by Ref. [153]. In contrast, for $0.5 < t < 1.48$, the entanglement spectrum exhibits a unique ground state level, with double degeneracies present in the excited levels. Strikingly, at $t = 1.48$, a level crossing leads to double degeneracy not only of the ground state, but crossings also occur between other levels at the same (or a similar) value of t. This leads to the scenario that, around $t \approx 1.48$, levels are pairwise quasi-degenerate (or degenerate). Interestingly, this region coincides with the regime where, based on our previous analysis of order parameters M and D, we expect to have a spin liquid.

In Fig. 5.16 we focus on the fully unpolarized system ($S_z = 0$), and investigate the dependence of the entanglement spectrum for different cuts through a rhombic system, as illustrated in Fig. 5.16(a). The most natural cuts are the ones parallel to one side of the rhombus. Clearly, in one of these two cases, the entanglement between the subsystems fully vanishes in the highly anisotropic regime $t \to 0$, because different rows do not interact. With our choice of having an even number of spins per row, also the other cut produces low entanglement, since in each row the two spins on the left and right side produce dimers, with little entanglement between the second and the third spin. Accordingly, these two cuts do not reproduce the exact two-fold degeneracy which we had found in the hexagonally shaped lattice at small t. However, the unsymmetric cut shown in Fig. 5.16 again leads to a four-fold quasidegeneracy of the ground state up to values of t as large as 0.8.

A clearer picture arises around $t \approx 1.4$. Independent of the cut, we find a sizable interval $1.38 \lesssim t \lesssim 1.55$, in which all levels are exactly two-fold degenrate. This finding gives a much stronger support for a spin liquid phase than the quasi-degeneracies due to level crossings which we had found for $t \approx 1.48$ in the hexagonal system. We also stress that the lowest entangle-

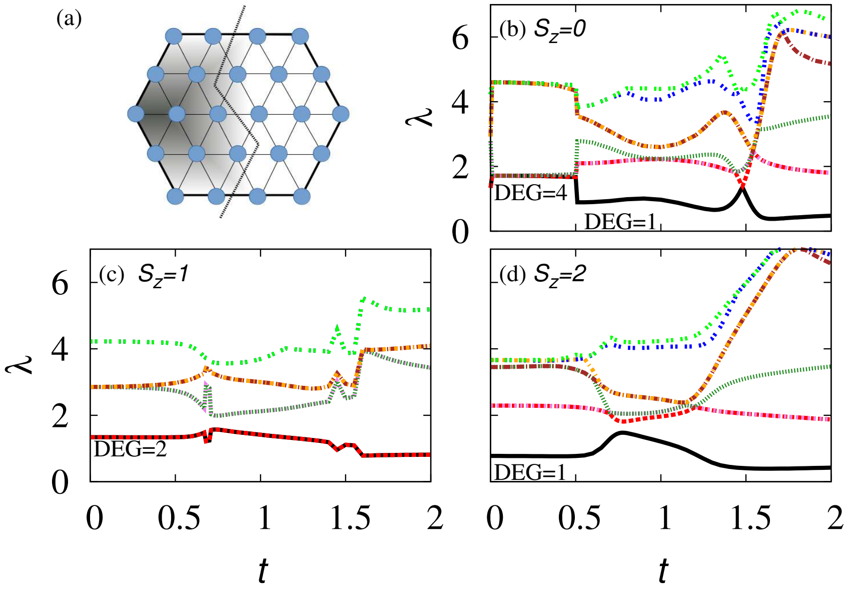

Figure 5.15: Entanglement spectrum (8 lowest values) for different spin polarizations (b–d), obtained in a $N = 24$ hexagonally shaped lattice with the cut shown in (a). DEG denotes the number of (quasi-)degenerate levels in the ground state.

ment eigenvalue barely depends on neither the cut nor the system geometry, suggesting that the system forms a uniform liquid in this region of t.

5.6.2 Inhomogeneous system ($V_i \neq 0$)

In the previous paragraph, we have shown that the system, to some extent, behaves similarly in different polarization sectors upon tuning the anisotropy t. This allows one to argue that the same behavior should persist in a shallow trap, where the system is approximated by homogeneous subsystems of different polarizations. In the present paragraph, we go a step further, and analyze the effect of a trap on short scales by diagonaliz-

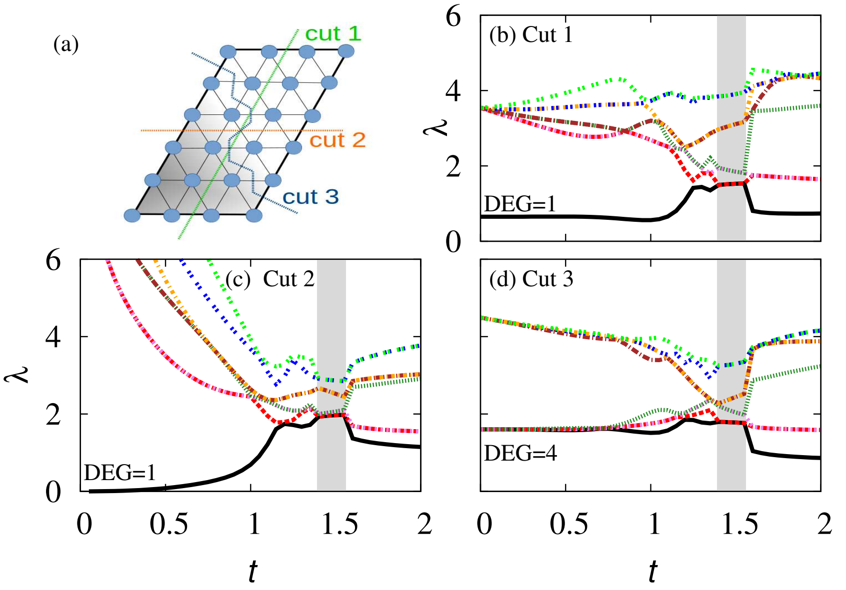

Figure 5.16: On a rhombic shaped lattice ($N = 24$ sites), we evaluate the entanglement spectrum for different cuts shown in (a). The eight lowest values of each entanglement spectrum are shown in b–d. The spin polarization is fixed to $S_z = 0$. DEG denotes the number of (quasi-)degenerate levels in the ground state. The grey area around $t \approx 1.4$, mark the regime where each level exhibits a two-fold degeneracy.

ing Hamiltonian (5.3) for $V_i = \frac{m}{2}\omega^2\mathbf{r}_i^2 = \eta\mathbf{r}_i^2$, with $\eta = 0.1$ (in units t_1/a^2) for typical trapping frequencies of 40 Hz. We will focus on the $S_z = 0$ sector, corresponding to half filling.

On the small lattice studied here, the inhomogeneities introduced by the trap, are rather weak: For the isotropic system, $t = 1$, we find an average population of 0.46 atoms on the 14 sites at the edge of the lattice, while the remaining 10 sites have an average population of 0.56 atoms. Accordingly, also the structure factor is barely modified: as shown in Figure 5.17(a), the peak position Q_x is practically indistinguishable for the two cases $\eta = 0$ and $\eta = 0.1$. Also the magnetic order parameter M, shown in Figure 5.17(b), exhibits a similar shape, though slightly smoothened near $t = 1.5$. Also the entanglement spectrum, plotted in Figure 5.18, shares important qualitative features with the one of the homogeneous system shown in Figure 5.15(a): For small values of t the ground state level has a perfect twofold degeneracy, and a fourfold quasidegeneracy. Again, the lifting of the degeneracy occurs abruptly near $t \approx 0.5$, although the precise value of the anisotropy is slightly increased by the trap. However, the level crossing observed in the homogeneous case around $t \approx 1.5$ does not take place in the trapped scenario. Whether this result questions the presence of a spin liquid phase in the trapped system, or whether degeneracies in the entanglement spectrum provide a relevant criterion for spin liquid behavior, cannot be decided here. Here, we find it interesting to notice that, while the behavior of the magnetic order parameter is hardly affected by the trap, the entanglement spectrum changes considerably.

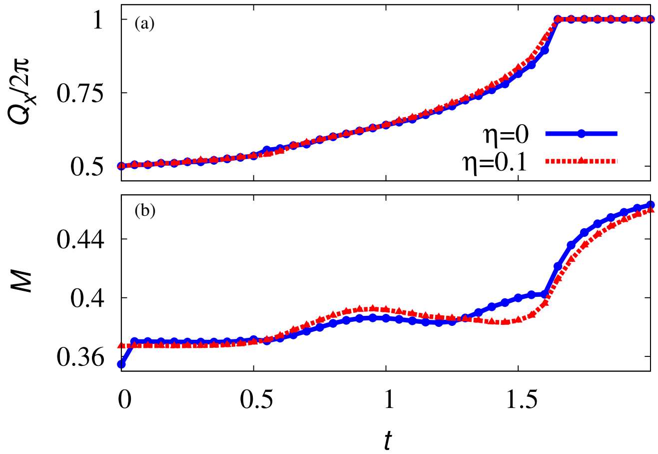

Figure 5.17: (a) Position Q_x of peak of structure factor $S(\mathbf{Q})$ as a function of anisotropy t at $S_z = 0$ in a homogeneous system and for $\eta = 0.1$. (b) Order parameter M as defined in Eq. (5.36).

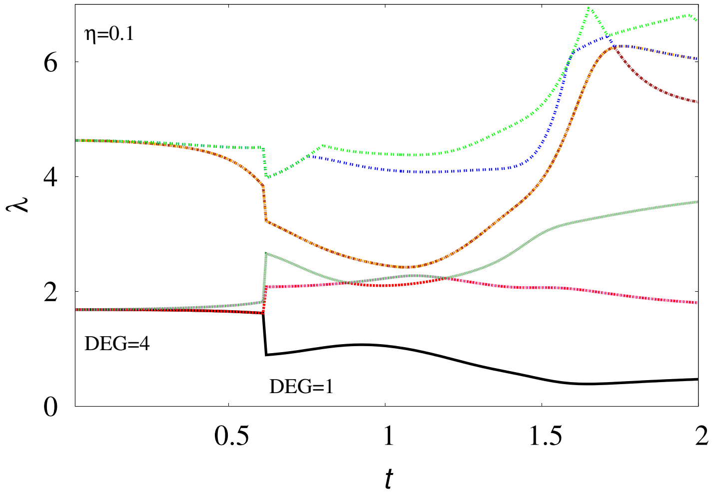

Figure 5.18: Entanglement spectrum (8 lowest values) at $S_z = 0$ in a trapped system at $\eta = 0.1$. D denotes the number of degenerate levels in the ground state.

To shed more light onto the role of the trap, we finally turn our attention to the excitation spectra. For selected t, we compare the spectra of the trapped and the homogeneous system in different polarization sectors in Figure 5.19(a–d). For the spectra of the homogeneous system, a tower-of-state feature [214, 215] has been noticed in Ref. [153]: In all polarization sectors, around $t = 1$ and $t = 2$ a small number of states at low energy is separated from states at higher energy by a large gap. This low-energy manifold is the basis from which Néel or spiral order can arise. In the thermodynamic limit, low-energy states at different S_z approach the same energy, and U(1) symmetry can spontaneously be broken. In contrast to this, relatively homogeneous level spacings are observed around $t \approx 0.6$ and $t \approx 1.4$ in *all* polarization sectors. Accordingly, a tower-of-state argument cannot be applied to those spectra, giving some evidence that no ordered phase will occur in these regions.

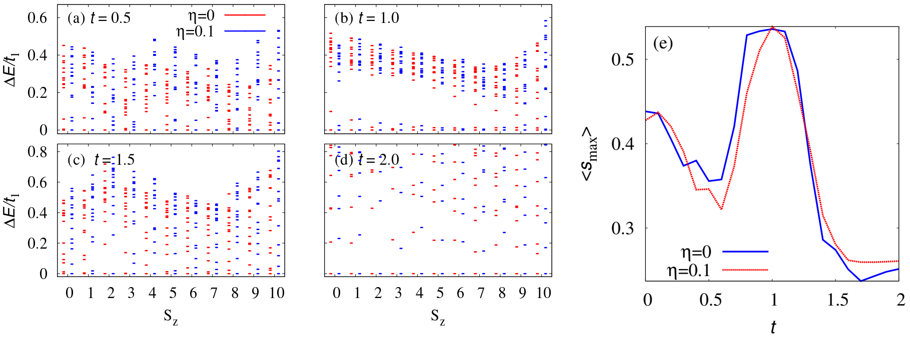

Figure 5.19: (a–d) Energy versus spin polarization at different t's for $S_z = 0$ in a trapped system for $\eta = 0.1$ and $\eta = 0$. (e) Largest level spacing $s_{\max}$ amongst ten lowest levels averaged over all polarization sectors, for a trapped system at $\eta = 0.1$ and for $\eta = 0$.

To quantify this different behavior we shall look at the gap in each polarization sector. However, quasi-degeneracies make it difficult or impossible to distinguish between levels which still should be considered gound states and excited states. For this reason, we will simply consider the largest level spacing $s_{max}(S_z)$ within the ten lowest states. The "tower of states" argument is applicable, if $s_{\max}$ is large in many or most polarization sectors. This would result in a large average value $\langle s_{\max} \rangle$, where the average is taken with respect to different spin polarizations. We further normalize this value by dividing by full spacing between the ten levels, such that $s_{\max}$ is maximal $(= 1)$ if the ten states are divided into two degenrate manifolds, while it is minimal $(= 0.1)$ if the levels are spaced homogeneously and the spectrum lacks a clear separation between low- and high-energy manifolds. Accordingly, a breakdown of the tower-of-state argument is indicated by minima of $s_{\max}$. This average is shown in Figure 5.19(e), for both a trapped and a homogeneous system. In both cases, it exhibits one pronounced minimum near $t \approx 0.6$. A second, less pronounced minimum is found around $t \approx 1.65$, which becomes further washed out in the presence of a trap.

5.7 Conclusions and Outlook

In this chapter we have studied the fate of QSL phases in realistic experimental conditions, namely, in presence of an harmonic confinement. The modified spin wave theory, which was previously formulated for bosons in a triangular lattice at half filling, has been re-derived for arbitrary filling factors. With this generalization, it can be used to capture, within a local density approximation, the physics of inhomogeneous systems. We have shown that the prediction of spin liquid behavior for an anisotropy $t \approx 1.65$ does not depend much on the filling factor, and should therefore survive in a trapped gas. This expectation has been backed by results from exact diagonalization in lattices of different sizes and geometries, up to 24 sites. Our exact diagonalization analysis has also ruled out the presence of an ordered non-magnetic phases like VBC that could explain the breaking of magnetic order in alternative to a QSL phase. These results support the existence of another QSL region at lower anisotropy, $t \approx 0.6$, which is not detected by MSW. Such discrepancy is not surprising. It is reasonable to expect that the MSW is able to detect a QSL phase only between two classical ordered phases –the QSL phase at $t \approx 1.65$ appears between spiral and 2D-Néel phases– while it is blind to transitions that are purely quantum. One may wonder that this happens only because the optimization is done starting by the classical solution. In fact unbiased direct searches of global minima provided the same or more energetic metastable solutions. Apparently, the optimal solution of the MSW is always a deformation of the classical one: perhaps, this is not so surprising because the spin wave approach is an expansion in $\frac{n}{2S}$ and the terms in $(\frac{n}{2S})^2$ included in the MSW are corrections to the terms considered in the LSW. The exact diagonalization approach have allowed us also to go beyond the local density approximation, and to study inhomogeneities on small scales. On this level, we have found no essential effect due to the trap for realistic choices of the trapping frequency. While the finite-size corrections are certainly expected to affect the exact diagonalization results, they should not exceed the 10-20 %. As the observables computed are global one would argue that the QSL behavior extends at least to entire lattice (of 24 spins) considered. The finite-size scale analysis we have performed in the homogeneous case further supports this picture. While final-size effects are not directly visible in the MSW because we have used periodic boundary conditions, they enter by determining the quality of local density approximation. Until the trap is not steep, and at the center is never so, the MSW suggests that, by taking optimal value of $t \approx 1.65$ at the center of the QSL region, the QSL phase should be visible even if the filling is changing considerably. Suppose, for instance, that the trap is tuned to have an occupation of around 3.7 atoms per site at the center, that to say 20% above the half-filling condition. Then, we could conclude that if we reach an occupation of 3.3 atoms per site –20% below half filling– at 10 lattice sites or more from the center, at the same time, we are within validity of local-density approximation in the QSL phase as predicted by MSW theory, and we limit the corrections due to the finite size as they are expected to go down as the inverse of the diameter of the region considered. Our study therefore provides strong hints for a robust QSL phase of bosons in anisotropic triangular lattices with antiferromagnetic tunnelings, which is not affected by weak trapping potentials as used in experiments.

The robustness of the QSL phase in presence of a weak harmonic confinement allow for the experimental investigation of these exotic quantum phases. The realization of the XX Hamiltonian for bosons in the strongly correlated regime relies on the periodic driving of the triangular optical lattice, which allows inverting the sign of the tunneling matrix elements as well as controlling their amplitude. The ability to tune the tunneling amplitude independently from the on-site interaction allows reaching strongly correlated phases where $U \gg |J_{eff}|$ without increasing the lattice depth. Indeed, as the effective tunneling J_{eff} follows a zeroth-order Bessel function as the shaking amplitude is increased, the system shall first enter a Mott-insulating phase before reaching the anti-ferromagnetic side of the phase diagram and thus the quantum spin liquid phase. Such a trajectory has allowed for a reversible crossing of the superfluid to Mott-insulator phase transition in a driven cubic lattice [204]. One limiting factor however are multiphoton resonances to higher lying Bloch bands, which critically reduce the coherence of the bosonic gas [216]. These resonances occur when a multiple of the shaking frequency matches the gap between the renormalized bands.

Therefore an optimized scheme for crossing the quantum phase transition while avoiding such resonances has to be developed.

CHAPTER 6

QUANTUM ANNEALING FOR THE NUMBER PARTITIONING PROBLEM USING A TUNABLE SPIN GLASS OF IONS

6.1 Introduction

Systems of trapped ultracold ions are probably the best controlled quantum systems of few or even many body particles. Ions in the trap at very low temperatures interact via quantum phonons, that is quantum fluctuations of ions positions. Since each of the ions have several internal states, these ion-phonon interactions lead effectively to realization of various, quite exotic, quantum spin models.

The spin-spin interactions in these models depend directly on the phononic eigenmodes of the system. If the latter are disordered or quasi-disordered, then the spin-spin interactions are disordered as well. The trapped ions system in this situation might behave as a spin glass. In this chapter we study that situation in detail, in particular we show that when we induce the spin-spin interactions with the addition of a laser field, we can achieve a situation where only one of the disordered, delocalized, phonon modes dominates the spin-spin interactions. This corresponds to an instance of the so called Mattis glass, which from the statistical physics point of view is equivalent to a ferromagnet, ergo relatively simple. From a mathematical point of view, however, the search of the GS of the Mattis Glass realizes an instance of NP-Hard partition problem.

This chapter has two parts, in the first one, we analyse how we can realize the NP-hard partition problem with trapped ions. In the second part, we answer a more fundamental question. We study how well is the spin-spin model describing the original spin-phonon model, equivalent to the many-particle generalization of the Jaynes-Cummings model. The focus of the study is in the comparison of the dynamical behaviour predicted by the two models.

This chapter is organized as follows. In Sec. 6.2 we explain how quantum annealing can be used in a spin glass system of ions. In Sec. 6.3 we present the main results. In Sec. 6.4, we provide further details on our semiclassical approximation. In Sec. 6.5 we show the results of the semiclassical approach applied to finite temperature. Here, we set the initial phonon population to non-zero thermal values. Finally, in the appendix we provide some further tests to our numerical integration method (appendix A.4), and a brief study of the optimal bias for the annealing protocol (appendix A.5).

6.2 Quantum annealing in spin glass systems of trapped ions

Spin models are paradigms of multidisciplinary science: They find several applications in various fields of physics, from condensed matter to high energy physics, but also beyond the physical sciences. In neuroscience, the famous Hopfield model describes brain functions such as associative memory by an interacting spin system [217]. This directly relates to computer and information sciences, where pattern recognition or error-free coding can be achieved using spin models [218]. Importantly, many optimization problems, like number partitioning or the travelling salesman problem, belonging to the class of NP-hard problems, can be mapped onto the problem of finding the ground state of a specific spin model [219, 220]. This implies that solving spin models is a task for which no general efficient classical algorithm is known to exist. In physics, analytic replica methods have been developed in the context of spin glasses [221, 222]. A controversial development, supposed to provide also an exact numerical understanding of spin glasses, regards the D-Wave machine. Recently introduced on the market, this device solves classical spin glass models, but the underlying mechanisms are not clear, and it remains an open question whether it provides a speed-up over the best classical algorithms [223–225].

This triggers interest in alternative quantum systems designed to solve general spin models via quantum simulation. A noteworthy physical system for this goal are trapped ions: Nowadays, spin systems of trapped ions are available in many laboratories [226–231], and adiabatic state preparation, similar to quantum annealing, is experimental state-of-art. Moreover, such system can exhibit long-range spin-spin interactions [232] mediated by phonon modes, leading to a highly connected spin model. The aim of this chapter is to demonstrate how to profit from these properties, using trapped ions as a quantum annealer of a classical spin glass model.

Quantum computers and quantum simulators are nowadays becoming a reality thanks to the advances in ion trapping and integrated superconducting technology [6, 233–236].

A possible device which is quickly being developed are quantum annealers. Annealing, as opposed to quenching, is a method to produce the ground state of a target Hamiltonian by slowly deforming/adjusting a well-known ground state of a different Hamiltonian. Annealing is in fact a concept originating from classical metallurgy, extended in the 1980s to classical optimization problems, and known as simulated annealing [237, 238]. In the current quantum versions, quantum annealing is very much analogous to quantum adiabatic computing, but is typically targeted towards the classical optimization problems. The idea is to add a simple, non-interacting, but non-commuting term to the original classical Hamiltonian. This simple additional term should dominate the system at the initial time, so that the ground state will be easy to find, since it will correspond to a non-interacting system. The non-commuting nature of the additional term ensures that the initial and target ground states are not symmetry protected. Then, the additional term is adiabatically removed and the ground state is expected to go slowly from the initial one to the one of the Hamiltonian of interest [239–241], see also the recent review [242]. This scheme is nowadays plausible with a large number of possible platforms, including trapped ions, cavity QED, circuit QED, superconducting junctions [243] and atoms in nanostructures. The first commercially accessible quantum annealers are in the market [223, 244, 245].

We have considered recently the exact quantum dynamics of few ion systems to demonstrate the robustness of chiral spin currents in a trapped-ion quantum simulator using Floquet engineering [246]. Our earlier works include studies of dual trapped-ion quantum simulators as an alternative route towards exotic quantum magnets [247], and studies of ion chains with long range interactions forming “magnetic loops” [248]. Topological edge states in periodically-driven trapped-ion chains [249], trapped ion quantum simulators of Rabi lattice models with discrete gauge symmetry [250], and hidden frustrated interactions and quantum annealing in trapped ion spin-phonon chains [251] were also considered recently. Novel ideas for spin-boson models simulated with trapped ions can be found in Ref. [252].

In Ref. [253], it has been proposed to use trapped ions for solving difficult optimization problems via quantum annealing. Such scheme, applied to the concrete example of number-partitioning, has come under scrutiny in Ref. [61] and it is exposed in the first part of this chapter. The idea is to profit from the known mapping between the number partitioning problem and the ground state of spin Hamiltonians [219]. In the interesting domain, where the number partitioning problem is notably difficult, the system is actually in the spin-glass-like phase, which renders finding the actual ground state an involved task for classical methods. The annealing method proposed was found to work well for small number of ions at zero temperature. In the second part of this chapter, we explore in detail a semiclassical approximation to the original problem, where the quantum correlations between the spins and the phonon bath are neglected. This, however, allows us to solve the Heisenberg equations of motion in an efficient way for much larger ion systems. Notably, the approach allows us to explore finite temperature effects on the annealing protocol.

We consider a setup described by a time-dependent Dicke-like model:

$$\begin{aligned} H_0(t) = &\sum_m \hbar\omega_m a_m^\dagger a_m + \sum_{i,m} \hbar\Omega_i \sqrt{\frac{\omega_{\text{recoil}}}{\omega_m}} \xi_{im} \sin(\omega_{\text{L}} t) \\ &\times \sigma_x^i (a_m + a_m^\dagger), \end{aligned} \tag{6.1}$$

with a_m annihilating a phonon in mode m with frequency ω_m and characterized by the normalized collective coordinates ξ_{im}. The second term in H_0 couples the motion of the ions to an internal degree of freedom (spin) through a Raman beam which induces a spin flip on site i, described by σ_x^i, and (de)excites a phonon in mode m. Here, Ω_i is the Rabi frequency, $\hbar\omega_{\text{recoil}}$ the recoil energy, and ω_{L} the beatnote frequency of the Raman lasers. Before also studying the full model, we consider a much simpler effective Hamiltonian, derived from Eq. (6.1) by integrating out the phonons [232, 254–256]. The model then reduces to a time-independent Ising-type spin Hamiltonian

$$H_J = -\hbar \sum_{ij} J_{ij}\, \sigma_x^i\, \sigma_x^j. \tag{6.2}$$

Each phonon mode contributes to the effective coupling J_{ij} in a factorizable way, proportional to $\xi_{im}\xi_{jm}$, and weighted by the inverse of the detuning from the mode $\delta_m = \omega_m - \omega_{\text{L}}$:

$$J_{ij} = \Omega_i \Omega_j \frac{\omega_{\text{recoil}}}{2\omega_{\text{L}}} \sum_m \frac{\xi_{im}\, \xi_{jm}}{\delta_m}. \tag{6.3}$$

The ξ_{im} imprint a pattern to the spin configuration, similar to the associative memory in a neural network [217, 257]. The connection between multi-mode Dicke models with random couplings, the Hopfield model, and spin glass physics has been the subject of recent research [258–260], and the possibility of addressing number partitioning was mentioned in this context [260].

Before proceeding, we remind the reader that the concept of a spin glass used in the literature may have different and controversial meanings (cf. [261–264]): i) long-range spin glass models [221] and neural networks [265, 266], believed to be captured by the Parisi picture [267, 268] and replica symmetry breaking. These lead to hierarchical organization of the exponentially degenerated free energy landscape, breakdown of ergodicity and aging, slow dynamics due to a continuous splitting of the metastable states with decreasing temperatures (cf. [269]). ii) Short-range spin glass models believed to be captured by the Fisher-Huse [270] droplet/scaling model with a single ground state (up to a total spin flip), but a complex structure of the domain walls. For these models, aging, rejuvenation and memory, if any, have different nature and occurrence [269, 271]; iii) Mattis glasses [272], where the huge ground state degeneracy becomes an exponential quasi-degeneracy, for which finding the ground state becomes computationally hard ([273], see Subsection “Increasing complexity”). Note that exponential (quasi)degeneracy of the ground states (or the free energy minima) characterizes also other interesting states: certain kinds of spin liquids or spin ice, etc.

Here we analyse the trapped ion setup. Even without explicit randomness ($\Omega_i = \Omega = \text{const.}$), the coupling to a large number of phonon modes suggests the presence of glassy behaviour. This intuition comes from the fact that the associative memory of the related Hopfield model works correctly if the number of patterns is at most $0.138N$, with N the number of spins [265]. For a larger number of patterns, the Hopfield model exhibits glassy behavior since many patterns have similar energy and the dynamics gets stuck in local minima. However, it is not clear *a priori* how the weighting of each pattern, present in Eq. (6.3), modifies the behavior of the spin model. In certain regimes the detuning suggests to neglect the contributions from all but one mode, leading to a Mattis-type model with factorizable couplings [272], $J_{ij} \propto \xi_{im}\xi_{jm}$. Strikingly, the possibility of negative detuning, i.e., antiferromagnetic coupling to a pattern, drives such system into a glassy phase, characterized by a huge low-energy Hilbert space. The antiferromagnetic Mattis model is directly connected to the potentially NP-hard task of number partitioning [273, 274]. Its solution can then be found via quantum annealing, i.e. via adiabatic ramping down of a transverse magnetic field, see also the proposal of Ref. [251] for a frustrated ion chain.

We start by giving analytical arguments to demonstrate glassy behaviour in the classical spin chains. Using exact numerics, we then focus on the quantum Mattis model. By calculating the magnetic susceptibility, and an Edward-Anderson-like order parameter, we distinguish between glassy, paramagnetic, and ferromagnetic regimes. The annealing dynamics is investigated using exact numerics and a semi-classical approximation. We demonstrate the feasibility of annealing for glassy instances. Finally, we show that the memory in the quantum Hopfield model is real-valued rather than binary. This property might be useful for various applications of quantum neural networks such as pattern recognition schemes.

6.3 Results

6.3.1 Tunable spin-spin interactions

We start our analysis by inspecting the phonon modes. For a sufficiently anisotropic trapping potential, the ions self-arrange in a line along the z-axis [275, 276]. The phonon Hamiltonian H_{ph} is obtained by a second-order expansion of Coulomb and trap potentials around these equilibrium positions z_i: $H_{\mathrm{ph}} = (m/2)\sum_{ij} V_{ij} q_i q_j$, with q_i the displacement of the ith ion from equilibrium. For the transverse phonon branch, V_{ij} is given by [232]

$$V_{ij} = \begin{cases} \omega_\perp^2 - \frac{e^2/m}{4\pi\epsilon_0} \sum_{i''(\neq i)} \frac{1}{|z_i - z_{i''}|^3}, & i = j \\ \frac{e^2/m}{4\pi\epsilon_0} \frac{1}{|z_i - z_j|^3}. & i \neq j \end{cases} \tag{6.4}$$

Our exact numerical simulations have been performed for six $^{40}\mathrm{Ca}^+$ ions in a trap of frequency $\omega_\perp = 2\pi \times 2.655$ MHz, as used in a recent experiment [230]. In order to maximize the bandwidth of the phonon spectrum and thereby

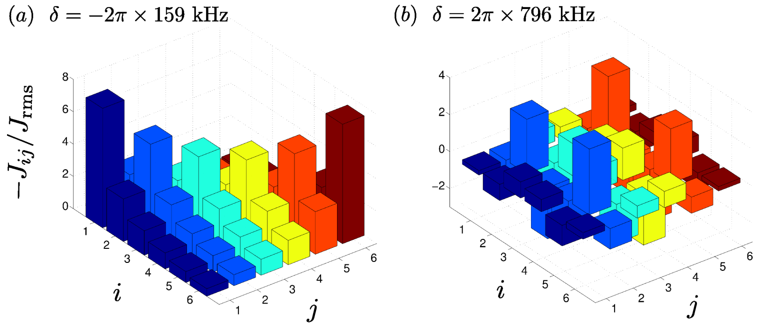

Figure 6.1: We plot the coupling constants J_{ij} (in units of $J_{\rm rms} \equiv \frac{1}{N(N-1)} \sum_{i \neq j} |J_{ij}|^2$), for a system of six ions at different detunings $\delta = \omega_N - \omega_{\rm L}$. Rabi frequencies are taken as constants $\Omega_i = \text{const.}$ **(a)** For negative detuning, $\delta = -2\pi \times 159$ kHz, interactions have a power-law decay. **(b)** For positive detuning, $\delta = 2\pi \times 796$ kHz, the coupling constants resemble a spin glass.

facilitate the annealing process, we choose the radial trap frequency ω_z as large as allowed to avoid zig-zag transitions, $\omega_z \lesssim 1.37\omega_\perp \cdot N^{-0.86}$. Diagonalizing the matrix V_{ij} leads to the previously introduced mode vectors $\boldsymbol{\xi}_m = (\xi_{1m}, \dots, \xi_{Nm})$, which are normalized to one, and ordered according to their frequency ω_m:

$$\boldsymbol{\xi}_{m'}^T V \boldsymbol{\xi}_m = \omega_m^2 \delta_{m,m'}. \tag{6.5}$$

The mode $\boldsymbol{\xi}_N$ with largest frequency, $\omega_N = \omega_\perp$, is the center-of-mass mode, $\xi_{iN} = N^{-1/2}$. Parity symmetry of V_{ij} is reflected by the modes, $\xi_{im} = \pm\xi_{(N+1-i)m}$, and even (+) and odd (−) modes alternate in the phonon spectrum. We focus on even N, for which all components ξ_{im} are non-zero. Except for the center-of-mass mode, all modes fulfil $\sum_i \xi_{im} = 0$.

Previous experiments [227–230, 277] have mostly been performed with a beatnote frequency $\omega_{\rm L}$ several kHz above ω_N, leading to an antiferromagnetic coupling $J_{ij} < 0$ with power-law decay, see Fig. 6.1(a). Despite the presence of many modes, the couplings J_{ij} then take an ordered structure. This work, in contrast, focuses on the regime $\omega_{\mathrm{L}} < \omega_N$, where modes with both positive and negative ξ_{im} contribute, and ferro- and antiferromagnetic couplings coexist, cf. Fig. 6.1(b). This reminds of the disordered scenario of common spin glass models like the Sherrington-Kirkpatrick model [221]. In the following we study the properties of the time-independent effective spin model, before considering the full time-dependent problem involving spin-phonon coupling.

6.3.2 Classical Mattis model

Close to a resonance with one phonon mode, simple arguments allow for deducing the spin configurations of the ground states. In this limit, we can neglect the other modes, leading to a Mattis model. A single pattern $\boldsymbol{\xi}_m$ then determines the coupling, $J_{ij} \propto \xi_{im}\xi_{jm}$. The sign of J_{ij} depends on the sign of the detuning: Below the resonance, we have $\mathrm{sign}(J_{ij}) = \mathrm{sign}(\xi_{im}\xi_{jm})$, and accordingly the energy $-\hbar J_{ij}\sigma_x^i\sigma_x^j$ is minimized if σ_x^i and σ_x^j are either both aligned or both anti-aligned with ξ_{im} and ξ_{jm}. Thus, we have a two-fold degenerate ground state given by the patterns $\pm[\mathrm{sign}(\xi_{1m}), \ldots, \mathrm{sign}(\xi_{Nm})]$. We refer to this scenario as the ferromagnetic side of a resonance.

Crossing the resonance, the overall sign of the Hamiltonian changes. Naively, one might assume that this should not qualitatively affect the physics, since we have $\frac{1}{N}\sum_{i\neq j}\xi_{im}\xi_{jm} = -\frac{1}{N} \to 0$, that is, there is an equal balance between positive and negative J_{ij}. This expectation, however, turns out to be false. Recalling the relation between the Mattis model and number partitioning [220, 273, 274], the antiferromagnetic model maps onto an optimization problem in which the task is to find the optimal bipartition of a given sequence of numbers $(\xi_i)_i$, such that the cost function $E = \left(\sum_{i\in\uparrow}\xi_i - \sum_{j\in\downarrow}\xi_j\right)^2$ is minimized. Here, the two partitions are denoted by $\uparrow$ and $\downarrow$. For a Hamiltonian of the form $H = \sum_{ij}\xi_i\sigma_x^i\xi_j\sigma_x^j = (\sum_i \xi_i\sigma_x^i)^2$, eigenvectors of σ_x^i are Hamiltonian eigenstates with an energy precisely given by the cost function E. Thus, in the limit of just one antiferromagnetic resonance, the ground state of H is exactly the configuration that minimizes the cost function.

With this insight, the ground states of the spin model are easily found exploiting the system's parity symmetry: For even modes, $\xi_{im} = \xi_{(N+1-i)m}$, and we simply have to choose $\langle\sigma_x^i\rangle = -\langle\sigma_x^{N+1-i}\rangle$ to minimize the cost function. For odd modes, $\xi_{im} = -\xi_{(N+1-i)m}$, and we must choose $\langle\sigma_x^i\rangle = \langle\sigma_x^{N+1-i}\rangle$. In both cases, this implies that we can choose half of the spins arbitrarily, leading to at least $2^{N/2}$ ground states.

The important observation is that an exponentially large number of ground states exists in the limit of being arbitrarily close above a resonance. This is a characteristic feature of spin glasses, yet it does not lead to computational hardness. In fact, as pointed out in Ref. [274], the number partitioning problem with exponentially many perfect partitions belongs to the "easy phase". How to reach hard instances will be explained in the section below.

Pushing our arguments further we consider the influence of a second resonance: In between two resonances, the exponential degeneracy of the antiferromagnetic coupling on one side is lifted by the influence of the ferromagnetically coupled mode on the other side. Interestingly, this does not lead to frustration, since even- and odd-parity modes alternate in the phonon spectrum, and the pattern favoured by the ferromagnetic coupling is always contained in the ground state manifold of the antiferromagnetic coupling. Accordingly, between two modes the ground state pattern is uniquely defined by the upper mode.

Beyond this two-mode approximation, we rely on numerical results. Taking into account all modes, exact diagonalization of a small system ($N \leq 10$) shows that the two-mode model captures the behaviour correctly: At any detuning, the degeneracy due to the nearest antiferromagnetic coupling is lifted in favour of the pattern of the next ferromagnetic coupling. In Fig. 6.2(a), we plot the cumulative density of states $\rho_{\text{cum}}(E)$, that is, the number of states with an energy below E. The corresponding phonon resonances ω_m are marked in Fig. 6.2(b). The curves clearly reflect the very different behaviour in the red- and blue-detuned regimes: Fig. 6.2 illustrates the quick increase of $\rho_{\text{cum}}(E)$ at low energies, when the laser detuning is chosen on the antiferromagnetic side of a phonon resonance. In contrast, a low density of states characterizes the system on the ferromagnetic side of a resonance. In intermediate regimes, as shown for $\delta = 2\pi \times 199$ kHz, the spectrum is symmetric.

A breakdown of the two-mode approximation is expected for large numbers of spins: Since the distance between neighbouring resonances approximately scales with $1/N$ (at fixed trap frequencies), the influence of additional modes grows with the system size. The combined contribution of all antiferromagnetically coupled modes tries to select the fully polarized configurations as the true ground state, while all ferromagnetically coupled modes, except for the center-of-mass mode, favour fully unpolarized configurations. As a consequence, it is *a priori* unclear which pattern will be selected in the presence of many modes.

This observation is crucial from a point of view of complexity theory. In the presence of parity symmetry neither the one-mode problem (i. e. the number partitioning problem), nor the two-mode approximation are hard problems, as they can be solved by simple analytic arguments. However, when many modes lift the degeneracy of the exponentially large low-energy manifold in an *a priori* unknown way, one faces the situation where a true but unknown ground state is separated only by a very small gap. Identifying this state then usually requires scanning an exponentially large number of low-energy states, and classical annealing algorithms can easily get stuck in a wrong minimum. Below, we discuss how a transverse magnetic field opens up a way of finding the ground state via quantum annealing. Moreover, we will discuss strategies to make also the one-mode model, i.e. the number partitioning problem, computationally complex.

6.3.3 Increasing complexity

As discussed above, the instances of the number partitioning problem realized in the ion chain are simple to solve due to parity symmetry. This is a convenient feature when testing the correct functioning of the quantum simulation, but our goal is the implementation of computationally complex and selectable instances of the problem in the device. One strategy is the

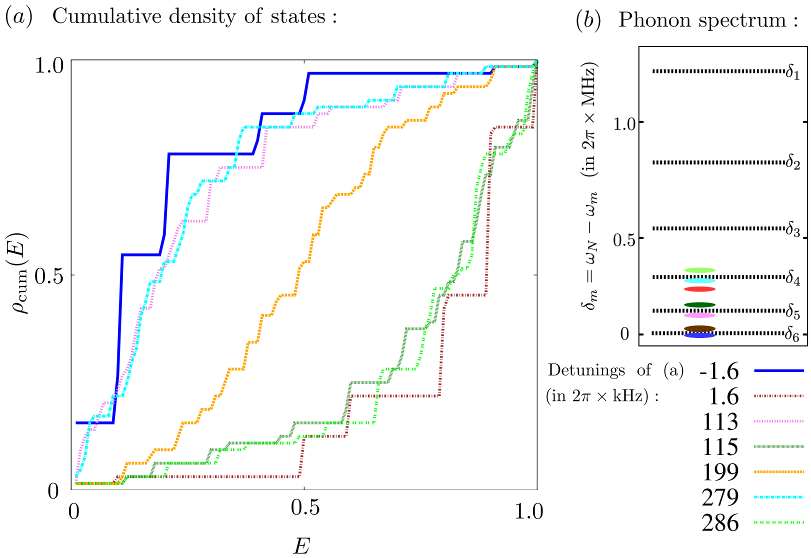

Figure 6.2: **(a)** For six ions and at trap frequency $\omega_z = 2\pi \times 770$ kHz, we plot the number of states (divided by the total Hilbert space dimension) below the normalized energy threshold (0: ground state energy, 1: energy of highest state), for different detunings from the center-of-mass mode. The density of states at low energies is seen to strongly increase when the detuning is slightly above a phonon resonance. In **(b)**, the position of the resonances (measured from the center-of-mass mode at $\delta_m = 0$) are shown.

use of microtraps to hold the ions [278]. The equilibrium positions of the ions can then be chosen at will, opening up the possibility to control the values of the ξ_{im}. The computational complexity of the number partitioning problem then depends on the precision with which the ξ_{im} can be tuned. If the number of digits can be scaled with the number of spins, one enters the regime where number partitioning is proven to be NP-hard [274]. Thus, the number of digits must at least be of order $\log_{10} N$, which poses no problem for realistic systems involving tens of ions.

Another way of enhancing complexity even within a parity-symmetric trap would be to "deactivate" some spins by a fast pump laser. For example, if all spins on the left half of the chain are forced to oscillate, $\sigma_x^j \to \sigma_x^j e^{i\omega_{\mathrm{pump}} t}$, the part of the Hamiltonian which remains time-independent poses a number partitioning problem of $N/2$ different numbers.

Another promising approach was recently suggested in Ref. [279]: Operating on the antiferromagnetic side of the center-of-mass resonance, single-site addressing allows one to use the Rabi frequency for defining the instance of the number-partitioning problem. This could indeed be the step to turn the trapped ions setup into a universal number-partitioning solver, where arbitrary user-defined instances can be implemented.

If one is not interested in the number-partitioning problem itself, one might also increase the system's complexity via resonant coupling to more than one mode. Equipping the Raman laser with several beatnote frequencies $\omega_{\mathrm{L}}^{(\mu)}$ and Rabi frequencies $\Omega_i^{(\mu)}$, it is possible to engineer couplings of the form [280]:

$$J_{ij} \propto \sum_{\mu=1}^{\mu_{\max}} \Omega_i^{(\mu)} \Omega_j^{(\mu)} \sum_{m=1}^{N} \frac{\xi_{im}\xi_{jm}}{\omega_m - \omega_{\mathrm{L}}^{(\mu)}}. \tag{6.6}$$

With an appropriate choice of Rabi frequencies and detunings, this allows for realizing the Hopfield model, $J_{ij} \propto \sum_{\mu=1}^{\mu_{\max}} \xi_{im_\mu}\xi_{jm_\mu}$, where each coupling μ is assumed to be in resonance with one mode m_μ. For ferromagnetic couplings, the low-energy states again are determined by the signs of the ξ_{im_μ}, but in general the different low-energy patterns are not degenerate, and a glassy regime is expected for large $\mu_{\max}$ [265].

6.3.4 Quantum phases

So far, we have considered classical spin chains lacking any non-commuting terms in the Hamiltonian. Quantum properties come into play if we either add an additional coupling $\sum_{ij} \sigma_y^i \sigma_y^j$, or a transverse magnetic field:

$$H_B = \hbar B \sum_i \sigma_z^i. \tag{6.7}$$

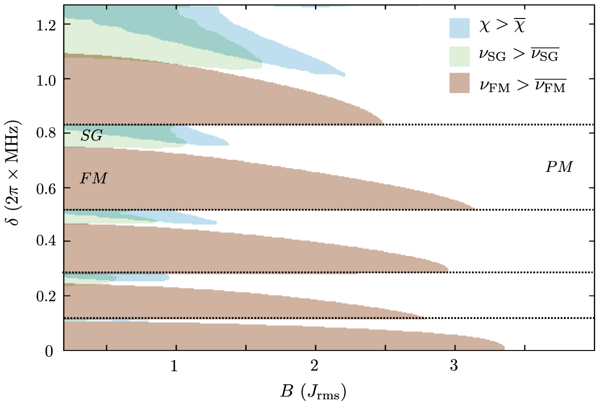

Figure 6.3: Upon varying the laser detuning δ and the transverse magnetic field B, we mark, for $N = 6$ ions and $\omega_z = 2\pi \times 770$ kHz, those regions in configuration space where the ferromagnetic order parameter $\nu_{\rm FM}$, the spin glass order parameter $\nu_{\rm SG}$, or the longitudinal magnetic susceptibility χ take larger than average values ($\overline{\nu_{\rm FM}} = 0.13$, $\overline{\nu_{\rm SG}} = 5$, $\overline{\chi} = 1.6$). Below each phonon resonance (marked by the dashed horizontal lines), there is a regime where large values of $\nu_{\rm SG}$ and χ indicate spin glass behaviour for sufficiently weak transverse field B. In order to break the Z_2 symmetry of the Hamiltonian, all quantities were calculated in the presence of a biasing field $\epsilon\sigma_x^1$ (with $\epsilon = -J_{\rm rms}$).

The latter has been realized in several experiments [228, 230, 277], and is convenient for our purposes, as the field strength B, if decaying with time, provides an annealing parameter: For large B, all spins are polarized along the z-direction, whereas for vanishing B one obtains the ground state of the classical Ising chain. As argued above, the latter exhibits spin glass phases with an exponentially large low-energy subspace. Even in those cases where the true ground state is known theoretically, finding it experimentally remains a difficult task. Our system hence provides an ideal test ground for experimenting with different annealing strategies.

Before presenting results for the simulated quantum annealing, let us first discuss the different phases expected for the effective Hamiltonian $H_{\text{eff}} = H_J + H_B + \epsilon\sigma_x^1$. The last term is a bias introduced to break the Z_2 symmetry. Our distinction between phases is based on certain quantities which combine thermal and quantum averages

$$\langle\langle\cdot\rangle^\alpha\rangle_T \equiv \frac{\sum_\lambda \langle\lambda|\cdot|\lambda\rangle^\alpha \exp(-E_\lambda/k_\mathrm{B}T)}{\sum_\lambda \exp(-E_\lambda/k_\mathrm{B}T)}, \tag{6.8}$$

with $|\lambda\rangle$ denoting Hamiltonian eigenstates at energy E_λ. For $\alpha = 1$, $\langle\langle\cdot\rangle^\alpha\rangle_T$ reduces to the normal thermal average. We will use low, but non-zero temperatures T of the order of the coupling constant, accounting in this way for the huge quasi-degeneracy in the glassy regime. The thermal average $\langle\cdot\rangle_T$ plays a role somewhat similar to the disorder average, as it averages over various quasi-ground states (pure thermodynamic phases). We therefore expect $\langle\langle\sigma_x^i\rangle\rangle_T$ to go to zero in the glassy phase. In contrast, a non-zero average $\langle\langle\sigma_x^i\rangle\rangle_T$ detects the ferromagnetic phase of the Mattis model, while it vanishes in the paramagnetic state. Taking its square to get rid of the sign, we obtain a global ferromagnetic order parameter by summing over all spins:

$$\nu_\mathrm{FM} = \frac{1}{N}\sum_i \langle\langle\sigma_x^i\rangle\rangle_T^2. \tag{6.9}$$

On the other hand, in the spirit of an Edwards-Anderson-like parameter, we consider thermal averages of squared quantum averages, i.e.

$$\nu_\mathrm{EA} = \frac{1}{N}\sum_i \langle\langle\sigma_x^i\rangle^2\rangle_T. \tag{6.10}$$

At sufficiently low temperature this average would still be zero for a paramagnetic system, but now it remains non-zero for both ferromagnetic and glassy systems. Accordingly, a parameter which is “large” only for glassy systems is given by the ratio $\nu_\mathrm{SG} = \frac{\nu_\mathrm{EA}}{\nu_\mathrm{FM}}$, used in Fig. 6.3 to detect glassy regions.

Thermal averages are difficult to measure, but the contained information is also present in linear response functions at zero temperature. Therefore, we have calculated the longitudinal magnetic susceptibility χ, i.e. the response of the system to a small local magnetic field h_x^j along the σ_x direction (in units J_{rms}):

$$\chi = \frac{J_{\mathrm{rms}}}{N} \sum_{ij} \left(\frac{\partial \langle \sigma_x^i \rangle}{\partial h_x^j} \right)^2 . \tag{6.11}$$

Due to the (quasi)degeneracy in the glass, one expects a huge response even from a weak field, and thus a divergent susceptibility.

We have calculated ν_{FM}, ν_{SG}, and χ, for $N = 6$ between $0 \leq 2\pi \times \delta \leq 8$ MHz, and $0 \leq B \leq 4J_{\mathrm{rms}}$. For the thermal averaging, we have chosen a temperature $k_{\mathrm{B}}T = J_{\mathrm{rms}}$. The results are summarized in Fig. 6.3, indicating the regions where these quantities take larger values than their configurational averages $\overline{\nu_{\mathrm{FM}}}$, $\overline{\nu_{\mathrm{SG}}}$, and $\overline{\chi}$, defined as $\overline{f} \equiv \int \mathrm{d}B \int \mathrm{d}\delta f(B,\delta)/(B_{\mathrm{max}}\delta_{\mathrm{max}})$. In this way, we identify and distinguish ferromagnetic behaviour below, and glassy behaviour above each resonance. Regions of large susceptibility χ overlap with regions of large ν_{SG}, attaining numerical values which are three orders of magnitude larger than the corresponding averages. For sufficiently strong field B, in contrast, none of these parameters is large, indicating paramagnetic behaviour.

Note that the existence of the purported glassy phase in the quantum case is an open problem. We provide here the evidence only for small systems, since it is numerically feasible and corresponds directly to current or near-future experiments. If we increase the complexity of our system by resonant coupling to many phonon modes, as discussed in the last paragraph of the previous subsection, the glassy behavior will result from the interplay of contributions of many modes – similarly as in the Hopfield model with Hebbian rule and random memory patterns. Here the beautiful results by Strack and Sachdev [258] –the "quantum" analog of the Amit *et al.* [266] machinery– can be applied directly to obtain the phase diagram for large N. If, however, we increase the complexity by random positioning of the ion traps, then the resonance condition will pick up the contribution from one dominant (random) mode, and the Hebbian picture will apply.

6.3.5 Simulated quantum annealing

We will now turn to the more realistic description of the system in terms of a time-dependent Dicke model, described by the Hamiltonian H_0 in Eq. (6.1) with an additional transverse field $H_B(t)$ from Eq. (6.7). We assume an exponential annealing protocol $B(t) = B_{\max} \exp(-t/\tau)$. Again we apply a bias field $h_{\text{bias}} = \hbar \epsilon \sigma_x^i$, lifting the Z_2 degeneracy of the classical ground state. We study the exact time evolution under the Hamiltonian $H(t) = H_0(t) + H_B(t) + h_{\text{bias}}$, using a Krylov subspace method [281], and truncating the phonon number to a maximum of two phonons per mode.

Initially, the system is cooled to the motional ground state, and spins are polarized along σ_z. Choosing $B_{\max} \gg \epsilon, J_{\text{rms}}$, this configuration is close to the ground state of the effective model $H_J + H_B + h_{\text{bias}}$ at $t = 0$. If the decay of $B(t)$ is slow enough, and if the entanglement between spins and phonons remains sufficiently low, the system stays close to the ground state for all times, and finally reaches the ground state of H_J.

We have simulated this process for $N = 6$ ions, as shown in Fig. 6.4. As a result of the annealing, we are not interested in the final quantum state, but only in the signs of $\langle \sigma_x^i \rangle$, which fully determine the system in the classical configuration. This provides some robustness. We find that for a successful annealing procedure, yielding the correct sign for all i, the number of phonons produced during the evolution should not be larger than 1. At fixed detuning, we can reduce the number of phonons by decreasing the Rabi frequency, at the expense of increasing time scales. As a realistic choice [231, 282], we demand that annealing is achieved within tens of milliseconds.

Fig. 6.4(a) shows that one can operate at a detuning $\delta = 2\pi \times 239$ kHz, that is, at the onset of a glassy phase according to Fig. 6.3. The mode vector which selects the ground state is $\boldsymbol{\xi}_5 = (0.61, 0.34, 0.11, -0.11, -0.34, -0.61)$, and the corresponding pattern can be read out after an annealing time $t \geq 15$ ms. On the other hand, even for long times, $\langle \sigma_x^{i=4} \rangle$ saturates only at -0.15, which is far from the classical value -1. As shown in Fig. 6.4(b), a slower annealing protocol leads to more robust results ($|\langle \sigma_x^i \rangle| > 0.52 \ \ \forall\ i$).

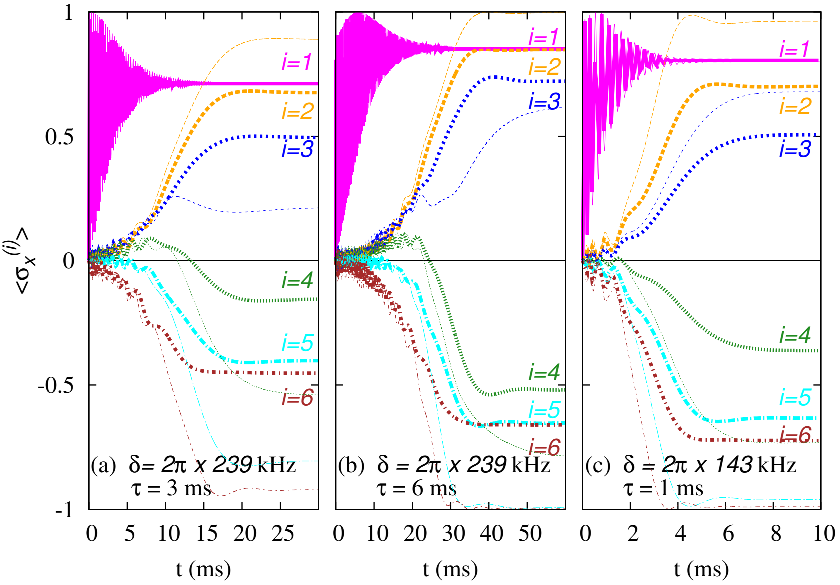

Figure 6.4: Unitary time evolution of the full system ($N = 6$) for different δ between the 4th and 5th resonance. The exact evolution (thick lines) compared to the semi-classical approximation (thin lines). In **(a,b)**, we operate at the onset of glassiness, $\delta = 2\pi \times 239$ kHz and the panel **(c)** considers a ferromagnetic instance, $\delta = 2\pi \times 143$ kHz. In (a) we have $B_{\mathrm{max}} = 50J_{\mathrm{rms}}$ and $\tau = 3$ ms. In (b) we have, $B_{\mathrm{max}} = 80J_{\mathrm{rms}}$ and $\tau = 6$ ms. Fast annealing, with $B_{\mathrm{max}} = 50J_{\mathrm{rms}}$ and $\tau = 1$ ms, is possible in the ferromagnetic instance in **(c)**. In all simulations, we have chosen $\Omega = 2\pi \times 50$ kHz, $\omega_{\mathrm{recoil}} = 2\pi \times 15$ kHz, and $\epsilon = -10$ kHz.

In Fig. 6.4(c), a much simpler instance in the ferromagnetic regime is considered. Good results ($|\langle\sigma_x^i\rangle| > 0.36 \ \ \forall\, i$) can then be obtained within only a few ms.

In addition, dephasing due to instabilities of applied fields and spontaneous emission processes disturb the dynamics of the spins. In Ref. [279] a master equation was derived that takes into account such noisy environment. To study the evolution of the system in this open scenario we have applied the Monte Carlo wave-function method [283]. As quantum jump operators are hermitian, σ_x^i for dephasing and σ_z^i for spontaneous emission, the evolution remains unitary, but is randomly interrupted by quantum jumps. Each jump has equal probability Γ, and the average number of jumps within the annealing time T is given by $\overline{n_{\text{jumps}}} = 2N\Gamma T$, which we chose close to 1.

Since a faithful description requires statistics over many runs, we restrict ourselves to a small system, $N = 4$, with short annealing times. In a sample of 100 runs, we noted 94 jumps (42 σ_x and 52 σ_z jumps). In 39 runs, no jump occurred. Amongst the 61 runs in which at least one jump occurred, 26 runs still produced the correct sign for all spin averages $\langle \sigma_x^i \rangle$. The full time evolution, averaged over all runs, is shown in Fig. 6.5. On average, the final result is $(0.65, 0.50, -0.41, -0.68)$, that is, our annealing with noise still produces the correct answer, but with lower fidelity.

Whether an individual jump harms the evolution crucially depends on the time at which it occurs: While a spin flip (σ_z noise) is harmless in the beginning of the annealing, a dephasing event (σ_x noise) at an early stage of the evolution leads to wrong results. Oppositely, at the end of the annealing procedure, dephasing becomes harmless while spontaneous emission falsifies the result. An optimal annealing protocol has to balance the effect of different noise sources against non-adiabatic effects in the unitary evolution.

6.3.6 Scalability

Above we have demonstrated the feasibility of the proposed quantum annealing scheme in small systems. The usefulness of the approach, however, depends crucially on its behaviour upon increasing the system size. While the exact treatment of the dynamics becomes intractable for longer chains,

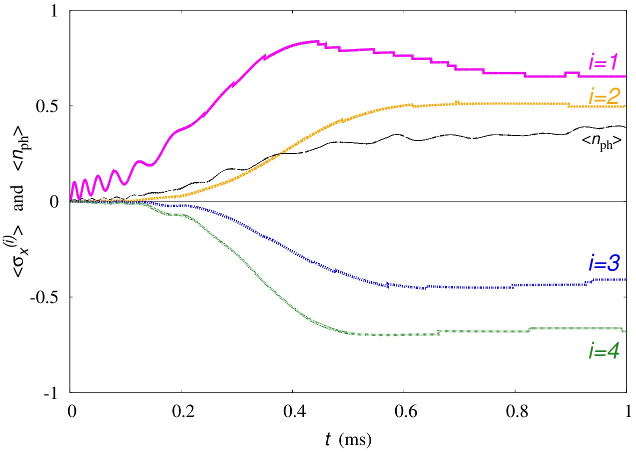

Figure 6.5: We consider $\Gamma = 0.03 J_{\text{rms}} \approx 120$ Hz and a total annealing time $T = 1$ ms, which produce on average one jump per run, $\overline{n_{\text{jumps}}} = 0.96$. We plot expectation values of the spins and total number of phonons as a function of time. Here, we have operated in the ferromagnetic regime between the second and third phonon resonance, $\delta = 2\pi \times 159$ kHz. Other parameter values are $\Omega = 2\pi \times 50$ kHz, $\omega_{\text{recoil}} = 2\pi \times 15$ kHz, $\omega_z = 2\pi \times 876$ kHz, $B_{\max} = 50 J_{\text{rms}} \approx 200$ kHz, $\epsilon = -10$ kHz, and $\tau = 0.1$ ms. Results correspond to averaging 100 runs.

an efficient description can be derived from the Heisenberg equations:

$$
\begin{aligned}
i\hbar \frac{\mathrm{d}}{\mathrm{d}t}\langle a_m \rangle &= \langle [a_m, H(t)] \rangle, \\
i\hbar \frac{\mathrm{d}}{\mathrm{d}t}\langle \sigma^i_\alpha \rangle &= \langle [\sigma^i_\alpha, H(t)] \rangle,
\end{aligned}
\tag{6.12}
$$

with $H = H_0(t) + H_B(t) + h_{\text{bias}}$. To solve this set of $5N$ first-order differential equations, we make a semi-classical approximation $\langle a_m \sigma^i_x \rangle \approx \langle a_m \rangle \langle \sigma^i_x \rangle$, and then proceed numerically using a fourth order Runge-Kutta algorithm. The semi-classical approximation is justified as long as the system remains close to the phonon vacuum. A direct comparison with exact results for six ions (see Fig. 6.4) shows that the semiclassical approach, while slightly overestimating fidelities, accurately reproduces all relevant time scales.

This approach allows us to extend our simulations up to $N = 22$ ions, at trap frequency $\omega_z = 2\pi \times 270$ kHz. We operate between the first and second resonance where the level spacing is largest, at a beatnote frequency $\omega_{\mathrm{L}} = \omega_1 + 0.2(\omega_2 - \omega_1)$, that is with a fixed relative detuning between the two modes. This choice corresponds to $\delta = 2\pi \times 1.2$ MHz in Fig. 6.3, characterized as a glassy instance of the system.

Our aim is to find the relation of annealing time, measured by the decay parameter τ, and systems size while the fidelity F is kept constant. For a practical definition we demand that F is zero when the annealing fails, that is when the sign of the spin averages $\langle \sigma_x^i \rangle$ does not agree with the classical target state for all i. If the annealing finds the correct signs, the robustness still depends on the absolute values of the spin averages. The fidelity is then defined as the smallest absolute value, $F = \min_i |\langle \sigma_x^i \rangle|$. Our results are summarized in Fig. 6.6: Firstly, this figure shows that for all sizes $N \leq 20$ large fidelities $F \geq 0.5$ can be produced within experimentally feasible time scales, $\tau \leq 30$ ms. Secondly, the time scale τ needed for a fidelity $F = 0.5$ fits well to a fourth-order polynomial in N (with subleading terms of the order $\exp(1/N)$):

$$\tau(N) = N^4 \tau_0 \exp(\gamma/N), \tag{6.13}$$

with τ_0 and γ being free fit parameters. Although the sample of 22 ions is too small to draw strong conclusions, it is noteworthy that the polynomial fit is more accurate than an exponential one. This suggests that the proposed quantum simulation is indeed an efficient way of solving a complex computational problem. One should also keep in mind that our estimates, based on a semi-classical approximation, neglect certain quantum fluctuations which could further speed-up the annealing process.

To study the scaling of dissipative effects, we have extended the Monte Carlo wave function approach to larger systems, which is feasible if the phonon dynamics is neglected. The unitary part of the evolution is then described by the effective Ising Hamiltonian $H_{\mathrm{eff}} = H_J + H_B(t) + h_{\mathrm{bias}}$. The dissipative part consists of random quantum jumps described by σ_x^i and σ_z^i.

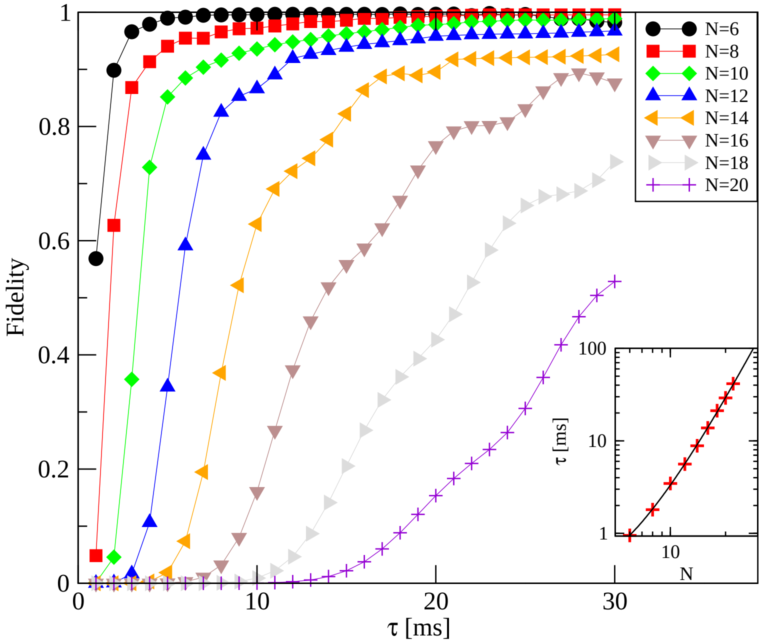

Figure 6.6: We solve the equations of motion, Eq. (6.12), for a glassy instance at different system sizes N, and plot the fidelity of the outcome as a function of the annealing time τ. In the inset, we investigate the scaling behaviour by plotting (in double-logarithmic scale) the value of τ which is needed for a fidelity $F = 0.5$ as a function of N. A fourth-order polynomial fit agrees very well with the data (black dashed line). The fit parameters, as defined by Eq. (6.13), are $\tau_0 = (90 \pm 40)$ ms and $\gamma = 12.0 \pm 1.2$. For all calculations, we have chosen a beatnote frequency between the two lowest resonances, $\omega_\mathrm{L} = 0.8\omega_1 + 0.2\omega_2$, $\omega_z = 2\pi \times 270$ kHz, and $\epsilon = -1$ kHz. The initial value of the transverse field was $B_\mathrm{max} = 10$ kHz.

The results for a glassy instance ($\delta = 2\pi \times 198$ kHz at $\omega_z = 2\pi \times 700$ kHz) are summarized in Table 6.1 for $N = 4, 6, 8$. The noise rate is chosen such that on average one quantum jump occurs in the system with four ions, while accordingly the system with eight ions suffers on average from two such events. In all cases, the annealing produces the correct pattern, $F > 0$. As expected, F decreases for larger systems, but fortunately rather slowly (from $F = 0.25$ at $N = 4$ to $F = 0.16$ at $N = 8$). If the total amount of noise is kept constant, i.e. $\Gamma \propto 1/N$, the annealing is found to profit from larger system sizes, since a quantum jump at spin i is unlikely to affect the sign of $\langle \sigma_x^j \rangle$ for $j \neq i$. We note that the spin values produced by the Monte Carlo wave function method cannot be described by a normal distribution. Importantly, the peak of each distribution, roughly coinciding with its median, is barely affected by the noise. Thus, larger fidelities can be obtained from the median rather than from the arithmetic mean of $\langle \sigma_x^i \rangle$.

6.3.7 Spin pattern in the quantum Mattis model

The quantum annealing discussed above exploits quantum effects in order to extract information encoded in the classical model. Now we search for information which is encoded in the quantum, but not in the classical model. Therefore, we focus on the ferromagnetic Mattis model, which in the classical case keeps a binary memory of a spin pattern, that is, of N bits. Our considerations can also be generalized to the Hopfield model [217], which memorizes multiple patterns. We will show how quantum effects can increase the amount of information encoded by these models.

Recall that in the classical case, the spin pattern was defined by a resonant mode in terms of the sign of each component. In the quantum case, however, one cannot simply replace classical spins by quantum averages, $\mathrm{sign}(\langle \sigma_x^i \rangle)$. Even in a weak transverse field B, this quantity vanishes due to the Z_2 symmetry, $\sigma_x \to -\sigma_x$. Instead, the pattern is reflected by $\lambda_i = \langle \Psi_1 | \sigma_x^i | \Psi_2 \rangle$, where $|\Psi_1\rangle$ and $|\Psi_2\rangle$ are the ground and first excited state. For small B, we find numerically $\mathrm{sign}(\lambda_i) = \mathrm{sign}(\xi_{im})$. For large B, the stronger relation $\lambda_i = \xi_{im}$ holds approximately, see Fig. 6.7. Thus, the former binary memory has become real-valued.

To show this behaviour, we note that for strong B, the ground state is fully polarized along z, and the first excited state is restricted to the N-

$N = 4$	closed system:	$(1.0, 0.97, -0.39, -0.42)$
	open system, mean values:	$(0.79, 0.70, -0.25, -0.32)$
	open system, median values:	$(1.0, 0.97, -0.39, -0.42)$
$N = 6$	closed system:	$(1.0, 0.99, 0.76, -0.40, -0.64, -0.66)$
	open system, mean values.	$(0.82, 0.68, 0.55, -0.23, -0.43, -0.46)$
	open system, median values:	$(1.0, 0.98, 0.76, -0.39, -0.64, -0.66)$
$N = 8$	closed system:	$(1.0, 0.99, 0.96, 0.58, -0.31, -0.70, -0.75, -0.77)$
	open system, mean values:	$(0.83, 0.69, 0.69, 0.40, -0.16, -0.43, -0.55, -0.53)$
	open system, median values:	$(1.0, 0.98, 0.94, 0.58, -0.30, -0.69, -0.75, -0.76)$

Table 6.1: **Annealing in effective spin model with and without noise.** We perform quantum annealing ($\tau = 3$ ms and $T = 30$ ms) for a glassy instance ($\delta = 2\pi \times 198$ kHz at $\omega_z = 2\pi \times 700$ kHz, $\epsilon = -1$ kHz) at different system sizes N, using an effective spin model description. The results $(\langle\sigma_x^1\rangle, \ldots, \langle\sigma_x^N\rangle)$, are shown for the closed-system dynamics and for a noisy system, with mean and median over a sample of 2000 runs. The average number of noisy event scales with the system size, and is adjusted to $4/N$. In all cases, the signs of $\langle\sigma_x^i\rangle$ reproduce correctly the mode pattern, and the fidelity decreases with the system size. In contrast to the arithmetic mean values, the median values in the noisy sample are barely affected by the noise.

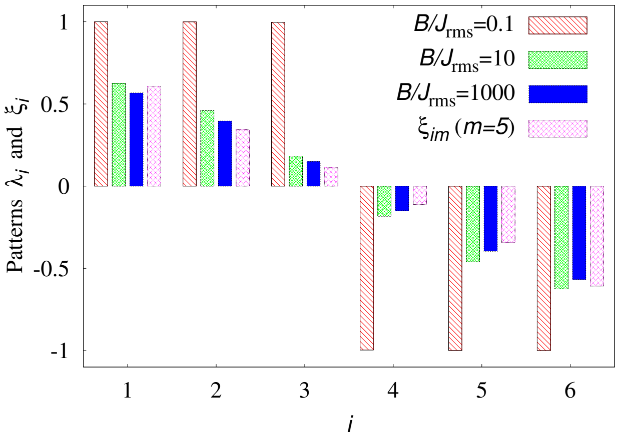

Figure 6.7: **From binary to real-valued patterns.** The spin expectation values λ_i approach the real values of the mode vector ξ_{im} when a sufficiently strong transverse magnetic field B is present. The shown data was obtained from the effective spin Hamiltonian for $N = 6$ ions in the ferromagnetic regime, $\delta = 2\pi \times 143$ kHz. Deviations from the equality $\lambda_i = \xi_{im}$ are smaller than 0.04.

dimensional subspace with one spin flipped, that is, $S_z = \sum_i \sigma_z^i = N - 2$. Within this subspace the Hamiltonian H_J is given by an $N \times N$ matrix approximately proportional to $\tilde{J}_{ij} = -\xi_{im}\xi_{jm}$ for $i \neq j$, and $\tilde{J}_{ii} =$ constant. Here we neglect all but the mth mode close to resonance.

It is easy to see that the vector $\boldsymbol{\xi}_m$ is a ground state of the matrix $-\xi_{im}\xi_{jm}$, which differs from $\tilde{J}_{ij}$ only by the diagonal elements, which approach unity for large N. The first excited state reads $|\Psi_2\rangle = \sum_{i=1}^{N} \xi_{im} |i\rangle$, where $|i\rangle$ denotes the state in which spin i is flipped relatively to all others (in the σ_z basis). This shows that $\lambda_i \approx \xi_{im}$, and the small deviations decrease quickly with N.

Measuring λ_i experimentally is possible by full state tomography. The absolute value of λ_i can be obtained via a simple σ_z^i measurement. In the limit of strong B-fields we have $\lambda_i = [(1 - \langle\sigma_z^i\rangle)/2]^{1/2}$.

Many applications are known for the classical spin system with couplings defined by spin patterns, reaching from pattern recognition and associative memory in the Hopfield model [217] to noise-free coding [218, 284]. Our analysis suggests that patterns given by real numbers could replace patterns of binary variables by exploiting the quantum character of the spins.

6.4 Details of the semiclassical approximation

Since the original proposals [232, 254] trapped ions quantum simulators are the subject of intensive theoretical and experimental research. Starting from realization of the simple instances of quantum magnetism [277], they have reached quite a maturity in the recent experimental developments (cf. [282, 285–290]). The recent paper by Bollinger's group [291], in addition to the excellent experimental work, contains also an outstanding analysis of quantum dynamics of the relevant Dicke model, in which the ions interact essentially with one phononic mode.

Quantum dynamics in general, and in particular for the Dicke-like ion-phonon models, are very challenging for numerical simulations. Exact treatments are possible for small systems only, so that various approximate methods have to be used. One of them is the truncated Wigner approximation, in which both ionic and phononic operators are replaced by complex numbers, the dynamics becomes "classical", and only the initial data mimic the "quantumness" of the problem [292]. This approach was used in Ref. [293] to study the quantum non-equilibrium dynamics of spin-boson models. More sophisticated "mean-field" approaches decorrelate ions from phonons, but treat at least either ions or phonons fully quantum mechanically – this approach is in particular analysed in the present chapter. Quantum aspects of the models in question were studied in the series of papers [294–296].

In this section we will develop a semiclassical approximation to the exact dynamics described above. This approximation will allow us to consider much larger systems.

6.4.1 Hamiltonian

Recalling the previous section, we study a chain of N trapped ions interacting by effective spin-spin interactions subjected to a transverse time-dependent magnetic field. Interactions are generated by Raman coupling the pseudo-spin degrees of freedom to the phonon modes which are obtained expanding the Coulomb force between the ions around their equilibrium positions [232]. The phonon spectrum is defined through its natural frequencies ω_k and modes ξ_k^i. The dynamics of the system is described by a time-dependent Hamiltonian that in the Schrödinger picture reads,

$$\begin{aligned}\mathcal{H}_{\mathrm{S}}(t)/\hbar &= \sum_k^M \omega_k \hat{a}_k^\dagger \hat{a}_k + \sum_{i,k}^{N,M} \Omega \eta_k^{(i)} \sin(\omega_{\mathrm{L}} t) \left(\hat{a}_k^\dagger + \hat{a}_k\right) \sigma_x^{(i)} \\ &+ \sum_i^N B(t)\, \sigma_z^{(i)} + \varepsilon \sigma_x^{(p)}, \end{aligned} \tag{6.14}$$

where $\hat{a}_k(\hat{a}_k^\dagger)$ is the annihilation (creation) operator of one phonon in the kth mode and ω_k is the frequency of that mode. The operators $\sigma_x^{(i)}$, $\sigma_y^{(i)}$, and $\sigma_z^{(i)}$ are the spin operators in the ith position. The frequencies Ω and ω_{L} are the Rabi frequency and the beatnote frequency of the laser, respectively. The dimensionless parameters $\eta_k^{(i)}$ are the Lamb-Dicke parameters proportional to the displacement of an ion i in the vibrational mode k, see Ref. [232]. As usual, t is time, and a time-dependent magnetic field $B(t)$ allows us to perform the quantum annealing. A small bias term, proportional to ε, has been added in the pth position to remove the $\mathcal{Z}_2$ degeneracy. The upper limit of the sum over the ions i is N, the number of ions. The upper limit of the sum in modes k is M, the number of modes. The total number of phonon modes is $3N$, but the Raman beam couples to only N modes, selected by the wave vector difference of the lasers. At this point, we may keep our analysis general by making no assumption about the number M of modes. However, all phonons which are considered are assumed to be coupled to the spin in the same way. Hereinafter, the upper limits of the sums will be omitted for brevity.

6.4.2 Equations of motion

We compute the Heisenberg equations of motion for the quantum average of every operator in the Hamiltonian, $\hat{a}_k$, $\hat{a}_k^\dagger$, $\sigma_x^{(i)}$, $\sigma_y^{(i)}$, and $\sigma_z^{(i)}$. Given that these are time independent operators, the calculation reduces to commutators. Additionally, we replace $\hat{a}_k^\dagger + \hat{a}_k$ by $2\,\mathrm{Re}\,[\hat{a}_k]$ and $\hat{a}_k - \hat{a}_k^\dagger$ by $2\mathrm{i}\,\mathrm{Im}\,[\hat{a}_k]$. The equations of motion (all with real coefficients) read,

$$\begin{aligned}
\frac{d\langle \mathrm{Re}\,[\hat{a}_k]\rangle}{dt} &= \omega_k \langle \mathrm{Im}\,[\hat{a}_k]\rangle \\
\frac{d\langle \mathrm{Im}\,[\hat{a}_k]\rangle}{dt} &= -\omega_k \langle \mathrm{Re}\,[\hat{a}_k]\rangle - \sin(\omega_{\mathrm{L}} t) \sum_j \Omega \eta_k^{(j)} \langle \sigma_x^{(j)} \rangle, \\
\frac{d\langle \sigma_x^{(i)}\rangle}{dt} &= -2B(t)\,\langle \sigma_y^{(i)}\rangle, \\
\frac{d\langle \sigma_y^{(i)}\rangle}{dt} &= -4\sum_l \Omega \eta_l^{(i)} \sin(\omega_{\mathrm{L}} t) \langle \mathrm{Re}\,[\hat{a}_l] \sigma_z^{(i)}\rangle \\
&\quad +2B(t)\,\langle \sigma_x^{(i)}\rangle - 2\varepsilon \langle \sigma_z^{(i)}\rangle \delta_{p,i}, \\
\frac{d\langle \sigma_z^{(i)}\rangle}{dt} &= 4\sum_l \Omega \eta_l^{(i)} \sin(\omega_{\mathrm{L}} t) \langle \mathrm{Re}\,[\hat{a}_l] \sigma_y^{(i)}\rangle + 2\varepsilon \langle \sigma_y^{(i)}\rangle \delta_{p,i}\,.
\end{aligned} \tag{6.15}$$

6.4.3 Annealing protocol

The functional form and value of Ω, $B(t)$ and ε determine the annealing protocol. In these annealing schemes, the initial value of the transverse magnetic field $B(t=0)$ must be sufficiently strong to initialize the system in the paramagnetic phase, that is, B must be larger than the effective spin-spin interactions $J \sim \Omega^2 \omega_{\mathrm{rec}}/(\delta \omega_{\mathrm{rad}})$, where ω_{rec} is the recoil energy of the photon-ion coupling, ω_{rad} is the radial trap frequency, and δ the detuning from the nearest phonon mode. For typical values, e.g. $\Omega \sim \delta \sim 100$ kHz, $\omega_{\mathrm{rec}} \sim 25$ kHz, $\omega_{\mathrm{rad}} \sim 5$ MHz, we obtain effective interactions $J \sim 1$ kHz, so we need an initial field strength $B(0) \sim 10$ kHz. The annealing scheme proceeds by turning down the magnetic field according to some functional form in order to adiabatically achieve the ground state of the Hamiltonian of interest. Given the adiabatic theorem, for a closed system initialized in the ground state, the final system is guaranteed to be in the ground state as long as the system is gapped along the annealing path, and the variation is slow enough. Generalization to open systems has been proposed in Ref. [297].

We have used a decreasing exponential form for the transverse magnetic field, $B\left(t\right) = B(0)\, e^{-\frac{t}{\tau}}$ with a decay rate τ. The other parameters, Ω and ε, remain constant. An example of the evolution of the system under this protocol is shown in Fig. 6.8. Initially, $\left\langle \hat{\sigma}_x^{(i)} \right\rangle = 0$ for all i, and the total phononic population is set to 0. Within tens of microseconds the phononic modes are populated. Not surprisingly, the mode next to the resonance becomes the most populated one, with a population being orders of magnitude larger than the population of the other modes. In contrast to these rapid changes of the phonon state, the spin dynamics is much slower. The spin expectations $\left\langle \hat{\sigma}_x^{(i)} \right\rangle$ remain mostly clustered around zero for hundreds of microseconds. When $B\left(t\right) \simeq \varepsilon$, the values $\left\langle \hat{\sigma}_x^{(i)} \right\rangle$ start to deviate from zero, and some acquire positive values, while others become negative. Thus, the spin curves separate from each other, and we call the time at which this happens the *separation time*. At some point after the separation time, the spin curves saturate, that is, from then on $\left\langle \hat{\sigma}_x^{(i)} \right\rangle$ remain constant in time. We define the *waiting time* as the time when all $\left\langle \hat{\sigma}_x^{(i)} \right\rangle$ have stopped varying. At the waiting time, the phononic populations stabilize around certain values, although their oscillations do never vanish.

The quantum annealer produces final values of $\left\langle \hat{\sigma}_x^{(i)} \right\rangle$ which are not fully polarized , that is, $| \left\langle \hat{\sigma}_x^{(i)} \right\rangle | < 1$. Thus, the final state differs from the classical ground state of the target Hamiltonian, that is, the Hamiltonian in the absence of a transverse field. Thus, we take as readout of the annealing protocol the average spin values [298–300]. This is not a problem, as long as for all spins the sign matches with the one in the classical state. As explained in detail in Ref. [61], the spin configuration of the target Hamiltonian is determined by the dominant mode, defined as the one with frequency just

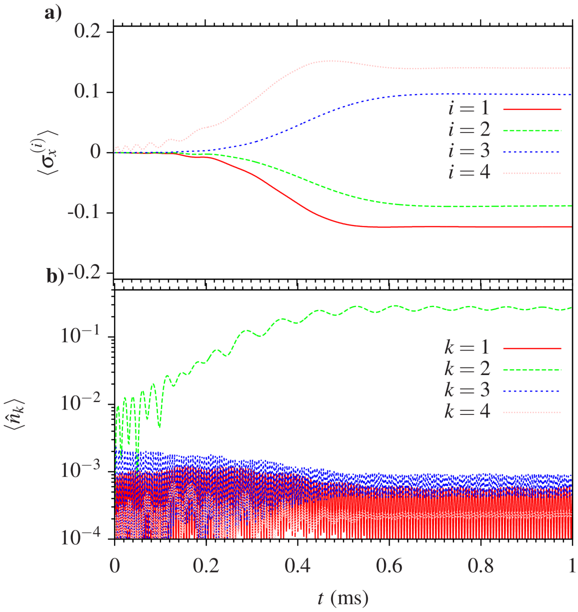

Figure 6.8: (Upper panel) Evolution of $\left\langle \hat{\sigma}_x^{(i)} \right\rangle$ in a system with 4 spins, with initial populations of phononic modes set to 0. The biased spin is the pink one, see text for details. (Lower panel) Evolution of the populations of the phononic modes in a system with 4 spins, with initial populations of phononic modes set to 0. $\delta = 1$ MHz.

below the beatnote frequency ω_{L}. There are different reasons why the final ground state might show a different spin pattern: Either, the annealing was too fast, that is, the value of τ was chosen too small, or the effective spin model is not valid. This is the case when ω_{L} is too close to a resonance ω_k.

6.4.4 Fidelity of the annealing protocol

In order to quantify the success of the annealing protocol, that is, the ability of the method to identify the target ground state of the spin system, we will define the following fidelity,

$$F = \begin{cases} \min\limits_i \left|\left\langle \sigma_x^{(i)} \right\rangle\right| & \text{if sign}\left[\left\langle \sigma_x^{(i)} \right\rangle\right] = \text{sign}\left[\eta_{k_d}^{(i)}\right], \forall i \\ 0 & \text{Otherwise} \end{cases}, \tag{6.16}$$

where η_{ij} is the ith component of the dominant mode k_d for a fixed value of the beatnote frequency ω_{L}. That is, the fidelity is zero if the signs of $\langle\sigma_x^i\rangle$ do not match the signs of η_i of the dominant mode. If the signs are reproduced, the value of the fidelity is defined as the smallest expectation value of the spins of the ions. Note that with this definition, any non-zero fidelity is good enough for correctly identifying the ground state pattern, assuming the absence of noise in the system.

6.4.5 Semiclassical approximation

Now we will develop a semiclassical approximation to the exact equations of motion, Eq. (6.15), that will allow us to study larger systems of ions and the effects of temperature on the annealing protocols. We make the following approximations:

$$\begin{aligned} \langle \hat{a}_k \sigma_\mu^{(i)} \rangle &\simeq \langle \hat{a}_k \rangle \langle \sigma_\mu^{(i)} \rangle \\ \langle \hat{a}_k^\dagger \sigma_\mu^{(i)} \rangle &\simeq \langle \hat{a}_k^\dagger \rangle \langle \sigma_\mu^{(i)} \rangle \end{aligned} \tag{6.17}$$

with $\mu = \{x, y, z\}$. These approximations ignore the quantum correlations in the coupling between bosonic and spin modes.

Additionally defining the auxiliary variables $S_k(t) \equiv \sin(\omega_{\mathrm{L}} t) \sum_j \Omega \eta_k^j \langle \sigma_x^{(j)} \rangle$ and $J^{(i)}(t) \equiv \sin(\omega_{\mathrm{L}} t)\Omega\left(2\sum_l \eta_l^i \langle \mathrm{Re}[\hat{a}_l]\rangle\right) + \varepsilon\delta_{p,i}$, we obtain the approximate equations of motion,

$$\begin{aligned} \frac{d\langle \mathrm{Re}[\hat{a}_k]\rangle}{dt} &= \omega_k \langle \mathrm{Im}[\hat{a}_k]\rangle, \qquad (6.18) \\ \frac{d\langle \mathrm{Im}[\hat{a}_k]\rangle}{dt} &= -\omega_k \langle \mathrm{Re}[\hat{a}_k]\rangle - S_k(t), \\ \frac{d\langle \vec{\sigma}^{(i)}\rangle}{dt} &= -2 \begin{pmatrix} 0 & B(t) & 0 \\ -B(t) & 0 & J^{(i)}(t) \\ 0 & -J^{(i)}(t) & 0 \end{pmatrix} \cdot \langle \vec{\sigma}^{(i)} \rangle \end{aligned}$$

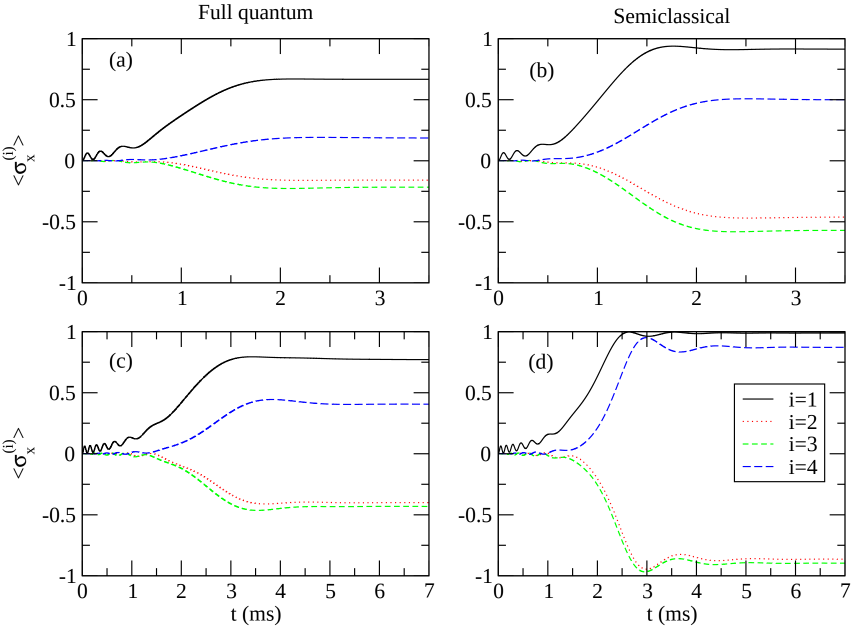

Figure 6.9: Quantum (a,c) and semiclassical (b,d) evolution of $\left\langle \hat{\sigma}_x^{(i)} \right\rangle$. The figure is computed with $N = 4$ ions with a detuning $\delta = 2900$ kHz. Panels (a) and (b) correspond to $\tau = 0.35$ ms and panels (c) and (d) to $\tau = 0.7$ ms.

where a spin vector notation, $\langle \vec{\sigma}^{(i)} \rangle = \left(\langle \sigma_x^{(i)} \rangle, \langle \sigma_y^{(i)} \rangle, \langle \sigma_z^{(i)} \rangle \right)$, has been used. This is a system of $2 \times M + 3 \times N$ non-linear first-order ordinary differential equations. Hence, it is numerically solved with a first order, ordinary differential equation solver that uses the Gragg–Bulirsch–Stoer method, step size control and order selection, called ODEX [301].

6.4.6 Comparison to full quantum evolution

To benchmark the semiclassical method, we have compared it against a full quantum evolution of the system using Krylov subspaces. The latter is a method to study the dynamical evolution under time-dependent Hamiltonians that computes a reduced evolution operator omitting contributions smaller than a certain threshold, that is, transitions to irrelevant states. Despite this disregard, the Krylov evolution can be considered an *exact* numerical simulation, as it iteratively determines which part of the Hilbert space is irrelevant at a given accuracy.

In both cases, semiclassical and full quantum, the evolution of a given initial state under a time-depending Hamiltonian is calculated with time steps in a recurrent way. In the fully quantum calculation, the time steps are of the order of 1 ns, while in the semiclassical description they are variable, but can be orders of magnitude larger. In the quantum case, we have to specify a quantum state —a complex vector in the joint Fock basis of phononic and spin modes—, containing the amplitudes of every state of the basis. In the semiclassical case, we only have to supply the initial mean values of every operator.

It should be noted that the exact quantum evolution requires truncating the maximum phonon number which in our case was set to two phonons per mode. Such truncation of the Hilbert space requires sufficiently cool systems. And even with this truncation, the quantum evolution is restricted to a small number of ions. Considering only one transverse phonon branch, i.e. N phonon modes, with a maximum population of two phonons per mode, the Hilbert space dimension is $2^N \times 3^N$, that is, a dimension of 46656 for $N = 6$ ions. The semiclassical approach, in contrast, allows us to explore larger systems.

Time evolution of $\left\langle \hat{\sigma}_x^{(i)} \right\rangle$

The semiclassical model captures well the qualitative behaviour of the evolution of $\left\langle \hat{\sigma}_x^{(i)} \right\rangle$, as exemplified in Fig. 6.9. In the figure we compare the semiclassical evolution with the exact dynamics for $N = 4$ ions for two different decay times. The discrepancy between semiclassical and exact evolution is smallest for shorter times ($t \lesssim \tau$), where the semiclassical model is able to correctly capture the details of the dynamical evolution, most notably

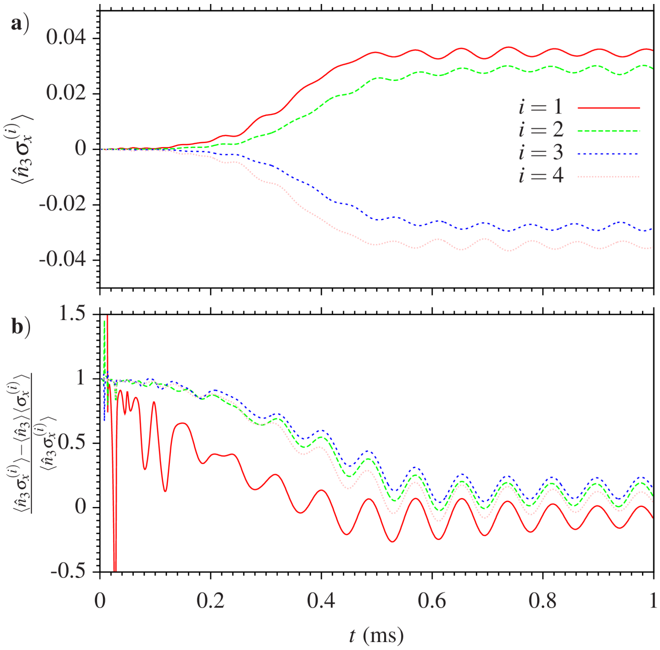

Figure 6.10: Evolution of $\left\langle \hat{n}_3 \hat{\sigma}_x^{(i)} \right\rangle$ (a) and of the relative difference $(\left\langle \hat{n}_3 \hat{\sigma}_x^{(i)} \right\rangle - \langle \hat{n}_3 \rangle \left\langle \hat{\sigma}_x^{(i)} \right\rangle)/\left\langle \hat{n}_3 \hat{\sigma}_x^{(i)} \right\rangle$ for a system of four spins with initial populations of phonons set to zero for a detuning $\delta = 1000$ kHz.

little wiggles in the evolution of the biased ion, $i = 1$. Importantly, the semiclassical model also agrees with the exact evolution regarding general features such as the separation time, and the sign of each $\left\langle \hat{\sigma}_x^{(i)} \right\rangle$ in the long-time limit. As discussed in more detail in the next paragraph, this enables a quite accurate prediction of annealing fidelities, despite the fact that the approximation disregards some quantum properties. Thus it provides a computationally efficient way to study the behaviour of larger systems.

For a better understanding of the errors in the semiclassical approach, we have exactly calculated the evolution of $\langle \hat{n}_3 \sigma_x^{(i)} \rangle$, see Fig. 6.10(a), and of $\langle \hat{n}_3 \rangle \langle \sigma_x^{(i)} \rangle$. As our semiclassical approximation is based on substituting the former correlator by the latter one, the discrepancy between both expressions is an indicator for the quality of the semiclassical approach. In Fig. 6.10(b), we plot the relative difference as a function of time: Initially, the phonon and spin degrees of freedom are taken as uncorrelated, thus, the semiclassical and the exact description coincide at $t = 0$. On short time scales, both correlators have small absolute values, but their relative difference becomes large. For times larger than the separation time, the absolute values of the correlators increase, and the relative errors decrease. On long time scales, the errors oscillate around mean values of the order 0.1. This observation suggests that the main errors made in the semiclassical approximation are introduced at short times, where the transverse magnetic field and its temporal derivative takes large values.

Fidelity

As we have seen the semiclassical approximation provides a reasonable description of the dynamics in many configurations. Let us now explore in more detail in which parameter regions it predicts the correct fidelity for the annealing protocol. In Fig. 6.11 we present a comparison of the fidelities obtained from the exact time evolution and from the semiclassical approach for a system of four ions. We tune through a broad range of beatnote frequencies ω_L, and vary the decay time τ of the magnetic field. The overall agreement is very good: Both methods predict a small fidelity when the field decays too fast (small τ), or when the system is too close to one of the phonon resonances. The semiclassical evolution, however, slightly overestimates the fidelity for small τ, and also slightly below each phonon resonance, that is, on the ferromagnetic side of the resonance. Notably, the semiclassical approach works quite well in the glassy regimes above the resonances, where it estimates correctly the regions in which the annealer fails for any annealing time.

As discussed earlier, the failure of the annealing protocol for small τ is due to non-adiabatic behaviour in the fast varying field. The failure near the resonance, though, cannot be fixed by increasing τ, and has its origin

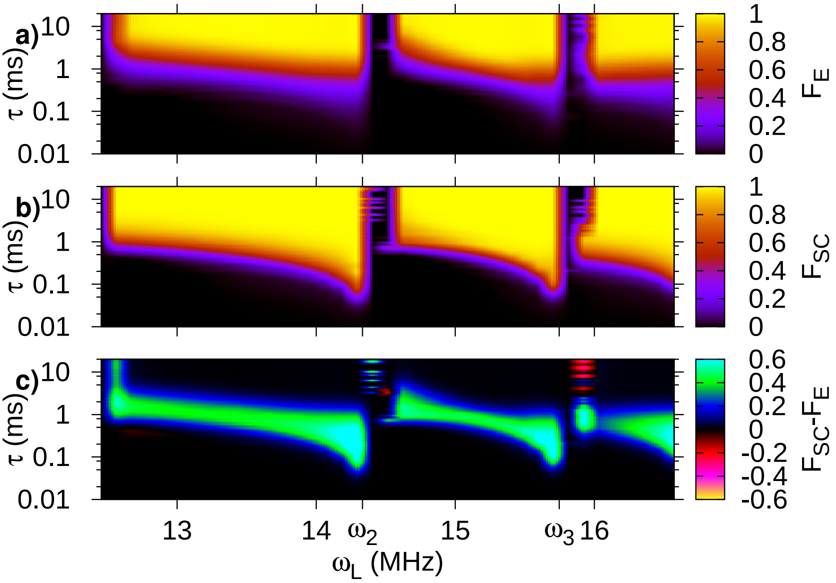

Figure 6.11: Fidelity obtained with the full quantum evolution F_{E} (a), the semiclassical model F_{SC} (b), and the difference between the semiclassical model and the full quantum (c). In both cases, we consider a system of four ions, and we plot the magnitudes as a function of ω_{L} and τ. The fidelity is readout after a time $20\,\tau$.

in the deviation from of the Dicke dynamics from the effective spin model. Although such deviations are expected on both sides of a phonon resonance, the region of zero fidelity is seen only on the glassy side of each resonance. From that perspective, the size of the spin gap seems to play a role as well, although in this regime we should not compare it to $\hbar/\tau$, but to those spin-phonon energy scales which are neglected in the effective spin model, that is, the first order term in a Magnus expansion, see Ref. [227].

The main advantage of the semiclassical model is that it can easily be applied to larger systems. In Fig. 6.12, we consider systems of six and eight ions. Notably, a broad region of zero fidelity occurs for eight ions between

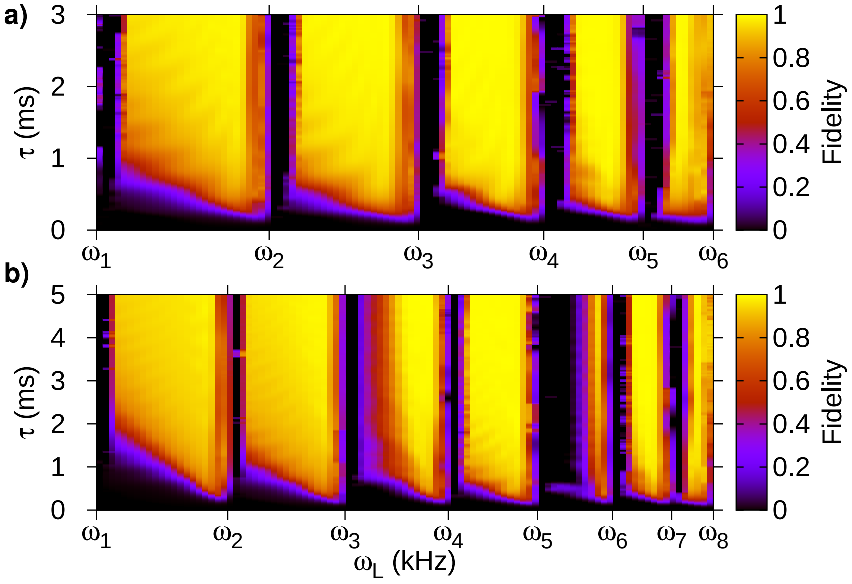

Figure 6.12: Fidelity of a system of six ions (a) and a system of eight ions (b) as a function of ω_L and τ using the semiclassical approximation. Final times are 20τ.

ω_5 and ω_6. Its origin is unclear to us, and further calculations on the fully quantum evolution would be needed in order to discriminate whether they are true effects or merely calculation artefacts.

We finish this section by discussing the factor which limits the scalability of the quantum annealer. As seen above, below a critical detuning from the resonance the fidelity drops to zero. This sets a limit to the scalability of the quantum annealer, because, with the number of modes being proportional to the number of ions, the mode spacing decreases when the system size is increased. However, we note that phonon spectra are not equidistant, and within the transverse branch, the phonon spacing is largest at the lower energetic end of the phonon spectrum. Thus, to achieve finite fidelity in an up-scaled system, one may need to operate in the regime of low-energy phonons. The semiclassical estimates in Ref. [61] suggest that the quantum annealing still works in systems with more than twenty ions, presumably large enough to detect quantum speed-up.

6.5 Finite temperature effects on the annealing protocol

Finite temperature effects are expected to reduce the quality of the annealing protocol, recently, however, thermal effects are shown to aid the annealing protocol for a 16-qubit problem in a superconducting setup [302]. In this section we study the robustness of the annealing protocol when the phonons are initially at finite temperature. To do so, we consider an initial state with phonon mode populations set as follows: we fix the temperature T of the phonons, then, the mean values of the number of phonons for each mode are sampled according to the a bosonic thermal bath probability distribution at T. With these initial conditions, the system is then evolved semiclassically according to Eqs. (6.18). This process is repeated with different initial values of the population of phonons, sampled appropriately. After the evolution, the statistical moments are calculated in order to infer the thermal properties of the system at the final time.

It should be noted that our dynamical model only captures the coherent Hamiltonian evolution, but no decoherence processes due to interactions with the environment. Thus, in order to account for all thermal effects, heating events, as they occur for instance due to trap inhomogeneities, should be taken into account by considering an increased initial temperature.

6.5.1 Classical thermal phonons

We assume that the initial populations of the phononic modes are determined by a phonon temperature. In the canonical ensemble, the expected value of the number operator of the phonons in the kth mode is,

$$\langle \hat{n}_k \rangle = \frac{1}{e^{\beta\hbar\omega_k} - 1} \,. \tag{6.19}$$

The corresponding Hamiltonian of the symmetrized phonon field is $\hat{\mathcal{H}}_{\rm ph} = \hbar \sum_k \omega_k \frac{\hat{a}_k^\dagger \hat{a}_k + \hat{a}_k \hat{a}_k^\dagger}{2}$. The expected value of the annihilation operator $\alpha_k \equiv \langle \hat{a}_k \rangle$ is sampled as,

$$P\left(\alpha_k\right) = \frac{1}{\pi \langle \hat{n}_k \rangle} e^{-\frac{|\alpha_k|^2}{\langle \hat{n}_k \rangle}} \, . \tag{6.20}$$

The complex-valued Gaussian probability distribution function (PDF) for the random variable α_k is a product of two Normal PDFs —one real the other purely imaginary—for the random variables $\mathrm{Re}\left[\alpha_k\right]$ and $\mathrm{Im}\left[\alpha_k\right]$. Both distributions have a mean $\mu = 0$ and variance $\sigma^2 = \hat{n}_k/2$. We thus use for convenience,

$$P\left(\alpha_k\right) = N\left(\mathrm{Re}\left[\alpha_k\right]; 0, \langle \hat{n}_k \rangle/2\right) N\left(\mathrm{Im}\left[\alpha_k\right]; 0, \langle \hat{n}_k \rangle/2\right) \, , \tag{6.21}$$

being $N\left(x; \mu, \sigma^2\right)$ the Normal PDF of the random variable x with mean μ and variance σ^2.

6.5.2 Effects of temperature on the protocol

To evaluate the effects of temperature on the proposed annealing protocol we will consider different initial temperatures and detunings. In all cases we will fix the decay time $\tau = 10$ ms. Fig. 6.13 shows the fidelity and the total phononic population per mode in the system. In the figure we compare results obtained with several values of ω_L and a broad range of temperatures of the phonons. Quite generally, panels (a) and (b) show that up to a certain temperature the fidelity is not affected by thermal phonons, but above this temperature the fidelity drops to zero. The value of this temperature strongly depends on the detuning, and decreases by several orders of magnitudes when we change from a far-detuned configuration to a near-resonance scenario. For instance, in the far-detuned regime at $\omega_{\rm L} = \omega_2 - 902.41$ kHz (solid squares) the critical temperature is of the order 0.1 K, while close to the resonance at $\omega_{\rm L} = \omega_2 - 35.33$ kHz (small triangles), the fidelity drop occurs at a temperature of the order 10^{-4} K. Such behaviour is seen both when we approach the phonon resonance from above (panel (b))or below (panel (a)), but we remind that above the resonance there is

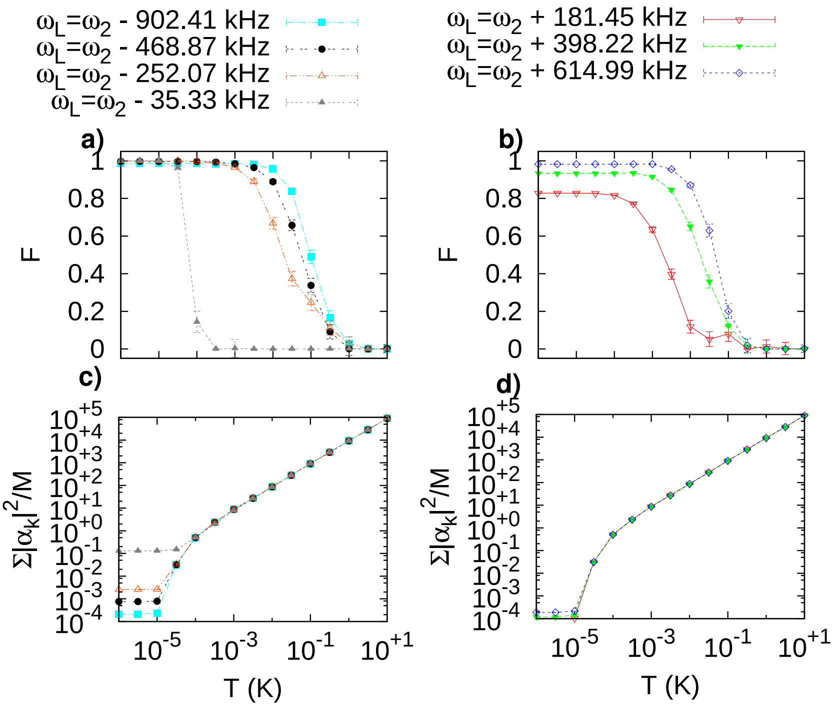

Figure 6.13: We plot the fidelity (a,b) and the square of the phonon coherences (c,d), as a function of the initial phonon temperature, as obtained from the semiclassical calculation for a system of four ions. Different lines correspond to different detunings. Panels (a) and (c) consider cases where the second phonon resonance is approached from below (where the magnetic order is ferromagnetic), while panels (b) and (d) consider cases where the same resonance is approached from above (where a glassy regime occurs near the resonance). In our system, the second resonance occurs at a frequency $\omega_2 = 14332.7$ kHz. All calculations were done for $\tau = 10$ ms. Each point is obtained by sampling over 1,000 runs. The ascribed error is 2σ.

a finite region in which the fidelity is zero even at $T = 0$, cf. the discussion of Fig.(6.11) in Sec. 6.4.6.

Regarding the phonon population, we assume that a reasonable estimate of $\langle \hat{n}_k \rangle$ is given by $|\alpha_k|^2$, as would be the case if the phonon field remains coherent. In Fig. 6.13(c,d), we may distinguish two different regimes: At low temperatures, i.e. for $T \lesssim 10^{-5}$ K, the final phonon population is dominated by those phonons which are produced by the spin-phonon coupling. The number of those phonons is independent from the temperature, and as shown earlier in Fig. 1(b), such phonons are generated also at $T = 0$. The proximity to the resonance induces a larger population of the dominant mode, resulting in a larger value for the population as we approach the resonance. In contrast, for high temperatures, the phonon population is dominated by thermal phonons present already in the beginning of the evolution. In this case, the phonon population is more or less constant during the evolution, and the population number strongly depends on the temperature, according to the initial values from the Boltzmann distribution. As in this case, the time evolution does not noticeably change the phonon distribution, initial and final distribution are very close, and so are initial and final temperature. Between the low- and high- temperature phase, there is a narrow crossover regime, where the number of dynamically generated phonons is similar to the number of thermal phonons. The temperature at which this happens generally depends on the detuning, i.e. on ω_{L}. In all cases, the fidelity drop occurs only in the high-temperature regime, that is, the number of thermal photons must be large compared to the dynamically generated phonons in order to negatively affect the spin evolution.

6.5.3 Thermal tolerance of the Lamb-Dicke regime

The Hamiltonian in Eq. 6.14 describes the trapped ion system when it is in the Lamb-Dicke regime, that is, for $kx \ll 1$. In a harmonic oscillator with frequency ω, we have$\langle x^2 \rangle = \frac{\hbar}{m\omega}\left(\langle n \rangle + \frac{1}{2}\right)$. With $k = \sqrt{2m\omega_{\mathrm{rec}}/\hbar}$, and introducing the Lamb-Dicke parameter $\eta = \sqrt{\omega_{\mathrm{rec}}/\omega}$, we re-write the

Lamb-Dicke condition as

$$\eta\sqrt{2\langle n\rangle+1} \ll 1\,. \tag{6.22}$$

All phonon frequencies ω are of the order of the radial trap frequency, $\omega_{\text{rad}} = 2\pi \times 2,655$ kHz. In our simulation, the recoil frequency is taken as $\omega_{\text{rec}} = 2\pi \times 15$ kHz, so we obtain a Lamb-Dicke parameter $\eta \approx 0.075$. Thus, the Lamb-Dicke regime requires $\sqrt{\langle n\rangle + 0.5} \ll 10$, which is fulfilled by a phonon occupation $\langle n\rangle \lesssim 1$. From that perspective, we have to disregard those calculations where the phonon population exceeds this number. From Fig. 6.13(c,d) we find that, for the Rabi frequency we have used, phonon numbers above 1 occur in the thermally dominated regime, independent from the detuning. This regime is characterized by temperatures $> 10^{-4}$ K.

CHAPTER 7

CONCLUSIONS

In this thesis we have covered a broad set of problems relevant in contemporary quantum many-body physics which can be tackled with exact diagonalisation tools. In this final chapter we present a brief summary and the main conclusions which can be drawn from this thesis following the different chapters.

Chapter 2: Cold bosons in optical lattices: a tutorial for exact diagonalisation

In Chapter 2 we presented in some detail the exact diagonalisation methodology which is common to most of the work presented in the thesis.

We have provided a comprehensive study of Bose-Hubbard models composed of a small number of atoms, $\simeq 10$ populating a small number of sites, $\simeq 10$. First, we have introduced the Bose-Hubbard model together with a detailed description of the exact diagonalization technique employed. Then we have concentrated in the Mott insulator to superfluid transition, first discussing its characterisation by means of exact overlaps with trial wave functions and secondly by performing finite size scaling of the gap.

We have also studied a highly biased lattice, in which one site is considerably deeper than the others. In this case, the system undergoes several transitions, from a fully localized state to a MI phase, going through partial superfluid phases, in which more and more atoms delocalized prior to localizing in the MI. The way the MI phase grows in population has been shown to proceed stepwise as the interaction is increased.

In the attractive interactions case, we have considered a small biased case, to understand the competition between attraction and localization. For sufficiently large attractive interactions, the system fully localizes due to the bias. At lower attractions, the system develops a cat like structure. Prior to this, the system goes through a state in which the number of populated Fock states is maximal.

Chapter 3: Quantum Hall phases of two-component bosons

In Chapter 3 we studied a system composed of two different kind of bosons in a 2D disc geometry subjected to an artificial perpendicular magnetic field. In this framework we discussed the different quantum Hall phases which appear as we vary the strength of the magnetic field. The results obtained from the exact diagonalisation calculations are well understood in terms of the trial wave functions derived in the composite fermion picture.

In particular we are able to identify the integer quantum Hall phase for bosons, which appears at $\nu = 2$, from the structure of the edge states. This phase could be realized in experiments with cold atoms, and detected by measuring pair-correlation functions.

Chapter 4: Topological phases of lattice bosons in a dynamical gauge field

In Chapter 4 we made an incursion into the physics of dynamical gauge fields. In contrast with the previous chapter, where the artificial perpendicular magnetic field was static, in this chapter we consider a model where the gauge field is dynamic.

We have studied topological properties of a bosonic quantum gas with an experimentally feasible, synthetic dynamical gauge field. The different topological phases have been identified by computing the Chern number. The Mott insulating phase provides a trivial vacuum, above which we study the one-particle excitations, forming gapped energy bands. Decreasing the interactions, we first observe transitions in the excited bands, from topologically non-trivial phases to gapless phases. In this respect, the system behaviour does not differ from the one of a system with static magnetic field. A particular feature of the dynamic gauge field is a topological transition in the ground state, in which the sign of the Chern number is inverted. In principle these kind of models could be implemented in ultracold atomic gases experiments. As in our proposal the length of the system in one dimension is very small a way to build it in a experimental set-up would be using synthetic dimensions.

Chapter 5: Modified spin-wave theory and spin liquid behaviour of cold bosons on an inhomogeneous triangular lattice

In this Chapter we have studied the fate of quantum spin liquid phases in realistic experimental conditions, namely, in presence of an harmonic confinement. The modified spin wave theory, originally formulated for bosons in a triangular lattice at half filling, was re-derived for arbitrary filling factors. With this generalization, it can be used to capture, within a local density approximation, the physics of inhomogeneous systems.

We have shown that the prediction of spin liquid behaviour for an anisotropy $t \approx 1.65$ does not depend much on the filling factor, and should therefore survive in a trapped gas. This expectation was backed by results from exact diagonalization in lattices of 24 sites. These results support the existence of another quantum spin liquid region at lower anisotropy, $t \approx 0.6$, which is not detected by modified spin wave. Such discrepancy is not surprising. It is reasonable to expect that the modified spin wave is able to detect a quantum spin liquid phase only between two classical ordered phases while it is blind to transitions that are purely quantum. Our study provides strong hints for a robust spin liquid phase of bosons in anisotropic triangular lattices with antiferromagnetic tunnellings, which is not affected by weak trapping potentials as used in experiments.

The robustness of the spin-liquid phase in presence of a weak harmonic confinement allow for the experimental investigation of these exotic quantum phases. The realization of the XX Hamiltonian for bosons in the strongly correlated regime relies on the periodic driving of the triangular optical lattice, which allows inverting the sign of the tunnelling matrix elements as well as controlling their amplitude. The ability to tune the tunnelling amplitude independently from the on-site interaction allows reaching strongly correlated phases where $U \gg |J_{eff}|$ without increasing the lattice depth. Indeed, as the effective tunnelling J_{eff} follows a 0th order Bessel function as the shaking amplitude is increased, the system shall first enter a Mott-insulating phase before reaching the anti-ferromagnetic side of the phase diagram and thus the quantum spin liquid phase. Such a trajectory has allowed for a reversible crossing of the superfluid to Mott-insulator phase transition in a driven cubic lattice [204]. One limiting factor however are multiphoton resonances to higher lying Bloch bands, which critically reduce the coherence of the bosonic gas [216]. These resonances occur when a multiple of the shaking frequency matches the gap between the renormalized bands. Therefore an optimized scheme for crossing the quantum phase transition while avoiding such resonances has to be developed.

Chapter 6: Quantum annealing for the number partitioning problem using a tunable spin-glass of ions

In Chapter 6 we present a proposal to solve the number partitioning problem by means of a quantum annealer made of a spin-glass of ions. Our work demonstrates the occurrence of Mattis glass behaviour in spin chains of trapped ions, if the detuning of the spin-phonon coupling is chosen between two resonances. In these regimes, the effective spin system has an exponentially large number of low-energy states, and finding its ground state corresponds to solving a number-partitioning problem. This establishes a direct connection between the properties of a physical system and the solution of a potentially NP-hard problem of computer science. Given the state-of-art in experiments with trapped ions, the physical implementation is feasible: In comparison to previous experiments with trapped ions [227–230, 277], only the detuning of the spin-phonon coupling needs to be adjusted. Differently from other approaches to spin glass physics, our scheme does not require any disorder. In its most natural implementation, parity symmetry allows one to analytically determine the ground state. Different ways to break this symmetry can be implemented to increase the complexity of the problem.

We have considered a chain of trapped ions with an internal state ("spin") coupled to vibrational modes via Raman lasers. The couplings are such that the effective model describing the ions is a long range spin model with tunable, pseudo-random couplings, leading to a spin-glass-like phase. The goal of our approach is the adiabatic distillation of the ground state in the glassy phase starting from a completely paramagnetic state. To this aim we consider the addition of a time-dependent transverse magnetic field. Our procedure goes as follows: At the initial time, the magnetic field is strong enough to ensure the ground state of the spins is a ferromagnetic state, with all spins aligned in the transverse direction. As time evolves we slowly, ideally adiabatically, remove the magnetic field such that the final Hamiltonian is our effective long-range spin model in the spin-glass-like phase.

The ion chain then becomes an ideal test ground for applying quantum simulation strategies to solve computationally complex problems. By applying a transverse field to the ions, quantum annealing from a paramagnet to the glassy ground state is possible. The ionic system may be used to benchmark quantum annealing, which has become a subject of very lively and controversial debate since the launch of the D-Wave computers [223, 224]. Exact calculations for small systems ($N = 6$) and approximative calculations for larger system ($N = 22$) demonstrate the feasibility of the proposed quantum annealing, and suggest a polynomial scaling of the annealing time. Accordingly, this approach may offer the sought-after quantum speed-up. In view of sizes of 30 and more ions already trapped in recent experiments (cf. Ref. [303]), a realization of our proposal could not only confirm our semi-classical results, but also go beyond the sizes considered here.

We have simulated our annealing protocol using the exact evolution by means of a Krylov subspace method which is feasible for a small number of ions. In order to consider larger systems as well as to study the effect of temperature on the time evolution we have developed a semiclassical formalism which ignores the quantum correlations between the ions and the phonons. The quality of this method has been benchmarked by comparing its predictions with the exact evolution for four ions. The semiclassical model is found to provide a very accurate qualitative picture of our proposed method, and allows us to correctly identify the parameter region where the annealing protocol works well. By means of the semiclassical model we have thus extended our study to larger number of ions, providing an accurate picture of the ability of the annealing protocol to find the correct ground state depending on the annealing time.

Finally, the semiclassical model has allowed us to study the robustness of the scheme for initial phonon states at finite temperature. We find that the effect of temperature strongly depends on the detuning from a phonon resonance. While in most configurations, the quantum annealing does not break down within the Lamb-Dicke regime, close to a resonance the situation is different. Here, the fidelity of the annealing may drop even before the Lamb-Dicke limit is reached. Thus, while state-of-art spin model simulations which are carried out far off any phonon resonance (e.g. Refs. [282, 290]) require only cooling to the Lamb-Dicke limit, quantum annealing in the interesting glassy regime requires more cooling. Accordingly, our finding motivates the development of new, more efficient cooling techniques, as for instance cooling based on electromagnetically-induced transparency [304–306], which is very well suited to simultaneously achieve low populations in all radial modes.

Outlook

Exact Diagonalization was the central theme of this doctoral thesis. It is a method which, obviously has its limitations –it can only been applied to systems of not too large size. Still, for many problems it is the unique method to give insights into approximate numerical results obtained for large systems. This thesis prove this fact with several important examples.

Exact diagonalizations will be used in QOT at ICFO and in the Quantum Technologies group at UB. For instance, there is a lot of interest in the systems in dynamical latices, in which bonds of the lattices are dynamical. Either possessing phonons or other degree of freedom. This locates ED in a good position, since one has to locate particles on the sites and phonons on the bonds. These models are used to understand fluctuating bond superconductivity or quantum simulators of quantum gauge lattices.

Particularly challenging uses are in the dynamical quantum dynamics. We have initiated this kind of quantum dynamics in Chapter 6. Possible applications of exact diagonalization in quantum dynamics involves few particle systems, small atomtronics devices, quantum simulators of intense light-matter interactions and studies of disordered system and many-body localization.

Appendix A

APPENDIX

A.1 Subroutines for the labelling procedure

Explicit Fortran subroutines to generate the Fock basis labelling as explained in Sect. 2.3.1. First we need to build the Pascal triangle, depending on the total number of sites and particles, this is done with **buildpascal**. Once this is generated, we can use **b2in** and **in2b**, to from the basis to the index or vice versa, respectively.

```
c original from A. V. Ponomarev (2009)
      subroutine buildpascal
c lc=number of sites +1
c nc=number of atoms +1
        parameter (lc=4,nc=3)

       double precision jbc
       integer cnkc(lc,nc)
```

```
       integer jmax
       common/pascal/jmax,cnkc

c builds the rotated pascal triangle
      do i = 1,lc
         cnkc(i,1) = 1
      end do
      do i = 1,lc
         do j = 2,nc
            cnkc(i,j) = 0
         end do
      end do
      do in1 = 2,lc
         cnkc(in1,2) = sum(cnkc(in1-1,1:2))
         if (nc-1.gt.1) then
         do in2 = 1,nc
          cnkc(in1,in2) = sum(cnkc(in1-1,1:in2))
         end do
        end if
      end do
      jmax = cnkc(lc,nc)
       end

c ----------------------------------------------
c Returns the many body state bi at position in
c ----------------------------------------------
c original from A. V. Ponomarev (2009)
      subroutine b2in(bi,in)
      implicit none
      integer in,lc,nc,jmax,ind_L,ind_N,indi,k,is,i
      parameter (lc=4,nc=3)
      integer cnkc(lc,nc),bi(lc),suma,M,in1,in2
      common/pascal/jmax,cnkc
c builds the rotated pascal triangle
```

```
      in=1
      do indi=1,lc-2
        do ind_N=0,bi(indi)

        if (bi(indi)-ind_N.gt.0) then
           suma=0.
            do k=1,indi-1
            suma=suma+bi(k)
            enddo
        if (lc-indi.gt.0.and.nc-ind_N-suma.gt.0) then
            is=0
           in=in+cnkc(lc-indi,nc-ind_N-suma)
        endif
        endif
        enddo
      enddo

      end

c ---------------------------------------------
c Returns the many body state bi at position in
c ---------------------------------------------
c original from A. V. Ponomarev (2009)
      subroutine in2b(in,bi)
      implicit none
      integer in,lc,nc,jmax,ind_L,ind_N,indi
      parameter (lc=4,nc=3)

      integer cnkc(lc,nc),bi(lc)
      common/pascal/jmax,cnkc

         indi = in-1
```

```
            bi = 0
            ind_L = lc-1
            ind_N = nc
            do while(ind_N.ne.1)
               if(indi.ge.cnkc(ind_L,ind_N)) then
                   indi=indi-cnkc(ind_L,ind_N)
                   bi(lc-ind_L)=bi(lc-ind_L)+1
                   ind_N = ind_N-1
               else
                   ind_L = ind_L-1
               end if
            end do
         end
```

A.2 Composite Fermion construction

A quite general feature of quantum Hall wave functions are strong anticorrelations between the particles, introduced by the magnetic fluxes. Formally, such anticorrelations are described by a Jastrow factor,

$$J_m(\{z\}) = \prod_{i<j}(z_i - z_j)^m, \tag{A.1}$$

which prohibits two particles to be at the same position $z = x + iy$. In the composite fermion picture [116], such Jastrow factors are interpreted as flux attachments, that is, J_m makes each particle to be seen by the other particles as a vortex with vorticity m. A system of N particles and N_Φ magnetic fluxes can thus alternatively be seen as a system of N *composite* particles, and $N'_\Phi \equiv N_\Phi - mN$ fluxes. For the exchange symmetry of the composite particles to be fermionic, m has to be odd (even) if the original particles are bosons (fermions). The appeal of the composite fermion picture is based on the fact that the composite particles very often turn out to form integer quantum Hall liquids, that is, their wave functions are simply given by a Slater determinant for a system with N'_Φ fluxes.

The composite fermion construction is often carried out for systems on the surface of a sphere. Such closed geometry offers the advantage that each Landau level has a finite number of states, which defines the notion of "filled" Landau levels. Each level then accounts for a well-defined, finite amount of magnetic flux, and the number of occupied Landau levels is uniquely defined by N'_{Φ}. Accordingly, one can also define a filling factor, $\nu = N/N_{\Phi}$, and in this way conveniently relate the system in the closed geometry to a thermodynamically large system in a plane geometry.

In this paper, we study a *small* system in a *plane* geometry. For a rotationally symmetric system, it then becomes most convenient to introduce the angular momentum L_z (in perpendicular direction to the system in the xy-plane) as a constant of the motion. By assuming that the system spends all angular momentum as relative angular momentum between pairs of particles, L_z (in units of $\hbar$) relates to the number of fluxes as

$$N_{\Phi} = \frac{L_z}{\frac{1}{2}(N-1)}. \tag{A.2}$$

In the thermodynamic limit, this can then be related to the filling factor, ν.

To perform the composite fermion construction, we note that the Jastrow term J_m consumes $\frac{m}{2}N(N-1)$ quanta of angular momentum. Accordingly, a state with quantum number L_z is described by the Jastrow term multiplied with a Slater determinant of total angular momentum $L'_z = L_z - \frac{m}{2}N(N-1)$. It may happen that $L'_z < 0$, a situation in which more fluxes have been attached to the particles than the magnetic field provides. Effectively, the composite particles then feel an opposite magnetic field. Such flux-reversion corresponds to a complex conjugation of the wave function.

For distributing the angular momentum L'_z over N composite fermions, we have to note that the Landau level structure implies that $\ell \geq -n$, where ℓ is the angular momentum, and n is the energy quantum number of the single-particle states. That is, in the lowest Landau level ($n = 0$), we have states with $\ell = 0, 1, 2, \dots$, whereas in higher Landau levels ($n > 0$) also states with negative angular momentum exist. Starting in the lowest

Landau level, we fill each single-particle state from $\ell = 0$ up to $\ell^{(1)}_{\text{max}}$, and similarly for higher levels from $\ell = -n$ to $\ell^{(n)}_{\text{max}}$. Different from the closed geometry, in the plane system there are no *a priori* values for the maximum angular momentum $\ell^{(n)}_{\text{max}}$ in each Landau level. However, changing $\ell^{(n)}_{\text{max}}$ will typically also modify the total angular momentum L'_z of the Slater determinant. Accordingly, specifying the angular momentum will fix this freedom.

We now turn to the two-component case discussed in this paper. In the main text, we have introduced the composite fermion wave functions as

$$\Psi^{[n_a,n_b]}_{L_z} = \mathcal{P}_{\text{LLL}} \left[\Phi_{n_a}(\{z_a\})\ \Phi_{n_b}(\{z_b\}) J(\{z\})\right] , \tag{A.3}$$

for a given L_z, and given numbers N_a and N_b of type-a and type-b particles (or pseudospin). In the Jastrow term $J(\{z\})$, no distinction between a and b particles is made. After the flux attachment, however, the two components should be independent, so we write $\Phi_{n_a}(\{z_a\})$ ($\Phi_{n_b}(\{z_b\})$ for the Slater determinant of the a (b) particles. The indices n_a (n_b) shall determine the number of occupied Landau levels in both Slater determinants, and negative values of n_a (n_b) shall denote the case of reversed flux. While in a closed geometry, this information would already uniquely define the wave function, the plane geometry, as explained above, allows for different ways of distributing N_a (N_b) particles to n_a (n_b) Landau levels. But again, the total angular momentum L_z can be used as an additional label.

Trying to make a connection to the thermodynamic limit and/or the system on the sphere, one associates the wave function $\Psi^{[n_a,n_b]}_{L_z}$ with a filling factor fully defined by the choice of $[n_a, n_b]$. It reads [106]:

$$\nu = \frac{n_a + n_b}{n_a + n_b + 1}. \tag{A.4}$$

There is one possibility for an integer filling factor, and thus an integer quantum Hall phase, at $n_a = n_b = -1$, and $\nu = 2$.

To exemplify the construction on the plane, we have listed in Table A.1 all composite fermion wave functions with $N_a = N_b = 3$. In this table, we give the corresponding angular momentum of the system and the

W.f.	L_z	L'_z	sp states occupied by a particles	sp states occupied by b particles
$\Psi_9^{[-1,-1]}$	9	-6	LLL: $\ell = 0, 1, 2$ (fr)	LLL: $\ell = 0, 1, 2$ (fr)
$\Psi_{12}^{[-2,-1]}$	12	-3	LLL: $\ell = 0, 1$; 1LL: $\ell = -1$ (fr)	LLL: $\ell = 0, 1, 2$ (fr)
$\Psi_{12}^{[-1,-2]}$	12	-3	LLL: $\ell = 0, 1, 2$ (fr)	LLL: $\ell = 0, 1$; 1LL:$\ell = -1$ (fr)
$\Psi_{15}^{[2,2]}$	15	0	LLL: $\ell = 0, 1$; 1LL:$\ell = -1$	LLL: $\ell = 0, 1$; 1LL:$\ell = -1$
$\Psi_{18}^{[2,1]}$	18	3	LLL: $\ell = 0, 1$; 1LL:$\ell = -1$	LLL: $\ell = 0, 1, 2$
$\Psi_{18}^{[1,2]}$	18	3	LLL: $\ell = 0, 1, 2$	LLL: $\ell = 0, 1$; 1LL:$\ell = -1$
$\Psi_{21}^{[1,1]}$	21	6	LLL: $\ell = 0, 1, 2$	LLL: $\ell = 0, 1, 2$

Table A.1: All composite fermion wave functions for $N_a = N_b = 3$ on a disk. sp stands for single-particle and fr for flux reversed.

composite fermions, L_z and L'_z, and we specify which single-particle states enter the construction. The listed wave functions yield all incompressible phases found on the Yrast line shown in Fig. 1 of the main part. While the choice $N_a = N_b$ implies that the z-component of spin S_z is zero, the total spin is given by the multiplicities of the composite fermion wave functions. For $n_a = n_b$, there is a single wave function and thus a singlet, whereas for $n_a \neq n_b$ (at least) two equivalent wave functions related through a spin rotation exist. The composite fermion construction then yields an SU(2) multiplet.

An important part in the definition of Eq. (A.3) is the projection operator $\mathcal{P}_{\text{LLL}}$ which shall bring the expression in the lowest Landau level, that is, the low-energy Hilbert space of the problem. Projecting in the lowest Landau level amounts for getting rid of complex conjugate variables z^*, which naturally occur when the Slater determinants extend to higher Landau levels. While there is no unique way of performing the projection, a natural way [116] is to replace the complex conjugate coordinate z^* by a derivative $\partial/\partial z$, leaving the total angular momentum of the wave function unchanged.

A.3 Evaluation of the Chern number

The twisted boundary conditions are particularly useful to characterize topological phases. They allow one to define Chern numbers in an interacting many-body system [145]. Quite generally, the Chern number is defined for the energy levels n of a Hamiltonian $\mathcal{H}(k_1, k_2) = \mathcal{H}(k_1 + 2\pi, k_2) = \mathcal{H}(k_1, k_2 + 2\pi)$, which periodically depends on two parameters k_1 and k_2 in the following way,

$$c_n = \frac{1}{2\pi\mathrm{i}} \int_0^{2\pi} dk_1 \int_0^{2\pi} dk_2 \; F_{12}^{(n)} \, (k_1, k_2) \tag{A.5}$$

where the Berry connection $\mathcal{A}_\mu^{(n)}(k_1,k_2)$ $(\mu = 1,2)$ and the associated strength $F_{12}^{(n)}(k_1,k_2)$ are given by

$$\mathcal{A}_\mu^{(n)}(k_1,k_2) = \langle n(k_1,k_2)|\, \partial_\mu \,|n(k_1,k_2)\rangle \tag{A.6}$$

$$F_{12}^{(n)}(k_1,k_2) = \partial_1 \mathcal{A}_2^{(n)}(k_1,k_2) - \partial_2 \mathcal{A}_1^{(n)}(k_1,k_2) \tag{A.7}$$

with $|n\,(k_1,k_2)\rangle$ being the n-th normalized eigenvector.

Following the method of Fukui *et al.* [307], the Chern numbers can conveniently be calculated by discretizing the parameter space,

$$\tilde{c}_n = \frac{1}{2\pi \mathrm{i}} \sum_{k_1} \sum_{k_2} \tilde{F}_{12}^{(n)}\,(k_1,k_2) \tag{A.8}$$

with the lattice field strength,

$$\begin{aligned} &\tilde{F}_{12}^{(n)}\,(k_1,k_2) = \ln\left[\frac{U_1^{(n)}(k_1,k_2)\,U_2^{(n)}(k_1+dk_1,k_2)}{U_1^{(n)}(k_1,k_2+dk_2)\,U_2^{(n)}(k_1,k_2)}\right], \\ &-\pi < \frac{1}{\mathrm{i}}\tilde{F}_{12}^{(n)}\,(k_1,k_2) \leq \pi \end{aligned} \tag{A.9}$$

being dk_μ the resolution of each parameter and $U_\mu^{(n)}$ the link variables from the eigenstates of the nth band,

$$U_\mu^{(n)} \equiv \frac{\big\langle n(k_1,k_2)\big|n(k_1+dk_1\delta_{1,\mu},k_2+dk_2\delta_{2,\mu})\big\rangle}{\big|\big\langle n(k_1,k_2)\big|n(k_1+dk_1\delta_{1,\mu},k_2+dk_2\delta_{2,\mu})\big\rangle\big|}\,. \tag{A.10}$$

A special case which is important for our purposes concerns the Chern number of degenerate bands. Since the eigenstates are not unique in the degenerate points, we cannot associate Chern numbers to individual states. For M degenerate or quasi-degenerate states, we consider the multiplet $\psi = (|n_1\rangle \cdots |n_M\rangle)$ to define a non-Abelian Berry connection $\mathcal{A} = \psi^\dagger d\psi$, which is an $M \times M$ matrix-valued one form associated to ψ. Then, we consider the overlap matrix

$$\left[u_\mu^{(n)}\right]_{ij} \equiv \big\langle n_i(k_1,k_2)\big|n_j(k_1+dk_1\delta_{1,\mu},k_2+dk_2\delta_{2,\mu})\big\rangle\,, \tag{A.11}$$

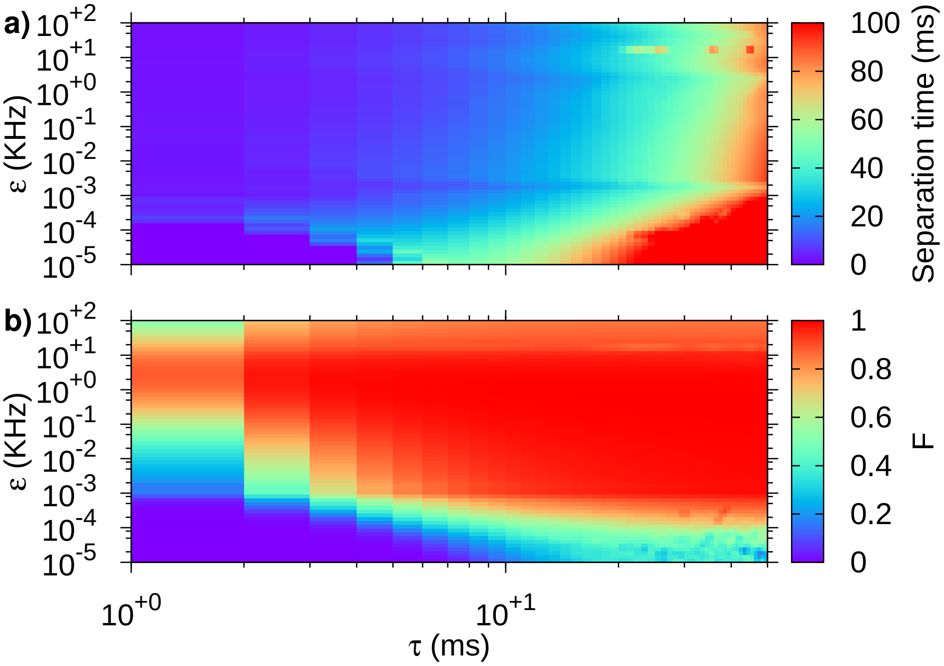

Figure A.1: Separation time (a)) and Fidelity (b)) of systems with 6 spins for several values of ε and τ, with initial populations of phononic modes set to 0. Waiting time is fixed to 20τ and $\omega_L = \omega_{\mathrm{N}} - 1500$ kHz.

in order to properly define the link variables

$$U_\mu^{(n)} \equiv \frac{\det\left[u_\mu^{(n)}\right]}{\left|\det\left[u_\mu^{(n)}\right]\right|} \tag{A.12}$$

Finally, the Chern number $\tilde{c}_\psi$ and field strength are calculated using Eqs. (A.8) and (A.9).

A.4 Robustness of the semiclassical calculation

One can test the quality of the integration method by checking whether the constants of motion are conserved. In time-independent systems, the total energy of the system is usually the conserved quantity which can be computed most easily. Unfortunately, since the Hamiltonian in Eq. 6.14 does not commute with itself at different times due to the transverse magnetic field in the annealing term, the total energy of the system is not conserved. Furthermore, it is challenging to find an analytical expression for an alternative conserved quantity given the infinitely non-commutativity of the Pauli matrices algebra. We have tested the integration method checking its time reversibility. The latter test has given relative differences below 10^-7, which is within the range of the computation precision.

A.5 Optimal bias for the exponential annealing function

Although the only function of the bias potential ϵ is to break $\mathscr{Z}_2$ symmetry in the target Hamiltonian, it turns out that the value and position of the bias have a non-negligible effect on the outcome of the annealing process. Here, we investigate which values of the bias ϵ and the annealing parameter τ minimize the separation time. As seen in Fig. A.1 a), the separation time is minimized for smaller values of τ, at any value of the bias larger than Hz. However, small τ are known to affect negatively the fidelity. As we see from Fig. A.1 b), there is, even for decay times as short as a few ms, a range of bias potentials (roughly between 1 kHz and 10 kHz), where the fidelity gets large. Thus, this range defines the optimal choice for ϵ, which we have also used in our calculations.

We also note that the magnitude of the bias provides a bound for the maximum absolute value of $\langle \sigma_x \rangle$, that is, the spin expectation on the biased site at the end of the annealing depends on the strength of the bias potential. For a weak bias, this spin will deviate only weakly from zero, limiting the overall fidelity.

Bibliography

[1] S.-J. Ran, B. Xi, C. Peng, G. Su, and M. Lewenstein, *Quantum simulation for thermodynamics of infinite-size many-body systems by O(10) sites*, Oct. 2018, arXiv:`1810.01612 [cond-mat, str-el]`.

[2] M. Lewenstein, A. Sanpera, and V. Ahufinger, *Ultracold atoms in optical lattices: simulating quantum many-body systems* (Oxford University Press, 2012).

[3] R. Feynman, “Simulating physics with computers”, Int. J. Theo. Phys. **21**, 467 (1982).

[4] D. Jaksch, C. Bruder, J. I. Cirac, C. W. Gardiner, and P. Zoller, “Cold bosonic atoms in optical lattices”, Phys. Rev. Lett. **81**, 3108–3111 (1998).

[5] M. Greiner, O. Mandel, T. Esslinger, T. W. Hänsch, and I. Bloch, “Quantum phase transition from a superfluid to a Mott insulator in a gas of ultracold atoms”, Nature **415**, 39 (2012).

[6] A. Acín, I. Bloch, H. Buhrman, T. Calarco, C. Eichler, J. Eisert, D. Esteve, N. Gisin, S. J. Glaser, F. Jelezko, S. Kuhr, M. Lewenstein, M. F. Riedel, P. O. Schmidt, R. Thew, A. Wallraff, I. Walmsley, and F. K. Wilhelm, “The quantum technologies roadmap: a european community view”, New J. Phys. **20**, 080201 (2018).

[7] J. I. Cirac and P. Zoller, “Goals and opportunities in quantum simulation”, Nat. Phys. **8**, 264–266 (2012).

[8] I. Bloch, J. Dalibard, and S. Nascimbène, “Quantum simulations with ultracold quantum gases”, Nat. Phys. **8**, 267–276 (2012).

[9] R. Blatt and C. F. Roos, “Quantum simulations with trapped ions”, Nat. Phys. **8**, 277–284 (2012).

[10] A. Aspuru-Guzik and P. Walther, “Photonic quantum simulators”, Nat. Phys. **8**, 285–291 (2012).

[11] A. A. Houck, H. E. Türeci, and J. Koch, “On-chip quantum simulation with superconducting circuits”, Nat. Phys. **8**, 292–299 (2012).

[12] N. Navon, S. Nascimbène, F. Chevy, and C. Salomon, "The equation of state of a low-temperature Fermi gas with tunable interactions", Science **328**, 729–732 (2010).

[13] M. J. H. Ku, A. T. Sommer, L. W. Cheuk, and M. W. Zwierlein, "Revealing the superfluid lambda transition in the universal thermodynamics of a unitary Fermi gas", Science **335**, 563–567 (2012).

[14] W. S. Bakr, J. I. Gillen, A. Peng, S. Fölling, and M. Greiner, "A quantum gas microscope for detecting single atoms in a Hubbard-regime optical lattice", Nature **462**, 74 (2009).

[15] J. F. Sherson, C. Weitenberg, M. Endres, M. Cheneau, I. Bloch, and S. Kuhr, "Single-atom-resolved fluorescence imaging of an atomic Mott insulator", Nature **467**, 68 (2010).

[16] H. Bernien, S. Schwartz, A. Keesling, H. Levine, A. Omran, H. Pichler, S. Choi, A. S. Zibrov, M. Endres, M. Greiner, V. Vuletić, and M. D. Lukin, "Probing many-body dynamics on a 51-atom quantum simulator", Nature **551**, 579–584 (2017).

[17] J. Zhang, G. Pagano, P. W. Hess, A. Kyprianidis, P. Becker, H. Kaplan, A. V. Gorshkov, Z.-X. Gong, and C. Monroe, "Observation of a many-body dynamical phase transition with a 53-qubit quantum simulator", Nature **551**, 601–604 (2017).

[18] Y. Tsuchimoto, P. Knüppel, A. Delteil, Z. Sun, M. Kroner, and A. Imamoğlu, "Proposal for a quantum interface between photonic and superconducting qubits", Phys. Rev. B **96**, 165312 (2017).

[19] M. W. Doherty, N. B. Manson, P. Delaney, F. Jelezko, J. Wrachtrup, and L. C. Hollenberg, "The nitrogen-vacancy colour centre in diamond", Phys. Rep. **528**, 1–45 (2013).

[20] *D-wave systems inc.* `https://www.dwavesys.com/home`, 2018, [Online; accessed 13-September-2018].

[21] A. Amo, J. Lefrère, S. Pigeon, C. Adrados, C. Ciuti, I. Carusotto, R. Houdré, E. Giacobino, and A. Bramati, "Superfluidity of polaritons in semiconductor microcavities", Nat. Phys. **5**, 805–810 (2009).

[22] H. Deng, H. Haug, and Y. Yamamoto, "Exciton-polariton Bose-Einstein condensation", Rev. Mod. Phys. **82**, 1489–1537 (2010).

[23] M. C. Rechtsman, J. M. Zeuner, Y. Plotnik, Y. Lumer, D. Podolsky, F. Dreisow, S. Nolte, M. Segev, and A. Szameit, "Photonic Floquet topological insulators", Nature **496**, 196–200 (2016).

[24] A. Mazurenko, C. S. Chiu, G. Ji, M. F. Parsons, M. Kanász-Nagy, R. Schmidt, F. Grusdt, E. Demler, D. Greif, and M. Greiner, "A cold-atom Fermi–Hubbard antiferromagnet", Nature **545**, 462–466 (2017).

[25] M. Schreiber, S. S. Hodgman, P. Bordia, H. P. Lüschen, M. H. Fischer, R. Vosk, E. Altman, U. Schneider, and I. Bloch, "Observation of many-body localization of interacting fermions in a quasirandom optical lattice", Science **349**, 842–845 (2015).

[26] C. R. Cabrera, L. Tanzi, J. Sanz, B. Naylor, P. Thomas, P. Cheiney, and L. Tarruell, "Quantum liquid droplets in a mixture of Bose-Einstein condensates", Science **359**, 301–304 (2018).

[27] C. Kokail, C. Maier, R. van Bijnen, T. Brydges, M. K. Joshi, P. Jurcevic, C. A. Muschik, P. Silvi, R. Blatt, C. F. Roos, and P. Zoller, *Self-verifying variational quantum simulation of the lattice Schwinger model*, Oct. 2018, arXiv:`1810.03421 [quant-ph]`.

[28] E. A. Martinez, C. A. Muschik, P. Schindler, D. Nigg, A. Erhard, M. Heyl, P. Hauke, M. Dalmonte, T. Monz, P. Zoller, and R. Blatt, "Real-time dynamics of lattice gauge theories with a few-qubit quantum computer", Nature **534**, 516–518 (2016).

[29] A. Osterloh, L. Amico, G. Falci, and R. Fazio, "Scaling of entanglement close to a quantum phase transition", Nature **416**, 608–610 (2002).

[30] L. Amico, R. Fazio, A. Osterloh, and V. Vedral, "Entanglement in many-body systems", Rev. Mod. Phys. **80**, 517–576 (2008).

[31] J. D. Bekenstein, "Black holes and the second law", Lett. Nuovo Cimento **4**, 737–740 (1972).

[32] J. D. Bekenstein, “Black holes and entropy”, Phys. Rev. D **7**, 2333–2346 (1973).

[33] J. D. Bekenstein, “Generalized second law of thermodynamics in black-hole physics”, Phys. Rev. D **9**, 3292–3300 (1974).

[34] M. Srednicki, “Entropy and area”, Phys. Rev. Lett. **71**, 666–669 (1993).

[35] J. Eisert, M. Cramer, and M. B. Plenio, “Colloquium: area laws for the entanglement entropy”, Rev. Mod. Phys. **82**, 277–306 (2010).

[36] S. Rachel, M. Haque, A. Bernevig, A. Laeuchli, and E. Fradkin, eds. (2014–2015): *Special issue: quantum entanglement in condensed matter physics.*

[37] P. Calabrese and J. Cardy, “Entanglement entropy and quantum field theory”, J. Stat. Mech. Theory Exp. **2004**, P06002 (2004).

[38] P. Calabrese, J. Cardy, and B. Doyon, “Entanglement entropy in extended quantum systems”, J. Phys. A **42**, 500301 (2009).

[39] J. Tura, R. Augusiak, A. B. Sainz, T. Vértesi, M. Lewenstein, and A. Acín, “Detecting nonlocality in many-body quantum states”, Science **344**, 1256–1258 (2014).

[40] D. Greif, M. F. Parsons, A. Mazurenko, C. S. Chiu, S. Blatt, F. Huber, G. Ji, and M. Greiner, “Site-resolved imaging of a fermionic Mott insulator”, Science **351**, 953–957 (2016).

[41] S. Trotzky, L. Pollet, F. Gerbier, U. Schnorrberger, I. Bloch, N. V. Prokof’ev, B. Svistunov, and M. Troyer, “Suppression of the critical temperature for superfluidity near the Mott transition”, Nat. Phys. **6**, 998–1004 (2010).

[42] M. Navascués, S. Pironio, and A. Acín, “A convergent hierarchy of semidefinite programs characterizing the set of quantum correlations”, New J. Phys. **10**, 073013 (2008).

[43] S. Pironio, M. Navascués, and A. Acín, “Convergent relaxations of polynomial optimization problems with noncommuting variables”, SIAM J. Optim. **20**, 2157–2180 (2010).

[44] T. Baumgratz and M. B. Plenio, “Lower bounds for ground states of condensed matter systems”, New J. Phys. **14**, 023027 (2012).

[45] P. Hauke, F. M. Cucchietti, L. Tagliacozzo, I. Deutsch, and M. Lewenstein, “Can one trust quantum simulators?”, Rep. Prog. Phys. **75**, 082401 (2012).

[46] C. Moura Alves and D. Jaksch, “Multipartite entanglement detection in bosons”, Phys. Rev. Lett. **93**, 110501 (2004).

[47] R. Islam, R. Ma, P. M. Preiss, M. Eric Tai, A. Lukin, M. Rispoli, and M. Greiner, “Measuring entanglement entropy in a quantum many-body system”, Nature **528**, 77–83 (2015).

[48] A. Elben, B. Vermersch, M. Dalmonte, J. I. Cirac, and P. Zoller, “Rényi entropies from random quenches in atomic Hubbard and spin models”, Phys. Rev. Lett. **120**, 050406 (2018).

[49] B. Vermersch, A. Elben, M. Dalmonte, J. I. Cirac, and P. Zoller, “Unitary n-designs via random quenches in atomic Hubbard and spin models: Application to the measurement of Rényi entropies”, Phys. Rev. A **97**, 023604 (2018).

[50] A. Lukin, M. Rispoli, R. Schittko, M. E. Tai, A. M. Kaufman, S. Choi, V. Khemani, J. Léonard, and M. Greiner, *Probing entanglement in a many-body-localized system*, May 2018, arXiv:`1805.09819 [cond-mat, quant-gas]`.

[51] A. Acín, N. Brunner, N. Gisin, S. Massar, S. Pironio, and V. Scarani, “Device-independent security of quantum cryptography against collective attacks”, Phys. Rev. Lett. **98**, 230501 (2007).

[52] F. Baccari, D. Cavalcanti, P. Wittek, and A. Acín, “Efficient device-independent entanglement detection for multipartite systems”, Phys. Rev. X **7**, 021042 (2017).

[53] J. Tura, R. Augusiak, A. Sainz, B. Lücke, C. Klempt, M. Lewenstein, and A. Acín, “Nonlocality in many-body quantum systems detected with two-body correlators”, Ann. Phys. (N. Y.) **362**, 370–423 (2015).

[54] J. Tura, G. De las Cuevas, R. Augusiak, M. Lewenstein, A. Acín, and J. I. Cirac, “Energy as a detector of nonlocality of many-body spin systems”, Phys. Rev. X **7**, 021005 (2017).

[55] F. Baccari, J. Tura, M. Fadel, A. Aloy, J.-D. Bancal, N. Sangouard, M. Lewenstein, A. Acín, and R. Augusiak, *Bell correlations depth in many-body systems*, Feb. 2018, arXiv:`1802.09516 [quant-ph]`.

[56] A. Aloy, J. Tura, F. Baccari, A. Acín, M. Lewenstein, and R. Augusiak, *Device-independent witnesses of entanglement depth from two-body correlators*, July 2018, arXiv:`1807.06027 [quant-ph]`.

[57] D. Raventós, T. Graß, M. Lewenstein, and B. Juliá-Díaz, “Cold bosons in optical lattices: a tutorial for exact diagonalization”, J. Phys. B **50**, 113001 (2017).

[58] T. Graß, D. Raventós, M. Lewenstein, and B. Juliá-Díaz, “Quantum Hall phases of two-component bosons”, Phys. Rev. B **89**, 045114 (2014).

[59] D. Raventós, T. Graß, B. Juliá-Díaz, L. Santos, and M. Lewenstein, “Topological phases of lattice bosons with a dynamical gauge field”, Phys. Rev. A **93**, 033605 (2016).

[60] A. Celi, T. Graß, A. J. Ferris, B. Padhi, D. Raventós, J. Simonet, K. Sengstock, and M. Lewenstein, “Modified spin-wave theory and spin-liquid behavior of cold bosons on an inhomogeneous triangular lattice”, Phys. Rev. B **94**, 075110 (2016).

[61] T. Graß, D. Raventós, B. Juliá-Díaz, C. Gogolin, and M. Lewenstein, “Quantum annealing for the number-partitioning problem using a tunable spin glass of ions”, Nat. Commun. **7**, 11524 (2016).

[62] D. Raventós, T. Graß, B. Juliá-Díaz, and M. Lewenstein, “Semiclassical approach to finite-temperature quantum annealing with trapped ions”, Phys. Rev. A **97**, 052310 (2018).

[63] M. P. A. Fisher, P. B. Weichman, G. Grinstein, and D. S. Fisher, “Boson localization and the superfluid-insulator transition”, Phys. Rev. B **40**, 546–570 (1989).

[64] P. Buonsante and A. Vezzani, “Ground-state bidelity and bipartite entanglement in the Bose-Hubbard model”, Phys. Rev. Lett. **98**, 110601 (2007).

[65] D. van Oosten, P. van der Straten, and H. T. C. Stoof, “Quantum phases in an optical lattice”, Phys. Rev. A **63**, 053601 (2001).

[66] M. P. Gelfand, R. R. P. Singh, and D. A. Huse, “Perturbation expansions for quantum many-body systems”, J. Stat. Phys. **59**, 1093–1142 (1990).

[67] J. K. Freericks and H. Monien, “Strong-coupling expansions for the pure and disordered Bose-Hubbard model”, Phys. Rev. B **53**, 2691–2700 (1996).

[68] D. S. Rokhsar and B. G. Kotliar, “Gutzwiller projection for bosons”, Phys. Rev. B **44**, 10328–10332 (1991).

[69] F. E. A. dos Santos and A. Pelster, “Quantum phase diagram of bosons in optical lattices”, Phys. Rev. A **79**, 013614 (2009).

[70] N. Teichmann, D. Hinrichs, M. Holthaus, and A. Eckardt, “Process-chain approach to the Bose-Hubbard model: Ground-state properties and phase diagram”, Phys. Rev. B **79**, 224515 (2009).

[71] T. D. Graß, F. E. A. dos Santos, and A. Pelster, “Excitation spectra of bosons in optical lattices from the Schwinger-Keldysh calculation”, Phys. Rev. A **84**, 013613 (2011).

[72] U. Schollwöck, “The density-matrix renormalization group”, Rev. Mod. Phys. **77**, 259–315 (2005).

[73] J. Carrasquilla, S. R. Manmana, and M. Rigol, “Scaling of the gap, fidelity susceptibility, and Bloch oscillations across the superfluid-to-Mott-insulator transition in the one-dimensional Bose-Hubbard model”, Phys. Rev. A **87**, 043606 (2013).

[74] N. Prokof’ev, B. Svistunov, and I. Tupitsyn, “‘Worm’ algorithm in quantum monte carlo simulations”, Phys. Lett. A **238**, 253–257 (1998).

[75] M. A. Cazalilla, R. Citro, T. Giamarchi, E. Orignac, and M. Rigol, "One dimensional bosons: from condensed matter systems to ultracold gases", Rev. Mod. Phys. **83**, 1405–1466 (2011).

[76] G. G. Batrouni, R. T. Scalettar, and G. T. Zimanyi, "Quantum critical phenomena in one-dimensional Bose systems", Phys. Rev. Lett. **65**, 1765–1768 (1990).

[77] G. G. Batrouni and R. T. Scalettar, "World-line quantum Monte Carlo algorithm for a one-dimensional Bose model", Phys. Rev. B **46**, 9051–9062 (1992).

[78] V. A. Kashurnikov, A. V. Krasavin, and B. V. Svistunov, "Mott-insulator-superfluid-liquid transition in a one-dimensional bosonic Hubbard model: Quantum Monte Carlo method", J. Exp. Theor. Phys. **64**, 99–104 (1996).

[79] J. I. Cirac, M. Lewenstein, K. Mølmer, and P. Zoller, "Quantum superposition states of Bose-Einstein condensates", Phys. Rev. A **57**, 1208–1218 (1998).

[80] B. Juliá-Díaz, D. Dagnino, M. Lewenstein, J. Martorell, and A. Polls, "Macroscopic self-trapping in Bose-Einstein condensates: Analysis of a dynamical quantum phase transition", Phys. Rev. A **81**, 023615 (2010).

[81] J. M. Zhang and R. X. Dong, "Exact diagonalization: the Bose–Hubbard model as an example", Eur. J. Phys. **31**, 591 (2010).

[82] O. Penrose and L. Onsager, "Bose-Einstein condensation and liquid helium", Phys. Rev. **104**, 576–584 (1956).

[83] O. Penrose, "On the quantum mechanics of helium II", Lond. Edinb. Dubl. Phil. Mag. **42**, 1373–1377 (1951).

[84] E. J. Mueller, T.-L. Ho, M. Ueda, and G. Baym, "Fragmentation of Bose-Einstein condensates", Phys. Rev. A **74**, 033612 (2006).

[85] Z. Bai, J. Demmel, J. Dongarra, A. Ruhe, and H. van der Vorst, *Templates for the solution of algebraic eigenvalue problems*, edited by Z. Bai, J. Demmel, J. Dongarra, A. Ruhe, and H. van der Vorst (Society for Industrial and Applied Mathematics, 2000).

[86] A. V. Ponomarev, private communication, 2009, The method has been used in [308], [309] and [310].

[87] R. Lehoucq, D. Sorensen, and C. Yang, *Arpack users' guide* (Society for Industrial and Applied Mathematics, 1998).

[88] A. M. Rey, "Ultracold bosonic atoms in optical lattices", PhD thesis (University of Maryland, 2004).

[89] M. Campostrini and E. Vicari, "Trap-size scaling in confined-particle systems at quantum transitions", Phys. Rev. A **81**, 023606 (2010).

[90] T. Mishra, J. Carrasquilla, and M. Rigol, "Phase diagram of the half-filled one-dimensional $t-V-V^{'}$ model", Phys. Rev. B **84**, 115135 (2011).

[91] F. K. Abdullaev and J. Garnier, "Bright solitons in Bose-Einstein condensates: Theory", in *Emergent nonlinear phenomena in Bose-Einstein condensates: Theory and experiment*, edited by P. G. Kevrekidis, D. J. Frantzeskakis, and R. Carretero-González (Springer Berlin Heidelberg, Berlin, Heidelberg, 2008), pp. 25–43.

[92] J. P. Gordon, "Interaction forces among solitons in optical fibers", Opt. Lett. **8**, 596–598 (1983).

[93] N. Cooper, "Rapidly rotating atomic gases", Adv. Phys. **57**, 539–616 (2008).

[94] K. v. Klitzing, G. Dorda, and M. Pepper, "New method for high-accuracy determination of the fine-structure constant based on quantized Hall resistance", Phys. Rev. Lett. **45**, 494–497 (1980).

[95] V. J. Goldman and B. Su, "Resonant tunneling in the quantum Hall regime: Measurement of fractional charge", Science **267**, 1010–1012 (1995).

[96] R. B. Laughlin, "Anomalous quantum Hall effect: An incompressible quantum fluid with fractionally charged excitations", Phys. Rev. Lett. **50**, 1395–1398 (1983).

[97] X.-G. Wen, "Topological orders and edge excitations in fractional quantum Hall states", Adv. Phys. **44**, 405–473 (1995).

[98] J. Froehlich, U. M. Studer, and E. Thiran, *Quantum Theory of Large Systems of Non-Relativistic Matter*, July 1995, arXiv:`cond-mat/9508062`.

[99] K. W. Madison, F. Chevy, W. Wohlleben, and J. Dalibard, "Vortex formation in a stirred Bose-Einstein condensate", Phys. Rev. Lett. **84**, 806–809 (2000).

[100] J. Dalibard, F. Gerbier, G. Juzeliū, and P. Öhberg, "Colloquium: artificial gauge potentials for neutral atoms", Rev. Mod. Phys. **83**, 1523–1543 (2011).

[101] N. Goldman, G. Juzeliūnas, P. Öhberg, and I. B. Spielman, "Light-induced gauge fields for ultracold atoms", Rep. Prog. Phys. **77**, 126401 (2014).

[102] I. Carusotto and C. Ciuti, "Quantum fluids of light", Rev. Mod. Phys. **85**, 299–366 (2013).

[103] Y.-M. Lu and A. Vishwanath, "Theory and classification of interacting integer topological phases in two dimensions: A Chern-Simons approach", Phys. Rev. B **86**, 125119 (2012).

[104] T. Senthil and M. Levin, "Integer quantum Hall effect for bosons", Phys. Rev. Lett. **110**, 046801 (2013).

[105] S. Furukawa and M. Ueda, "Integer quantum Hall state in two-component Bose gases in a synthetic magnetic field", Phys. Rev. Lett. **111**, 090401 (2013).

[106] Y.-H. Wu and J. K. Jain, "Quantum Hall effect of two-component bosons at fractional and integral fillings", Phys. Rev. B **87**, 245123 (2013).

[107] N. Regnault and T. Senthil, "Microscopic model for the boson integer quantum Hall effect", Phys. Rev. B **88**, 161106 (2013).

[108] X.-G. Wen, “Theory of the edge states in fractional quantum HALL effects”, Int. J. Mod. Phys. B **06**, 1711–1762 (1992).

[109] A. Balatsky and M. Stone, “Vertex operators and spinon edge excitations in the spin-singlet quantum Hall effect”, Phys. Rev. B **43**, 8038–8043 (1991).

[110] J. E. Moore and F. D. M. Haldane, “Edge excitations of the $\nu = 2/3$ spin-singlet quantum Hall state”, Phys. Rev. B **55**, 7818–7823 (1997).

[111] Y.-H. Wu, G. J. Sreejith, and J. K. Jain, “Microscopic study of edge excitations of spin-polarized and spin-unpolarized $\nu = 2/3$ fractional quantum Hall effect”, Phys. Rev. B **86**, 115127 (2012).

[112] T. Graß, B. Juliá-Díaz, N. Barberán, and M. Lewenstein, “Non-abelian spin-singlet states of two-component Bose gases in artificial gauge fields”, Phys. Rev. A **86**, 021603 (2012).

[113] S. Furukawa and M. Ueda, “Quantum Hall states in rapidly rotating two-component Bose gases”, Phys. Rev. A **86**, 031604 (2012).

[114] E. Ardonne and K. Schoutens, “New class of non-abelian spin-singlet quantum Hall states”, Phys. Rev. Lett. **82**, 5096–5099 (1999).

[115] C. Nayak, S. H. Simon, A. Stern, M. Freedman, and S. Das Sarma, “Non-abelian anyons and topological quantum computation”, Rev. Mod. Phys. **80**, 1083–1159 (2008).

[116] J. K. Jain, *Composite fermions* (Cambridge University Press, 2007).

[117] N. R. Cooper and N. K. Wilkin, “Composite fermion description of rotating Bose-Einstein condensates”, Phys. Rev. B **60**, R16279–R16282 (1999).

[118] B. I. Halperin, “Strongly correlated states of a small cold-atom cloud from geometric gauge fields”, Helv. Phys. Acta **56**, 75 (1983).

[119] B. Juliá-Díaz, D. Dagnino, K. J. Günter, T. Graß, N. Barberán, M. Lewenstein, and J. Dalibard, “Strongly correlated states of a small cold-atom cloud from geometric gauge fields”, Phys. Rev. A **84**, 053605 (2011).

[120] D. Jaksch, H.-J. Briegel, J. I. Cirac, C. W. Gardiner, and P. Zoller, “Entanglement of atoms via cold controlled collisions”, Phys. Rev. Lett. **82**, 1975–1978 (1999).

[121] O. Mandel, M. Greiner, A. Widera, T. Rom, T. W. Hänsch, and I. Bloch, “Controlled collisions for multi-particle entanglement of optically trapped atoms”, Nature **425**, 937 (2003).

[122] O. Mandel, M. Greiner, A. Widera, T. Rom, T. W. Hänsch, and I. Bloch, “Coherent transport of neutral atoms in spin-dependent optical lattice potentials”, Phys. Rev. Lett. **91**, 010407 (2003).

[123] M. Genske, W. Alt, A. Steffen, A. H. Werner, R. F. Werner, D. Meschede, and A. Alberti, “Electric quantum walks with individual atoms”, Phys. Rev. Lett. **110**, 190601 (2013).

[124] E. Zohar, J. I. Cirac, and B. Reznik, “Simulating compact quantum electrodynamics with ultracold atoms: probing confinement and nonperturbative effects”, Phys. Rev. Lett. **109**, 125302 (2012).

[125] L. Tagliacozzo, A. Celi, A. Zamora, and M. Lewenstein, “Optical abelian lattice gauge theories”, Ann. Phys. (N. Y.) **330**, 160–191 (2013).

[126] D. Banerjee, M. Bögli, M. Dalmonte, E. Rico, P. Stebler, U.-J. Wiese, and P. Zoller, “Atomic quantum simulation of $\mathbf{U}(N)$ and $\mathbf{SU}(N)$ non-abelian lattice gauge theories”, Phys. Rev. Lett. **110**, 125303 (2013).

[127] E. Zohar, J. I. Cirac, and B. Reznik, “Cold-atom quantum simulator for $\mathbf{SU}(2)$ Yang-Mills lattice gauge theory”, Phys. Rev. Lett. **110**, 125304 (2013).

[128] L. Tagliacozzo, A. Celi, P. Orland, M. W. Mitchell, and M. Lewenstein, “Simulation of non-abelian gauge theories with optical lattices”, Nat. Commun. **4**, 2615 (2013).

[129] S. Chang, “The neutron and proton weigh in, theoretically”, Phys. Today **68**, 17–18 (2015).

[130] J. Struck, M. Weinberg, C. Ölschläger, P. Windpassinger, J. Simonet, K. Sengstock, R. Höppner, P. Hauke, A. Eckardt, M. Lewenstein, and L. Mathey, "Engineering Ising-XY spin-models in a triangular lattice using tunable artificial gauge fields", Nat. Phys. **9**, 738 (2013).

[131] M. Aidelsburger, M. Lohse, C. Schweizer, M. Atala, J. T. Barreiro, S. Nascimbène, N. R. Cooper, I. Bloch, and N. Goldman, "Measuring the Chern number of Hofstadter bands with ultracold bosonic atoms", Nat. Phys. **11**, 162 (2014).

[132] M. Mancini, G. Pagano, G. Cappellini, L. Livi, M. Rider, J. Catani, C. Sias, P. Zoller, M. Inguscio, M. Dalmonte, and L. Fallani, "Observation of chiral edge states with neutral fermions in synthetic Hall ribbons", Science **349**, 1510–1513 (2015).

[133] B. K. Stuhl, H.-I. Lu, L. M. Aycock, D. Genkina, and I. B. Spielman, "Visualizing edge states with an atomic Bose gas in the quantum Hall regime", Science **349**, 1514–1518 (2015).

[134] M. J. Edmonds, M. Valiente, G. Juzeliūnas, L. Santos, and P. Öhberg, "Simulating an interacting gauge theory with ultracold Bose gases", Phys. Rev. Lett. **110**, 085301 (2013).

[135] S. Greschner, G. Sun, D. Poletti, and L. Santos, "Density-dependent synthetic gauge fields using periodically modulated interactions", Phys. Rev. Lett. **113**, 215303 (2014).

[136] T. Keilmann, S. Lanzmich, I. McCulloch, and M. Roncaglia, "Statistically induced phase transitions and anyons in 1D optical lattices", Nat. Commun. **2**, 361 (2011).

[137] O. Dutta, A. Przysiężna, and J. Zakrzewski, "Spontaneous magnetization and anomalous Hall effect in an emergent dice lattice", Sci. Rep. **5**, 11060 (2015).

[138] S. Greschner and L. Santos, "Anyon Hubbard model in one-dimensional optical lattices", Phys. Rev. Lett. **115**, 053002 (2015).

[139] S. Greschner, D. Huerga, G. Sun, D. Poletti, and L. Santos, “Density-dependent synthetic magnetism for ultracold atoms in optical lattices”, Phys. Rev. B **92**, 115120 (2015).

[140] A. Przysiężna, O. Dutta, and J. Zakrzewski, “Rice–Mele model with topological solitons in an optical lattice”, New J. Phys. **17**, 013018 (2015).

[141] A. Bermudez and D. Porras, “Interaction-dependent photon-assisted tunneling in optical lattices: a quantum simulator of strongly-correlated electrons and dynamical gauge fields”, New J. Phys. **17**, 103021 (2015).

[142] D. R. Hofstadter, “Energy levels and wave functions of bloch electrons in rational and irrational magnetic fields”, Phys. Rev. B **14**, 2239–2249 (1976).

[143] D. Jaksch and P. Zoller, “Creation of effective magnetic fields in optical lattices: the Hofstadter butterfly for cold neutral atoms”, New J. Phys. **5**, 56 (2003).

[144] D. J. Thouless, M. Kohmoto, M. P. Nightingale, and M. den Nijs, “Quantized Hall conductance in a two-dimensional periodic potential”, Phys. Rev. Lett. **49**, 405–408 (1982).

[145] Q. Niu, D. J. Thouless, and Y.-S. Wu, “Quantized Hall conductance as a topological invariant”, Phys. Rev. B **31**, 3372–3377 (1985).

[146] L. Santos, M. A. Baranov, J. I. Cirac, H.-U. Everts, H. Fehrmann, and M. Lewenstein, “Atomic quantum gases in kagome lattices”, Phys. Rev. Lett. **93**, 030601 (2004).

[147] B. Damski, H.-U. Everts, A. Honecker, H. Fehrmann, L. Santos, and M. Lewenstein, “Atomic Fermi gas in the trimerized kagome lattice at 2/3 filling”, Phys. Rev. Lett. **95**, 060403 (2005).

[148] B. Damski, H. Fehrmann, H.-U. Everts, M. Baranov, L. Santos, and M. Lewenstein, “Quantum gases in trimerized kagome lattices”, Phys. Rev. A **72**, 053612 (2005).

[149] A. Eckardt, P. Hauke, P. Soltan-Panahi, C. Becker, K. Sengstock, and M. Lewenstein, “Frustrated quantum antiferromagnetism with ultracold bosons in a triangular lattice”, EPL **89**, 10010 (2010).

[150] J. Struck, C. Ölschläger, R. Le Targat, P. Soltan-Panahi, A. Eckardt, M. Lewenstein, P. Windpassinger, and K. Sengstock, “Quantum simulation of frustrated classical magnetism in triangular optical lattices”, Science **333**, 996–999 (2011).

[151] J. Struck, C. Ölschläger, M. Weinberg, P. Hauke, J. Simonet, A. Eckardt, M. Lewenstein, K. Sengstock, and P. Windpassinger, “Tunable gauge potential for neutral and spinless particles in driven optical lattices”, Phys. Rev. Lett. **108**, 225304 (2012).

[152] P. Hauke, O. Tieleman, A. Celi, C. Ölschläger, J. Simonet, J. Struck, M. Weinberg, P. Windpassinger, K. Sengstock, M. Lewenstein, and A. Eckardt, “Non-abelian gauge fields and topological insulators in shaken optical lattices”, Phys. Rev. Lett. **109**, 145301 (2012).

[153] P. Hauke, T. Roscilde, V. Murg, J. I. Cirac, and R. Schmied, “Modified spin-wave theory with ordering vector optimization: frustrated bosons on the spatially anisotropic triangular lattice”, New J. Phys. **12**, 053036 (2010).

[154] P. Hauke, T. Roscilde, V. Murg, J. I. Cirac, and R. Schmied, “Modified spin-wave theory with ordering vector optimization: spatially anisotropic triangular lattice and $J_1 J_2 J_3$ model with Heisenberg interactions”, New J. Phys. **13**, 075017 (2011).

[155] P. Hauke, “Quantum disorder in the spatially completely anisotropic triangular lattice”, Phys. Rev. B **87**, 014415 (2013).

[156] L. Balents, “Spin liquids in frustrated magnets”, Phys. Rev. B **464**, 199 (2010).

[157] P. W. Anderson, “Resonating valence bonds: a new kind of insulator?”, Mater. Res. Bull. **8**, 153–160 (1973).

[158] Anderson, P. W., “The resonating valence bond state in La_2CuO_4 and superconductivity”, Science **235**, 1196–1198 (1987).

[159] S. A. Kivelson, D. S. Rokhsar, and J. P. Sethna, “Topology of the resonating valence-bond state: solitons and high-T_c superconductivity”, Phys. Rev. B **35**, 8865–8868 (1987).

[160] V. Kalmeyer and R. B. Laughlin, “Equivalence of the resonating-valence-bond and fractional quantum Hall states”, Phys. Rev. Lett. **59**, 2095–2098 (1987).

[161] X. G. Wen, F. Wilczek, and A. Zee, “Chiral spin states and superconductivity”, Phys. Rev. B **39**, 11413–11423 (1989).

[162] G. Misguich and C. Lhuillier, “Two-dimensional quantum antiferromagnets”, in *Frustrated spin systems* (World Scientific, 2012), pp. 229–306.

[163] C. Lhuillier, *Frustrated quantum magnets*, Feb. 2005, arXiv:`cond-mat/0502464`.

[164] F. Alet, A. M. Walczak, and M. P. Fisher, “Exotic quantum phases and phase transitions in correlated matter”, Physica A **369**, 122–142 (2006).

[165] C. Waldtmann, H.-U. Everts, B. Bernu, C. Lhuillier, P. Sindzingre, P. Lecheminant, and L. Pierre, “First excitations of the spin 1/2 Heisenberg antiferromagnet on the kagome lattice”, Eur. Phys. J. B **2**, 501–507 (1998).

[166] N. Read and S. Sachdev, “Large-**N** expansion for frustrated quantum antiferromagnets”, Phys. Rev. Lett. **66**, 1773–1776 (1991).

[167] X. G. Wen, “Mean-field theory of spin-liquid states with finite energy gap and topological orders”, Phys. Rev. B **44**, 2664–2672 (1991).

[168] X. G. Wen, *Quantum field theory of many-body systems: From the origin of sound to an origin of light and electrons* (Oxford University Press, 2007).

[169] A. Y. Kitaev, “Fault-tolerant quantum computation by anyons”, Ann. Phys. (N. Y.) **303**, 2–30 (2003).

[170] R. Moessner and S. L. Sondhi, “Resonating valence bond phase in the triangular lattice quantum dimer model”, Phys. Rev. Lett. **86**, 1881–1884 (2001).

[171] R. Moessner and S. L. Sondhi, “Resonating valence bond liquid physics on the triangular lattice”, Prog. Theor. Phys. Supp. **145**, 37–42 (2002).

[172] O. I. Motrunich, “Variational study of triangular lattice spin 1/2 model with ring exchanges and spin liquid state in $\kappa-(\mathrm{ET})_2\mathrm{Cu}_2(\mathrm{CN})_3$”, Phys. Rev. B **72**, 045105 (2005).

[173] Y. Shimizu, K. Miyagawa, K. Kanoda, M. Maesato, and G. Saito, “Spin liquid state in an organic mott insulator with a triangular lattice”, Phys. Rev. Lett. **91**, 107001 (2003).

[174] T.-K. Ng and P. A. Lee, “Power-law conductivity inside the Mott gap: application to $\kappa-(\mathrm{BEDT-TTF})_2\mathrm{Cu}_2(\mathrm{CN})_3$”, Phys. Rev. Lett. **99**, 156402 (2007).

[175] F. L. Pratt, P. J. Baker, S. J. Blundell, T. Lancaster, S. Ohira-Kawamura, C. Baines, Y. Shimizu, K. Kanoda, I. Watanabe, and G. Saito, “Magnetic and non-magnetic phases of a quantum spin liquid”, Nature **471**, 612 (2011).

[176] T.-H. Han, J. S. Helton, S. Chu, D. G. Nocera, J. A. Rodriguez-Rivera, C. Broholm, and Y. S. Lee, “Fractionalized excitations in the spin-liquid state of a kagome-lattice antiferromagnet”, Nature **492**, 406 (2012).

[177] M. Fu, T. Imai, T.-H. Han, and Y. S. Lee, “Evidence for a gapped spin-liquid ground state in a kagome Heisenberg antiferromagnet”, Science **350**, 655–658 (2015).

[178] M. Amusia, K. Popov, V. Shaginyan, and W. Stefanowicz, *Theory of heavy-fermion compounds - Theory of strongly correlated Fermi-systems* (Springer International Publishing, 2014).

[179] S. Yan, D. A. Huse, and S. R. White, “Spin-liquid ground state of the $S = 1/2$ kagome Heisenberg antiferromagnet”, Science **332**, 1173–1176 (2011).

[180] S. Depenbrock, I. P. McCulloch, and U. Schollwöck, “Nature of the spin-liquid ground state of the $S = 1/2$ Heisenberg model on the kagome lattice”, Phys. Rev. Lett. **109**, 067201 (2012).

[181] M. Levin and X.-G. Wen, "Detecting topological order in a ground state wave function", Phys. Rev. Lett. **96**, 110405 (2006).

[182] A. Kitaev and J. Preskill, "Topological entanglement entropy", Phys. Rev. Lett. **96**, 110404 (2006).

[183] S. Furukawa and G. Misguich, "Topological entanglement entropy in the quantum dimer model on the triangular lattice", Phys. Rev. B **75**, 214407 (2007).

[184] S. V. Isakov, M. B. Hastings, and R. G. Melko, "Topological entanglement entropy of a Bose–Hubbard spin liquid", Nat. Phys. **7**, 772 (2011).

[185] Y. Zhang, T. Grover, and A. Vishwanath, "Entanglement entropy of critical spin liquids", Phys. Rev. Lett. **107**, 067202 (2011).

[186] H.-C. Jiang, Z. Wang, and L. Balents, "Identifying topological order by entanglement entropy", Nat. Phys. **8**, 902 (2012).

[187] Y. Zhang, T. Grover, and A. Vishwanath, "Topological entanglement entropy of $\mathbb{Z}_2$ spin liquids and lattice Laughlin states", Phys. Rev. B **84**, 075128 (2011).

[188] T. Grover, Y. Zhang, and A. Vishwanath, "Entanglement entropy as a portal to the physics of quantum spin liquids", New J. Phys. **15**, 025002 (2013).

[189] M. Punk, D. Chowdhury, and S. Sachdev, "Topological excitations and the dynamic structure factor of spin liquids on the kagome lattice", Nat. Phys. **10**, 289 (2014).

[190] A. Wietek, A. Sterdyniak, and A. M. Läuchli, "Nature of chiral spin liquids on the kagome lattice", Phys. Rev. B **92**, 125122 (2015).

[191] K. Kumar, K. Sun, and E. Fradkin, "Chiral spin liquids on the kagome lattice", Phys. Rev. B **92**, 094433 (2015).

[192] F. Kolley, S. Depenbrock, I. P. McCulloch, U. Schollwöck, and V. Alba, "Phase diagram of the J_1−J_2 Heisenberg model on the kagome lattice", Phys. Rev. B **91**, 104418 (2015).

[193] H.-C. Jiang, H. Yao, and L. Balents, “Spin liquid ground state of the spin-$\frac{1}{2}$ square J_1-J_2 Heisenberg model”, Phys. Rev. B **86**, 024424 (2012).

[194] S.-S. Gong, W. Zhu, and D. N. Sheng, “Emergent chiral spin liquid: fractional quantum Hall effect in a kagome Heisenberg model”, Sci. Rep. **4**, 6317 (2014).

[195] S.-S. Gong, W. Zhu, L. Balents, and D. N. Sheng, “Global phase diagram of competing ordered and quantum spin-liquid phases on the kagome lattice”, Phys. Rev. B **91**, 075112 (2015).

[196] A. Kitaev, “Anyons in an exactly solved model and beyond”, Ann. Phys. (N. Y.) **321**, January Special Issue, 2–111 (2006).

[197] I. Kimchi and A. Vishwanath, “Kitaev-Heisenberg models for iridates on the triangular, hyperkagome, kagome, fcc, and pyrochlore lattices”, Phys. Rev. B **89**, 014414 (2014).

[198] K. Li, S.-L. Yu, and J.-X. Li, “Global phase diagram, possible chiral spin liquid, and topological superconductivity in the triangular Kitaev–Heisenberg model”, New J. Phys. **17**, 043032 (2015).

[199] I. Rousochatzakis, U. K. Rössler, J. van den Brink, and M. Daghofer, “Kitaev anisotropy induces mesoscopic $\mathbb{Z}_2$ vortex crystals in frustrated hexagonal antiferromagnets”, Phys. Rev. B **93**, 104417 (2016).

[200] M. Lewenstein, A. Sanpera, V. Ahufinger, B. Damski, A. Sen(De), and U. Sen, “Ultracold atomic gases in optical lattices: mimicking condensed matter physics and beyond”, Adv. Phys. **56**, 243–379 (2007).

[201] L.-M. Duan, E. Demler, and M. D. Lukin, “Controlling spin exchange interactions of ultracold atoms in optical lattices”, Phys. Rev. Lett. **91**, 090402 (2003).

[202] R. Schmied, T. Roscilde, V. Murg, D. Porras, and J. I. Cirac, “Quantum phases of trapped ions in an optical lattice”, New J. Phys. **10**, 045017 (2008).

[203] A. Eckardt and M. Holthaus, “Avoided-level-crossing spectroscopy with dressed matter waves”, Phys. Rev. Lett. **101**, 245302 (2008).

[204] A. Zenesini, H. Lignier, D. Ciampini, O. Morsch, and E. Arimondo, "Coherent control of dressed matter waves", Phys. Rev. Lett. **102**, 100403 (2009).

[205] N. Goldman and J. Dalibard, "Periodically driven quantum systems: effective hamiltonians and engineered gauge fields", Phys. Rev. X **4**, 031027 (2014).

[206] W. Nolting and A. Ramakanth, *Quantum theory of magnetism* (Springer-Verlag Berlin Heidelberg, 2009).

[207] J. H. Xu and C. S. Ting, "Modified spin-wave theory of low-dimensional quantum spiral magnets", Phys. Rev. B **43**, 6177–6180 (1991).

[208] M. Takahashi, "Modified spin-wave theory of a square-lattice antiferromagnet", Phys. Rev. B **40**, 2494–2501 (1989).

[209] F. J. Dyson, "General theory of spin-wave interactions", Phys. Rev. **102**, 1217–1230 (1956).

[210] S. Maleev, "Scattering of slow neutrons in ferromagnets", J. Exp. Theor. Phys. **6**, 776 (1958), [Zh. Eksp. Teor. Fiz. **33**, 4, 1010 (1957)].

[211] A. W. Sandvik and C. J. Hamer, "Ground-state parameters, finite-size scaling, and low-temperature properties of the two-dimensional $S = \frac{1}{2}$ XY model", Phys. Rev. B **60**, 6588–6593 (1999).

[212] F. Pollmann, A. M. Turner, E. Berg, and M. Oshikawa, "Entanglement spectrum of a topological phase in one dimension", Phys. Rev. B **81**, 064439 (2010).

[213] F. Kolley, S. Depenbrock, I. P. McCulloch, U. Schollwöck, and V. Alba, "Entanglement spectroscopy of su(2)-broken phases in two dimensions", Phys. Rev. B **88**, 144426 (2013).

[214] P. W. Anderson, "An approximate quantum theory of the antiferromagnetic ground state", Phys. Rev. **86**, 694–701 (1952).

[215] B. Bernu, P. Lecheminant, C. Lhuillier, and L. Pierre, "Exact spectra, spin susceptibilities, and order parameter of the quantum Heisenberg antiferromagnet on the triangular lattice", Phys. Rev. B **50**, 10048–10062 (1994).

[216] M. Weinberg, C. Ölschläger, C. Sträter, S. Prelle, A. Eckardt, K. Sengstock, and J. Simonet, “Multiphoton interband excitations of quantum gases in driven optical lattices”, Phys. Rev. A **92**, 043621 (2015).

[217] J. J. Hopfield, “Neural networks and physical systems with emergent collective computational abilities”, Proc. Natl. Acad. Sci. U.S.A. **79**, 2554–2558 (1982).

[218] H. Nishimori, *Statistical physics of spin glasses and information processing: an introduction* (Oxford University Press, 2001).

[219] F. Barahona, “On the computational complexity of Ising spin glass models”, J. Phys. A **15**, 3241 (1982).

[220] A. Lucas, “Ising formulations of many **NP** problems”, Front. Physics **2**, 5 (2014).

[221] D. Sherrington and S. Kirkpatrick, “Solvable model of a spin-glass”, Phys. Rev. Lett. **35**, 1792–1796 (1975).

[222] Mézard, M., Parisi, G., Sourlas, N., Toulouse, G., and Virasoro, M., “Replica symmetry breaking and the nature of the spin glass phase”, J. Phys. (Paris) **45**, 843–854 (1984).

[223] T. F. Rønnow, Z. Wang, J. Job, S. Boixo, S. V. Isakov, D. Wecker, J. M. Martinis, D. A. Lidar, and M. Troyer, “Defining and detecting quantum speedup”, Science **345**, 420–424 (2014).

[224] H. G. Katzgraber, F. Hamze, and R. S. Andrist, “Glassy chimeras could be blind to quantum speedup: designing better benchmarks for quantum annealing machines”, Phys. Rev. X **4**, 021008 (2014).

[225] V. S. Denchev, S. Boixo, S. V. Isakov, N. Ding, R. Babbush, V. Smelyanskiy, J. Martinis, and H. Neven, “What is the computational value of finite-range tunneling?”, Phys. Rev. X **6**, 031015 (2016).

[226] A. Friedenauer, H. Schmitz, J. T. Glueckert, D. Porras, and T. Schaetz, “Simulating a quantum magnet with trapped ions”, Nat. Phys. **4**, 757 (2008).

[227] K. Kim, M.-S. Chang, R. Islam, S. Korenblit, L.-M. Duan, and C. Monroe, “Entanglement and tunable spin-spin couplings between trapped ions using multiple transverse modes”, Phys. Rev. Lett. **103**, 120502 (2009).

[228] K. Kim, M.-S. Chang, S. Korenblit, R. Islam, E. E. Edwards, J. K. Freericks, G.-D. Lin, L.-M. Duan, and C. Monroe, “Quantum simulation of frustrated Ising spins with trapped ions”, Nature **465**, 590 (2010).

[229] J. W. Britton, B. C. Sawyer, A. C. Keith, C.-C. J. Wang, J. K. Freericks, H. Uys, M. J. Biercuk, and J. J. Bollinger, “Engineered two-dimensional Ising interactions in a trapped-ion quantum simulator with hundreds of spins”, Nature **484**, 489 (2012).

[230] P. Jurcevic, B. P. Lanyon, P. Hauke, C. Hempel, P. Zoller, R. Blatt, and C. F. Roos, “Quasiparticle engineering and entanglement propagation in a quantum many-body system”, Nature **511**, 202 (2014).

[231] P. Richerme, Z.-X. Gong, A. Lee, C. Senko, J. Smith, M. Foss-Feig, S. Michalakis, A. V. Gorshkov, and C. Monroe, “Non-local propagation of correlations in quantum systems with long-range interactions”, Nature **511**, 198 (2014).

[232] D. Porras and J. I. Cirac, “Effective quantum spin systems with trapped ions”, Phys. Rev. Lett. **92**, 207901 (2004).

[233] R. Barends, J. Kelly, A. Megrant, A. Veitia, D. Sank, E. Jeffrey, T. C. White, J. Mutus, A. G. Fowler, B. Campbell, Y. Chen, Z. Chen, B. Chiaro, A. Dunsworth, C. Neill, P. O’Malley, P. Roushan, A. Vainsencher, J. Wenner, A. N. Korotkov, A. N. Cleland, and J. M. Martinis, “Superconducting quantum circuits at the surface code threshold for fault tolerance”, Nature **508**, 500–503 (2014).

[234] N. M. Linke, D. Maslov, M. Roetteler, S. Debnath, C. Figgatt, K. A. Landsman, K. Wright, and C. Monroe, “Experimental comparison of two quantum computing architectures”, Proc. Natl. Acad. Sci. U.S.A. **114**, 3305–3310 (2017).

[235] C. Monroe and J. Kim, “Scaling the ion trap quantum processor”, Science **339**, 1164–1169 (2013).

[236] M. H. Devoret and R. J. Schoelkopf, “Superconducting circuits for quantum information: An outlook”, Science **339**, 1169–1174 (2013).

[237] S. Kirkpatrick, C. D. Gelatt, and M. P. Vecchi, “Optimization by simulated annealing”, Science **220**, 671–680 (1983).

[238] V. Černý, “Thermodynamical approach to the traveling salesman problem: An efficient simulation algorithm”, J. Optim. Theory. Appl. **45**, 41–51 (1985).

[239] J. Brooke, D. Bitko, T. F. Rosenbaum, and G. Aeppli, “Quantum annealing of a disordered magnet”, Science **284**, 779–781 (1999).

[240] T. Kadowaki and H. Nishimori, “Quantum annealing in the transverse Ising model”, Phys. Rev. E **58**, 5355–5363 (1998).

[241] E. Farhi, J. Goldstone, S. Gutmann, J. Lapan, A. Lundgren, and D. Preda, “A quantum adiabatic evolution algorithm applied to random instances of an **NP**-complete problem”, Science **292**, 472–475 (2001).

[242] T. Albash and D. A. Lidar, “Adiabatic quantum computation”, Rev. Mod. Phys. **90**, 015002 (2018).

[243] M. W. Johnson, M. H. S. Amin, S. Gildert, T. Lanting, F. Hamze, N. Dickson, R. Harris, A. J. Berkley, J. Johansson, P. Bunyk, E. M. Chapple, C. Enderud, J. P. Hilton, K. Karimi, E. Ladizinsky, N. Ladizinsky, T. Oh, I. Perminov, C. Rich, M. C. Thom, E. Tolkacheva, C. J. S. Truncik, S. Uchaikin, J. Wang, B. Wilson, and G. Rose, “Quantum annealing with manufactured spins”, Nature **473**, 194 (2011).

[244] S. Boixo, T. F. Rønnow, S. V. Isakov, Z. Wang, D. Wecker, D. A. Lidar, J. M. Martinis, and M. Troyer, “Evidence for quantum annealing with more than one hundred qubits”, Nat. Phys. **10**, 218–224 (2014).

[245] T. M. Lanting, *D-wave 2000q*, `https://www.youtube.com/watch?v=_Y9sVY-XBfI`, Youtube, 2017, Adiabatic Quantum Computing Conference 2017 (AQC 2017).

[246] T. Graß, A. Celi, G. Pagano, and M. Lewenstein, “Chiral spin currents in a trapped-ion quantum simulator using Floquet engineering”, Phys. Rev. A **97**, 010302 (2018).

[247] T. Graß, M. Lewenstein, and A. Bermudez, “Dual trapped-ion quantum simulators: an alternative route towards exotic quantum magnets”, New J. Phys. **18**, 033011 (2016).

[248] T. Graß, C. Muschik, A. Celi, R. W. Chhajlany, and M. Lewenstein, “Synthetic magnetic fluxes and topological order in one-dimensional spin systems”, Phys. Rev. A **91**, 063612 (2015).

[249] P. Nevado, S. Fernández-Lorenzo, and D. Porras, “Topological edge states in periodically driven trapped-ion chains”, Phys. Rev. Lett. **119**, 210401 (2017).

[250] P. Nevado and D. Porras, “Rabi lattice models with discrete gauge symmetry: phase diagram and implementation in trapped-ion quantum simulators”, Phys. Rev. A **92**, 013624 (2015).

[251] P. Nevado and D. Porras, “Hidden frustrated interactions and quantum annealing in trapped-ion spin-phonon chains”, Phys. Rev. A **93**, 013625 (2016).

[252] A. Lemmer, C. Cormick, D. Tamascelli, T. Schaetz, S. F. Huelga, and M. B. Plenio, “A trapped-ion simulator for spin-boson models with structured environments”, New J. Phys. **20**, 073002 (2018).

[253] P. Hauke, L. W. Bonnes, M. Heyl, and W. Lechner, “Probing entanglement in adiabatic quantum optimization with trapped ions”, Front. Physics **3**, 21, 21 (2015).

[254] F. Mintert and C. Wunderlich, “Ion-trap quantum logic using long-wavelength radiation”, Phys. Rev. Lett. **87**, 257904 (2001).

[255] H. Schmitz, A. Friedenauer, C. Schneider, R. Matjeschk, M. Enderlein, T. Huber, J. Glueckert, D. Porras, and T. Schaetz, "The "arch" of simulating quantum spin systems with trapped ions", Appl. Phys. B **95**, 195–203 (2009).

[256] C.-C. J. Wang and J. K. Freericks, "Intrinsic phonon effects on analog quantum simulators with ultracold trapped ions", Phys. Rev. A **86**, 032329 (2012).

[257] M. Pons, V. Ahufinger, C. Wunderlich, A. Sanpera, S. Braungardt, A. Sen(De), U. Sen, and M. Lewenstein, "Trapped ion chain as a neural network: error resistant quantum computation", Phys. Rev. Lett. **98**, 023003 (2007).

[258] P. Strack and S. Sachdev, "Dicke quantum spin glass of atoms and photons", Phys. Rev. Lett. **107**, 277202 (2011).

[259] S. Gopalakrishnan, B. L. Lev, and P. M. Goldbart, "Frustration and glassiness in spin models with cavity-mediated interactions", Phys. Rev. Lett. **107**, 277201 (2011).

[260] P. Rotondo, M. Cosentino Lagomarsino, and G. Viola, "Dicke simulators with emergent collective quantum computational abilities", Phys. Rev. Lett. **114**, 143601 (2015).

[261] D. L. Stein and C. M. Newman, "Spin glasses: Old and new complexity", Complex Syst. **20**, 115 (2011).

[262] D. L. Stein and C. M. Newman, *Spin glasses and complexity* (Princeton University Press, 2013).

[263] M. A. Moore, H. Bokil, and B. Drossel, "Evidence for the droplet picture of spin glasses", Phys. Rev. Lett. **81**, 4252–4255 (1998).

[264] T. Aspelmeier, H. G. Katzgraber, D. Larson, M. A. Moore, M. Wittmann, and J. Yeo, "Finite-size critical scaling in Ising spin glasses in the mean-field regime", Phys. Rev. E **93**, 032123 (2016).

[265] D. J. Amit, H. Gutfreund, and H. Sompolinsky, "Storing infinite numbers of patterns in a spin-glass model of neural networks", Phys. Rev. Lett. **55**, 1530–1533 (1985).

[266] "Statistical mechanics of neural networks near saturation", Ann. Phys. (N. Y.) **173**, 195–203 (1987).

[267] G. Parisi, "The order parameter for spin glasses: a function on the interval 0-1", J. Phys. A **13**, 1101 (1980).

[268] M. Mezard, G. Parisi, and M. A. Virasoro, *Spin glass theory and beyond* (World Scientific, 2014).

[269] E. Vincent, "Ageing, rejuvenation and memory: the example of spin-glasses", in *Ageing and the glass transition*, edited by M. Henkel, M. Pleimling, and R. Sanctuary (Springer Berlin Heidelberg, Berlin, Heidelberg, 2007), pp. 7–60.

[270] D. S. Fisher and D. A. Huse, "Ordered phase of short-range Ising spin-glasses", Phys. Rev. Lett. **56**, 1601–1604 (1986).

[271] F. Lefloch, J. Hammann, M. Ocio, and E. Vincent, "Can aging phenomena discriminate between the droplet model and a hierarchical description in spin glasses?", EPL **18**, 647 (1992).

[272] D. Mattis, "Solvable spin systems with random interactions", Phys. Lett. A **56**, 421–422 (1976).

[273] S. Mertens, "Phase transition in the number partitioning problem", Phys. Rev. Lett. **81**, 4281–4284 (1998).

[274] S. Mertens, *The Easiest Hard Problem: Number Partitioning*, Oct. 2003, arXiv:`cond-mat/0310317`.

[275] A. Steane, "The ion trap quantum information processor", Appl. Phys. B **64**, 623–643 (1997).

[276] D. James, "Quantum dynamics of cold trapped ions with application to quantum computation", Appl. Phys. B **66**, 181–190 (1998).

[277] A. Friedenauer, H. Schmitz, J. T. Glueckert, D. Porras, and T. Schaetz, "Simulating a quantum magnet with trapped ions", Nat. Phys. **4**, 757 (2008).

[278] A. Bermudez, T. Schaetz, and D. Porras, “Photon-assisted-tunneling toolbox for quantum simulations in ion traps”, New J. Phys. **14**, 053049 (2012).

[279] P. Hauke, L. Bonnes, M. Heyl, and W. Lechner, “Probing entanglement in adiabatic quantum optimization with trapped ions”, Front. Physics **3**, 21 (2015).

[280] S. Korenblit, D. Kafri, W. C. Campbell, R. Islam, E. E. Edwards, Z.-X. Gong, G.-D. Lin, L.-M. Duan, J. Kim, K. Kim, and C. Monroe, “Quantum simulation of spin models on an arbitrary lattice with trapped ions”, New J. Phys. **14**, 095024 (2012).

[281] T. J. Park and J. C. Light, “Unitary quantum time evolution by iterative Lanczos reduction”, J. Chem. Phys. **85**, 5870–5876 (1986).

[282] P. Jurcevic, H. Shen, P. Hauke, C. Maier, T. Brydges, C. Hempel, B. P. Lanyon, M. Heyl, R. Blatt, and C. F. Roos, “Direct observation of dynamical quantum phase transitions in an interacting many-body system”, Phys. Rev. Lett. **119**, 080501 (2017).

[283] K. Mølmer, Y. Castin, and J. Dalibard, “Monte Carlo wave-function method in quantum optics”, J. Opt. Soc. Am. B **10**, 524–538 (1993).

[284] N. Sourlas, “Spin-glass models as error-correcting codes”, Nature **339**, 693 (2014).

[285] M. Mielenz, H. Kalis, M. Wittemer, F. Hakelberg, R. Schmied, M. Blain, P. Maunz, D. Leibfried, U. Warring, and T. Schaetz, *Freely configurable quantum simulator based on a two-dimensional array of individually trapped ions*, Dec. 2015, arXiv:`1512.03559 [quant-ph]`.

[286] H. Kalis, F. Hakelberg, M. Wittemer, M. Mielenz, U. Warring, and T. Schaetz, “Motional-mode analysis of trapped ions”, Phys. Rev. A **94**, 023401 (2016).

[287] A. Lambrecht, J. Schmidt, P. Weckesser, M. Debatin, L. Karpa, and T. Schaetz, “Long lifetimes and effective isolation of ions in optical and electrostatic traps”, Nat. Photonics **11**, 704–707 (2017).

[288] H.-K. Li, E. Urban, C. Noel, A. Chuang, Y. Xia, A. Ransford, B. Hemmerling, Y. Wang, T. Li, H. Häffner, and X. Zhang, "Realization of translational symmetry in trapped cold ion rings", Phys. Rev. Lett. **118**, 053001 (2017).

[289] J. Zhang, P. W. Hess, A. Kyprianidis, P. Becker, A. Lee, J. Smith, G. Pagano, I.-D. Potirniche, A. C. Potter, A. Vishwanath, N. Y. Yao, and C. Monroe, "Observation of a discrete time crystal", Nature **543**, 217 (2017).

[290] J. Zhang, G. Pagano, P. W. Hess, A. Kyprianidis, P. Becker, H. Kaplan, A. V. Gorshkov, Z.-X. Gong, and C. Monroe, "Observation of a many-body dynamical phase transition with a 53-qubit quantum simulator", Nature **551**, 601–604 (2017).

[291] A. Safavi-Naini, R. J. Lewis-Swan, J. G. Bohnet, M. Garttner, K. A. Gilmore, E. Jordan, J. Cohn, J. K. Freericks, A. M. Rey, and J. J. Bollinger, *Exploring adiabatic quantum dynamics of the Dicke model in a trapped ion quantum simulator*, Nov. 2017, arXiv:`1711.07392 [quant-ph]`.

[292] D. Walls and G. Milburn, 2nd Edition (Springer, Berlin, 2008).

[293] A. Piñeiro Orioli, A. Safavi-Naini, M. L. Wall, and A. M. Rey, "Nonequilibrium dynamics of spin-boson models from phase-space methods", Phys. Rev. A **96**, 033607 (2017).

[294] M. L. Wall, A. Safavi-Naini, and A. M. Rey, "Boson-mediated quantum spin simulators in transverse fields: XY model and spin-boson entanglement", Phys. Rev. A **95**, 013602 (2017).

[295] M. Gärttner, J. G. Bohnet, A. Safavi-Naini, M. L. Wall, J. J. Bollinger, and A. M. Rey, "Measuring out-of-time-order correlations and multiple quantum spectra in a trapped-ion quantum magnet", Nat. Phys. **13**, 781–786 (2017).

[296] M. L. Wall, A. Safavi-Naini, and A. M. Rey, "Simulating generic spin-boson models with matrix product states", Phys. Rev. A **94**, 053637 (2016).

[297] L. C. Venuti, T. Albash, D. A. Lidar, and P. Zanardi, "Adiabaticity in open quantum systems", Phys. Rev. A **93**, 032118 (2016).

[298] K. Nishimura, H. Nishimori, A. J. Ochoa, and H. G. Katzgraber, "Retrieving the ground state of spin glasses using thermal noise: performance of quantum annealing at finite temperatures", Phys. Rev. E **94**, 032105 (2016).

[299] K. Nishimura and H. Nishimori, "Quantum annealing with a nonvanishing final value of the transverse field", Phys. Rev. A **96**, 042310 (2017).

[300] N. Chancellor, S. Szoke, W. Vinci, G. Aeppli, and P. A. Warburton, "Maximum-entropy inference with a programmable annealer", Sci. Rep. **6**, 22318 (2016).

[301] E. Hairer, S. P. Nørsett, and G. Wanner, *Solving Ordinary Differential Equations I. Nonstiff Problems.* 2nd ed., Springer Series in Comput. Mathematics (Springer-Verlag, Berlin Heidelberg, 1993).

[302] N. G. Dickson, M. W. Johnson, M. H. Amin, R. Harris, F. Altomare, A. J. Berkley, P. Bunyk, J. Cai, E. M. Chapple, P. Chavez, F. Cioata, T. Cirip, P. deBuen, M. Drew-Brook, C. Enderud, S. Gildert, F. Hamze, J. P. Hilton, E. Hoskinson, K. Karimi, E. Ladizinsky, N. Ladizinsky, T. Lanting, T. Mahon, R. Neufeld, T. Oh, I. Perminov, C. Petroff, A. Przybysz, C. Rich, P. Spear, A. Tcaciuc, M. C. Thom, E. Tolkacheva, S. Uchaikin, J. Wang, A. B. Wilson, Z. Merali, and G. Rose, "Thermally assisted quantum annealing of a 16-qubit problem", Nat. Commun. **4**, 1903 (2013).

[303] M. Ramm, T. Pruttivarasin, and H. Häffner, "Energy transport in trapped ion chains", New J. Phys. **16**, 063062 (1989).

[304] C. F. Roos, D. Leibfried, A. Mundt, F. Schmidt-Kaler, J. Eschner, and R. Blatt, "Experimental demonstration of ground state laser cooling with electromagnetically induced transparency", Phys. Rev. Lett. **85**, 5547–5550 (2000).

[305] Y. Lin, J. P. Gaebler, T. R. Tan, R. Bowler, J. D. Jost, D. Leibfried, and D. J. Wineland, "Sympathetic electromagnetically-induced-transparency laser cooling of motional modes in an ion chain", Phys. Rev. Lett. **110**, 153002 (2013).

[306] R. Lechner, C. Maier, C. Hempel, P. Jurcevic, B. P. Lanyon, T. Monz, M. Brownnutt, R. Blatt, and C. F. Roos, "Electromagnetically-induced-transparency ground-state cooling of long ion strings", Phys. Rev. A **93**, 053401 (2016).

[307] T. Fukui, Y. Hatsugai, and H. Suzuki, "Chern numbers in discretized Brillouin zone: Efficient method of computing (spin) Hall conductances", J. Phys. Soc. Jpn. **74**, 1674–1677 (2005).

[308] A. V. Ponomarev, S. Denisov, and P. Hänggi, "Thermal equilibration between two quantum systems", Phys. Rev. Lett. **106**, 010405 (2011).

[309] A. V. Ponomarev, S. Denisov, and P. Hänggi, "Lévy distribution in many-particle quantum systems", Phys. Rev. A **81**, 043615 (2010).

[310] A. V. Ponomarev, S. Denisov, and P. Hänggi, "ac-Driven atomic quantum motor", Phys. Rev. Lett. **102**, 230601 (2009).